

Measurement of the Electrical Resistivity Profile in the Madison Symmetric Torus

by

Jay K. Anderson

A dissertation submitted in partial fulfillment of the  
requirements for the degree of

Doctor of Philosophy

(Physics)

at the

University of Wisconsin–Madison

2001

# Measurement of the Electrical Resistivity Profile in the Madison Symmetric Torus

Jay K. Anderson

Under the supervision of Assistant Professor Cary B. Forest

At the University of Wisconsin-Madison

## Abstract

A two dimensional, toroidal equilibrium reconstruction code has been developed for the reversed field pinch. The parallel current density profile has been measured by incorporating several diagnostics into the code. A new fitting technique of derivatives of magnetic signals has been developed to determine the inductive electric field profile. During periods of low MHD activity, Ohm's law obeys its simplest form and the ratio of measured E and J profiles determines the plasma electrical resistivity profile. Presented is an upper bound of  $Z_{eff}$  through spectroscopic measurements of bremsstrahlung and several pollutants in the near infrared wavelength region. This enables a comparison of the measured resistivity with Spitzer and neoclassical models.

The computed resistivity profile is consistent with the Spitzer model and there is no need to invoke an anomaly factor when describing the resistivity in the reversed field pinch. The second primary result is that a bremsstrahlung measurement in MST is not feasible over the majority of MST operating conditions. An overwhelming emission continuum due to neutral particles and wall recycling complicates extraction of the relatively dim bremsstrahlung contribution. The standard definition of  $Z_{eff} = \frac{\sum_s n_s Z_s^2}{n_e}$  is not sufficient to describe collisionality in the edge of MST due to the effects of non-fully stripped impurity ions.

Second version distributed. Corrected are Figure 6.12 and several typographical errors.

## Acknowledgements

The work presented in this dissertation is far from an individual effort. The first order of business is to thank the many that made this come together. Many thanks to my committee (Stewart Prager, Clint Sprott, Ray Fonck and Dave Anderson) for finding time to go through this document, and particularly to my adviser, Cary Forest, for his interest, contributions, enthusiasm and guidance in this work. You need to relax a bit, pal.

Much of the work here pertains to the attempts at measuring  $Z_{eff}$  and due credit should be given to many. Those who most directly contributed to the cause while I was on the team are Dan Den Hartog, Philip Andrew, Brett Chapman, Susana Castillo, Darren Craig, Stefan Gerhardt, and Rob O'Connell. A thank you also goes to Dr. Jim Lawler for applying a small slice of his expertise to this problem.

To the scientific staff, including John Sarff, Dan Den Hartog, Gennady Fiksel, Chris Hegna, Abdul Almagri, Darren Craig, Brett Chapman, Diane Demers, and Rob O'Connell: thank you. Your advice and insight have definitely been needed. In the interest of brevity specifics cannot be mentioned; all input and discussions have been useful and greatly appreciated.

A thank you goes to the MST engineering and technical staff, which certainly will never be matched in its quality nor breadth of knowledge: Paul Nomm, Tom Lovell, Mark Thomas, Steve Oliva, Jim Adney, Paul Wilhite, Larry Smith, Bill Zimmerman, Mikhail Reyfman, Don Holly, John Laufenberg, and Roch Kendrick. If one had to hand pick a dozen people who could collectively accomplish anything, this group might be the best bet. Many thanks also to Dale Schutte, Linda Jones and Kay Shatrawka for keeping this place up and running. Lee Potratz and the others in the machine shop certainly deserve my gratitude for putting up with inferior drawings and a variety of creative requests.

I'd also like to thank the undergraduates who were so unfortunate to draw me as a TA during the 2000-2001 school year. The hours in class were therapy to a strong burnout candidate.

My peers during 17<sup>th</sup> to 22<sup>nd</sup> grade, fellow graduate students, have made a huge impact. To the 'old' guys: you'll not be forgotten. In particular, Jim Chapman, Eduardo Fernandez, Kevin Mirus, Paul Fontana (that was only a warning), Alex Hansen, Ching-Shih Chiang, Nick Lanier,

and Neal Crocker- without all of your guidance years ago, I could never have become the qualified MST operator I am today. My contemporaries and officemates deserve specific mention: Art Blair for convenient RF consulting, the HIBP guys Uday Shah and Dr. J. Lei for actually using MSTFit, Cavendish McKay and the Escort with an attitude, Susana Castillo and shared  $Z_{eff}$  frustrations, Mark Nornberg- everyone's L<sup>A</sup>T<sub>E</sub>X companion, and Derek Bayer- the MST third deck invader.

A big thank you goes to the basketball, softball, tennis, volleyball, and card players, and especially the biking gang for keeping me alive. Sleep deprivation would probably have gotten the best of me without a little exercise and relaxation. Between the biweekly *Sunrise Series*, a weekend *Buss Stop Run!* and the annual *Suicide Century* there've been some pretty good times. It's awfully hard to beat the sunrise over Lake Monona. A few of the many who I've had the pleasure of logging many miles with are Don Holly, Adam Bayliss, John Wright and Diane Demers. I'm particularly indebted to Ted Biewer, for everything from literally thousands of miles of drafting, to making the grad school experience fairly tolerable to contributing enormously to the research presented here. I'll be forever grateful for you sharing your technical expertise in differential cross section (DCS) theory.

Finally, to my family and those closest to me, whom I have most regrettably neglected in an attempt to finish this work: Thank you for the years of steadfast support. The sacrifices made during graduate school have been enormous; lost time cannot be made up. Reflecting on the choices you make to meet career goals can go on for a long time; I'll wonder for years if all the decisions made were the right ones. Some things, however, I just know.

This work has been partially supported by USDOE Magnetic Fusion Science Fellowship program.

# Contents

<i>Abstract</i> . . . . .	i
<i>Acknowledgments</i> . . . . .	i
<i>Table of Contents</i> . . . . .	iv
<i>List of Tables</i> . . . . .	ix
<i>List of Figures</i> . . . . .	x
<b>1 Introduction</b>	<b>1</b>
1.1 Motivation . . . . .	2
1.2 The Reversed Field Pinch . . . . .	2
1.2.1 The Madison Symmetric Torus . . . . .	4
1.2.2 Pulsed Poloidal Current Drive . . . . .	8
1.2.3 Background of Equilibrium Studies in the RFP . . . . .	11
1.2.4 Need for Improved Modeling . . . . .	16
1.2.5 Ohm's Law and Resistivity in the RFP . . . . .	18
1.3 Electrical Resistivity . . . . .	20
1.3.1 Measurement of $Z_{eff}$ . . . . .	23
1.4 Overview of this Work . . . . .	26
<b>2 Hardware</b>	<b>33</b>

2.1	General Survey Spectrometer . . . . .	34
2.1.1	Wavelength Calibration . . . . .	34
2.1.2	Intensity Calibration . . . . .	36
2.2	Filtered Photodiode Array . . . . .	38
2.2.1	Wavelength Response . . . . .	41
2.2.2	Photodiode Calibration Procedure . . . . .	43
2.2.3	H $_{\alpha}$ Measurement and Calibration . . . . .	46
2.2.4	Colinear Arrangement . . . . .	48
2.3	Monochromator and Photomultiplier Tube . . . . .	49
2.4	Conclusion . . . . .	52
<b>3</b>	<b>Feasibility of a Bremsstrahlung Measurement on MST</b>	<b>54</b>
3.1	Introduction . . . . .	55
3.2	Electron-Ion Bremsstrahlung . . . . .	56
3.3	Gaunt Factor Calculation . . . . .	61
3.3.1	Power Law Fit . . . . .	61
3.3.2	Non-Maxwellian effects . . . . .	63
3.4	Wavelength Considerations . . . . .	63
3.5	Pollutant Radiation in MST . . . . .	67
3.5.1	Line Radiation . . . . .	67
3.5.2	Recombination . . . . .	72
3.5.3	Blackbody Radiation . . . . .	75
3.5.4	Molecular Hydrogen Emission . . . . .	78
3.5.5	H $_{\alpha}$ Emission . . . . .	80
3.5.6	Electron-Atom Bremsstrahlung . . . . .	83
3.5.7	Continuous Emission from Charge Exchange Recombination . . . . .	88

3.6	Coping with Pollution . . . . .	90
3.6.1	Separation of Measured NIR Signal . . . . .	92
3.7	Screening Effect of Non-fully Stripped Ions . . . . .	94
3.8	Conclusions . . . . .	102
<b>4</b>	<b>Resistivity Profile Based on Measured <math>Z_{eff}</math></b>	<b>107</b>
4.1	Bremsstrahlung Measurement of $Z_{eff}$ . . . . .	108
4.2	Discussion . . . . .	115
4.2.1	Impurity Density Measurements . . . . .	117
4.2.2	Rutherford Scattering . . . . .	117
4.2.3	Radiated Power . . . . .	118
4.3	Resistivity Models . . . . .	120
4.4	Modeled Resistivity Profile . . . . .	124
4.5	Summary . . . . .	125
<b>5</b>	<b>Reconstruction of the RFP Equilibrium: MSTFit</b>	<b>127</b>
5.1	Introduction . . . . .	128
5.1.1	Grad Shafranov Equilibrium in an Axisymmetric Torus . . . . .	128
5.1.2	Reconstructing the RFP Equilibrium . . . . .	133
5.1.3	Free Parameters . . . . .	134
5.2	Solution Method . . . . .	139
5.2.1	Initialization . . . . .	141
5.2.2	Computation of Grad Shafranov Equilibrium . . . . .	141
5.2.3	Comparison to Data . . . . .	147
5.2.4	Minimization . . . . .	148
5.2.5	Code Termination . . . . .	150
5.3	Linear versus Nonlinear Fitting . . . . .	151

5.4	Data Fitting . . . . .	151
5.4.1	External Diagnostics . . . . .	152
5.4.2	Edge Diagnostics . . . . .	156
5.4.3	Internal Magnetics . . . . .	158
5.4.4	Pressure Diagnostics . . . . .	167
5.5	Output . . . . .	169
5.5.1	Equilibrium Quantities . . . . .	169
5.5.2	Inversions . . . . .	170
5.6	Uncertainty Analysis of Equilibrium . . . . .	173
5.6.1	Error in Equilibrium Quantities . . . . .	173
5.6.2	Sensitivity Study to Internal Diagnostics . . . . .	176
5.6.3	Error Introduced by Modeling . . . . .	179
5.7	Reconstructed MHD Equilibrium . . . . .	179
5.8	Analysis of 400kA PPCD Discharge . . . . .	187
5.9	Summary . . . . .	189
<b>6</b>	<b>Determination of the Inductive Electric Field Profile</b>	<b>191</b>
6.1	Introduction . . . . .	192
6.1.1	Calculation of Parallel Electric Field . . . . .	193
6.1.2	Power Deposition Profile . . . . .	197
6.2	Finite Difference of Equilibria . . . . .	199
6.2.1	Application of Finite Difference Technique to Standard Plasma . . . . .	202
6.2.2	Finite Difference Calculation in PPCD Plasma . . . . .	204
6.3	Time Derivative Fitting . . . . .	208
6.3.1	Evaluation of Solution . . . . .	209
6.3.2	Edge Magnetics . . . . .	210

6.3.3	Internal Magnetics . . . . .	211
6.3.4	Pressure Diagnostics . . . . .	213
6.3.5	Results of Time Derivative Fitting, PPCD Plasma . . . . .	213
6.4	Ohm's Law and Resistivity . . . . .	215
6.5	Uncertainty in Electric Field . . . . .	216
6.6	Conclusions . . . . .	217
<b>7</b>	<b>Conclusions: Agreement of Measured and Modeled Resistivity Profiles</b>	<b>219</b>
7.1	Summary . . . . .	220
7.2	Results . . . . .	221
7.3	Future Work . . . . .	222
7.3.1	Resistivity, $Z_{eff}$ Measurements . . . . .	222
7.3.2	Equilibrium and Electric Field Modeling . . . . .	225
7.3.3	General . . . . .	226
	<b>Appendix A: Multicolor Background Survey</b>	<b>228</b>
A.1	Visible and NIR Continuum Wavelength Response . . . . .	228
A.2	Line Integrated Signals . . . . .	233
A.3	Behavior of Continuum Measurements Versus $H_{\alpha}$ Emission . . . . .	236
	<b>Appendix B: MSTFit Outputs</b>	<b>241</b>
B.1	Equilibrium Quantities . . . . .	241
B.2	Particle Transport Analysis . . . . .	244
B.3	Energy Transport Analysis . . . . .	247
B.4	MHD Stability Analysis . . . . .	254
B.5	EQDSK Files . . . . .	254

# List of Tables

1.1	Published Bremsstrahlung Measurements . . . . .	24
2.1	H $_{\alpha}$ Pollution of Visible and NIR Bremsstrahlung Attempts . . . . .	42
2.2	Typical Photodiode Calibration versus Wavelength . . . . .	45
3.1	Blackbody Emission from Hot Al Wall . . . . .	76
4.1	Total Input Power Based on $Z_{eff}$ Assumptions . . . . .	115
5.1	Diagnostics Incorporated in MSTFit . . . . .	152
6.1	Diagnostics Incorporated in $\frac{d}{dt}$ MSTFit . . . . .	210
B.1	Standard MSTFit Flux Surface-averaged Profiles and 0D Quantities . . . . .	243
B.2	Standard Outputs of Particle Transport Analysis . . . . .	246
B.3	Standard Outputs of Energy Transport Analysis . . . . .	253

# List of Figures

1.1	Generic Toroidal Pinch Experiment . . . . .	3
1.2	Typical Magnetic Field Profiles in the RFP . . . . .	4
1.3	The Madison Symmetric Torus . . . . .	5
1.4	Operational Signals, Standard MST Discharge . . . . .	7
1.5	Operational Signals, PPCD Discharge . . . . .	9
1.6	Low Magnetic Fluctuation Level During PPCD Experiments . . . . .	10
1.7	Evolution of Equilibrium Through a Sawtooth Cycle . . . . .	13
1.8	Cylindrical Models of the RFP Equilibrium . . . . .	15
1.9	Insufficiency of Edge Diagnostics Alone in Equilibrium Reconstruction . . . . .	17
1.10	Measured Spectrum with Expected Bremsstrahlung. . . . .	25
2.1	CVI Wavelength Calibration . . . . .	35
2.2	Lab Sphere Output . . . . .	36
2.3	CCD Intensity Calibration . . . . .	37
2.4	NIR Bremsstrahlung Viewing Chords on MST . . . . .	38
2.5	Photodiode Amplifier Schematic . . . . .	39
2.6	Wavelength Response of NIR Filters . . . . .	41
2.7	Filter Rejection of $H_{\alpha}$ Emission . . . . .	42
2.8	Photodiode System Calibration . . . . .	43

2.9	Photodiode Linearity . . . . .	44
2.10	Typical Photodiode Signal . . . . .	45
2.11	Transmission of $H_{\alpha}$ Filter . . . . .	46
2.12	Colinear NIR/ $H_{\alpha}$ Measurement . . . . .	48
2.13	Monochromator Dial Calibration . . . . .	49
2.14	Narrow Band Visible Bremsstrahlung Measurement . . . . .	50
2.15	Narrow Band Wavelength Response . . . . .	50
2.16	Photomultiplier Tube Calibration . . . . .	51
2.17	PMT Signal . . . . .	51
3.1	Measured Visible Spectrum in MST . . . . .	55
3.2	Electron-Ion Interaction . . . . .	57
3.3	Gaunt Factor in MST Plasmas . . . . .	62
3.4	Non-Maxwellian Distribution Effects on Measured Bremsstrahlung . . . . .	64
3.5	Evaluation of Ultraviolet Bremsstrahlung Attempt . . . . .	66
3.6	Measured Background Emission and Expected Bremsstrahlung . . . . .	68
3.7	Visible Line Free Region in MST . . . . .	69
3.8	Line Free and Wide Band Visible Measurements . . . . .	70
3.9	NIR Spectrum in MST . . . . .	71
3.10	NIR Spectrum in MST During Pulsed Discharge Cleaning . . . . .	72
3.11	Radiative Recombination Cartoon . . . . .	73
3.12	NIR Emission During Recombination Phase of Discharge . . . . .	74
3.13	Calculated Recombination Contribution . . . . .	75
3.14	Post-Discharge Radiation . . . . .	76
3.15	Blackbody Radiation Test . . . . .	77
3.16	$D_2$ Emission in MST . . . . .	80

3.17 Atomic Ionizations per $H_{\alpha}$ Photon . . . . .	81
3.18 Electron-neutral Bremsstrahlung . . . . .	83
3.19 Neutral Density . . . . .	84
3.20 Relative Strength of Neutral Bremsstrahlung . . . . .	87
3.21 Variation of Slope with Viewing Chord . . . . .	88
3.22 Rate Coefficients for Radiative Processes in MST . . . . .	88
3.23 Continuous Emission from Charge Exchange . . . . .	89
3.24 NIR vs $H_{\alpha}$ Emission . . . . .	91
3.25 NIR- $H_{\alpha}$ Slope Versus $n_e$ and $T_e$ . . . . .	92
3.26 NIR Emission and Neutral Density Versus Time: Helium Discharge . . . . .	93
3.27 Linearity of NIR and He I Signals: Helium Discharge . . . . .	94
3.28 Extraction of Bremsstrahlung Emission from NIR, $H_{\alpha}$ Signals: Standard Plasma . . . . .	95
3.29 Extraction of Bremsstrahlung Emission from NIR, $H_{\alpha}$ Signals: PPCD Plasma . . . . .	96
3.30 Screened Ionic Potential Effects of Helium, Carbon, Oxygen . . . . .	98
3.31 Screened Ionic Potential Effects of Aluminum . . . . .	99
3.32 NIR and $H_{\alpha}$ Emission in an Impure Plasma . . . . .	100
3.33 Impurity and Bremsstrahlung Signals in an Impure Plasma . . . . .	101
4.1 Bremsstrahlung Emission Determined by Extrapolation to Zero Pollutant . . . . .	108
4.2 Line Integrated Bremsstrahlung Signals . . . . .	109
4.3 Inverted Bremsstrahlung Emission Profile . . . . .	110
4.4 Inverted Electron Density Profile . . . . .	112
4.5 Calculated $Z_{eff}$ Profile . . . . .	113
4.6 $Z_{eff}$ Profile with Corrected Edge Emission . . . . .	114
4.7 Simulations of Hard x-ray Flux . . . . .	116
4.8 Total Radiated Power During PPCD . . . . .	119

4.9	Trapped Particle Fraction . . . . .	123
4.10	Modeled Resistivity Profiles Based on $T_e$ and $Z_{eff}$ . . . . .	124
5.1	MSTFit Coordinate System . . . . .	129
5.2	MSTFit Basis Functions . . . . .	136
5.3	Free Parameter Position Mapping . . . . .	137
5.4	Triangular Mesh Grid in MSTFit Solution . . . . .	139
5.5	MSTFit Flow Chart . . . . .	140
5.6	Modeling of Flux Conserving Shell . . . . .	146
5.7	Fixed Boundary Green's Tables . . . . .	147
5.8	Downhill Simplex Minimization Technique . . . . .	150
5.9	Poloidal Array Diagnostic . . . . .	154
5.10	Correction of Systematic Error in Poloidal Array . . . . .	156
5.11	Edge Current Measurement Constraint . . . . .	157
5.12	FIR Polarimeter Diagnostic . . . . .	159
5.13	$q(0)$ Constraint to MSTFit . . . . .	162
5.14	$q(0)$ Fitting Contribution to $\chi^2$ . . . . .	163
5.15	The Motional Stark Effect Diagnostic . . . . .	164
5.16	The Heavy Ion Beam Probe Diagnostic . . . . .	165
5.17	HIBP Constraint on the Equilibrium . . . . .	166
5.18	Thomson Scattering Diagnostic . . . . .	168
5.19	Two Dimensional Inversion of Asymmetric Emission . . . . .	174
5.20	Surface Plot of $\chi^2$ : Typical Equilibrium . . . . .	175
5.21	Uncertainty in Reconstructed Equilibrium . . . . .	177
5.22	Sensitivity of $F'(0)$ Free Parameter to MSE Diagnostic . . . . .	178
5.23	MSTFit Result: 400kA Standard, Prior to Sawtooth Crash . . . . .	181

5.24	MSTFit Result: 400kA Standard, Following Sawtooth Crash . . . . .	182
5.25	MSTFit Result: 400kA PPCD Discharge . . . . .	183
5.26	Comparison of Equilibria: Pre- and Post- Sawtooth Crash . . . . .	185
5.27	Comparison of Equilibria: Standard and PPCD . . . . .	186
5.28	Uncertainty in 400kA PPCD Equilibrium . . . . .	188
6.1	Parallel Electric Field Calculations: Standard Plasma . . . . .	196
6.2	Power Deposition Profile: Standard Plasma . . . . .	199
6.3	Operational Signals for Electric Field Calculation: Standard Plasma . . . . .	201
6.4	Time Series of Equilibria: Standard Plasma . . . . .	202
6.5	Linear Evolution of Equilibria: Standard Plasma . . . . .	203
6.6	Operational Signals for Electric Field Calculation: PPCD Plasma . . . . .	204
6.7	Time Series of Equilibria: PPCD . . . . .	205
6.8	Linear Evolution of Equilibria: PPCD . . . . .	206
6.9	Intolerable Uncertainty in Linear Evolution: PPCD . . . . .	207
6.10	Time Derivative Quality of Fit: PPCD . . . . .	214
6.11	Time Derivative Fitting: PPCD . . . . .	215
6.12	Power Deposition Profile: PPCD . . . . .	216
6.13	Resistivity Profile . . . . .	217
7.1	Measured, Modeled Resistivity . . . . .	221
7.2	Edge Probe Measurement of Resistivity . . . . .	224
A.1	Wavelength Response Measurement: 1040nm . . . . .	229
A.2	Wavelength Response Measurement: 700nm . . . . .	229
A.3	Wavelength Response Measurement: 620nm . . . . .	230
A.4	Wavelength Response Measurement: 520nm . . . . .	230
A.5	Wavelength Response Measurement: 500nm . . . . .	231

A.6 Wavelength Response Measurement: 420nm . . . . .	231
A.7 Wavelength Response Measurement: 350nm . . . . .	232
A.8 Line Integrated Profiles: $H_\alpha$ and Three Bremsstrahlung Attempts . . . . .	234
A.9 Line Integrated Profiles: Four Visible Bremsstrahlung Attempts . . . . .	235
A.10 Emission at 1040nm vs $H_\alpha$ . . . . .	237
A.11 Emission at 700nm vs $H_\alpha$ . . . . .	237
A.12 Emission at 620nm vs $H_\alpha$ . . . . .	238
A.13 Emission at 520nm vs $H_\alpha$ . . . . .	238
A.14 Emission at 500nm vs $H_\alpha$ . . . . .	239
A.15 Emission at 420nm vs $H_\alpha$ . . . . .	239
A.16 Emission at 350nm vs $H_\alpha$ . . . . .	240

# Chapter 1

## Introduction

### Abstract

This chapter presents a background and overview of the work presented in this dissertation. The magnetohydrodynamic equilibrium, electrical resistivity, and Ohm's law are considered in the reversed field pinch plasma. Measurements of  $Z_{eff}$ , parallel current density and inductive electric field are required in this work. Past measurements of these quantities in other fusion research devices are reviewed.

## 1.1 Motivation

This dissertation offers strong evidence that the resistivity in the reversed field pinch (RFP) is not anomalous. Rather, it is well explained by a simple Ohm's law and the Spitzer model during low MHD periods. At other times, a fluctuation-induced motional  $\mathcal{EMF}$  (and perhaps other terms) must be included in Ohm's law. Without due consideration, this leads to an overall resistivity that can appear much higher, but with a proper treatment of Ohm's law there is no evidence of a deviation from the standard model.

Resistivity is fundamentally important to the reversed field pinch. An accurate measurement of the electrical resistivity is essential for several physics and technical issues in plasma physics. The Ohmic input power and energy confinement time, found through a combination of measurements and modeling, require a resistivity profile. The kink-tearing instabilities and corresponding MHD activity which are dominant in the RFP are attributed to a small but finite plasma resistivity. Estimating the non-inductive (e.g. dynamo) component of the electric field requires both accurate modeling of the E and J fields and a measurement of the resistivity profile.

This chapter presents an overview of the work entailed in this dissertation. It begins with a discussion of the RFP and in particular the Madison Symmetric Torus (MST) and its enhanced confinement mode PPCD. Following is an overview of the magnetohydrodynamic equilibrium of the RFP and a brief review of equilibrium models previously used to describe MST. Computation of a resistivity profile based on the Spitzer or neoclassical models relies on a measurement of the electron temperature (through Thomson scattering) and the effective ion charge profile, measured on MST via bremsstrahlung emission.

## 1.2 The Reversed Field Pinch

The reversed field pinch is perhaps the simplest toroidal configuration used in fusion research. A general schematic of the reversed field pinch is shown in Figure 1.1. A toroidal magnetic field is

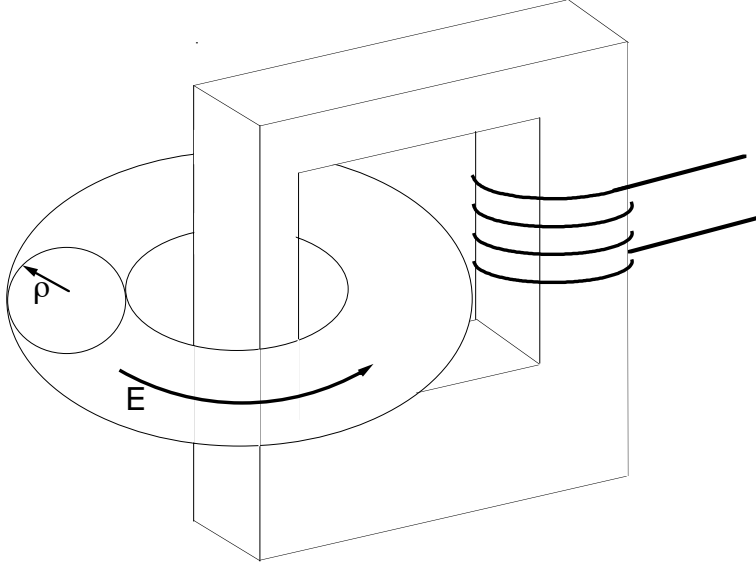


Figure 1.1: Generic sketch of a toroidal pinch experiment

applied, and after creating an initial plasma, a large toroidal electric field is applied by pulsing the transformer. The plasma acts as a single-turn secondary and a toroidal current is driven. The toroidal current in turn creates a poloidal magnetic field of strength similar to that of the toroidal field, and the plasma seeks its preferred (minimum-energy, or relaxed) state.

During relaxation, a poloidal mean field  $\mathcal{EMF}$  drives current parallel to the magnetic field in the edge of the plasma, thereby creating toroidal flux[1]. Induced currents in the conducting shell, in an opposition to the increasing toroidal flux, produce a toroidal magnetic field which is reversed relative to the initial field. This results in the distinguishing characteristic of the RFP: the toroidal magnetic field profile decreases monotonically from the core toward the edge, crosses zero and is reversed in the extreme edge. Typical MST magnetic field profiles (Figure 1.2) show the  $B_\phi$  reversal.

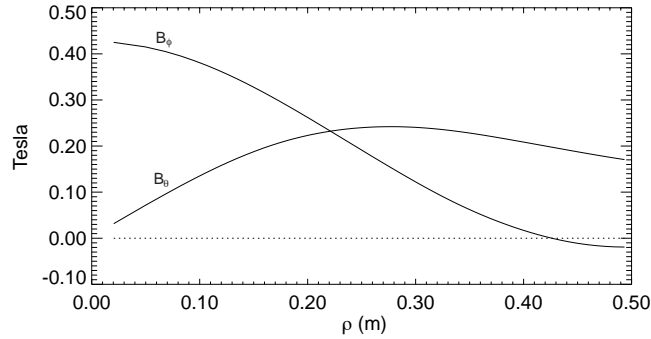


Figure 1.2: Typical magnetic field profiles for the RFP. The toroidal field starts at a large value in the core and drops monotonically to the wall, crossing zero and reversing at  $r/a \sim 0.9$ . The poloidal field, created entirely by toroidal plasma current, starts at zero in the core and becomes stronger than the toroidal field near the edge.

### 1.2.1 The Madison Symmetric Torus

The Madison Symmetric Torus is a large toroidal (major radius 1.5m, minor radius 0.52m) reversed field pinch, sketched in Figure 1.3. Reversal of the toroidal field occurs naturally due to induced currents in the close fitting conducting shell (5 cm aluminum); it is then maintained by driving current in the shell through a transformer and capacitor bank energy supply. The proximity of the conducting shell imposes a boundary condition of  $\mathbf{B} \cdot \hat{n} = 0$  on the field at the wall, implying the shell is a surface of constant poloidal flux. Toroidal flux is pumped into the MST through a gap that extends along the inboard major radius (180 degrees poloidal), breaking the conductivity around a poloidal loop (toroidal gap). Similarly, poloidal flux is applied through a poloidally extending gap. In the MST, all of the poloidal magnetic field is produced by toroidal current in the plasma and induced stabilizing toroidal currents in the shell. It is necessary to drive toroidal current in the plasma but not in the conducting shell, however plasma-induced stabilizing currents must have a complete toroidal path. The clever designers of MST[2] solved this problem by linking the transformer with the plasma, but the gap in the vacuum vessel prevents it from linking the transformer core. Toroidal conductivity in the shell is established with three continuity windings,

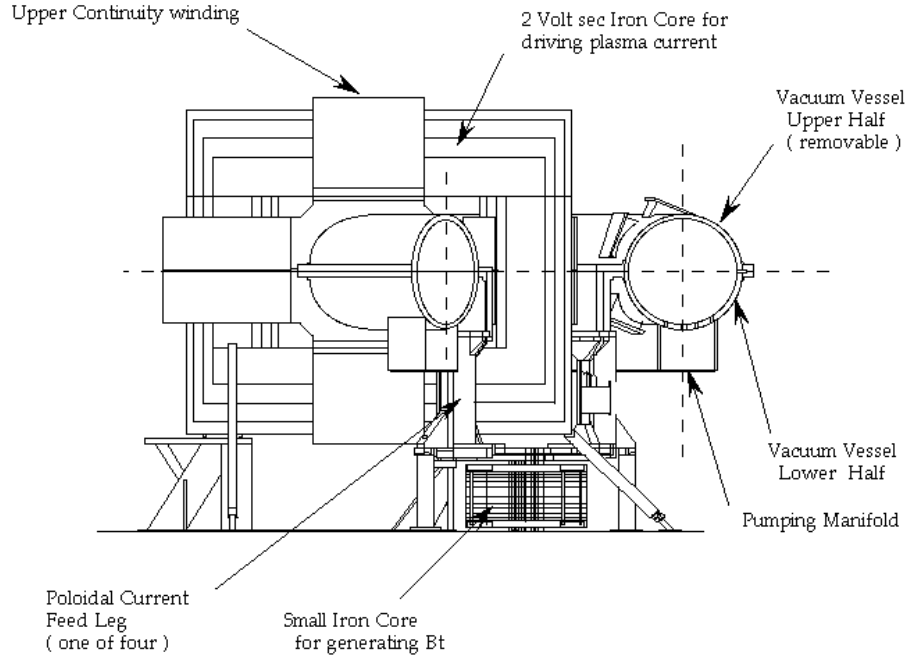


Figure 1.3: The Madison Symmetric Torus

which are thick aluminum sheets extending from the gap back along their respective directions, then extend outward and behind the iron core before meeting the other side of the gap.

Standard operations of MST are with a plasma current between 150 and 500kA at line averaged densities of  $\bar{n}_e = 0.4 - 2.5 \times 10^{19} \text{m}^{-3}$ . The central electron temperature is typically  $T_e < 500\text{eV}$  and the length of the pulse is  $\lesssim 60\text{ms}$ . Operational signals from a standard discharge are shown in Figure 1.4. The applied toroidal voltage a) drops rapidly during the plasma current b) ramp up and rapid heating of the plasma. The reversal parameter c)

$$F = \frac{B_\phi(a)}{\langle B_\phi \rangle} \quad (1.1)$$

and pinch parameter d)

$$\Theta = \frac{B_\theta(a)}{\langle B_\phi \rangle} \quad (1.2)$$

are used to characterize MST discharges. The noisy signal e) is the poloidal loop voltage measured at the toroidally extending gap ( $V_{tg}$ ). The noise on this signal is indicative of the level of magnetic fluctuations in the plasma. The large spikes correspond to rapid jumps in the total flux f) generated by spontaneous MHD relaxation events (sawteeth), and a resulting sharp decrease in the toroidal field at the wall g). Also shown is a typical line-averaged electron density h).

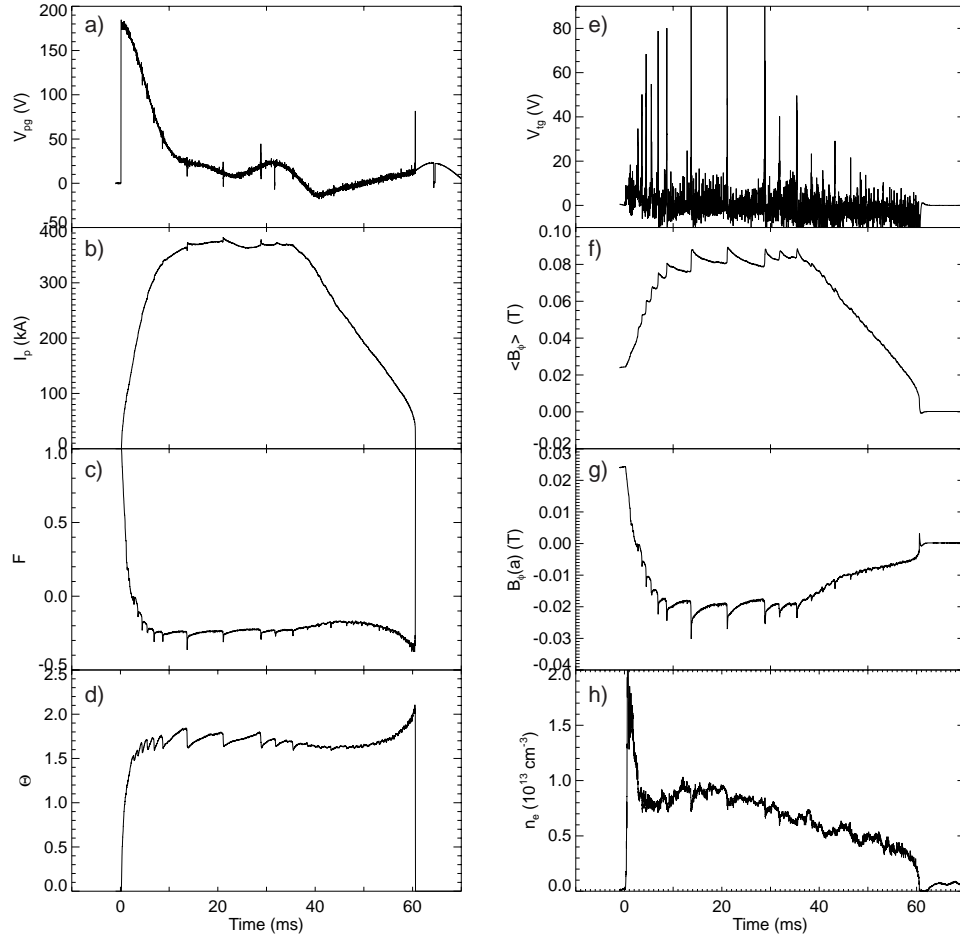


Figure 1.4: Operational signals of a standard MST discharge. Shown are the applied toroidal voltage  $V_{pg}$  a), the total driven toroidal current b), the reversal  $F$  c) and pinch  $\Theta$  d) parameters; the applied poloidal loop voltage ( $V_{tg}$ ) e), the toroidal magnetic flux f), the toroidal field at the wall g), and the line averaged electron density h).

## 1.2.2 Pulsed Poloidal Current Drive

The primary result of this dissertation is the agreement between measured and modeled resistivity profiles during periods of very low magnetic fluctuations. These conditions are realized during a current profile control experiment dubbed Pulsed Poloidal Current Drive (PPCD). During PPCD, an externally applied inductive electric field (which commences at  $t = 13\text{ms}$  and ends after  $t = 20\text{ms}$ ) drives poloidal current at the edge of MST. The operational signals for this experiment are shown in Figure 1.5. The main changes during the experiment are rapidly changing gap voltages (poloidal gap in a), toroidal gap in e), a corresponding drop in toroidal flux (f), a sharp decrease in the toroidal field at the wall g), and corresponding changes in  $F$  c) and  $\Theta$  d). Also noteworthy is that the noise on the toroidal gap voltage (poloidal loop voltage) is greatly reduced during the latter stages of the experiment, indicative of a drop in magnetic fluctuation level. As discussed below in Section 1.2.5, a poloidal  $\mathcal{EMF}$  is required to drive parallel current at the edge to maintain the RFP equilibrium; in normal MST operations this is attributed to correlated velocity and magnetic fluctuations occurring in discrete bursts, sawteeth. In PPCD, the inductively applied electric field takes the place of the fluctuation-induced dynamo field required to maintain the equilibrium, and the necessity of the magnetic fluctuations is removed. Addition of edge current has been shown to theoretically stabilize magnetic fluctuations[3] and measurements indeed indicate a drastic reduction in fluctuation amplitude and a corresponding increase in electron temperature and particle and energy confinement[4]. The decrease of fluctuation amplitude is shown in Figure 1.6 where PPCD is in effect between  $t = 13$  and  $20\text{ms}$ . Soon after the onset of PPCD, the  $\tilde{b}$  amplitude drops below the 1% level and remains there until the end of the experiment. In this work it is postulated (and verified) that in the extremely low fluctuation periods, a simple expression for the parallel Ohm's law,  $E_{\parallel} = \eta J_{\parallel}$  (see Section 1.2.5) is consistent with measurements, and a comparison between the measured and modeled resistivity profiles can proceed without concern of non-inductive electric fields.

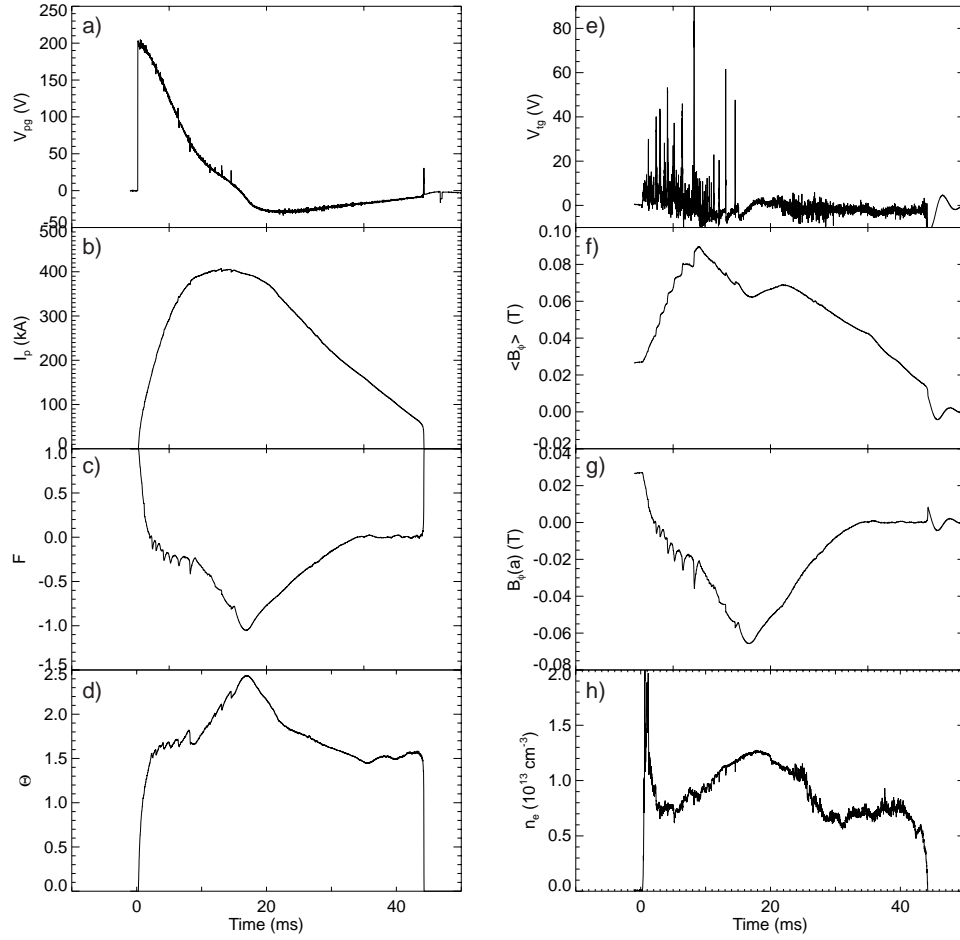


Figure 1.5: Operational signals of a PPCD discharge. Shown are the applied toroidal voltage ( $V_{pg}$ ) a), the total driven toroidal current b), the reversal  $F$  c) and pinch  $\Theta$  d) parameters; the applied poloidal loop voltage ( $V_{tg}$ ) e), the toroidal magnetic flux f), the toroidal field at the wall g), and the line averaged electron density h).

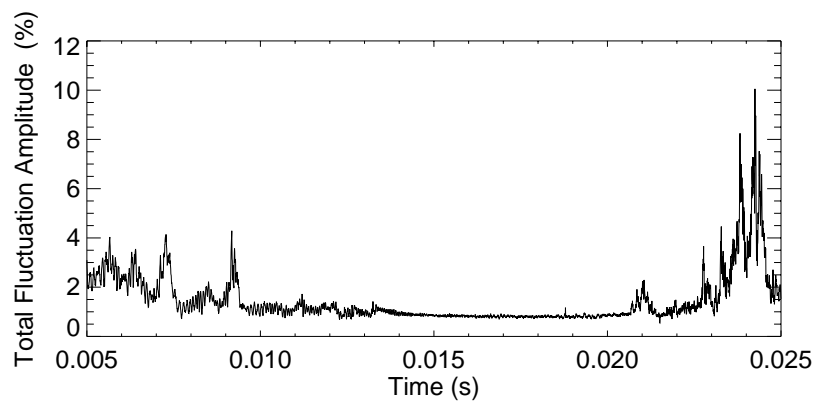


Figure 1.6: Low magnetic fluctuation level during PPCD ( $t = 13 - 20\text{ms}$ ).

### 1.2.3 Background of Equilibrium Studies in the RFP

Determination of the MHD equilibrium is a necessary part of the physics research in the RFP. In addition to the Ohm's law studies in this dissertation, a flux surface geometry is required for interpretation of temperature and density measurements, and the equilibrium current density profile must be well determined to investigate tearing mode stability (among other things).

In their comprehensive work, Bodin and Newton[5] review several models for the RFP equilibrium, ranging from pressure free to high  $\beta$  models. An overview of models that have been applied to MST is presented below. Comparison between the models is most easily done with the dimensionless parameter

$$\lambda = \mu_0 a \frac{\mathbf{J} \cdot \mathbf{B}}{B} \quad (1.3)$$

which represents the normalized parallel current density. The use of a dimensionless parameter to describe the equilibrium removes the need for an additional free parameter in the modeling. An overall scale factor, determined by the total plasma current, is needed to generate magnetic field profiles from these models.

#### Bessel Function Model

Arguably the most influential paper on the RFP equilibrium was written by Taylor in 1974[6], in which the minimum energy state was found subject to the constraint of global helicity conservation (perfectly conducting plasma). The result for a pressure free plasma is

$$\nabla \times \mathbf{B} = \lambda \mathbf{B} \quad (1.4)$$

where  $\lambda$  is a constant. In a cylindrical geometry, this leads to equilibrium profiles given by

$$\begin{aligned} B_\phi &= B_0 J_0(\lambda r) \\ B_\theta &= B_0 J_1(\lambda r) \end{aligned} \tag{1.5}$$

where  $J_0$  and  $J_1$  are the zeroth and first order Bessel functions and this is referred to as the Bessel Function Model (BFM). This theoretical investigation of the RFP remarkably predicts reversal of the toroidal field inside the plasma for  $\lambda a > 2.404$ , which is experimentally observed. A distinguishing feature of this characterization is that  $\lambda$  is constant, or referring to equation 1.3, the ratio of parallel current density to magnetic field does not change with radius, and the equilibrium is completely specified by the single parameter  $\lambda$  (and the overall scale factor  $B_0$ ). The single parameter description results in a predicted reversal and pinch parameter as functions of  $\lambda$  only; hence an  $F - \Theta$  graph is a unique curve.

### Modified Bessel Function Model

One prediction of the BFM is that the current at the plasma boundary is nonzero, which is contradicted by experimental measurements[7]. A refinement to this model resolves this inconsistency; it was proposed[8] that  $\lambda(r)$  is constant from the center out to a critical radius  $r_{crit}$ , and falls linearly for  $r > r_{crit}$  to zero at the boundary. This preserves the physics of the BFM over the bulk of the plasma interior and relies on finite resistivity near the plasma edge to allow the dissipation of helicity and hence the drop in  $\lambda$ . Typical MBFM profiles are shown in Figure 1.8. In this model, two free parameters,  $\lambda$  and  $r_{crit}$  are used (again along with an overall scale factor) to specify the equilibrium. By the addition of the second free parameter, both  $F$  and  $\Theta$  can be matched by the equilibrium model.

### Polynomial Function Model and Modified Polynomial Function Model

An alternative to the MBFM that allows  $\lambda$  to go to zero at the plasma boundary and allows for finite pressure (proposed by Sprott[9]) is called the polynomial function model (PFM). The Bessel functions in the fields of the BFM are expanded in terms of polynomials, and only enough terms are kept to satisfy the boundary conditions of zero edge current, and vanishing first and second derivatives of  $\lambda$  at  $r = 0$ . The results from the PFM are similar to those of the MBFM, with profiles of  $B_\phi$ ,  $B_\theta$ ,  $J_\phi$ , and  $J_\theta$  described as polynomials in  $r/a$  specified by a single parameter. The parameter in the PFM is  $\Theta_0 = \mu_0 a J_\phi(0) / 2B_\phi(0)$ , the normalized central current density; again an overall scale factor is present in the field profiles. A primary advantage of the PFM is that the predicted perpendicular diamagnetic current is consistent with  $\beta$  values observed in experiment. Being limited to a single parameter (like the BFM) to describe the profiles, this model predicts a unique relationship between the RFP parameters  $F$  and  $\Theta$ , the field reversal and pinch parameters respectively. This is in contrast with experiment where the  $F$  vs  $\Theta$  curve deviates from a line, a typical example of this is shown in Figure 1.7. A generalization of the PFM, called the modified

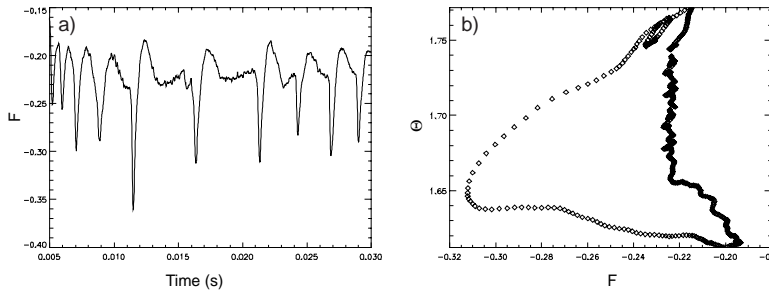


Figure 1.7: a) A trace of  $F$  versus time shows that the equilibrium of the RFP evolves in time. b) Trace of  $F$  versus  $\Theta$  curve from a standard MST discharge through a sawtooth cycle. The reversal and pinch parameters complete a full cycle but do not lie on a straight line.

polynomial function model (MPFM)[10] is similar to the PFM, with the boundary condition of  $\lambda''(0) = 0$  removed. This allows an exact solution of the remaining boundary conditions ( $J(1) = 0$  and  $\lambda'(0) = 0$ ) with the same number of terms in the polynomials. The MPFM results for the

current density and magnetic field profiles are

$$\begin{aligned}
B_\phi &= B_\phi(0) [1 - \Theta_0^2 (r/a)^2 + \Theta_0^2 (r/a)^4 / 2] \\
B_\theta &= B_\phi(0)(r/a) [\Theta_0 - (2\Theta_0 - 3C) (r/a)^2 + (\Theta_0 - 2C) (r/a)^4] \\
J_\phi &= 2B_\phi(0) [\Theta_0 - 2(2\Theta_0 - 3C) (r/a)^2 + 3(\Theta_0 - 2C) (r/a)^4] / \mu_0 a \\
J_\theta &= 2B_\phi(0)\Theta_0^2 (r/a) [1 - (r/a)^2] / \mu_0 a
\end{aligned} \tag{1.6}$$

which can be expressed in terms of the measured quantities  $F$  and  $\Theta$  by

$$\begin{aligned}
\Theta_0 &= \sqrt{(6 - 6F)/(3 - 2F)} \\
C &= \Theta/(3 - 2F)
\end{aligned} \tag{1.7}$$

The MPFM equilibrium profiles are illustrated with the other models in Figure 1.8. As in the MBFM, using two parameters in the nondimensionalized modeling allows this model to reproduce both  $F$  and  $\Theta$ .

### Alpha Model

The alpha model[11] is another alternative to the MBFM which allows the value of  $\lambda$  to be relatively constant over much of the plasma interior and match experiment by decreasing smoothly to zero at the plasma boundary. The PFM and MPFM are found by expanding the Bessel functions of the BFM and are thus restricted to match the shape of the BFM near the core, thereby representing a relaxed current profile. The alpha model allows for a different class of profile shapes in the core and edge regions, thereby better approximating experiment where the current profile evolves and is not always in its relaxed (minimum energy) state. Including a pressure term in the radial force balance equation implies

$$\nabla \times \mathbf{B} = \lambda \mathbf{B} + \frac{\beta_0}{2B^2} \mathbf{B} \times \nabla P \tag{1.8}$$

where  $\beta_0$  and  $\nabla P$  describe the pressure profile and

$$\lambda = \lambda_0 \times (1 - (r/a)^\alpha) \quad (1.9)$$

characterizes the parallel current. The parameters  $\lambda_0$  and  $\alpha$  are uniquely determined by the experimental quantities  $F$  and  $\Theta$  and a third parameter  $\beta_0$ , which is typically specified based on limited experimental observations of temperature and density. For high values of  $\alpha$ , the profile is flat through the central regions and very steep at the edge. Conversely, for low values of  $\alpha$  the profile is peaked, and gradients exist over much of the radius.

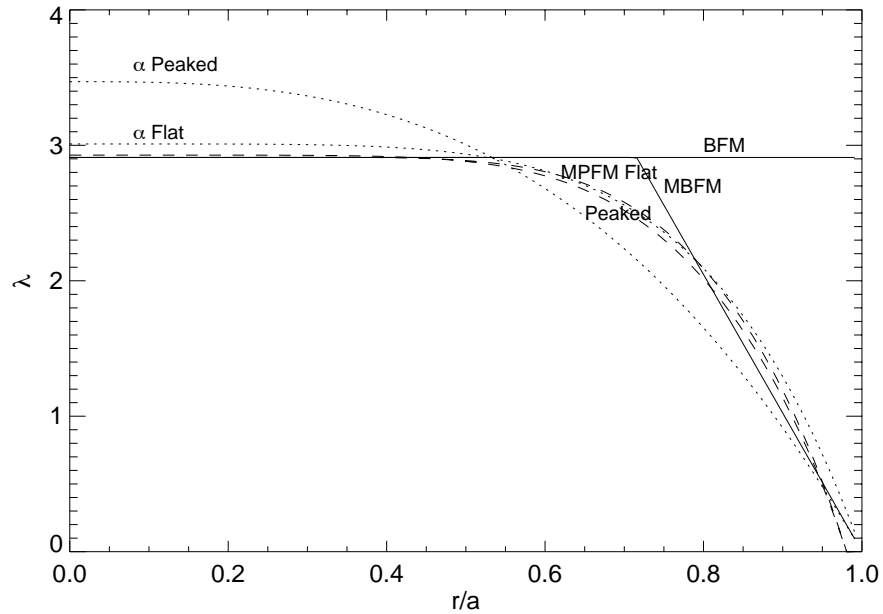


Figure 1.8: Cylindrical Models of the RFP equilibrium

Figure 1.8 shows the  $\lambda$  profiles for the MPFM and alpha model for two cases corresponding to different values of  $F$  and  $\Theta$ . The profiles referred to as 'flat' are  $F = -0.20$ ,  $\Theta = 1.60$  and the 'peaked' cases are  $F = -0.25$ ,  $\Theta = 1.75$ . For comparison, a typical plot of the BFM and MBFM is also included. The MPFM (shown in dashed lines) shows only a small change between the different

conditions, and the alpha model (dotted lines) shows a significant change between the two sets of parameters and qualitatively shows the ability to predict equilibria away from the Taylor state.

#### 1.2.4 Need for Improved Modeling

Upgrades in the diagnostics on MST have enabled profile and highly accurate measurements of some quantities. This has justified and thus motivated the current development of toroidal modeling for the MST equilibrium. While this is not a new concept, this is the first application of a code which fits all available data while determining the equilibrium in MST. A key point is that the equilibrium determination is partially based on internal diagnosis of the plasma, which is necessary for an accurate profile reconstruction of the equilibrium. In a recent paper, Pustovitov (2001) presents a review of equilibrium reconstruction publications[12], and the debate in the community over a lingering topic: Is it possible to determine the MHD equilibrium from external magnetic measurements? There are several published papers expressing optimism[13, 14, 15], but it is alas a theoretical reality that external magnetics cannot alone determine equilibrium profiles[16, 17, 18, 19, 20, 21]. In his paper, Pustovitov presents a theoretical treatment of the limitations of edge magnetics. It is unnecessary to reproduce them here; it is sufficient to point out that a wide range of distinguishable current profiles produce identical edge signals in MST. Figure 1.9 demonstrates exactly this, where two very different current profiles produce identical edge signals used in the models above. It should be noted that there is a distinguishable difference between these two equilibria in the predicted poloidal asymmetry factor, which is in fact an additional external measurement. However, none of the above cylindrical models are adjustable to fit these data when determining the equilibrium. With a first order toroidal correction, it is possible to predict poloidal array signals as a means of evaluating the models.

The approach taken in the tokamak community has now been applied to the RFP. Namely, a rather involved calculation

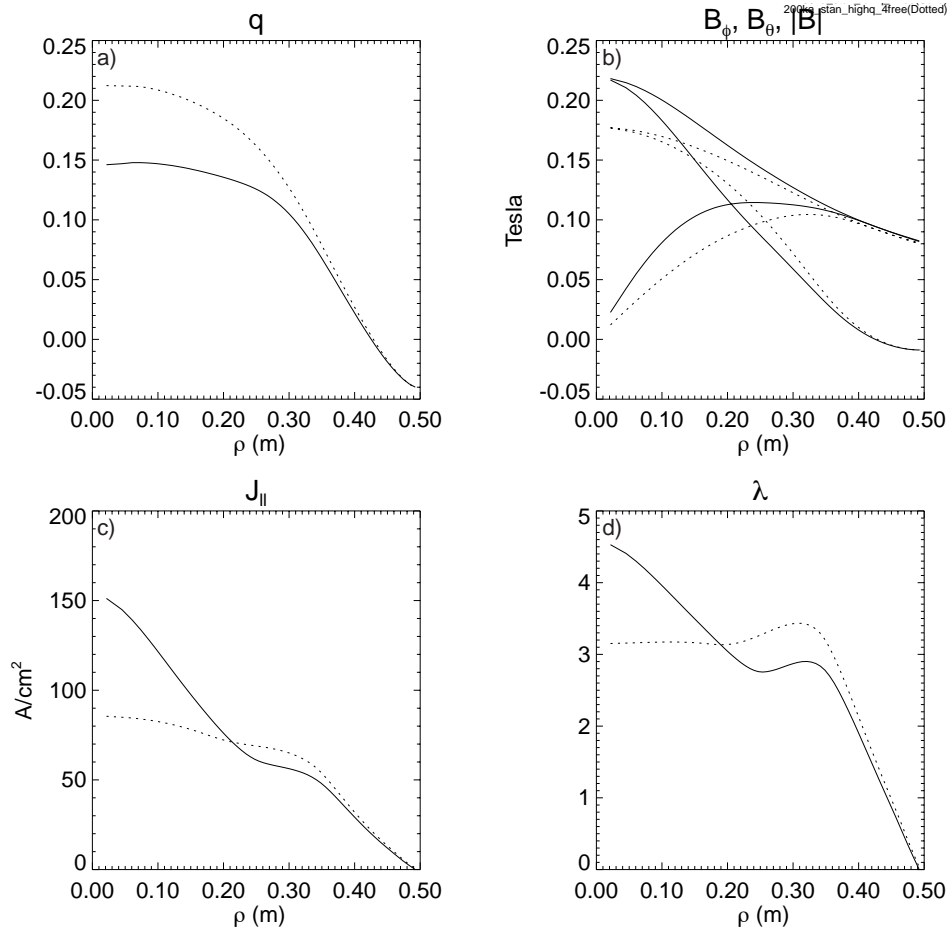


Figure 1.9: These two very different equilibrium current profiles produce identical (to within .1%) values of  $F$ ,  $\theta$ , and  $I_p$ .

1. determines the axisymmetric solution of Maxwell's equations (in a torus)
2. satisfies radial force balance  $\mathbf{J} \times \mathbf{B} = \nabla P$  and,
3. best fits all the available data.

This general approach is not limited in its ability to accurately predict experimental signals, and is extensible to many free parameters with nearly arbitrary profiles of  $\lambda$  and pressure. The accuracy of the solution is ultimately limited by the data used to constrain the fit. Described in detail in Chapter 5 is MSTFit, a new equilibrium reconstruction code that fits data from all edge and

internal diagnostics on MST while finding a consistent equilibrium.

### 1.2.5 Ohm's Law and Resistivity in the RFP

As the parallel current density remains finite and the magnetic field becomes primarily poloidal near the edge, the equilibrium evidently has poloidal current. Resistive decay of toroidal flux induces a poloidal electric field, but this process can only maintain the equilibrium for a time scale much shorter than the observed RFP equilibrium. Indeed, a non-inductive field must periodically regenerate toroidal flux to maintain the equilibrium. The mechanism which generates this field in MST is attributed to correlated velocity and magnetic field perturbations[22, 23, 24] occurring in discrete bursts (sawteeth).

As they supply the necessary poloidal current drive, magnetic fluctuations are necessary to sustain the RFP equilibrium, but at the same time they are responsible for degraded heat and particle confinement. Writing the full parallel force balance equation leads to the generalized Ohm's law[25] appropriate for the RFP

$$-\frac{m_e}{e^2 n} \frac{\partial \mathbf{j}}{\partial t} + \mathbf{E} + \mathbf{v} \times \mathbf{B} - \frac{1}{en} \mathbf{j} \times \mathbf{B} + \frac{\nabla P_e}{en} = \eta \mathbf{j} \quad (1.10)$$

and by writing each quantity as a mean plus a fluctuating part, standard arguments[22] lead to the neglect of several small terms and the parallel Ohm's law

$$\mathcal{E} \equiv \langle E \rangle_{\parallel} + \langle \tilde{\mathbf{v}} \times \tilde{\mathbf{b}} \rangle_{\parallel} = \eta \langle J \rangle_{\parallel} \quad (1.11)$$

is appropriate for MST. Here  $\langle \rangle$  represents the flux surface average and  $\langle E_{\parallel} \rangle$  is the axisymmetric part of the  $\mathcal{EMF}$ .

If the correct form of Ohm's law is ignored and an effective plasma resistivity is computed, the word 'anomaly' is required. Asserting that  $E_{\parallel} = \eta J_{\parallel}$ , an effective on-axis resistivity can be

defined[26, 27] as

$$\eta^*(0) = \frac{V_\phi(0)}{2\pi R J_\phi(0)} \quad (1.12)$$

which can in turn be used to define an anomaly factor

$$Z_{eff}^*(0) = \frac{\eta^*(0)}{\eta_{Spitzer,Z=1}(0)}. \quad (1.13)$$

This calculation is not straightforward since the toroidal loop voltage is in general not measured at the axis. Calculating  $V_\phi(0)$  from the boundary measurement requires accurate time-dependent behavior of the poloidal magnetic field profile. Under some conditions, the anomaly factor ( $Z_{eff}^*$ ) has estimated values as high as fifteen[26] which certainly cannot be explained by realistic impurity concentrations. Calculating an anomaly factor in this fashion is not justified. Quoting Ortolani and Schnack[1]:

Reversed-field pinch plasmas characteristically require an anomalously large loop voltage to drive a given plasma current. In the past, this voltage anomaly has been interpreted in terms of an enhancement, of unknown origin, to the plasma resistivity. Instead, we will see that an increase in loop voltage is a natural consequence of the magnetic fluctuations that are responsible for plasma relaxation.

It is to be emphasized that this anomalous loop voltage, or effective plasma resistance, arises from the MHD fluctuations alone; the actual plasma resistivity may still be classical. The effect of the dynamo fluctuations is to convert poloidal flux into toroidal flux. Thus the external circuit must not only supply the poloidal flux to maintain the desired mean current, but must feed the dynamo as well. The more active the dynamo, the more excess flux must be supplied. This excess rate of poloidal flux input appears as anomalous loop voltage.

The MHD activity appears as a mean field  $\mathcal{EMF}$  in Ohm's law. Proper treatment of this term removes any need to associate 'anomalous' with RFP resistivity. Schoenberg and Moses[28] presented an estimate of the resistivity in the presence of an RFP dynamo on ZT-40M which agreed with the Spitzer value to within a factor of two. However, in their work equilibrium modeling was limited, the estimate of  $Z_{eff}$  was limited to a lower bound, and neoclassical corrections were not

considered. In the plasmas studied in this work, the excess terms in Ohm's law serendipitously vanish during PPCD and a more quantitative study of the measured resistivity with the models is made. Resistivity in the RFP is not anomalous.

### 1.3 Electrical Resistivity

Electrical resistivity is a measure of the response of electrons to an externally applied electric field. An applied electric field will produce an electrical current,  $E = \eta J$ , where the resistivity is determined by the collisionality of the material. The current density is the charge density  $ne$  multiplied by the average speed of the charge carriers,  $v_d$ , which is the speed of a particle achieved from uniform acceleration under the influence of the electric field for the average time between momentum-stopping collisions,  $\tau$ . This implies the simplest form of Ohm's law is in fact a parallel force balance equation: the driving force (applied E) is balanced by a resistive drag force.

This leads to an introductory level physics result for the electrical resistivity

$$\frac{E}{J} = \eta = \frac{1}{\sigma} = \frac{m\nu}{ne^2} \quad (1.14)$$

where the collision time  $\tau$  has been replaced by the inverse of the collision frequency  $\nu$ .

The exact same equation appears in modern physics textbooks and in solid state physics textbooks where the collision frequency is tailored to the particular problem being addressed, (e.g. a free electron gas, an electron in a regular crystal lattice, or at a PN junction). It therefore does not come as a surprise to find equation 1.14 in plasma physics books[29, 30] in introductory remarks regarding plasma resistivity. The fundamentally different physics are contained in the electron collision frequency.

An electron moving through a plasma is influenced by the Coulomb potential of all other charged particles in the plasma. The upper bound on length over which it is reasonable to consider this

interaction is the Debye length, beyond which the mobility of other free charges effectively screens out the potential. There are a great many particles in the Debye sphere acting on the test electron, implying the force felt is the sum of many individual fields, predominantly collective behavior. Each nearly elastic electron-ion interaction leads to a deflection of the electron without a significant loss of energy. When the initial trajectory has been altered by  $90^\circ$  the parallel momentum is lost; it typically takes many interactions to sum to one such collision.

The Coulomb collision with a single ion leads to a velocity change of

$$\Delta v_{\parallel} = -\frac{2Z_i^2 e^4}{(4\pi\epsilon_0)^2 m_e^2 b^2 v^3} \quad (1.15)$$

where  $b$  is the impact parameter of the incident electron onto the stationary point ion. The net drag force (and collision frequency) is found by accounting for all ions and integrating over impact parameters

$$F_{\parallel} = m_e \frac{\Delta v_{\parallel}}{\Delta t} = -m_e v_{\parallel} \nu = -\frac{4\pi Z_i^2 e^4}{(4\pi\epsilon_0)^2 m_e v^2} \int_0^{\infty} \frac{db}{b} \quad (1.16)$$

where the factor of  $n_i v \times 2\pi b db$  is the number of ions per unit time the electron encounters at a particular impact parameter. The integral over impact parameter is divergent at both the upper and lower bounds, so in practice the range is bounded by physical considerations. The upper limit is the Debye length, as the Coulomb field from an ion farther away decays exponentially. The lower bound is typically set at the impact parameter for which  $90^\circ$  scattering occurs from the interaction with one ion, and the Coulomb logarithm is defined

$$\ln\Lambda \equiv \int_{b_{min}}^{b_{max}} \frac{db}{b} \quad (1.17)$$

which, under the approximations above is a weakly varying function of electron density and tem-

perature and is a numerical factor of  $\sim 17$  in the core of MST to  $\sim 15$  near the edge.

The collision frequency is thus

$$\nu(v) = \frac{n_i Z_i^2 e^4 \ln \Lambda}{(4\pi\epsilon_0)^2 m_e^2 v^3} \quad (1.18)$$

for a single ion species. The total collision frequency is determined by summation over all ion species

$$\nu_{ei} = \frac{n_e Z_{eff} e^4 \ln \Lambda}{(4\pi\epsilon_0)^2 m_e^2 v^3} \quad (1.19)$$

which motivates the definition  $Z_{eff} \equiv \frac{\sum_s n_s Z_s^2}{n_e}$ .  $Z_{eff}$  is the effective ionic charge used in determining the collisionality (and hence electrical resistivity) in a plasma.

Under the assumption of a Maxwellian distribution of electrons, the velocity is related to the temperature. One interesting point is that the collisionality, and hence resistivity, decreases with an increase in temperature in a plasma (owing to the  $v^{-3} \propto T_e^{-3/2}$  dependence of the Coulomb collision frequency) contrasting the resistance in a metal or semiconductor where the collisionality increases with temperature. The zeroth order resistivity is

$$\eta(T_e, Z_{eff}) = 1.04 \times 10^{-4} \frac{Z_{eff} \ln \Lambda}{T_e^{3/2}} [\Omega\text{m}] \quad (1.20)$$

with  $T_e$  in eV. Corrections to this result were made first by Spitzer and Härm[25] in 1953 (due to  $e^-$ - $e^-$  collisions), and neoclassical (geometry and trapped particle) effects were included significantly later. These corrections appear as multiplicative factors and will be discussed in Chapter 4. A third correction arising from the presence of non-fully stripped ions[31] is typically ignored, but is important under certain conditions in MST (see Section 3.7). The presence of fast electrons (non-Maxwellian distribution) leads to an enhanced conductivity and this effect may well prove

important in MST. It is interesting to note that a plasma at 100eV conducts about as well as stainless steel, and at 1keV it conducts as well as copper[32].

Measurements of the global plasma resistivity have been made in several tokamaks, with the comparison to theory leading to mixed results[33]. Some tokamaks report agreement with the Spitzer resistivity model, such as PBX-M[33], TEXT[34], PLT[35] and ASDEX[36]; while others (TFTR[37], JT-60[38], JET[39]) were better described by the neoclassical model. A full resistivity profile measurement made on DIII-D[40] properly incorporating non-inductively driven current (neutral beam, bootstrap) and full profile diagnostic capabilities agrees with the neoclassical model.

The fact that parallel transport is so well understood on tokamaks begs the question of whether  $\eta$  in the RFP can also be explained by neoclassical theory.

### 1.3.1 Measurement of $Z_{eff}$

Estimation of the resistivity requires knowledge of the electron temperature and  $Z_{eff}$  (as well as a very weak dependence on electron density). Routine measurements (Thomson scattering, interferometry) are used in MST to measure the electron temperature and density, but the measurement of  $Z_{eff}$  is less straightforward. It is clear that the effective ion charge profile is a key in determining the plasma resistivity, but how does one measure it?

One way is to spectroscopically identify lines of several charge states from every measurable impurity and use collisional radiative modeling (CRM) to deduce densities of each charge state. This is a very involved process for machines with even a small number of impurities. Data presented in this work show that MST plasmas are riddled with lines from several impurities including He, B, C, N, O, and Al among others. Accurate CRM for the number of charge states in MST is a monumental undertaking which has not been attempted in this work.

Development of ways to measure  $Z_{eff}$  with diagnostic neutral beams, either through Rutherford scattering or by simple beam attenuation measurements, are currently underway on MST. These,

too, are complicated by competing atomic processes.

The most widely used technique to measure  $Z_{eff}$  is through bremsstrahlung in the visible or near infrared. Discussed in detail in Chapter 3, continuous emission from electron-ion encounters is directly proportional to  $\frac{Z_{eff}n_e^2}{\sqrt{T_e}}$ . An absolute emissivity measurement in the absence of all other sources of radiation (with measured electron density and temperature profiles) will specify  $Z_{eff}$ . Table 1.1 is a list of published bremsstrahlung measurements; included for comparison is this work on MST.

The  $n_e^2$  dependence of bremsstrahlung emission suggests this measurement is better suited for high

Machine	$\lambda$ (nm)	Typical $n_e$ ( $\text{m}^{-3}$ )
DIII-D[41]	536	$\sim 1 \times 10^{20}$
Tore-Supra[42]	523.5	$\sim 1 \times 10^{20}$
JET[43, 44]	523	$0.2 - 1 \times 10^{20}$
ASDEX[36]	1040	$\sim 1 \times 10^{20}$
C-Mod[45]	536	$\geq 10^{20}$
TCV[46]	1040	$\sim 1 \times 10^{20}$
RFX[47]	523.6,700,1044	$\sim 5 \times 10^{19}$
MST	1040	$\sim 1 \times 10^{19}$

Table 1.1: Reported measurements of bremsstrahlung are prevalent in high electron density machines

density plasmas, however it is challenging even for these machines as ‘generic recycling light’[48] and ‘molecular pseudocontinua’[45] pollute the measurements. In MST, the situation appears quite dismal (demonstrated in Figure 1.10) where the measured spectrum in a standard MST discharge is plotted with the expected bremsstrahlung emission of a  $Z_{eff} = 2.0$  plasma (solid line at bottom). The two dashed lines are identified pollutants (see Chapter 3), which strongly out-radiate bremsstrahlung. Due to the abundance of contamination, green (523, 536nm) bremsstrahlung measurements of the MST plasma are not feasible. The situation is somewhat better in the NIR (around 1040nm) for MST but is still unapproachable in standard discharges; this will be discussed

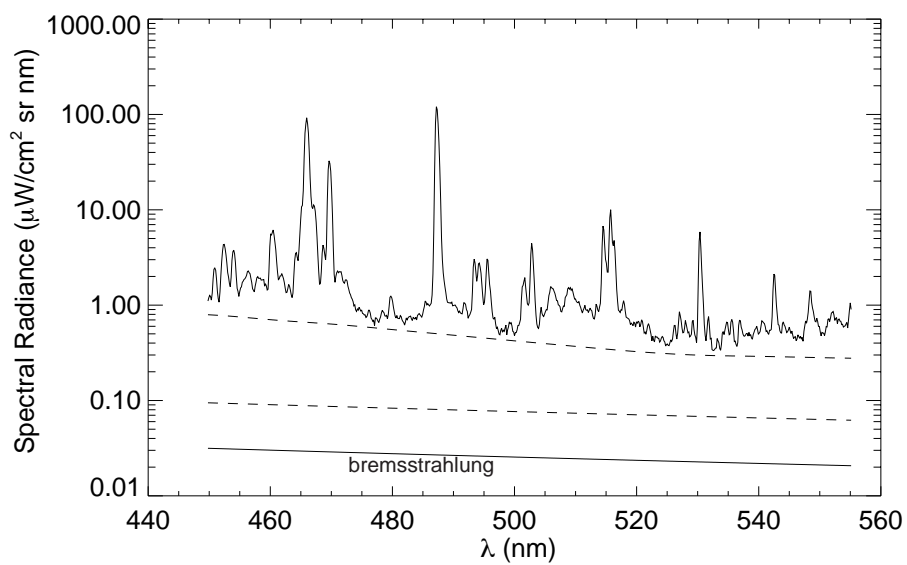


Figure 1.10: Measured spectrum in a standard MST discharge along with the expected bremsstrahlung (bottom solid line), and two identified pollutants (dashed lines). Note the logarithmic scale.

in detail in Chapter 3.

In PPCD experiments on MST, where an order of magnitude drop in neutral particle density leads to a proportionate reduction in the two identified pollutants, bremsstrahlung is a significant fraction of the total emission and an accurate measurement is conceivable.

## 1.4 Overview of this Work

This thesis presents evidence that the resistivity in the RFP is not anomalous but is consistent with the Spitzer model based on data from 400kA PPCD plasmas. Neoclassical theory is not challenged, as an accurate measurement of the full electron distribution is required to adequately distinguish between the models in the presence of fast electrons. Neoclassical corrections to the Spitzer model increase the resistivity, while super-thermal electrons reduce the resistivity. These plasmas are selected as the bremsstrahlung measurement is limited to the hottest, most dense corner of the MST operating range, while minimal magnetic fluctuations are required for the asserted form of Ohm's law which ignores any axisymmetric contribution from the correlated magnetic field and velocity fluctuations. The result of Chapter 4 is the Spitzer resistivity profile based on electron temperature and  $Z_{eff}$  measurements. Concluding Chapter 5 is a full equilibrium reconstruction (primarily the parallel current density profile), and Chapter 6 includes a calculation of the inductive electric field profile. Finally, Chapter 7 demonstrates agreement to within experimental uncertainty of these profiles with a simple Ohm's law.

The legacy of this work is undoubtedly the MSTFit equilibrium reconstruction code (Chapter 5). Development of this code has made possible a variety of analyses as it makes available equilibrium profile information incorporating all diagnostics. In this work, the measured current density profile is used to investigate the resistivity of the RFP plasma.

The resistivity analysis also requires an inductive electric field profile. This has been done previously by taking finite time differences of equilibrium quantities[40]. It is shown that while this

method is satisfactory for electric fields arising from standard flux consumption, the rate of change of the equilibrium in PPCD experiments is too great to use this method. A new technique, which solves the time derivative of the Grad-Shafranov equation constrained by the time derivatives of magnetic signals, is used to find the inductive parallel electric field profile.

The secondary result of this work, (presented first in Chapters 2 - 4) is that an upper bound on  $Z_{eff}$  has been set through a near-infrared bremsstrahlung measurement. While limited to a very small operating range of MST, it has enabled a comparison between modeled and measured resistivity profiles. This section of the dissertation is (at least attempted to be) organized in a lucid manner, in flagrant contrast to the fashion in which the work was actually performed. Chapter 2 is an overview of the hardware used for various quantitative spectroscopic measurements in the pursuit of a  $Z_{eff}$  measurement. A significant effort was spent isolating and identifying the radiative processes that prohibit a standard bremsstrahlung measurement on MST. These results may lend some insight to difficulties with bremsstrahlung measurements elsewhere in the fusion community and are summarized in Chapter 3. Finally, in Chapter 4 the technique used to convert the measured emission to a  $Z_{eff}$  profile is described, and the resistivity profiles based on the Spitzer and neoclassical models are computed.

The second section of this dissertation pertains to the equilibrium modeling of the RFP. Chapter 5 is a complete description of MSTFit, a new axisymmetric toroidal equilibrium reconstruction code specifically suited for the RFP equilibrium. The code features a fully nonlinear technique which finds the solution to the Grad-Shafranov equation that best fits the experimental data. The nonlinear technique, while making the code considerably slower than a linear Grad-Shafranov solver such as EFIT[49], allows a great deal of flexibility in adding equilibrium constraints. Studies with MSTFit ultimately lead to the determination of the equilibrium quantities and their uncertainties, including the parallel current density profile, based on experimental data. Chapter 6 is a description of the determination of the inductive electric field profiles utilizing a time series of MSTFit

equilibria and a new method of fitting the derivatives of signals.

Finally, in Chapter 7 the results of the two previous sections are brought together. The primary result of this work is that the measured current density and electric field profiles are shown to agree with the Spitzer resistivity profile although experimental uncertainties make it impossible to quantitatively rule out the neoclassical model.

This dissertation concludes with a summary and a discussion of further work in these areas. Diagnostic upgrades may solidify the measurement of bremsstrahlung emission and the extraction of  $Z_{eff}$  profiles. Experimental evidence of an enhancement of resistivity in standard discharges, reasoned to be a result of non-fully stripped impurities present in the plasma edge, can be pursued with a direct measurement of edge resistivity. There are vast opportunities to pursue with MSTFit and equilibrium modeling.

Included as an appendix are many interesting data resulting from the spectroscopic studies that are not fundamental to the physics of this dissertation. Also in the appendices are several detailed discussions of the various outputs of the MSTFit code, which may prove helpful to future users.

# Bibliography

- [1] S. Ortolani and D. D. Schnack, *Magnetohydrodynamics of Plasma Relaxation*, Singapore, World Scientific, River Edge, NJ, 1993.
- [2] R. N. Dexter, D. W. Kerst, T. W. Lovell, S. C. Prager, and J. C. Sprott, *Fusion Technologies* **19**, 131 (1991).
- [3] C. R. Sovinec, *Magnetohydrodynamic Simulations of Noninductive Helicity Injection in the Reversed Field Pinch and Tokamak*, PhD thesis, University of Wisconsin-Madison, 1995.
- [4] B. E. Chapman, A. F. Almagri, J. K. Anderson, C. S. Chiang, D. Craig, G. Fiksel, N. E. Lanier, S. C. Prager, J. S. Sarff, M. R. Stoneking, and P. W. Terry, *Physics of Plasmas* **5**, 1848 (1998).
- [5] H. A. B. Bodin and A. A. Newton, *Nuclear Fusion* **20**, 1255 (1980).
- [6] J. B. Taylor, *Physical Review Letters* **33**, 1139 (1974).
- [7] B. E. Chapman, T. M. Biewer, P. K. Chattopadhyay, C. S. Chiang, D. Craig, N. A. Crocker, D. J. Den Hartog, G. Fiksel, P. W. Fontana, S. C. Prager, and J. S. Sarff, *Physics of Plasmas* **7**, 3491 (2000).
- [8] K. F. Schoenberg, R. F. Gribble, and J. A. Phillips, *Nuclear Fusion* **22**, 1433 (1982).
- [9] J. C. Sprott, *Physics of Fluids* **31**, 2266 (1988).
- [10] W. Shen and J. C. Sprott, *Physics of Fluids B* **3**, 1225 (1991).
- [11] V. Antoni, P. Martin, and S. Ortolani, *Nuclear Fusion* **29**, 1759 (1989).
- [12] V. D. Pustovitov, *Nuclear Fusion* **41**, 721 (2001).
- [13] A. B. Kuznetsov, S. V. Shchepetov, and D. Y. Sychugov, *Nuclear Fusion* **34**, 185 (1994).

- [14] S. V. Shchepetov and A. B. Kuznetsov, *Nuclear Fusion* **36**, 1097 (1996).
- [15] A. B. Kuznetsov and S. V. Shchepetov, *Nuclear Fusion* **37**, 371 (1997).
- [16] J. L. Luxon and B. B. Brown, *Nuclear Fusion* **22**, 813 (1982).
- [17] L. L. Lao, H. St. John, R. D. Stambaugh, A. G. Kellman, and W. Pfeiffer, *Nuclear Fusion* **25**, 1611 (1985).
- [18] B. J. Braams, *Plasma Physics and Controlled Fusion* **33**, 715 (1991).
- [19] L. L. Lao, J. R. Ferron, R. J. Groebner, W. Howl, H. St. John, E. J. Strait, and T. S. Taylor, *Nuclear Fusion* **30**, 1035 (1990).
- [20] J. Blum, E. Lazzaro, J. O'Rourke, B. Keegan, and Y. Stephan, *Nuclear Fusion* **30**, 1475 (1990).
- [21] F. Alladio and P. Micozzi, *Nuclear Fusion* **35**, 305 (1995).
- [22] H. Ji, A. F. Almagri, S. C. Prager, and J. S. Sarff, *Physical Review Letters* **73**, 668 (1994).
- [23] J. T. Chapman, *Spectroscopic Measurement of the MHD Dynamo in the MST Reversed Field Pinch*, PhD thesis, University of Wisconsin-Madison, 1998.
- [24] J. P. Wainwright, M. G. Haines, and C. G. Gimblett, *Plasma Physics and Controlled Fusion* **37**, 1449 (1995).
- [25] L. Spitzer Jr., *Physics of Fully Ionized Gases*, Interscience Publishers, John Wiley and Sons, New York, New York, 1962.
- [26] L. Gabellieri, M. Giubbilei, S. Martini, S. Ortolani, M. E. Puiatti, and P. Scarin, *Nuclear Fusion* **27**, 863 (1987).
- [27] Z. Yoshida, *Physics of Fluids B* **4**, 1534 (1992).
- [28] K. F. Schoenberg, R. W. Moses Jr., and R. L. Hagenson, *Physics of Fluids* **27**, 1671 (1984).
- [29] J. Callen, *Fundamentals of Plasma Physics*, University of Wisconsin, Madison, WI, 2000.
- [30] F. F. Chen, *Introduction to Plasma Physics and Controlled Fusion*, Plenum Press, New York, NY, 1984.
- [31] V. D. Kirillov, B. A. Trubnikov, and S. A. Trushin, *Soviet Journal of Plasma Physics* **1**, 117 (1975).

- [32] R. J. Goldston and P. H. Rutherford, *Introduction to Plasma Physics*, Institute of Physics Publishing, Philadelphia, PA, 1995.
- [33] S. M. Kaye, F. M. Levinton, R. Hatcher, R. Kaita, C. Kessel, B. LeBlanc, D. C. McCune, and S. Paul, *Physics of Fluids B* **4**, 651 (1992).
- [34] J. L. Porter, P. E. Phillips, S. C. McCool, S. B. Kim, D. W. Ross, W. H. Miner, and J. C. Wiley, *Nuclear Fusion* **27**, 205 (1987).
- [35] E. Meservey, M. Bitter, C. Daughney, D. Eames, P. Efthimion, E. Hinnov, R. Hulse, D. Post, K. Sato, S. Suckewer, and S. von Goeler, *Nuclear Fusion* **24**, 3 (1984).
- [36] H. Röhr and K. H. Steuer, *Review of Scientific Instruments* **59**, 1875 (1988).
- [37] M. C. Zarnstorff, K. McGuire, M. G. Bell, B. Grek, D. Johnson, D. McCune, H. Park, A. Ramsey, and G. Taylor, *Physics of Fluids B* **2**, 1852 (1990).
- [38] M. Kikuchi, M. Azumi, S. Tsuji, K. Tani, and H. Kubo, *Nuclear Fusion* **30**, 343 (1990).
- [39] D. V. Bartlett, R. J. Bickerton, M. Brusati, et. al., *Nuclear Fusion* **28**, 73 (1988).
- [40] C. B. Forest, K. Kupfer, T. C. Luce, P. A. Politzer, L. L. Lao, M. R. Wade, D. G. Whyte, and D. Wroblewski, *Physical Review Letters* **73**, 2444 (1994).
- [41] D. G. Whyte, M. R. Wade, D. F. Finkenthal, K. H. Burrell, P. Monier-Garbet, B. W. Rice, D. P. Schissel, W. P. West, and R. D. Wood, *Nuclear Fusion* **38**, 387 (1999).
- [42] M. T. Fall, *Mesure de la Charge Moyenne Ionique, par le Rayonnement Bremsstrahlung dans le Visible, Sur Tore Supra*, PhD thesis, L'Universite Paris xi Orsay, 1991.
- [43] H. Weisen, D. Pasini, A. Weller, and A. W. Edwards, *Review of Scientific Instruments* **62**, 1531 (1991).
- [44] N. J. Peacock, K. D. Lawson, R. Barnsley, and H. Chen, *Review of Scientific Instruments* **71**, 317 (1999).
- [45] E. S. Marmor, R. L. Boivin, R. S. Granetz, J. W. Hughes, and B. Lipschultz, *Review of Scientific Instruments* **72**, 940 (2001).
- [46] J. J. Rommers, R. Behn, B. P. Duval, S. Franke, and Z. A. Pietrzyk, *Proceedings of the 8th International Symposium on Laser-Aided Plasma Diagnostics*, 235 (1997).

- [47] L. Carraro, S. Costa, M. E. Puiatti, F. Sattin, P. Scarin, and M. Valisa, *Plasma Physics and Controlled Fusion* **42**, 731 (2000).
- [48] D. Whyte, Private communication.
- [49] L. L. Lao, J. R. Ferron, R. J. Groebner, W. Howl, H. St. John, E. J. Strait, and T. S. Taylor, *Nuclear Fusion* **30**, 1035 (1990).

## Chapter 2

# Hardware

### Abstract

Several spectroscopic instruments used to quantitatively measure emission in the near-infrared (NIR), visible and near ultraviolet on MST are described. Specifically this chapter addresses the wavelength response and calibration of (1) a 0.5m spectrometer with a CCD camera array detector, (2) a set of filtered photodiode detectors used for measuring both dim background emission and  $H_{\alpha}$  line emission, and (3) a monochromator used in conjunction with either a photodiode or a photomultiplier tube for measuring very specific narrow portions of wavelength space.

## 2.1 General Survey Spectrometer

The CVI spectrometer, used for a variety of tasks in the pursuit of a bremsstrahlung measurement, is a 0.5 m spectrometer with a 750×240 pixel CCD array detector on the exit plane. It is utilized for surveying line emission and background continua from plasmas and for wavelength calibration of other diagnostics. A computer interface allows selection of a nominal central wavelength and a grating (150 or 1800 groove per millimeter gratings are used in these experiments, a 3600/mm grating is also available). Good wavelength resolution ( $\Delta\lambda \sim 0.3\text{nm}$  for the 150/mm grating,  $\Delta\lambda \sim 0.02\text{ nm}$  for the 1800/mm) is achieved while there is poor time resolution ( $\Delta t \gtrsim 10\text{ ms}$ ) available with this particular CCD detector. The spectrometer with this detector is well suited to visible wavelengths, with rapid loss of efficiency into the ultraviolet and infrared. Measurements presented here are typically the sum of spectra from many shots, where the detector array collects light for 30 milliseconds during the discharge. It is necessary to calibrate both the wavelength and absolute intensity measurements, the techniques employed for each are presented here.

### 2.1.1 Wavelength Calibration

It is necessary to have an accurate wavelength calibration for identification of impurity lines and to calibrate the wavelength response of other instruments. The wavelength axis of the CVI is calibrated utilizing a two point, six spectrum method. Two distinct atomic lines are selected which bound the target wavelength;  $\text{H}_\alpha$  (656.3 nm) and  $\text{H}_\beta$  (486.1 nm) are used in the case illustrated in Figure 2.1 to calibrate near  $\lambda = 523\text{nm}$ . For each of the atomic lines, three spectra are measured with the nominal central wavelength above, near, and below the target line to position the sharp peak at three different locations on the CCD array detector. The wavelength axis is modeled as

$$\lambda = \lambda_{nom} - \lambda_{off} + (P - 375)/750 * W \quad (2.1)$$

where  $P$  is the channel, or pixel number of the CCD array readout (1-750),  $W$  is the full width of the wavelength axis,  $\lambda_{nom}$  is the nominal central wavelength, and  $\lambda_{off}$  is the difference between the actual central wavelength and the nominal central wavelength. By taking three different spectra, three values of  $\lambda_{nom}$  and  $P$  are set, where  $P$  is the pixel number of the line of interest, whose wavelength is  $\lambda$  in equation 2.1. A line is fit to the three points; the slope determines  $W$  and the

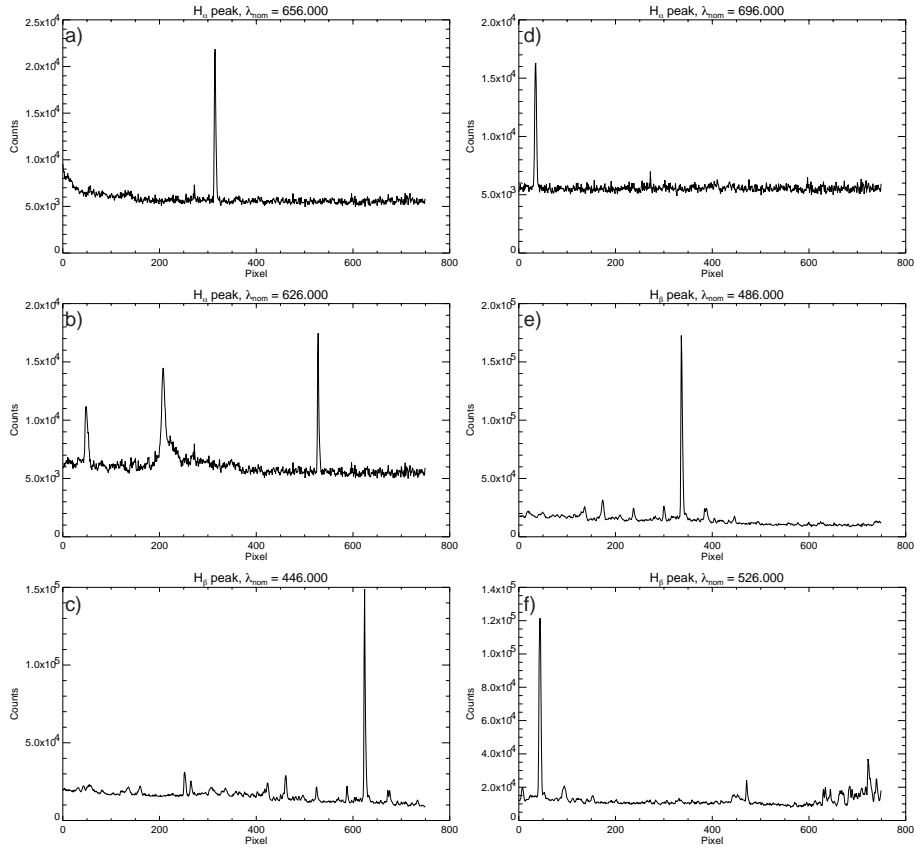


Figure 2.1: CVI wavelength calibration for the 150/mm grating. The result is:  
 $\lambda = \lambda_{nom} + 6.2\text{nm} + (P - 375)/750 \times 104.1\text{nm}$ .

intercept specifies  $\lambda_{off}$ . This method absolutely calibrates the wavelength axis for a central value equal to the wavelength of the line. The process is repeated for a second line, which typically leads to slightly different values for  $\lambda_{off}$  and  $W$ ; the final calibration is determined by interpolating the values of  $\lambda_{off}$  and  $W$  to the target wavelength. For the particular case shown here, the actual

wavelength axis as a function of pixel number is

$$\lambda = \lambda_{nom} + 6.2\text{nm} + (P - 375)/750. \times 104.1\text{nm}.$$

The exact same method can be applied for the 1800/mm grating; the calibration is

$$\lambda = \lambda_{nom} - 2.9\text{nm} + (\text{pixel} - 375)/750. \times 7.95\text{nm}.$$

Having a well calibrated wavelength axis enables identification of impurities from their tabulated lines. Frequent comparison to known lines ensures that the calibration is stable over the course of a day-long experiment.

### 2.1.2 Intensity Calibration

A quantitative measurement of the continuum between atomic lines is possible with an absolutely calibrated detector on the spectrometer. The intensity calibration of the CCD array detector is performed using an integrating lab sphere[1] as the known source. Figure 2.2 is a plot of the spectral radiance versus wavelength over the calibrated range. This source can calibrate a

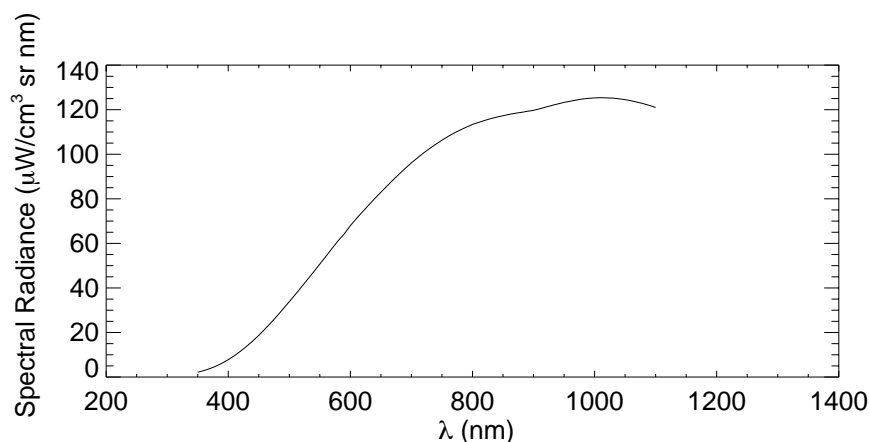


Figure 2.2: Output of calibration lamp is nearly constant over 1030 - 1050nm range.

diagnostic effectively from the NIR down to the short visible ( $\sim 400 \text{ nm} \lesssim \lambda \lesssim 1100 \text{ nm}$ ), and the quality of calibration degrades rapidly at shorter wavelengths. Two effects must be measured to incorporate a calibration at a given wavelength: the sensitivity at the central wavelength and the

shape over the wavelength range. The sensitivity at the central wavelength is primarily an effect of the quantum efficiency of CCD camera. The second effect is the change in measured sensitivity with position on the CCD array, which is primarily a dispersive effect associated with the grating and optics, although there is some change in the CCD quantum efficiency over the wavelength range measured.

The input fiber optic to the spectrometer is directed at the calibrated source, and spectra are taken at central wavelengths spanning the range of the source. The data are a total number of counts for each channel. The calibration of the wavelength axis is then used to convert the channel to a width in wavelength. Thus, by dividing the number of counts by the collection time, the number of counts per unit time and per unit wavelength is determined. Calibration is finalized by specifying the incident spectral radiance (power per unit area, wavelength, and solid angle) from the known source. The sensitivity of the CCD array detector is the ratio of the measured counts/sec/nm to the incident spectral radiance. Figure 2.3 shows measurements of the calibration at several wavelengths; the data show it is possible to make absolutely calibrated measurements

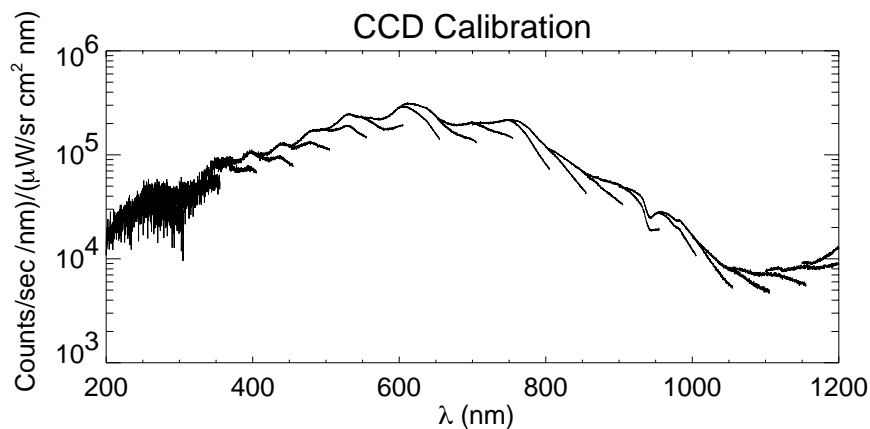


Figure 2.3: CCD intensity calibration, 150/mm grating.

from the short visible to the near infrared ( $350\text{nm} \lesssim \lambda \lesssim 1100\text{ nm}$ ).

## 2.2 Filtered Photodiode Array

The primary diagnostic used to measure the continuum radiation in this work is a set of photodiode detectors with filters that select a specific wavelength range. Thirteen poloidal viewing chords on a box port, as well as four toroidally displaced ( $5^\circ$ ) edge viewing chords (two inboard, two outboard) accommodate the array of detectors. Figure 2.4 shows the geometry along with a typical NIR detector. The optics detailed in the inset sample a nearly cylindrical volume[2] leading

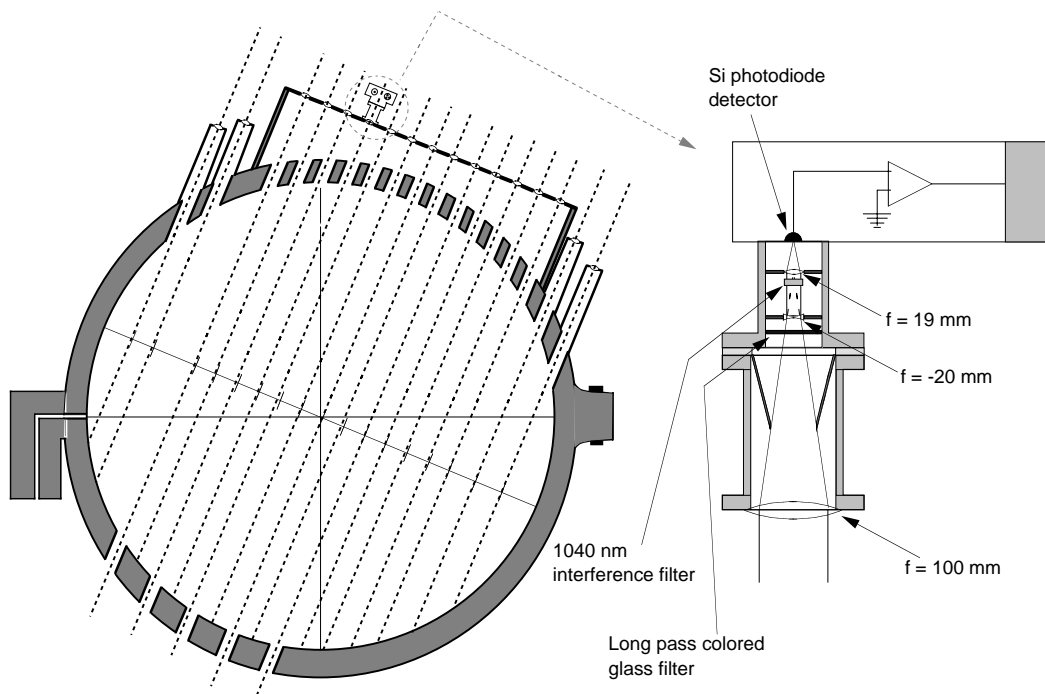


Figure 2.4: Schematic of NIR Bremsstrahlung measurement with 17 chord array geometry.

to a standard line integrated emission measurement. At the focal point of the optics is a silicon photodiode which drives a three stage amplifier, whose schematic is shown in Figure 2.5. The first stage is a current-to-voltage conversion which precedes a frequency compensation stage and a final amplification (nominal gain is 20) with DC offset control.

The measured signal is the emissivity collected over the sample volume in the wavelength range allowed by the filter scheme. This is the line integral of emissivity convolved with the wavelength

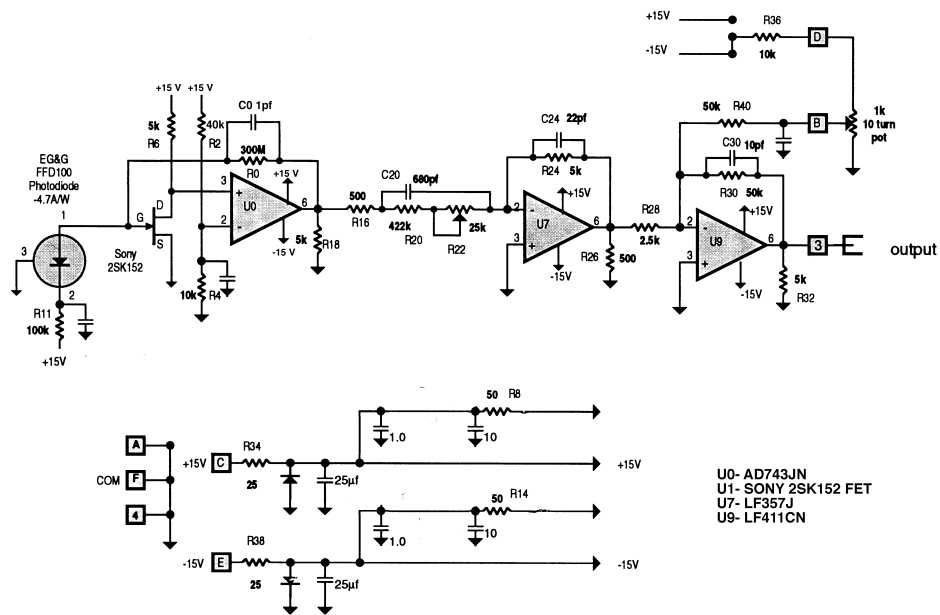


Figure 2.5: Schematic of amplifier circuit used with photodiode detectors.

transfer function (Section 2.2.1)

$$V_{\text{meas}} = \kappa \int_0^{\infty} \int_0^L \iint_A f(\lambda) \epsilon(\lambda, r) \Delta\Omega(r) dA dl d\lambda \quad (2.2)$$

where  $\kappa$  is the calibration of the photodiode and amplifier system (Section 2.2.2), converting the power collected in Watts to signal out in Volts. For a line averaged signal, the elements at each

position  $l$  along the chord contribute equally to the total, or

$$\iint_{A(l)} \Delta\Omega(r, l) dA = \text{Constant} \equiv A\Delta\Omega \quad (2.3)$$

which results in

$$V_{meas} = \kappa A\Delta\Omega \int_0^\infty \int_0^L f(\lambda) \epsilon(\lambda, l) dl d\lambda \quad (2.4)$$

Noting that the bremsstrahlung spectrum falls off as  $1/\lambda^2$ , which is very nearly constant over the range of 1030nm through 1050nm<sup>1</sup>, simplification of equation 2.4 is allowed by treating the emissivity as a constant over the wavelength integration

$$V_{meas} = \kappa A\Delta\Omega \int_0^\infty f(\lambda) d\lambda \int_0^L \epsilon(l) dl \quad (2.5)$$

or defining a new calibration  $\kappa'$ ,

$$\kappa' \equiv \kappa A\Delta\Omega \int_0^\infty f(\lambda) d\lambda \quad (2.6)$$

the measured voltage is

$$V_{meas} = \kappa' \int_0^L \epsilon(l) dl. \quad (2.7)$$

The absolute emissivity level on MST can then be quantified from the measured signal level after  $\kappa'$  is determined (Section 2.2.2).

---

<sup>1</sup>Section 2.2.1 shows this is the important wavelength range

### 2.2.1 Wavelength Response

The choice of filter(s) determines the wavelength range of emission collected. While measurements presented in Chapters 3 and 4 are at several different wavelengths, the ultimate MST bremsstrahlung measurement is made at 1040nm, with two filters used. The first is a long pass colored glass filter which transmits only about  $10^{-8}$  of the incident visible light and nearly 100% of the infrared. This eliminates possible signal pollution from  $H_{\alpha}$  and other bright visible and uv lines. The second is an interference filter with a pass band of  $\sim 10$  nm centered at 1040 nm. The measured wavelength response is shown in Figure 2.6, where the spectra of the calibrated sphere are

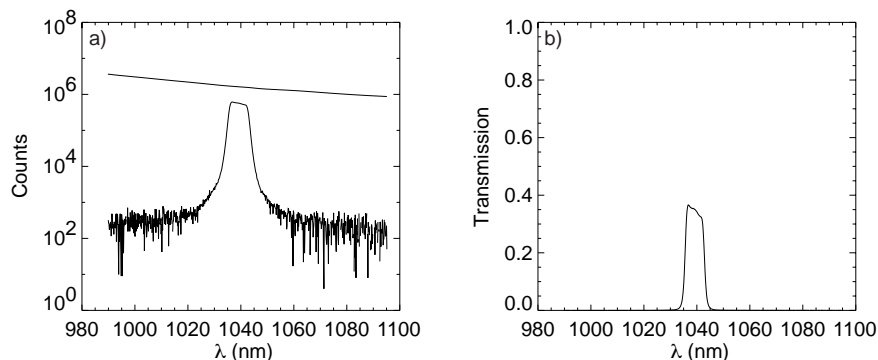


Figure 2.6: Transmission of 1040nm filter. a) shows the measured spectra of a calibrated light source with and without the filters in place. b) is the ratio of the two spectra, or the measured wavelength transfer function.

shown with and without the filters in place; the ratio of the two yields the measured transmission.

In addition to the measurement made in the NIR, several visible wavelengths (350, 420, 500, 520, and 620nm) have been investigated. The wavelength response for each is measured in a fashion identical to that for the NIR pass band and can be found in Appendix A. For the visible wavelengths the use of the long pass filter is not possible, thereby leaving the opportunity for  $H_{\alpha}$  pollution. To quantify this effect, the transmittance at 656.3nm of each band pass filter is measured. Figure 2.7 is an example of this measurement in the 520nm range. Plot a) is the transmission near the pass band

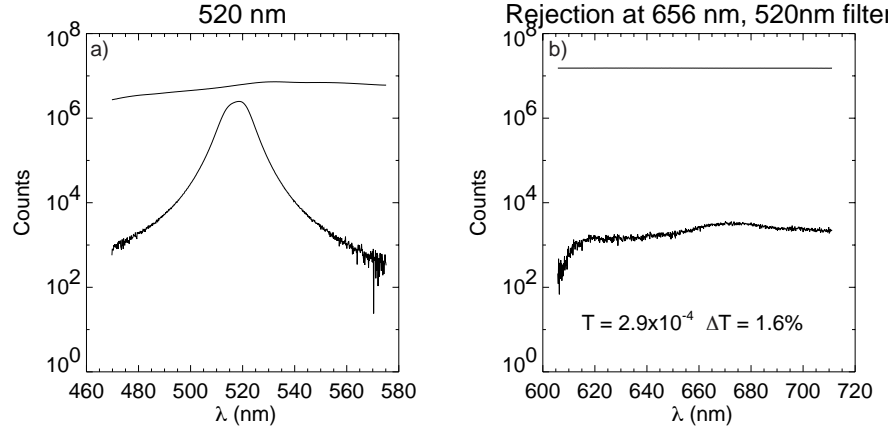


Figure 2.7: Filter rejection measurement: 520nm pass band filter.

at 520nm, while plot b) is the transmission at the H $\alpha$  wavelength. The measured H $\alpha$  transmittance is just over  $10^{-4}$  for this filter. Table 2.1 below contains the results of direct H $\alpha$  contamination at each of the measured wavelengths; the second column utilizes measurements of the absolute intensity at each wavelength and of H $\alpha$  (see Appendix A) to estimate the fraction of the measured signal at each wavelength due to H $\alpha$  contamination. The value quoted at 1040nm is an upper bound due to experimental limitations of the spectrometer; the transmission according to the filter specifications is two orders of magnitude lower, as is the expected H $\alpha$  contamination. These

$\lambda$ (nm)	H $\alpha$ / $\epsilon_\lambda$	H $\alpha$ Transmission	H $\alpha$ Contamination
350	200	$3.9 \times 10^{-5}$	.78%
420	150	$1.1 \times 10^{-4}$	1.65%
500	200	$2.2 \times 10^{-4}$	4.4%
520	300	$2.9 \times 10^{-4}$	8.7%
620	200	$5.4 \times 10^{-4}$	10.8%
700	200	$2.3 \times 10^{-4}$	4.6%
1040	3000	$\leq 4.8 \times 10^{-6}$	$\leq 1.44\%$

Table 2.1: Measured transmission of each wavelength band at the H $\alpha$  wavelength. Using typical emissivity values, an estimate of the contamination is made.

ratios are important in ruling out  $H_\alpha$  pollution as the demise of bremsstrahlung attempts on MST considered in Chapter 3.

### 2.2.2 Photodiode Calibration Procedure

An accurate calibration of the detectors is essential in quantitative emission measurements; the technique described here applies to continuum measurements at all of the wavelengths considered. The calibration setup is designed to mimic the geometry of the detector on MST, shown in Figure 2.8. The lab sphere offers a very sensitive luminance control and specifications to convert to

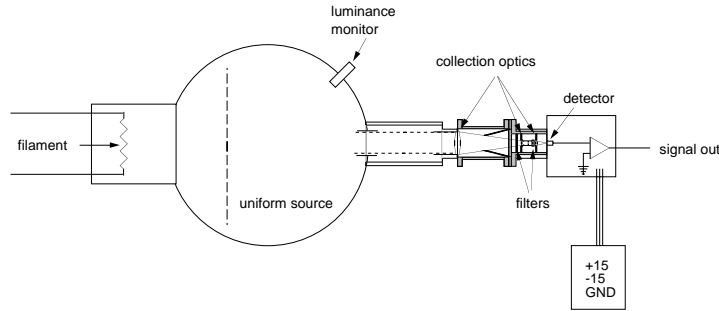


Figure 2.8: Photodiode system calibration procedure.

spectral radiance,  $R$  (in  $\frac{W}{cm^2 sr nm}$ ) on its surface. Again, the measurement is described by equation 2.2, but now the collected power is not totaled over a volume, but rather on the surface of the sphere. This is effectively a  $\delta$  function integration over the path length,

$$\epsilon(l) \propto \delta(l - r_{\text{sphere}}) \quad \text{with} \quad R = \int \epsilon(l) dl \quad (2.8)$$

reducing this to an integration over area at the surface of the sphere. Noting that the optics and geometry are identical to those on MST, the product  $A\Delta\Omega$  is identical in calibration and in measurement. Specification data sketched in Figure 2.2 show that the radiance is nearly a constant over the  $\sim 10\text{nm}$  wavelength band of interest. These simplifications lead to a result similar to

equation 2.5, and the simplification of path length integration to a single surface leads to

$$V_{cal} = \kappa A \Delta \Omega \int_0^\infty f(\lambda) d\lambda R \equiv \kappa' R. \quad (2.9)$$

The detectors respond linearly to a change in luminance, as shown in Figure 2.9, and the source

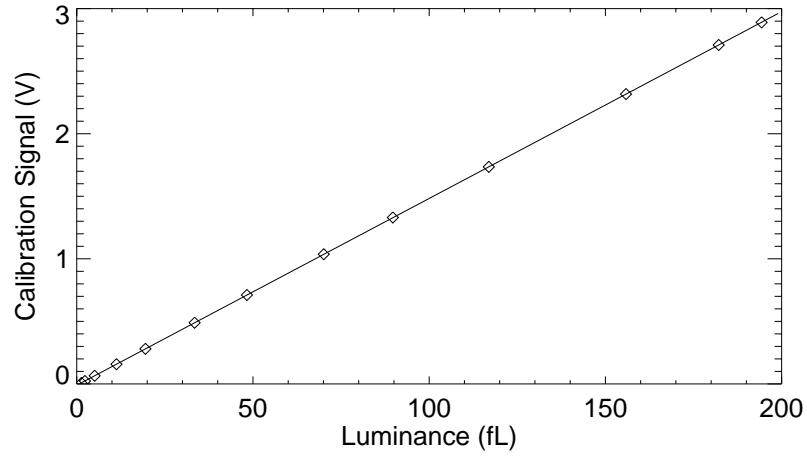


Figure 2.9: Typical plot of detector response to luminance, this slope is 0.0146 V/fL and the specification at 1040nm is 11546 fL equals  $1.249 \times 10^{-4} \frac{\text{W}}{\text{sr cm}^2 \text{ nm}}$ .

specifications provide the conversion from luminance to spectral radiance at a given wavelength.

This leads to the desired form of the calibration from equation 2.9

$$\kappa' = \frac{V_{cal}}{R} = \frac{\Delta V}{\Delta L} \left( \frac{L}{R} \right)_{\lambda, spec} \quad (2.10)$$

which maps units of real collected spectral radiance to an output voltage. A slope  $\frac{\Delta V}{\Delta L}$  of .0146 V/fL taken from Figure 2.9 and the lamp specification of  $\frac{L}{R} = 11546 \text{ fL} / 1.249 \times 10^{-4} \frac{\text{W}}{\text{sr cm}^2 \text{ nm}}$  yields  $\kappa' = 1.03 \times 10^6 \text{ V} \frac{\text{sr cm}^2 \text{ nm}}{\text{W}}$  for a typical detector at 1040nm.

The calibration procedure for the visible continuum measurements is exactly as described above, but a different specification for radiance to luminance conversion must be applied. A summary of

typical calibration values for each selected wavelength is given in Table 2.2 below.

$\lambda$ (nm)	Slope $\frac{\Delta V}{\Delta L}$ ( $\frac{V}{\mu L}$ )	Radiance spec. $\frac{\Delta L}{\Delta R}$ $\left(\frac{fL}{W/cm^2 \text{ nm sr}}\right)$	Calibration $\left(\frac{V}{W/cm^2 \text{ nm sr}}\right)$
1040	$1.12 \times 10^{-2}$	$9.24 \times 10^7$	$1.03 \times 10^6$
700	$4.79 \times 10^{-3}$	$1.20 \times 10^8$	$5.76 \times 10^5$
620	$4.72 \times 10^{-3}$	$1.70 \times 10^8$	$8.02 \times 10^5$
520	$1.92 \times 10^{-4}$	$2.84 \times 10^8$	$5.47 \times 10^5$
500	$6.52 \times 10^{-4}$	$3.41 \times 10^8$	$2.22 \times 10^5$
420	$1.87 \times 10^{-4}$	$9.97 \times 10^8$	$1.86 \times 10^5$
350	$1.56 \times 10^{-5}$	$5.33 \times 10^9$	$8.29 \times 10^4$

Table 2.2: Typical calibration values for NIR/visible continuum measurements

The photodiode detectors are well designed and quite reliable; they have good time response (typically sampled at 200kHz, but could be run higher), aren't particularly sensitive to noise and are very easy to calibrate. A sample signal is shown in Figure 2.10. This is a nice clean signal,

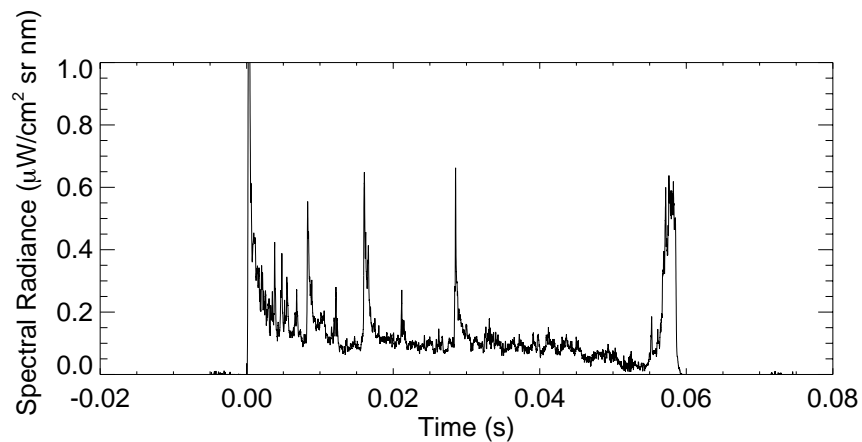


Figure 2.10: A typical calibrated signal from the photodiode detectors. This signal is a measurement of the emission at 1040nm in a standard MST discharge.

as the startup and termination light are real. The large spikes appearing during  $.01s < t < .03s$  correspond to sawteeth and an accompanying jump in (non-bremsstrahlung) emissivity.

### 2.2.3 $H_\alpha$ Measurement and Calibration

Substitution of the pass band filter accommodates a measurement of  $H_\alpha$  emission with the identical optics, detector and electronics with two subtle differences. The first is that the intensity of the  $H_\alpha$  emission is much stronger than that of the underlying continuum, so the level must be attenuated prior to reaching the diode. In practice, a pinhole aperture is placed in front of the last collection optic, which satisfactorily decreases the incident light to allow the detector to operate without saturation.

The second subtle difference is related to absolute calibration of the detector due to the line type (versus continuum) nature of the emission, while being calibrated from a continuous source. The emission of the sphere is nearly constant over the wavelength region of interest again, as shown in Figure 2.11. Also shown is the measured transfer function and the position of the  $H_\alpha$  line

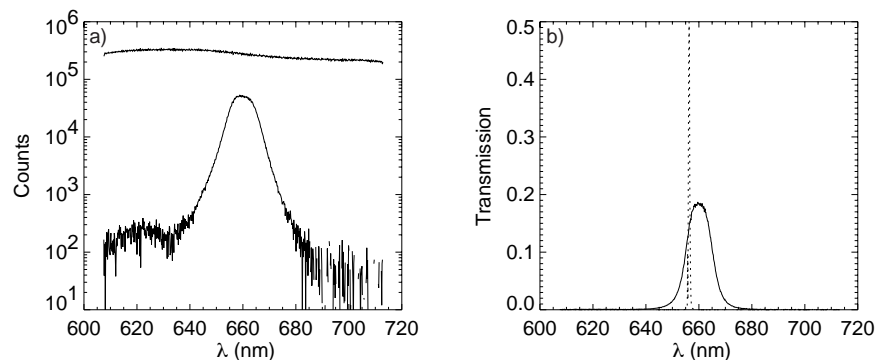


Figure 2.11: a) is the output of the lab sphere from 600-700nm along with the transmitted light through the filter. b) is the computed transfer function, along with the position of the  $H_\alpha$  line.

(measured on a hydrogen glow discharge lamp) which nearly coincides with the peak transmittance. The narrow band passed by the filters justifies the assumption of a constant spectral radiance from the calibrating sphere over the sensitive wavelength range. However, the situation is quite different when measuring the  $H_\alpha$  emission on MST. With line radiation, the emissivity is nowhere near constant over a 10nm wide window; this affects the calibration.

The development of the line measurement calibration proceeds by recalling equation 2.4

$$V_{meas} = \kappa A \Delta \Omega \int_0^\infty \int_0^L f(\lambda) \epsilon(\lambda, l) dl d\lambda \quad (2.11)$$

where the optics, detector and viewing geometry are identical to those in the continuum measurements. Figure 2.11 clearly shows that the emissivity is not constant over the pass band of the filter, as the measured width of the  $H_\alpha$  line is much narrower than the collection band. In fact, for line radiation quite the opposite situation occurs. The filter response function is nearly constant over the region in wavelength space in which the emissivity is nonzero, or  $\epsilon(\lambda) \sim \delta(\lambda - \lambda_{H_\alpha})$ . Substituting an emissivity of this form into equation 2.11 gives

$$V_{meas} = \kappa A \Delta \Omega f(\lambda_{H_\alpha}) \int_0^L I_{H_\alpha}(l) dl \quad (2.12)$$

where the intensity,  $I$ , is the total  $H_\alpha$  emission integrated over all wavelengths, in units of  $\frac{W}{cm^2 sr}$ .

It is necessary to express the measured  $H_\alpha$  emission in terms of  $\kappa'$  to utilize the existing calibration. Recalling the definition in equation 2.9, one can write

$$V_{meas} = \kappa' \frac{f(\lambda_{H_\alpha})}{\int_0^\infty f(\lambda) d\lambda} \int_0^L I_{H_\alpha}(l) dl \quad (2.13)$$

and the remaining hurdle is computing the two numerical quantities based on the wavelength response. The integral over the entire transfer function  $\int_0^\infty f(\lambda) d\lambda$  is easily computed, resulting in the numerical factor 2.189 nm. The value  $f(\lambda_{H_\alpha})$  is calculated by averaging the transmission (shown in Figure 2.11) over the width of the  $H_\alpha$  line, yielding 0.1423. These two corrections are applied to the calibration obtained for the linear output voltage versus luminance plot as in Figure 2.9.

### 2.2.4 Colinear Arrangement

After careful consideration, discussed in Chapter 3, it was determined that the best attempt to measure bremsstrahlung on MST is by measuring the NIR and  $H_\alpha$  emission simultaneously. Only minor modifications to the existing hardware, shown in Figure 2.12, are required for this adaptation. A common microscope slide (BK7,  $R \lesssim 10\%$ ) is used as a partially reflecting surface, directing

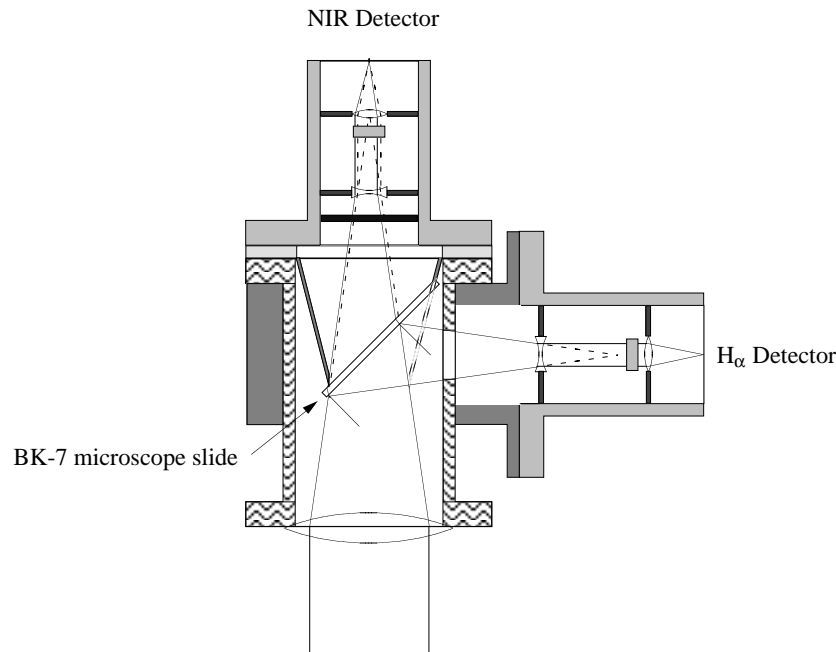


Figure 2.12: Colinear NIR/ $H_\alpha$  measurement.

a small fraction of the incident light out of a hole carefully positioned in the side of the detector mount, while transmitting the majority of the light down the original path. As the  $H_\alpha$  emission is several thousand times brighter than the background bremsstrahlung, an  $H_\alpha$  detector is mounted to collect the diffuse reflected light. Larger pinhole apertures replaced the existing pinholes to compensate for the decrease in incident light, and recalibration of the both the NIR and  $H_\alpha$  detectors was performed on a test stand identical to the optics on the machine. Eight viewing chords were subjected to these modifications, enabling a profile measurement which will be presented in Chap-

ter 4.

## 2.3 Monochromator and Photomultiplier Tube

Two separate experiments were performed that required a very specific narrow wavelength sample. One was a measurement of background emission in a line free region at  $523\pm.5\text{nm}$ , and the other was a direct measurement of a helium line at  $587\pm 3\text{nm}$ . A Jarrel-Ash monochromator with adjustable entrance and exit slit widths and a dial-controlled grating angle enables the narrow band measurements. An accurate calibration of the wavelength dial is performed by monitoring the central transmitted wavelength with the CVI spectrometer versus dial reading. Figure 2.13 demonstrates good linear behavior, and the equation  $\lambda = -240.3\text{nm} + .1017\times\text{dial}$  fits the data.

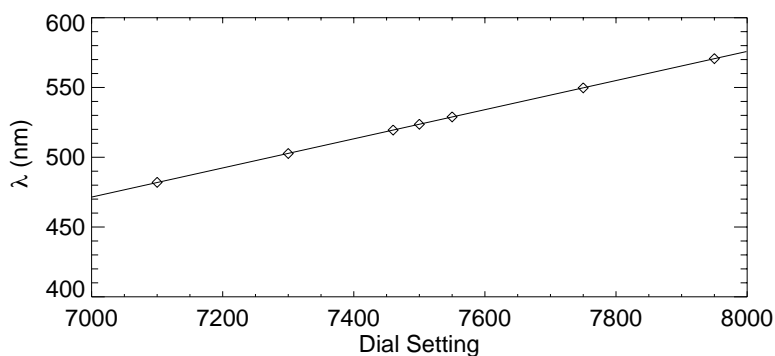


Figure 2.13: Wavelength calibration of the monochromator dial:  $\lambda = -240.3\text{nm} + .1017\times\text{dial}$

Figure 2.14 is a sketch of the setup used for the narrow band visible measurement. The optics (identical to those in the photodiode setup described in Section 2.2) direct the collected light into a fiber optic which carries it to the monochromator. A 520nm pass band filter<sup>2</sup> is used to obtain about  $10^{-4}$  rejection of stray light (presumably from atomic lines) more than 40nm away, and the monochromator provides another factor of  $10^{-4}$  rejection for light at wavelengths outside

<sup>2</sup>This filter has significant transmittance at 523nm, the measured wavelength response can be found in Appendix A

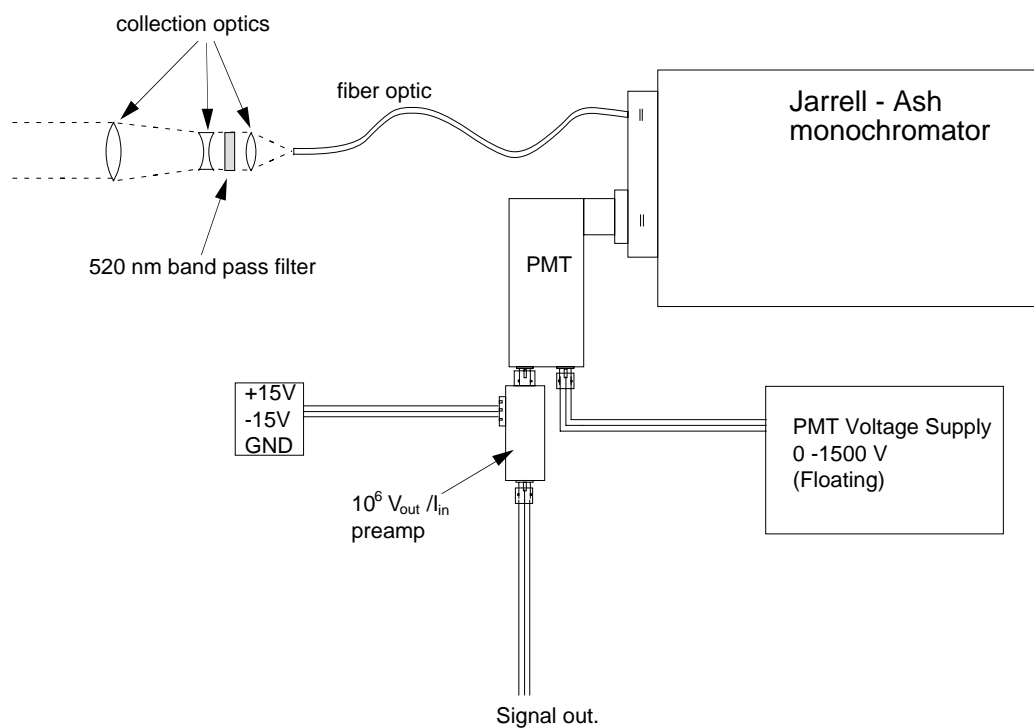


Figure 2.14: Schematic of narrow band visible bremsstrahlung measurement.

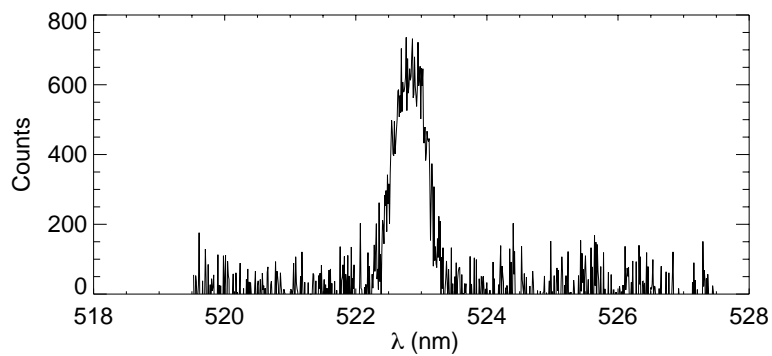


Figure 2.15: Wavelength response of the monochromator for the narrow band measurement.

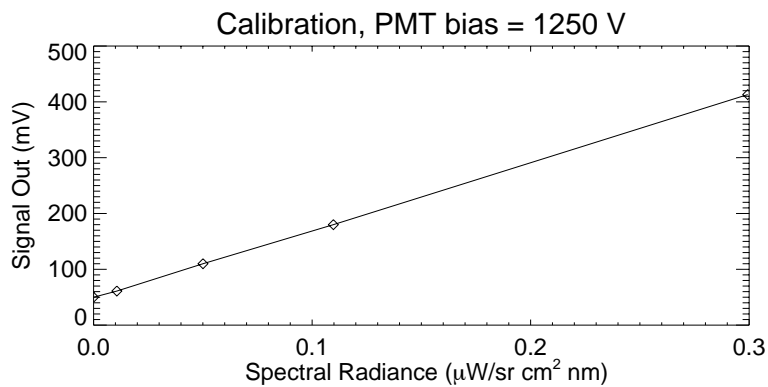


Figure 2.16: Calibration of the photomultiplier tube at 1250 V. The result is  $\kappa' = 1.11 \times 10^8 \text{ V } \frac{\text{sr cm}^2 \text{ nm}}{\text{W}}$ ,  $\sim 10^2$  times more sensitive than the NIR photodiode.

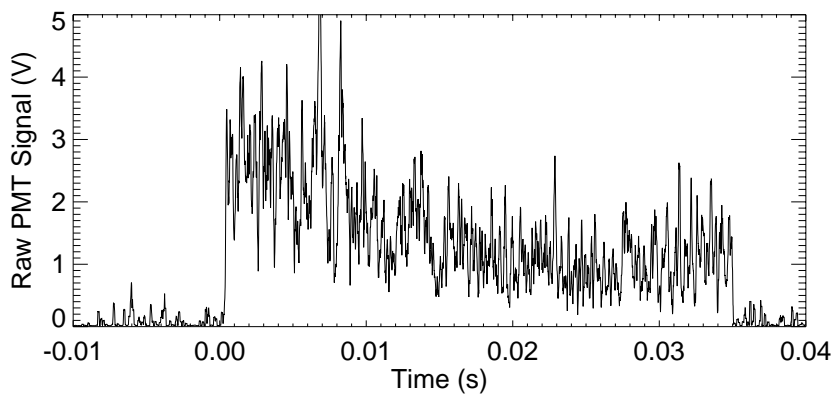


Figure 2.17: Measured emission with PMT at  $523.5 \pm 0.5 \text{ nm}$  on MST, DC offset removed.

the desired range of 523-524nm. The intended narrow response is demonstrated in Figure 2.15. This technique gives about  $10^{-8}$  rejection of the dominant (hydrogen) lines in MST. The absolute intensity calibration is a straightforward process, as the loss in the monochromator does not need to be independently determined. With the system completely assembled, the collection optics are removed from MST and placed on the calibrated lab sphere. Calibration was performed at a variety of bias voltages on the PMT. Shown in Figure 2.16 is a sample plot of the calibration at a bias voltage of 1250V. At this setting, there is enough sensitivity ( $\kappa' = 1.11 \times 10^8 \text{ V } \frac{\text{sr cm}^2 \text{ nm}}{\text{W}}$ ,  $\sim 10^2$  times more sensitive than the NIR photodiode) to measure pure, unpolluted bremsstrahlung. Calibration was performed at bias voltages of 500, 750 and 1000V. The PMT exhibits nice linear behavior over the entire range of bias voltages, and the dark current (measured signal from a PMT with no incident light) appears as a DC offset to the signal and is easily dealt with. Figure 2.17 is a sample signal from the PMT during an MST discharge. Although significantly noisier than the photodiode signals, the measurements were successful.

In an independent experiment, this apparatus was used to measure the intensity of a neutral helium line (587 nm) in helium discharges. The 520nm pass band filter was removed and the monochromator was set to collect over a 6nm width centered about 587nm. The signal was sufficiently high so that a PMT was not required, instead an unfiltered photodiode was mounted to the exit slit of the monochromator and calibrated as described above.

## 2.4 Conclusion

Although there are no scientific results presented in this chapter, accurate wavelength and intensity calibrations of spectroscopic equipment are fundamental to bremsstrahlung and general emission measurements. The calibration procedure of the diagnostics used in this thesis are documented here.

# Bibliography

- [1] Optronic Laboratories, Inc., *OL Series 455: Integrating Sphere Calibration Standard*, 1998, Manual No: M000077 Revision: G.
- [2] J. T. Chapman, D. J. Den Hartog, and R. J. Fonck, A near-infrared bremsstrahlung diagnostic for the MST RFP, PLP Report 1116, University of Wisconsin, Madison, 1992, Poster Presented at 1992 APS-DPP Meeting.

## Chapter 3

# Feasibility of a Bremsstrahlung Measurement on MST

### Abstract

Measuring  $Z_{eff}$  via bremsstrahlung emission has proven difficult in MST, as the amount of continuous radiation is much greater than explicable via bremsstrahlung. In this chapter, the electron-ion bremsstrahlung process and its predicted emissivity are described. The measured continuum in MST is much larger than bremsstrahlung. Possible sources of contaminant radiation that have received full consideration but are not a factor are molecular and atomic (and specifically the  $H_\alpha$ ) lines, recombination, blackbody emission, and non-Maxwellian effects. Continuous emission from molecular dissociation pollutes the visible measurement, while electron-neutral bremsstrahlung and continuous emission from charge exchange are the primary pollutants in the near infrared. A bremsstrahlung measurement can proceed under certain conditions (high electron temperature and density) by monitoring these pollutants through the neutral particle density. The screening effect of non-fully stripped ions is non-negligible in standard MST operating regimes, and leads to an enhanced collisionality and an accompanying increase in resistivity and bremsstrahlung emission.

### 3.1 Introduction

A measurement of  $Z_{eff}$  is necessary for a complete study of the plasma resistivity. Successful measurements of  $Z_{eff}$  have been made on many fusion research devices and with limited success on RFX, a machine very similar to MST, through a measurement of bremsstrahlung in either the visible or near-infrared (NIR) regions. There has been considerable effort to measure bremsstrahlung (and hence  $Z_{eff}$ ) on MST in these regions, but the results have consistently shown an inexplicably high radiation level. The troubles are illustrated in Figure 3.1, where the spectrum in MST near 500nm is shown. The measured emission is almost two orders of magnitude brighter than the underlying

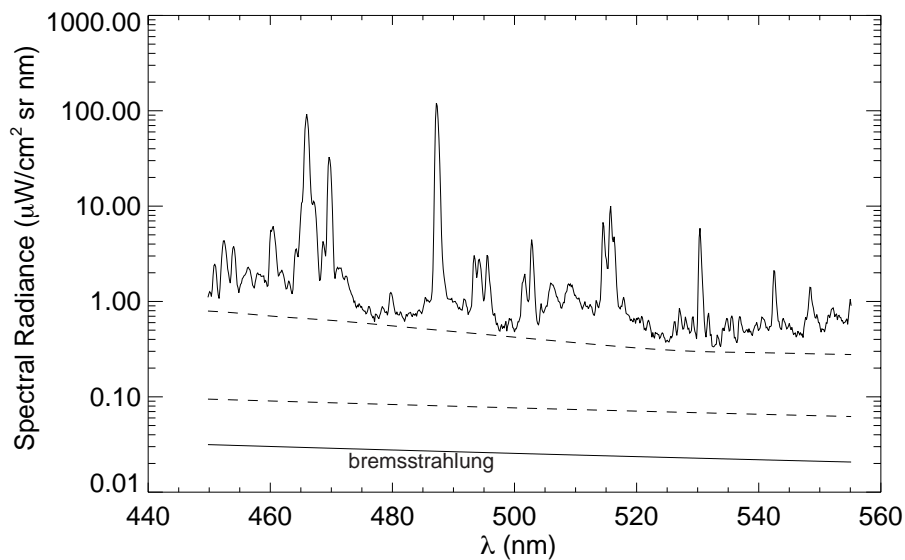


Figure 3.1: The measured spectrum in MST near 500nm. Included are the expected bremsstrahlung emission for  $Z_{eff} = 2$  (solid line at the bottom), estimated neutral hydrogen pollution (lower dashed line, see Section 3.5.6) and light from molecular hydrogen, likely due to molecular dissociation (upper dashed line), see Section 3.5.4.

bremsstrahlung. The lower dashed line is the pollution from neutral hydrogen, and the upper dashed line is light from molecular hydrogen, likely due to molecular dissociation. In order to make a quantitative measurement of bremsstrahlung, all other sources of light must be either

absent or accounted for.

A study of the emission from an electron undergoing a nearly elastic collision with an ion (bremsstrahlung) is used to optimize the choice of wavelength for the measurement. The absolutely calibrated measurement returns an emissivity much higher than possible for electron-ion bremsstrahlung; several possible sources of pollutant radiation are then considered in an attempt to explain the measurements, including line radiation, recombination, blackbody emission, molecular emission, continuous emission from charge exchange interactions, electron neutral bremsstrahlung and the screening effect of non-fully stripped ions. A non-Maxwellian electron distribution is investigated as a possible source of error in the measurement as well.

With the primary sources of radiation at each wavelength identified, it was determined that the best chance to measure bremsstrahlung is in the NIR (1040nm) where emission is well described by electron-ion bremsstrahlung plus neutral hydrogen pollution. The extreme edge of the plasma is further contaminated, but this model allows an upper bound measurement of  $Z_{eff}$  over much of the plasma volume with modest experimental uncertainty. The model is confirmed by a repeat of the experiment in helium plasmas.

## 3.2 Electron-Ion Bremsstrahlung

The fundamental interaction governing the collective behavior of a plasma is the Coulomb collision between an ion and an electron. This interaction is the root of both the plasma electrical resistivity and bremsstrahlung emission. When an electron encounters an ion in a thermalized situation, the ion is effectively stationary as its mass is much greater than that of the electron. Figure 3.2 is a sketch of the trajectory of the electron in a typical encounter. The Coulomb force falls off as the square of the distance between the two particles but continues to be a factor over very long range. In a plasma, the upper bound over which it is reasonable to consider this interaction is the Debye length, beyond which the mobility of other free charges in the plasma effectively screens

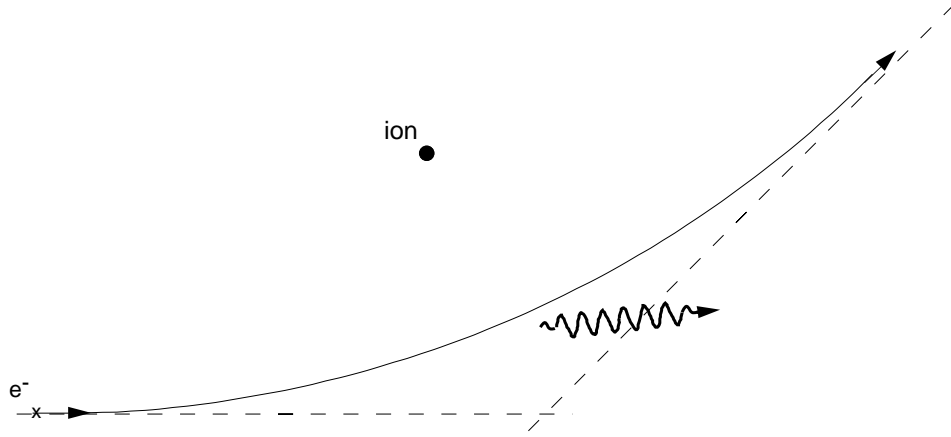


Figure 3.2: Nearly elastic collision between electron and ion.

out the test ion charge. The electron undergoes a change of momentum as its direction changes, but its kinetic energy is nearly conserved. The electron will undergo many of these encounters as it travels through the plasma, and a collision is defined as the sum of the interactions up to the point where the electron has been deflected 90 degrees from its original path, and hence its initial parallel momentum has been lost. Due to the long range nature of this interaction compared to electron-neutral collisions (where the ionic charge is screened out on an atomic length scale, see Section 3.5.6 below), the electron-ion collision rate is much higher than that of electron-neutral collisions under most plasma conditions[1].

During its acceleration, the electron radiates according to classical electrodynamics[2]. This is known as bremsstrahlung, or 'braking radiation'. The far field spectrum of bremsstrahlung is elegantly found[2, 3] by writing the standard expression for radiation from an accelerating particle and taking a Fourier transform. The result

$$\frac{d^2W}{d\Omega_s d\omega} = \frac{e^2 \omega^2}{16\pi^3 \epsilon_0 c} \left| \int_{-\infty}^{\infty} \hat{n} \times \left( \hat{n} \times \frac{\mathbf{v}}{c} \right) e^{i\omega(t' - \hat{n} \cdot \mathbf{r}/c)} dt' \right|^2 \quad (3.1)$$

is an integral over the particle trajectory resulting in a general expression for radiation from a

free electron. The power  $W$  radiated per unit solid angle and frequency is found in terms of the frequency  $\omega$  and the velocity, where the unit vector  $\hat{n}$  points from the charged particle to the observation point, treated as a constant in the far field case.

It may be noted that this form of the equation is independent of acceleration, while the velocity of the particle appears in the integrand. This is simply a mathematical trick, as the fundamental integral containing the acceleration is identified as a perfect differential, and the result in equation 3.1 is obtained by integrating by parts.

For the specific case of electron-ion bremsstrahlung, the particle orbit is known[3] (assuming a stationary ion) to be a hyperbola described by

$$r = \frac{b^2}{b_{90}(1 + \epsilon \cos\theta)} \quad (3.2)$$

where  $b$  is the impact parameter. This formula utilizes the definitions of

$$b_{90} = \frac{Ze^2}{4\pi\epsilon_0 m_e v_i^2} \quad (3.3)$$

as the impact parameter corresponding to 90 degree scattering where  $v_i$  is the initial electron velocity and

$$\epsilon = \left[ 1 + \left( \frac{b}{b_{90}} \right)^2 \right]^{1/2} \quad (3.4)$$

as the eccentricity of the orbit. Following Hutchinson's treatment of this problem by integrating equation 3.1 over impact parameters, and assuming isotropic radiation while integrating over solid angle, the power spectrum per electron is

$$\frac{dP}{d\omega} = \frac{Z^2 e^6}{(4\pi\epsilon_0)^3} \frac{16\pi}{3\sqrt{3}} \frac{n_i}{m_e^2 c^3} \times \frac{G(\omega, v)}{v_i}. \quad (3.5)$$

$G$  is the Gaunt factor which determines the spectral power density for a classical free-free<sup>1</sup> interaction, and includes the lump sum of all quantum mechanical effects as corrections. To calculate the radiation per unit volume  $j(\omega)$  in a plasma, the power density per unit electron must be integrated over the electron distribution function as

$$4\pi j(\omega) = \int \frac{dP}{d\omega} f(v) d^3\mathbf{v} = \frac{Z^2 e^6}{(4\pi\epsilon_0)^3} \frac{16\pi}{3\sqrt{3}} \frac{n_i}{m_e^2 c^3} \int_0^\infty \frac{G(\omega, v)}{v} 4\pi v^2 f(v) dv \quad (3.6)$$

and can be simplified by assuming a Maxwellian electron distribution at temperature  $T$ . The integration over the distribution function can be rewritten as

$$\int_0^\infty \frac{G(\omega, v)}{v} 4\pi v^2 f(v) dv = \left(\frac{2m_e}{\pi T}\right)^{1/2} n_e \int_0^\infty G(\omega, E' + \hbar\omega) e^{-(E' + \hbar\omega)/T} \frac{dE'}{T} \quad (3.7)$$

utilizing a change of variables based on the physical consideration that a photon of energy  $\hbar\omega$  cannot be emitted for an incident electron energy less than this value. By defining the Maxwellian averaged free-free Gaunt factor as

$$\bar{g}_{ff}(\omega, T) \equiv \int_0^\infty G(\omega, E' + \hbar\omega) e^{-(E'/T)} \frac{dE'}{T} \quad (3.8)$$

equation 3.6 becomes

$$4\pi j(\omega) = n_e n_i Z^2 \left(\frac{e^2}{4\pi\epsilon_0}\right)^3 \frac{16\pi}{3\sqrt{3}m_e^2 c^3} \left(\frac{2m_e}{\pi T}\right)^{1/2} e^{-\hbar\omega/T} \bar{g}_{ff}. \quad (3.9)$$

This form is of particular interest as it shows that all the effects of the distribution function appear in the calculation of the average Gaunt factor. This calculation encircles a great deal of physics to produce a dimensionless quantity varying from unity to almost six, depending on plasma conditions. This will be addressed in detail Section 3.3 along with the effects of a non-Maxwellian distribution

---

<sup>1</sup>Initial and final states of the electron are free, as opposed to bound. Recombination is a free-bound interaction.

(which are negligible at 1040 nm).

In preparation for comparison with experiment, equation 3.9 is converted from radiation per unit frequency  $j(\omega)$  to unit wavelength  $\epsilon(\lambda)$  per steradian by utilizing  $\frac{d\omega}{d\lambda} = \frac{2\pi c}{\lambda^2}$

$$\epsilon(\lambda) = A \frac{\bar{g}_{ff} n_e n_i Z^2 e^{-\frac{hc}{\lambda T_e}}}{\lambda^2 \sqrt{T_e}} \left[ \frac{\text{W}}{\text{cm}^3 \text{ nm sr}} \right] \quad (3.10)$$

and the constant

$$A \equiv \frac{1}{2} \left( \frac{e^2}{4\pi\epsilon_0} \right)^3 \frac{16\pi}{3\sqrt{3} m_e^2 c^3} \sqrt{\frac{2m_e}{\pi}} \times c = 1.516 \times 10^{-30} \frac{\text{W}}{\text{cm}^3 \text{ nm sr}} \frac{\text{nm}^2}{(\text{cm}^{-3})^2} \times \sqrt{\text{eV}} \quad (3.11)$$

is identified.

Equation 3.10 holds for all ion species in the plasma; the total bremsstrahlung emission is found by summing over all species. The definition of  $Z_{eff}$  which appears in Section 1.3 for resistivity

$$Z_{eff} = \frac{\sum_s n_s Z_s^2}{\sum_s n_s Z_s} = \frac{\sum_s n_s Z_s^2}{n_e} \quad (3.12)$$

also appears here for emission; using this results in

$$\epsilon(\lambda) = A \frac{\bar{g}_{ff} n_e^2 Z_{eff} e^{-\frac{hc}{\lambda k T_e}}}{\lambda^2 \sqrt{T_e}} \left[ \frac{\text{W}}{\text{cm}^3 \text{ nm sr}} \right]. \quad (3.13)$$

A simple extraction of  $Z_{eff}$  awaits the accurate measurement of bremsstrahlung, electron density and temperature profiles and an accurate calculation of the Gaunt factor. For visible and NIR wavelengths, the photon energy is much less than the electron temperature and the exponential factor can be ignored.

### 3.3 Gaunt Factor Calculation

The Gaunt factor determines the spectral power density of a free-free interaction with quantum mechanical corrections[4] arising from the wave/particle duality of a free electron. The incident and outgoing electron energies are characterized by effective state numbers,  $\eta$ ,

$$\eta_i^2 = \frac{Z^2 R_y}{E_i} \quad \text{and} \quad \eta_f^2 = \frac{Z^2 R_y}{E_f} \quad (3.14)$$

where  $Z$  is the charge of the ion, and the photon energy is

$$\frac{1}{\eta_f^2} = \frac{1}{\eta_i^2} - \frac{h\nu}{Z^2 R_y}. \quad (3.15)$$

The quantum mechanics have been done, (first by Sommerfeld 1953; Bethe and Salpeter 1956) and results are plotted for photon energies and temperatures relevant to a laboratory plasma by Karzas and Latter[5]. They also present values for the Gaunt factor averaged over a Maxwellian electron distribution; tabulated values of  $\bar{g}_{ff}$  based on their results (as a function of  $u = \frac{h\nu}{kT}$  and  $\gamma^2 = \frac{Z^2 R_y}{kT}$ ) are published[6] for a range that includes those necessary for an NIR bremsstrahlung measurement on MST ( $-3 < \log u < 0$ ;  $-2 < \log \gamma^2 < 2$ ). These are accurate to within 1%; the results are plotted in Figure 3.3. The wavelength dependence (not shown) is very weak over the range covering the visible to NIR, however, there is a significant dependence on both temperature and ionic charge. The latter makes the extraction of  $Z_{eff}$  somewhat complicated.

#### 3.3.1 Power Law Fit

The  $Z$  dependence of the Gaunt factor necessitates an extra step in the analysis. An iterative method can be used, where after measuring the bremsstrahlung emissivity, electron density and temperature profiles, a Gaunt factor profile is calculated based on an asserted flat  $Z_{eff} = 1$  profile. From there, a  $Z_{eff}$  profile can be computed from the measured quantities and the Gaunt factor,

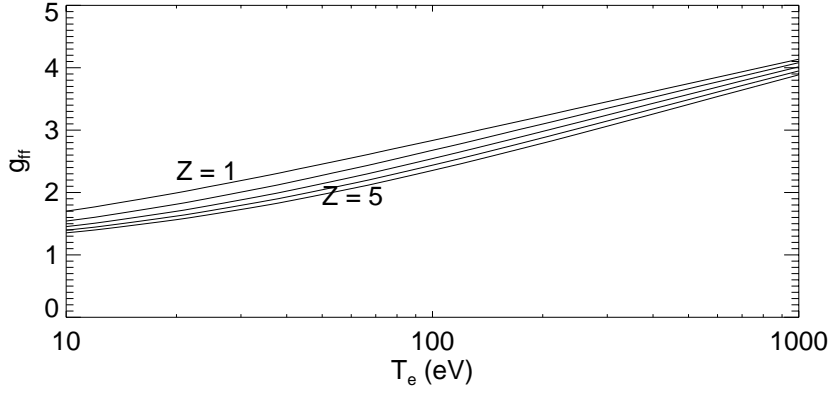


Figure 3.3: Maxwellian averaged Gaunt factor at 1040nm The top curve is for an ionic charge of 1, followed by  $Z = 2, 3, 4, 5$ .

leading (probably) to a  $Z_{eff}$  profile that is somewhat different. It is straightforward, but slow, to iterate the Gaunt factor and  $Z_{eff}$  profiles until convergence.

A second method, which avoids the iterative process, has been developed for  $Z_{eff}$  measurements at JET[7], TFTR[8], and DIII-D[9], (and quite possibly everywhere else) by fitting an analytic function to match the calculated Gaunt factors. By using a power law fit in temperature and  $Z_{eff}$ , equation 3.13 can be solved directly for  $Z_{eff}$ . The TFTR result is (with  $T_e$  in keV)

$$\bar{g}_{ff} = 3.77 Z_{eff}^{-0.055} T_e^{0.182} \quad (3.16)$$

which matches the exact values for 536nm over the range of  $Z_{eff} = 1 - 5$  and  $T_e$  of 50eV - 10keV to within a few percent. The best fit for 1040nm on the more MST-like temperature range of 20eV - 1keV is given (with  $T_e$  in eV) by

$$\bar{g}_{ff} = 1.251 Z_{eff}^{-0.09} (T_e - 8.5)^{0.175} \quad (3.17)$$

where the empirical scaling matches the exact values to within 5% over this temperature range.

If one were ever to get to the point in this measurement where this became a significant error, it could easily be removed by reverting back to an iterative solution.

### 3.3.2 Non-Maxwellian effects

To study the effect of a non-Maxwellian distribution, one of the various numerical approximations[3] for  $G(\eta_i, \eta_f)$  is used rather than the tabulated values of  $\bar{g}_{ff}$ . Comparison between the distribution-integrated results for a Maxwellian and a perturbed Maxwellian (bump-on-tail) distribution demonstrate that the effects are not important in the NIR. There are potentially important effects at long wavelengths[10] near  $\omega \approx \omega_{pe}$ , ( $\lambda \gg 1040$  nm) and very pronounced effects at photon energies near the perturbation to the distribution ( $\lambda \ll 1040$ nm). Figure 3.4. shows the effects of three different non-Maxwellian distributions to the wavelength behavior of the Gaunt factor. Each leads to an enhanced G at photon energies near the disturbance in the distribution function. Non-maxwellian effects do not pose a threat to an NIR bremsstrahlung measurement. However, the Gaunt factor enhancement at high photon energies makes x-ray diagnostics sensitive to fast particles. The third plot in Figure 3.4 does not show a catastrophic amount of x-rays; the plot is the ratio of the perturbed to unperturbed Gaunt factors and both values are quite low. This does show, however, that if a small x-ray flux was used for a bremsstrahlung measurement of  $Z_{eff}$ , it would be foiled by the presence of even a very small fast population under the Maxwellian assumption. An accurate description of the full distribution function is required to approach an x-ray measurement of  $Z_{eff}$ .

## 3.4 Wavelength Considerations

Selecting a finite width wavelength region over which to make a measurement of the bremsstrahlung continuum is complicated by the presence of other sources of radiation. It is necessary to find a region free of other sources of light and yet still have a measurable amount of bremsstrahlung. Owing to the  $\frac{e^{-hc/\lambda kT_e}}{\lambda^2}$  dependence, a short wavelength limit is reached where the photon energy

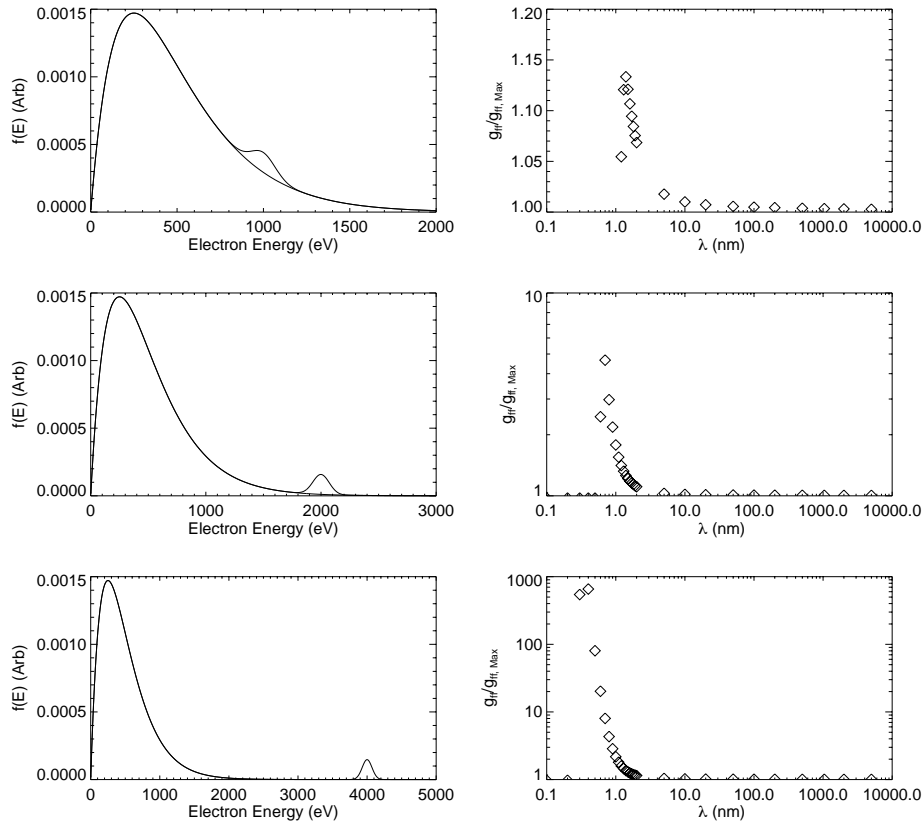


Figure 3.4: For the perturbed distributions (left column) the ratio of the computed Gaunt factor to the Maxwellian Gaunt factor is plotted (right column). As expected, there is an enhancement where the photon energy is comparable to the energy of the hot tail particles.

approaches the electron temperature. The edge temperature of MST is typically about 20eV, corresponding to a photon wavelength of about 60nm (in the ultraviolet). This eliminates the feasibility of an x-ray bremsstrahlung measurement in hopes of deducing a  $Z_{eff}$  profile, and incidentally this range of photons is particularly sensitive to non-Maxwellian (fast) electrons in the distribution as described in Section 3.3. X-rays are however, a worthy choice for determining core  $Z_{eff}$  values with appropriate modeling of the non-Maxwellian electrons.

The second factor to consider is the  $1/\lambda^2$  dependence, which prohibits an indefinitely long wavelength measurement. For use with the robust filtered photodiode diagnostic (as opposed to a

more expensive APD or PMT detector), several nanowatts need to be collected. For typical MST electron densities ( $10^{13}\text{cm}^{-3}$ ) and temperatures (200 eV), the maximum wavelength to expect one nanowatt of total power collected over 10 nm of the continuum is on the order of 3000nm. The silicon photodiodes are not sensitive to  $\lambda > \frac{hc}{\sim 0.7\text{eV}} \sim 1700\text{nm}$ , limiting the measurement to the near-infrared or shorter wavelengths.

In assessing a given wavelength region, the background emission (away from atomic or molecular lines) is compared to bremsstrahlung-like behavior. In the range under consideration, according to equation 3.13 the emission should fall off as  $1/\lambda^2$  and should be proportional to the square of the electron density. The ultraviolet is an unattractive option, as an abundance of atomic lines makes it impractical to find a sufficiently wide line-free region to measure the underlying continuum. Aluminum, an impurity that MST will alas never completely eradicate due to plasma-wall interactions, has 1007 possible line transitions between 60nm and 240nm, and over that range there is no gap of even 1 nanometer between the transitions[11]. Although many, if not most, of these transitions are very uncommon there are other pollutants in the ultraviolet, including molecular hydrogen emission[12] (details in Section 3.5.4). Nonetheless, a region that appears to be free of numerous bright lines is identified near 200nm, and an investigation of the background is possible.

The data in Figure 3.5, a background study near 200nm, show that this portion of the ultraviolet is not a good alternative. As the quantum efficiency of the CCD detector decreases rapidly with wavelength through this range, the shape of the background has no real meaning, and should not be compared to  $1/\lambda^2$ . This wavelength region is also out of the range of the calibrated source, so absolute emission measurement here is not currently accessible. However, given that the quantum efficiency is constant over the course of a day, useful information (albeit discouraging) is winnowed from the data by taking the ratio of spectra for different conditions and comparing to expected bremsstrahlung signatures. Figure 3.5.a) is the measured spectrum for a 200kA MST standard

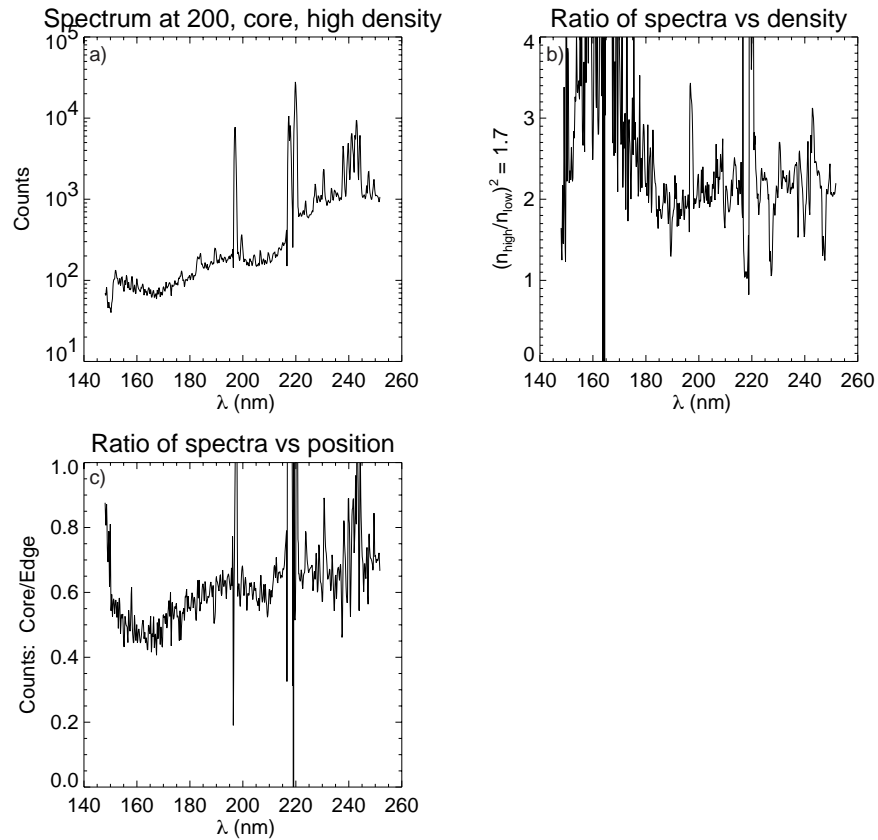


Figure 3.5: a) is the spectrum at 200nm in 200kA standard MST discharge. b) is the ratio of spectra at different densities, and c) the ratio of spectra on two different viewing chords.

discharge. There are several apparent lines, but also a seemingly broad background to investigate. Plot b) is the ratio of averaged spectra over 10 shots at two different electron densities. The square of the density ratio for these shots is 1.7, so for bremsstrahlung a ratio of 1.7 is expected between the two signals. There is some encouraging data near 190 nm, where the measured ratio is nearly the same as the predicted. Plot c) is necessary to restore order and rule out the possibility that bremsstrahlung is being measured. By taking the ratio of the average spectra at the core and at the edge, it is shown that the background emission is higher (by nearly a factor of two) at the outboard edge. Accounting for the  $n_e^2$  dependence of bremsstrahlung and the different lengths of the two chords, the only way to explain the edge peaked signal is by non-bremsstrahlung pollution.

The visible or near infrared are the best candidates for a bremsstrahlung measurement. It is imperative to determine the sources of excess radiation in the wavelength ranges of the attempted bremsstrahlung measurements. As will become apparent, there is no wavelength region in MST where bremsstrahlung is dominant; the other sources of light must be quantitatively extracted from the measurement to have any hope of determining  $Z_{eff}$ .

## 3.5 Pollutant Radiation in MST

### 3.5.1 Line Radiation

In a plasma with substantial neutral or partially ionized atom densities, line emission can be a significant contributor to the total emission. An electron colliding with the atom can impart some (or all) of its kinetic energy to the atom resulting in excitation of a bound electron of the atom. It later radiates back to its non-excited state giving off a quantized photon, very easily recognized in a measured spectrum as a sharp, high intensity peak above the background.

The MST plasma is characterized by strong line emission from hydrogen and a variety of impurities (dominant are He, B, C, N, O, Al and others) ranging in wavelength from the UV to the NIR. Avoiding line pollution in the bremsstrahlung measurement is indeed the first concern when selecting a wavelength, as strong lines are typically more than an order of magnitude brighter than the underlying continuum. In order to develop a robust bremsstrahlung diagnostic, it is necessary to find a region free of lines over all MST operating conditions. A spectral survey of the MST plasmas (see reference [13]) identifies several nearly line free regions.

Ideally, a spectral width of at least 10nm free of lines would be used to measure the continuum, as the the signal to noise ratio is improved by collecting more light. Unfortunately, the spectral survey indicates that 10nm free of lines is not attainable in MST. Inspection of the spectral survey, however, reveals several wavelength regions where it appears that the continuum averaged over an

approximate 10 nm window contributes significantly more light than the dim lines in the region.

The points selected are centered on 350, 420, 500, 520, 620, 700<sup>2</sup>, and 1040 nm.

The absolutely calibrated measurement described in Section 2.2 was performed simultaneously on adjacent core viewing chords for each of the seven wavelengths to obtain spectral information of the background continuum. Figure 3.6 shows the measurements are much higher than the expected

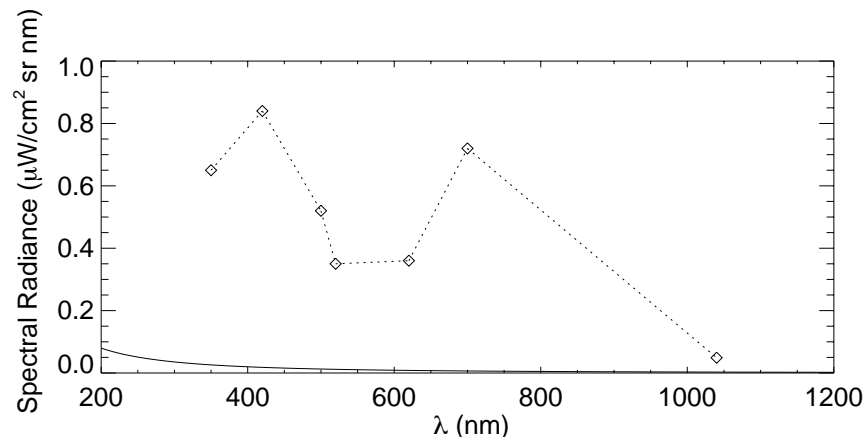


Figure 3.6: The measured background emission at several wavelengths in the visible to NIR. The expected bremsstrahlung emission for the quintessential MST plasma is plotted in a solid line, more than an order of magnitude below the measured emission.

bremsstrahlung level at all wavelengths, demanding further investigation of the possibility of line contamination. While the visible measurements have a significant transmission at 656.3nm, (see Section 2.2.1) the absolutely calibrated measurements show that  $H_{\alpha}$  pollution contributes only a small fraction of the measured emission. The detector at 1040nm is better suited for  $H_{\alpha}$  rejection as the colored glass filter rejects a very high percentage ( $T \sim 10^{-8}$ ) of light below about 800nm. Thus,  $H_{\alpha}$  pollution plays only a small role in the visible measurements, and has effectively no contribution to the NIR measurement.

The second possibility of line contamination to explore is quite the opposite of transmission of the brightest line around. The spectrum in MST shows a vast number of lines, with a sparse set

<sup>2</sup>Measurements at 700nm are polluted by a He I line at 707nm; therefore this wavelength is not further considered.

of apparently line free regions. Upon measurements of the line free regions with a finer grating (1800/mm) in the spectrometer, several faint lines are noticed. This effect is illustrated in Figure 3.7, where an apparently line free region with the coarse grating shows three distinct lines. The NIST database of atomic lines and transitions[11] presents several possible lines from the dominant MST impurities in each of the wavelength bands of attempted bremsstrahlung measurements. In fact, a comprehensive search of the ultraviolet to infrared range shows that there are no 10nm wide wavelength ranges completely free of lines from H, He, B, C, N, O, and Al.

The possibility of a plethora of dim lines polluting each of the measurements is removed through an independent experiment. A perusal of the NIST database led to the discovery that the region from 523 to 524nm is completely free of lines from hydrogen and the dominant MST impurities. The spectrum measured on MST shown in Figure 3.7 corroborates the line free assertion. An

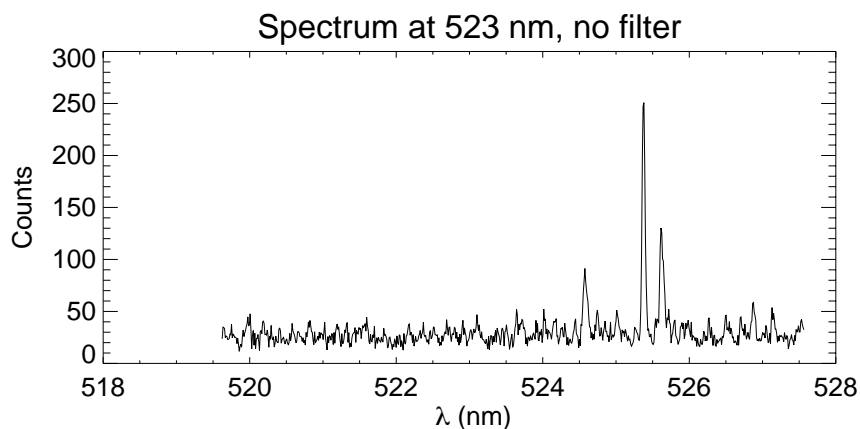


Figure 3.7: An MST spectrum shows no lines in the range of 523-524 nm. Three dim lines appear at slightly higher wavelength.

experiment was designed to measure only the emission from this region.

While the filtered photodiodes typically collect light over  $\Delta\lambda \sim 10\text{nm}$ , the line-free measurement samples a significantly smaller wavelength region and as such the total power collected is expected to be too small for these detectors. The apparatus described in Section 2.3 is designed to perform

this line free measurement. A four point radial profile measurement of the emission in this line free

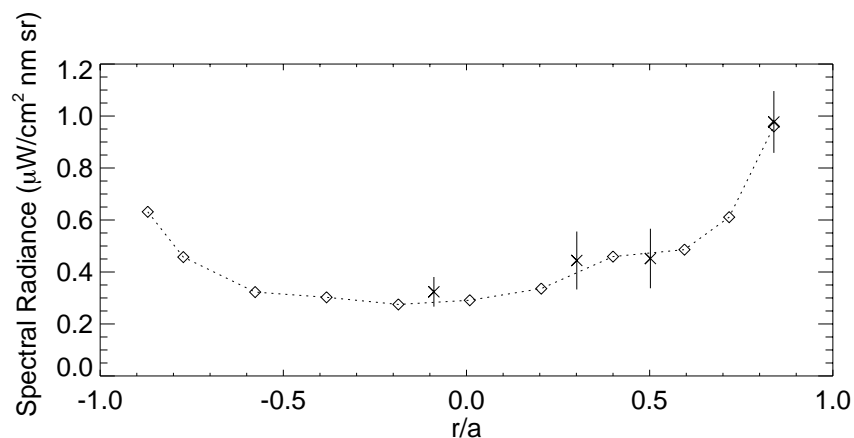


Figure 3.8: Narrow band visible bremsstrahlung measurement results: solid points are a profile measured by a diode collecting over 10 nm in in similar conditions (error bars are smaller than plot symbol), and a 4 point profile measurement made by the PMT collecting over 1 nm.

region was performed. The data from this experiment, although suffering from a much worse signal to noise ratio, are in quantitative agreement with the filtered photodiode experiment performed earlier, as shown in in Figure 3.8.

This proves that line radiation is not the source of the brighter-than-bremsstrahlung emission in the measurement at 520nm. While this offers no direct proof that the measurements at other wavelengths are not polluted by atomic lines, this confirms that there is at least one other source of pollutant emission.

Line radiation at 1040nm, where a bremsstrahlung attempt is best suited, does not seem to be a problem. While the NIST database indicates there are allowed transitions from low charge states of MST impurities, namely C I, N I and O II, the measured spectrum shown in Figure 3.9 indicates that the line emission is not significant there. Shown in the plot is the measured spectrum, (which is quite noisy as this wavelength range is at the cutoff of the CCD sensitivity), along with the predicted bremsstrahlung for  $Z_{eff} = 2$  and the transfer function of the NIR filtered photodiode detector. Hydrogen and helium lines well above the continuum are observed outside of the wavelength range

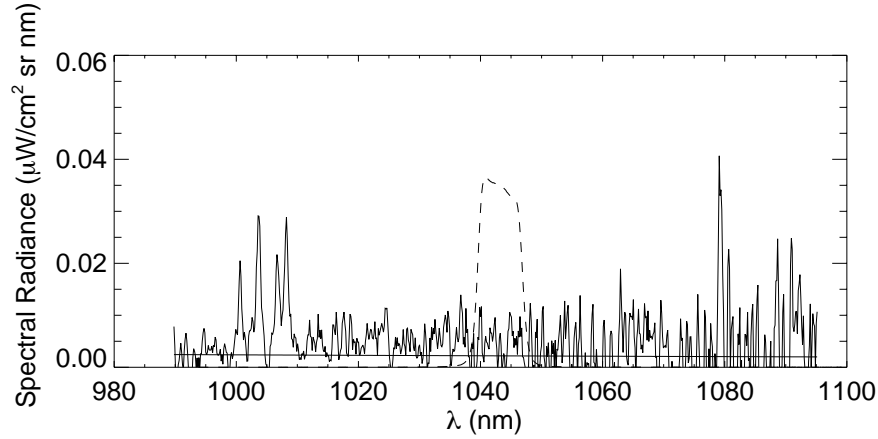


Figure 3.9: Measured spectrum in the NIR. A few dim lines are insignificant compared to the background continuum but may be significant compared to the underlying bremsstrahlung. Shown also are the expected bremsstrahlung from  $Z_{eff} = 2$  and the wavelength transfer function of the NIR filtered photodiode detectors.

of interest, both at longer (1078, 1090nm) and shorter (1003, 1009nm) wavelength. This shows the diagnostic would detect a bright line in the collection range and therefore bright line pollution can be ruled out of the 1040nm measurement. Due to diagnostic limitations, it is impossible to resolve whether the spiky background spectrum is indicative of many dim lines, as the variation is within the  $\sqrt{N}$  counting noise. In an attempt to isolate the low charge state impurity lines with this spectrometer, it is necessary to collect light from the cool part of the plasma for a very long time. Spectroscopic monitoring of pulsed discharge cleaning (PDC) provides a solution to this challenge. PDC is a very low temperature helium discharge aimed at removing impurities from the vacuum vessel and is typically run several hours per night. Figure 3.10 is a measure of the line emission from PDC in the NIR. Several helium lines are identified, however the range of 1031-1067nm is free of helium lines and the dim lines in this region are due to impurities. Only one very dim line is in the pass band of the NIR filter scheme; lines are not the primary pollutant at 1040nm.

This low charge state line may prove troublesome in the absence of other contaminants, but it is extremely edge localized. The reliability of the NIR bremsstrahlung measurement is thus

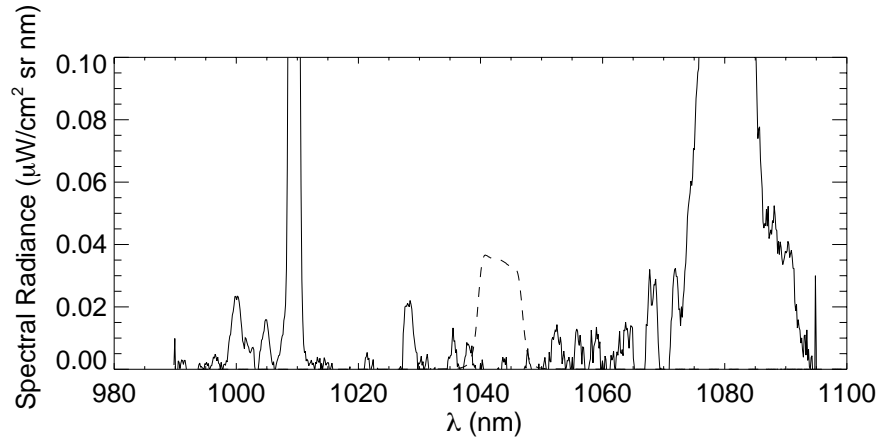


Figure 3.10: Spectrum of cold He plasma in the NIR. Helium lines are identified at: 1003, 1013, 1031, 1067, 1083, 1091, and 1099nm. Unidentified impurity lines in the range of 1030nm - 1065nm are apparent but the range covered by the NIR bremsstrahlung measurement (dashed line) is free of significant line pollution.

compromised in this region. However, in the event that this line radiation does not dominate bremsstrahlung, an invertible emission profile may be obtained and meaningful emission from the core can be measured.

### 3.5.2 Recombination

A second source of continuum radiation from an electron-ion encounter is recombination, sketched in Figure 3.11. While a popular suspect (considered as a possible pollutant in references[3, 14, 15]), this is not a significant contributor to the emission in MST. It has been given full consideration here as the measured emission for a standard MST discharge shows a signature that could be explained by recombination, plotted in Figure 3.12. As the discharge draws to a close at  $t \geq 0.03s$ , the line averaged density begins to drop rapidly, presumably due to a loss of electrons to recombination. An observed coincident increase in the measured emission corroborates the hypothesis that recombination is polluting the bremsstrahlung measurement.

Free-bound recombination emits a structured spectrum through the visible and infrared[3] de-

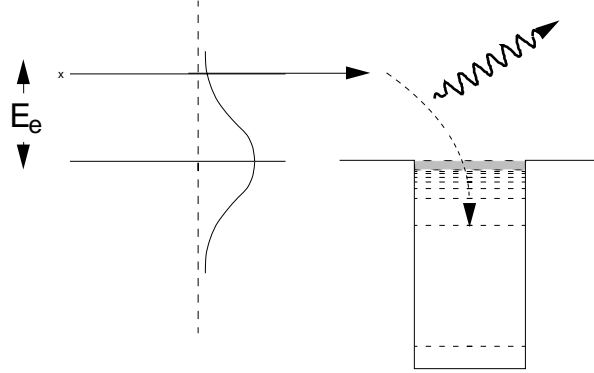


Figure 3.11: Recombination cartoon

scribed by

$$\frac{1}{2}m_e v^2 = \frac{-Z^2 |R_y|}{n^2} + h\nu \quad (3.18)$$

where the initially free electron is captured to a bound state (level  $n$ ), with the excess energy being emitted as a photon. As the electron's initial kinetic energy is non-negative, there are no photons with  $h\nu < \frac{Z^2 R_y}{n^2}$  for a given state  $n$ . The electron velocity distribution (temperature) determines the deviation of the actual radiation from the set of discrete lines. The emission for a Maxwellian distribution is [3]

$$\epsilon(\lambda) = A \frac{n_e n_i Z^2 e^{-\frac{hc}{\lambda k T_e}}}{\lambda^2 \sqrt{T_e}} \times \left[ \sum_n \frac{Z^2 R_y}{T_e} \frac{2}{n^3} G_n e^{Z^2 R_y / n^2 T_e} \right]. \quad (3.19)$$

This formula is identical to equation 3.10 for bremsstrahlung emission with the free-free Gaunt factor replaced by the term in brackets. The ratio of recombination to bremsstrahlung is then

$$\frac{\epsilon_{fb}}{\epsilon_{ff}} = \sum_n \frac{Z^2 R_y}{T_e} \frac{2}{n^3} \frac{G_n}{\bar{g}_{ff}} e^{Z^2 R_y / n^2 T_e} \quad (3.20)$$

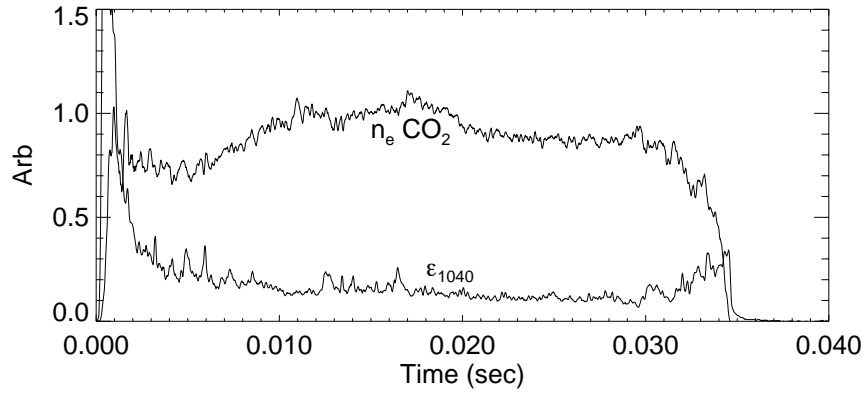


Figure 3.12: Emission at 1040nm grows late in the discharge, coincident with a sharp decrease in electron density.

where the summation is over the principle quantum numbers  $n$  of the atom. Due to this temperature dependence, recombination may become significant as the electron temperature gets very small. Figure 3.13 shows the bremsstrahlung (dashed line) and the total emission (bremsstrahlung plus recombination, solid line) for hydrogen at  $T_e = 20\text{eV}$ . A large step is evident near 365 nm, where the transition to the  $n=2$  level becomes energetically available. This indicates that the measurement at 350nm may be polluted by hydrogenic recombination, particularly at low electron temperature.

The contribution in the NIR is negligible, and the calculation clearly shows that for MST-like temperatures (of  $T_e > 5\text{eV}$ ) recombination is not a polluter in the NIR, while a small correction may be needed at the short end of the visible. An exhaustive calculation of recombination and bremsstrahlung emission for several species<sup>3</sup> (H, He, B, C, N, O, Al) versus wavelength and temperature results in the same conclusion: recombination is not a factor at 1040nm.

<sup>3</sup>It should be noted that these calculations are done for fully stripped atoms. For partially stripped ions, it is adequate to use the ionic charge rather than the nuclear charge for  $Z$  in the calculations. Accurately treating the problem of partial ionization leads to a decrease in recombination by a factor of  $\xi/2n^2$  where  $\xi$  is the available number of holes in the lowest unfilled shell[3]. Thus, the calculation presented here is an upper bound for partially ionized impurities.

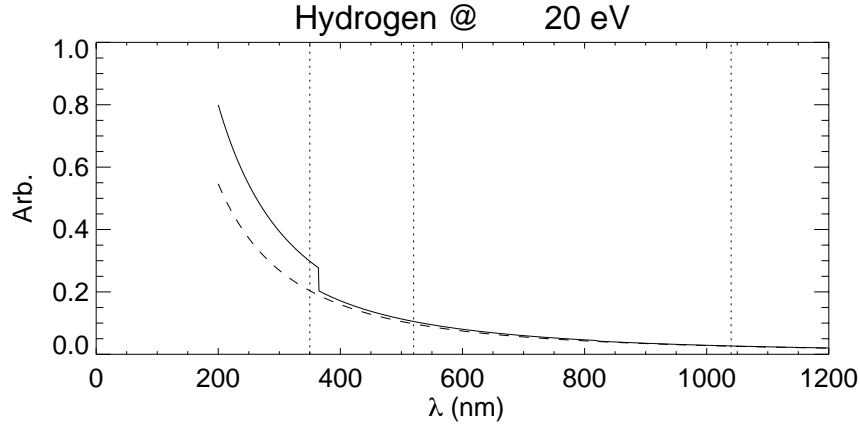


Figure 3.13: Bremsstrahlung and recombination emission expected for 20eV electron-proton encounters. The dashed line is the bremsstrahlung, and the solid line is the total emission. Recombination is the difference between the two.

### 3.5.3 Blackbody Radiation

After dismissing recombination, Figure 3.12 is further scrutinized at the time immediately after the discharge has ended. After the electron density has gone to zero, whereupon bremsstrahlung and recombination have gone to zero squared, there is still a finite signal on the detectors. Figure 3.14 shows an expanded view of the termination behavior of density, plasma current and emission at 1040nm. The plasma current and density go to zero simultaneously, while the emission falls off on roughly a one millisecond time scale. The response time of the diode and amplifier is much faster[16] meaning that there is a real source of light persisting beyond the end of the discharge. One possible explanation is blackbody radiation from a hot surface on the opposing side of the vacuum vessel, and could conceivably dominate bremsstrahlung during hotter portions of the discharge.

A simple calculation shows that the post-discharge emission is consistent with a blackbody near 600 Kelvin. The energy density for a blackbody is[17]

$$u_\nu d\nu = \frac{8 \pi h \nu^3}{e^{\frac{h\nu}{kT}} - 1} d\nu \quad (3.21)$$

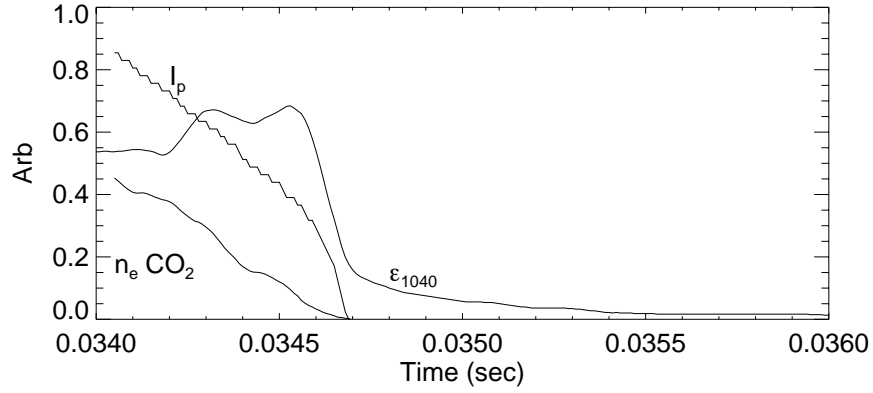


Figure 3.14: Emission at 1040nm persists after the plasma has terminated.

and for 1035 to 1050nm,  $\nu = 2.855 - 2.897 \times 10^{14}$  Hz, or  $d\nu \approx .021 \times 10^{14}$  Hz and  $\bar{\nu} = 2.876 \times 10^{14}$  Hz. The expected intensity of radiation is

$$I = u \times \frac{c}{4} \quad (3.22)$$

which is tabulated below.

T (K)	$u_\nu d\nu$ (J/m <sup>3</sup> )	I (W/m <sup>2</sup> )
300	$3.23 \times 10^{-22}$	$2.42 \times 10^{-14}$
400	$3.19 \times 10^{-17}$	$2.39 \times 10^{-9}$
500	$3.16 \times 10^{-12}$	$2.37 \times 10^{-6}$
600	$8.44 \times 10^{-11}$	$2.36 \times 10^{-4}$
700	$9.93 \times 10^{-10}$	$6.32 \times 10^{-3}$
800	$6.75 \times 10^{-9}$	$7.44 \times 10^{-2}$
900	$3.13 \times 10^{-8}$	$5.06 \times 10^{-1}$

Table 3.1: Expected blackbody emission from a hot wall versus temperature. A blackbody between 600-700 K emits enough NIR radiation to pollute the measurement.

The last point is at 900K, the melting point of aluminum. For comparison's sake, our standard 200eV,  $1.0 \times 10^{-13} \text{ cm}^{-3}$ ,  $Z_{eff} = 1.0$  plasma, emitting bremsstrahlung into  $4\pi$  steradians over a

100cm long viewing chord, and detected over a  $\Delta\lambda$  of 8nm leads to an intensity of  $3. \times 10^{-3} \text{ W/m}^2$ ; similar to a blackbody between 600 and 700K. The measured decay time could be explained by a small sample of hot aluminum in good thermal contact with an infinite heat sink, analogous to a small ring at the port losing heat to the bulk of the MST vacuum vessel.

This possible contaminant theory is dispelled through experiment. Five of the 17 chords in the NIRB array have a 1.25 inch port directly across the vacuum vessel ( $\approx 1$  meter away) along the line of sight from the detector. At that distance, the collection optics see the edge of the port[16]. The post-discharge signal is observed on all chords, but the hot aluminum theory is ruled out utilizing one of the chords with an opposing hole. The photodiode detector has a circular collection area with a diameter of 2.5 mm. Measurements with successively smaller apertures (machined to diameters of 2.0, 1.6, 1.2 and 0.8 mm) in place were then conducted. With the smaller apertures in place, the opposing port is eliminated from the field of view and light emitted from the wall will not be detected. Therefore it is expected that the post-discharge emission will be relatively constant with exposed area until the wall is removed from the field of view, whereupon it should go to zero. Figure 3.15 demonstrates that the measured light after the plasma does not disappear, but

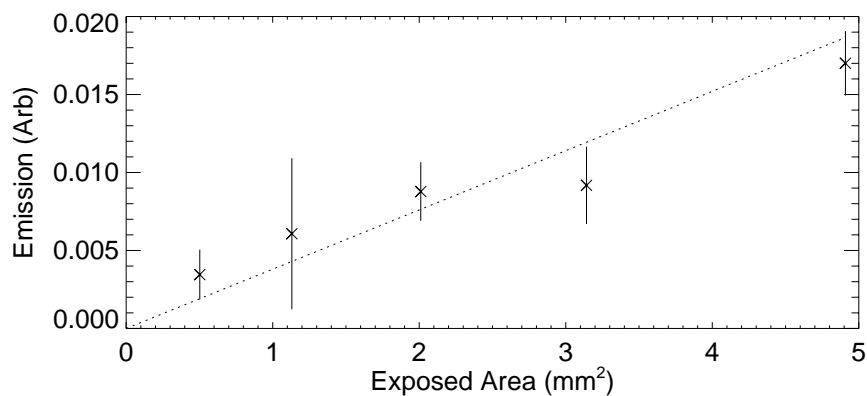


Figure 3.15: Apertured diode experiment results: The collected power at the termination of the shot decreases approximately linearly with exposed area. For a hot wall contaminant, one expects a sharp drop to zero signal for the smaller areas.

it is consistent with linear scaling with exposed area. These data indicate that the post-discharge emission is not from a hot wall, but emanates from the interior of the vacuum vessel.

### 3.5.4 Molecular Hydrogen Emission

Molecular hydrogen has been used as a scapegoat for difficulties with bremsstrahlung measurements throughout the fusion community, though the accusations are quite vague. In a recent publication, the bremsstrahlung team on Alcator C-Mod reports high levels of broadband visible emission associated with puffs of diatomic molecules ( $D_2$ ,  $N_2$ ,  $O_2$ ), but no corresponding jump in emission for a helium puff[15] and attribute the emission to a molecular pseudocontinuum. As MST is fueled by puffing hydrogen gas into the vacuum vessel, there is a substantial molecular population. Additionally, plasma-wall interaction leads to recycling of particles, most of which are in the molecular (as opposed to atomic) state[18]. A significant effort has been conducted on MST to identify the processes that lead to molecular emission, leading to the conclusion that visible and ultraviolet wavelengths are quite polluted with molecular emission, while the NIR is mostly free.

There are a number of processes through which molecular hydrogen (or deuterium) can emit radiation[12]. There is a strong contribution to the visible continuum in MST due to dissociation of hydrogen (deuterium) molecules which in fact makes a visible bremsstrahlung measurement impractical. Electron transitions in molecular hydrogen lead to band emission of lines ranging from the ultraviolet to the visible[19, 20] but there are no electronic emission bands in the 1040nm range of the NIR. Emission associated with rotational and vibrational excitations of the molecule, which typically exists in lower energy ranges and could be prevalent in the infrared, is found to avoid our measurement range as well.

Explanation of measured emission in MST is elucidated by taking a quick look at a hydrogen glow discharge lamp. Figure 3.16 is a measured spectrum from said lamp, along with background measurements from MST discharges. The visible continuum in MST looks like a big  $H_2$  lamp. There

is an increase in the lamp emission near 600nm, likely due to the Fulcher- $\alpha$  band of molecular lines[19]; radiation from these transitions has been measured and identified[21] in the divertor region of tokamaks. A second radiative process from molecular hydrogen proves detrimental to the visible bremsstrahlung measurement in MST. There is a well known molecular dissociation continuum which starts below 200 nm and extends to almost 600nm[22, 23, 24, 25, 26]. The upper radiating electronic level of  $H_2$  is bound and the lower level is unbound on a repulsive molecular potential curve. The steep unbound potential curve<sup>4</sup> spreads out the radiation over a vast range of wavelengths. A spectrum of background emission (between atomic lines) in the shorter visible wavelengths with the filtered photodiode detectors demonstrates that this mechanism is at work in the MST plasma. Figure 3.16(a) is a spectrum taken of a hydrogen glow discharge lamp, where the molecular dissociation is known to be a dominant radiative process, along with calibrated emission measurements at 350, 420, 500, 520 and 620nm in MST discharges. The shape of the spectrum supplies conclusive evidence that molecular emission is in fact the dominant process in the continuum radiation in this wavelength range. The measurement is repeated in PPCD discharges, and with the reduced wall interaction and recycling, the continuum emission drops by about a factor of ten, but the shape shows that molecular dissociation is still the dominant process. The abundance of molecules throughout all types of discharges in MST prohibits a measurement of electron-ion bremsstrahlung in the range of 350 - 600nm.

The NIR appears clear of molecular contaminants. Several astrophysical plasmas, known to be rotten with molecular hydrogen, have been studied[27, 28, 29, 30, 31, 32, 33, 34, 35, 36, 37, 38, 39]. The short answer is that although there are a handful of possible transitions, the NIR is mostly invisible to  $H_2$  emission; and of particular interest the range of 1030 - 1050nm is apparently free of any measurable transitions.

---

<sup>4</sup>Potential curve can be seen in reference [25].

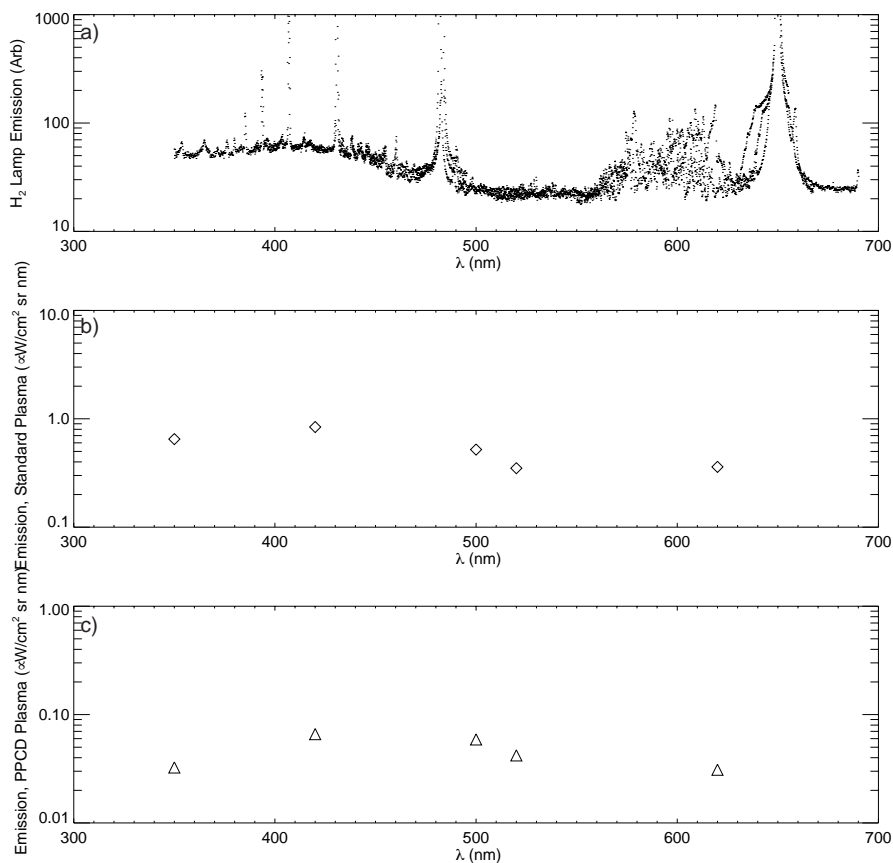


Figure 3.16: Measured emission from (top: a) a glow discharge hydrogen lamp (middle: b) a standard MST discharge and (bottom: c) an enhanced confinement (PPCD) MST discharge. The structure in the spectrum in a) is due to a continuous emission due to molecular dissociation. b) and c) demonstrate that this process dominates the measured visible continuum in MST.

### 3.5.5 $H_{\alpha}$ Emission

The emission from the  $n=3$  to  $n=2$  transition of the hydrogen atom ( $H_{\alpha}$ , 656.3 nm) is the brightest line in the visible to NIR spectrum in MST. This may play a role in the NIR measurement in two ways. First, as the  $H_{\alpha}$  emission is several orders of magnitude brighter than the background continuum, insufficient filtering may lead to a contamination of the continuum measurement. This has been carefully considered, with the results tabulated in Chapter 2, and it is determined that direct  $H_{\alpha}$  contamination is not a significant source of measured light.

However,  $H_\alpha$  emission proves to be a good way to monitor the pollutant<sup>5</sup> emission as they are both proportional to the neutral density. Lanier[40] gives a succinct explanation of this emission and its use to determine the neutral density. The power radiated through the  $H_\alpha$  line is given by the number of photons (multiplied by the energy per photon) per unit time. The rate of  $H_\alpha$  photons is related to the number of ionizations due to electron impact ( $\langle \sigma v \rangle_{ei}$ ), and the ratio is fairly constant over the MST parameter range. This allows the use of the well known electron impact ionization rate to describe  $H_\alpha$  emission. The number of ionizations per  $H_\alpha$  photon ( $N_{ion,h\nu}$ ) has been calculated as a function of electron density and temperature using ADAS[41] and matches the previously published values[42] as well as graphical recovery of the data allows. The

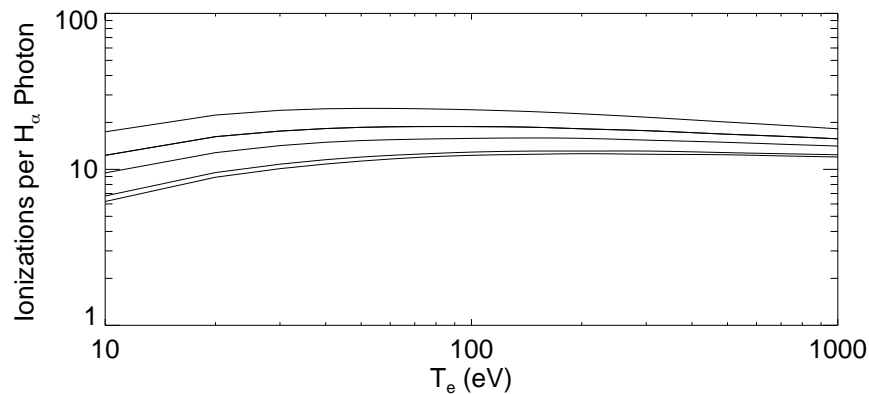


Figure 3.17: Number of electron-impact ionizations per  $H_\alpha$  photon. The top curve is at  $n_e = 5 \times 10^{13} \text{ cm}^{-3}$ , and sequentially lower traces are at  $n_e = 1 \times 10^{13}$ ,  $5 \times 10^{12}$ ,  $1 \times 10^{12}$ ,  $5 \times 10^{11} \text{ cm}^{-3}$ .

ADAS calculation, shown in Figure 3.17, easily incorporates the electron density and temperature dependence. While the number of ionizations per photon is very nearly constant over most of the MST plasma, the extreme edge is where most ionizations occur and there is a considerable

---

<sup>5</sup>This will be made apparent in the upcoming sections.

temperature dependence in this region. This leads to a formula for  $H_\alpha$  emission given by

$$\gamma_{H_\alpha} = \frac{h\nu}{4\pi} n_e n_0 \frac{\langle\sigma v\rangle_{ion}(n_e, T_e)}{N_{ion, h\nu}(n_e, T_e)} \quad (3.23)$$

which carries units of  $\frac{W}{cm^3 sr}$ . An absolutely calibrated array of detectors (Chapter 2) enables an inversion of the  $H_\alpha$  emission, and with a measured electron temperature and density profile, the neutral density is computed

$$n_0(R, Z) = \frac{4\pi\gamma_{H_\alpha}(R, Z) N_{ion, h\nu}(n_e, T_e)}{h\nu n_e(R, Z) \langle\sigma v\rangle_{ion}(n_e, T_e)} \quad (3.24)$$

where the two-dimensional nature of  $H_\alpha$  emission is incorporated. This is a good estimate of neutral density, although it assumes that all  $H_\alpha$  photons result from electron impact excitation.

In reality, molecular hydrogen complicates this situation[18]. Dissociation of hydrogen molecules can leave one of the atoms in an excited state, where it will produce an  $H_\alpha$  photon a certain percentage of the time without being related to electron-atom excitation. There are further issues if one tries to extend this to calculating the electron source rate, as molecular ionization can significantly contribute to the electron source without producing the proportional number of  $H_\alpha$  photons. Sawada and Fujimoto calculate the number of ionizations per  $H_\alpha$  photon originating from molecular hydrogen and show that it is an order of magnitude higher than that for atomic hydrogen. Further complications arise when their calculations show that more than 90% of the neutral hydrogen in a tokamak edge is molecular, as opposed to atomic.

This section has been included to give some background to the neutral particle estimate used in the electron-neutral bremsstrahlung section. The points of complication introduced above should forewarn the reader that neutral particle calculations presented here are only estimates.

### 3.5.6 Electron-Atom Bremsstrahlung

An electron interacting with a neutral atom leads to continuous emission in a fashion similar to electron-ion bremsstrahlung[10]. This proves to be a significant source of light in the near-infrared in MST. As the free electron impinges on the neutral atom, it is subject to a partially screened Coulomb force and is accelerated. This process is also described by the development in Section 3.2 differing only in its proportionality to neutral atom density (as opposed to ion density) and a modified cross section.

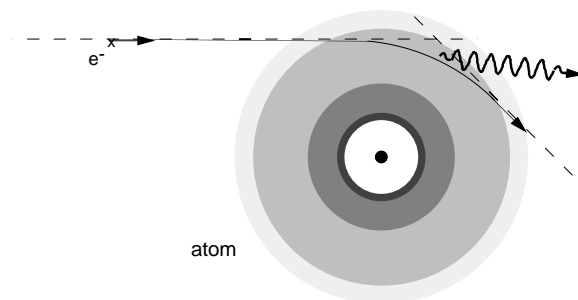


Figure 3.18: Collision between an electron and a neutral atom.

Several empirical observations point toward neutral hydrogen as the primary source of radiation in the NIR. First, the line integrated data collected in the NIR is noticeably two-dimensional, with a much stronger outboard emission. This feature is also apparent in the  $H_{\alpha}$  emission. The emission of both the NIR signals and the  $H_{\alpha}$  signals drop by an order of magnitude in PPCD discharges. Neutral emission also explains the increase in emission near the end of the discharge and the emission that persists after the end of the discharge. As previously speculated, recombination occurs near the cooling at the end of the discharge noted by a rapid decrease in line integrated density. The radiation from the recombination process is not to blame for the NIR pollution, but it does lead to a significant rise in the neutral density. The emission persisting beyond the end of

the discharge is attributed to a high neutral density and an extremely low<sup>6</sup> electron density.

The neutral particle density is known to be quite high in the edge of MST. Using equation 3.24 and the poloidally asymmetric inversion technique described in Chapter 5, the neutral particle density is estimated. The results of the inversion are shown in Figure 3.19, and show that the density is strongly edge peaked as it exceeds  $10^{12}\text{cm}^{-3}$  and drops below  $10^{10}\text{cm}^{-3}$  in the inboard

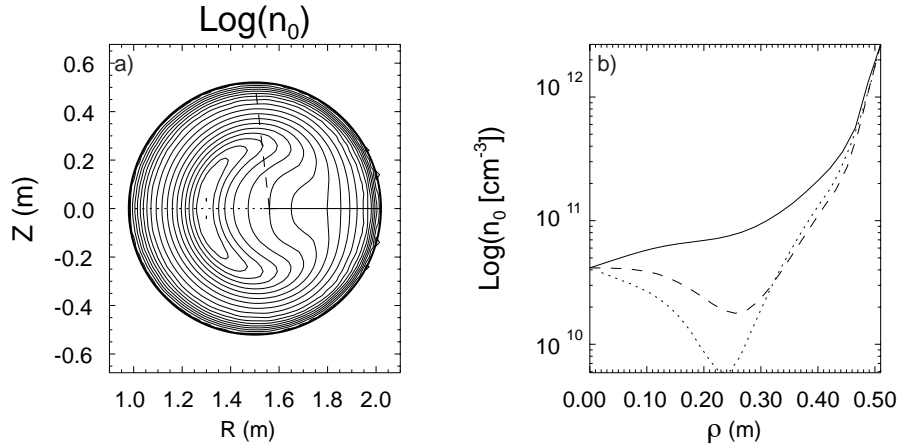


Figure 3.19: Inverted profile of neutral deuterium density. a) is a contour plot of the logarithm of the neutral density in  $\text{cm}^{-3}$ . There are 3 rays plotted from the magnetic axis to the last closed surface, the neutral particle density along each ray is plotted in b). There is a distinct inboard-outboard asymmetry in neutral density.

mid-radius region.

The electron neutral bremsstrahlung emissivity is calculated from the measured neutral density and electron density and temperature profiles following Dalgarno and Lane[43]. The analytical formula for the neutral bremsstrahlung emission cross section (in  $\text{cm}^2\text{s}$ ) is

$$\frac{d\sigma_{\nu}(E)}{d\nu} = \frac{8r_e}{3c} \frac{E}{h\nu} \left(1 - \frac{h\nu}{E}\right)^{1/2} \left[ q_0(E - h\nu) + \left(1 - \frac{h\nu}{E}\right) q_0(E) \right] \quad (3.25)$$

where  $r_e$  is the classical electron radius,  $c$  is the speed of light,  $E$  is the initial electron energy,

<sup>6</sup> An electron density well below the resolution of the interferometer is sufficient to explain the measured emission.

$h\nu$  is the photon energy, and  $q_0$  is the electron momentum damping cross section as a function of electron energy. This formula uses the phase-shift approximation to deal with the quantum mechanics, (applicable for low energy photons  $h\nu \ll T_e$  which is satisfied at 1040nm in MST), and eliminates the trouble of computing Gaunt factors<sup>7</sup>.

Integrating over the electron distribution  $f(E)$

$$Q_\lambda d\lambda = \frac{h\nu}{4\pi} n_0 n_e \left( \int_{h\nu}^{\infty} v \frac{d\sigma_\nu(E)}{d\nu} \frac{d\nu}{d\lambda} f(E) dE \right) d\lambda \quad (3.26)$$

gives the spectral emission coefficient (in W/cm<sup>3</sup> sr nm) where  $n_e$  is the electron density and  $n_0$  is the neutral density. Using the tabulated cross section values for hydrogen[45], the neutral bremsstrahlung emissivity is calculated. The somewhat surprising result is that electron-neutral bremsstrahlung is stronger than electron-ion bremsstrahlung under certain MST conditions, namely at high neutral density. Park et.al.[44] measured neutral bremsstrahlung in an atmospheric pressure, low temperature ( 1-2 eV) helium plasma. They show a clear spectrum (with good  $1/\lambda^2$  dependence), and present the electron neutral bremsstrahlung emissivity per unit electron and gas density. The calculation here, when given similar conditions, matches their values to within 2%, implying there are no silly arithmetic errors.

Both the  $H_\alpha$  and neutral bremsstrahlung emissivities (see equations 3.26 and 3.23) are proportional to the neutral particle density. Monitoring neutral bremsstrahlung via  $H_\alpha$  emission hinges on the assumption that the line integrated emissivities of each are proportional to each other. It is clear from equations 3.26 and 3.23 that for a given electron density and temperature the electron-neutral and  $H_\alpha$  emissivities are directly proportional. Each could be rewritten as the product of  $n_e n_0 f(n_e, T_e)$  where the function  $f$  carries all the relevant information about the radiative process; the ratio of the two is simply  $f_{e-n}(n_e, T_e)/f_{H\alpha}(n_e, T_e)$ . In experiment, the electron density and temperature vary considerably over the chord, and in general the ratio of the two functions will

---

<sup>7</sup>See references 10-14 of reference[44].

not be constant. However, the line integrated emission of each is weighted by the neutral density, which is extremely edge peaked. In the limit of a  $\delta$  function, the ratio of the two functions is again a constant.

The linearity of the line integrated signals is investigated for low current standard plasmas in Figure 3.20. The measured neutral density (via  $H_\alpha$  emission), electron density and electron temperature profiles are mapped onto the chords viewed by the NIR detector array. Figure 3.20 a) is the measured  $H_\alpha$  emission and the predicted  $H_\alpha$  signals found by integrating equation 3.23 over the viewing chords. As expected, the predicted signals match the data and this plot simply verifies an accurate inversion of the neutral density. Equations 3.13 and 3.26 are integrated over the viewing chords to predict the line integrated electron-ion (assuming a flat  $Z_{eff} = 2$  profile) and electron-neutral bremsstrahlung emission. Figure 3.20 b) demonstrates that the neutral bremsstrahlung (denoted by +) is considerably stronger than its electron-ion (denoted by x) counterpart under these conditions. Figure 3.20 c) and d) show the ratio of electron-neutral bremsstrahlung to the  $H_\alpha$  emission at all points in the plasma using experimental electron density and temperature. The core of the plasma is covered in c), while d) shows the ratio at the edge. While the local values are fairly constant near  $3 \times 10^{-5}$  in the core, they drop to  $\sim 1.5 \times 10^{-5}$  at the edge. Also shown in 3.20 d) are the ratios of the line integrated electron-neutral to  $H_\alpha$  emissivities versus chord. It is included on this plot to demonstrate that, even though the central chords view a much hotter, denser part of the plasma, all the chords have similar ratios, with the extremes differing only by  $\sim 30\%$ . The values are similar to the edge values, as expected from the edge peaked neutral density. The sensitivity of the ratio to varying electron density and temperature profile shape is thus quite small. It exhibits very little change during PPCD experiments, where the neutral density can drop by an order of magnitude, but the neutral density profile remains extremely edge peaked. In these cases, the electron-neutral bremsstrahlung contribution becomes much smaller, but the proportionality to measured  $H_\alpha$  remains.

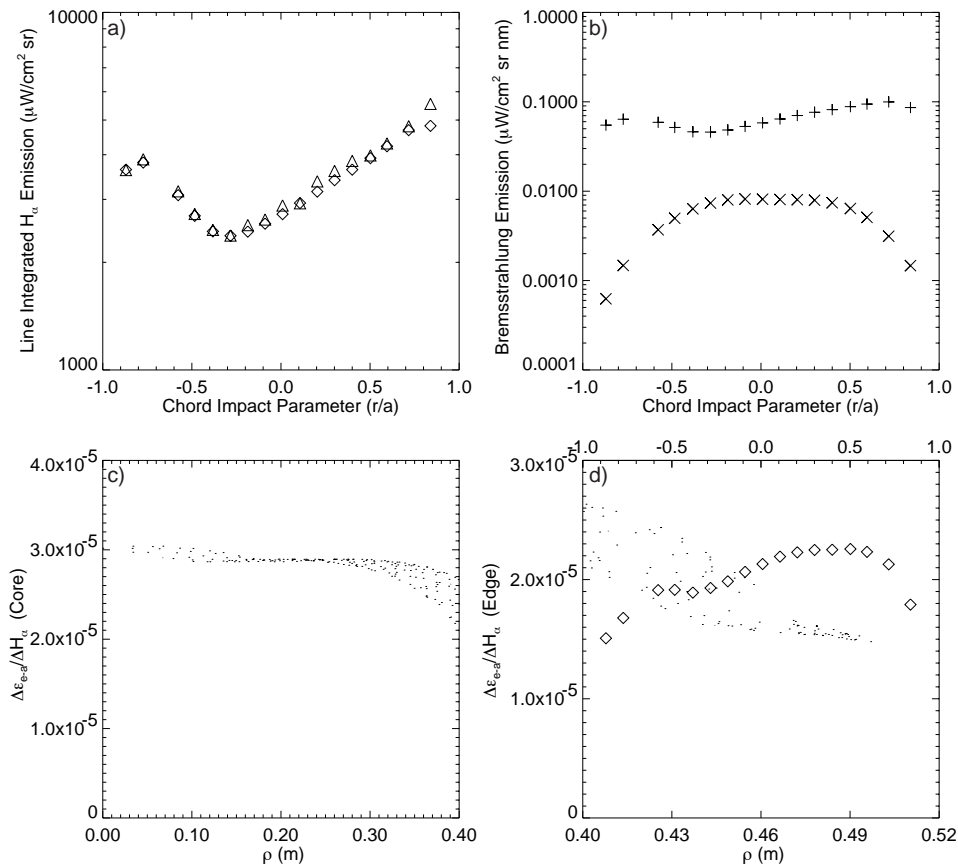


Figure 3.20: a) Measured  $H_\alpha$  emission and the predicted  $H_\alpha$  signals; b) neutral bremsstrahlung (+) is considerably stronger than its electron-ion (x) counterpart; c), d) ratio of electron-neutral bremsstrahlung to the  $H_\alpha$  emission. Also in d) are the ratios of the line integrated electron-neutral to  $H_\alpha$  emissivities versus chord impact parameter.

The predicted linearity between  $H_\alpha$  and the NIR signal is experimentally verified, however the measured slope is significantly higher than the predicted values. Figure 3.21 shows the predicted slopes from electron-neutral bremsstrahlung and the measured slopes from an ensemble of several standard MST discharges characterized by a similar  $H_\alpha$  emission profile. The general shape is reproduced as central viewing chords have a slightly higher slope than the edge chords, but the discrepancy in values implies there is at least one other source of light proportional to the neutral density.

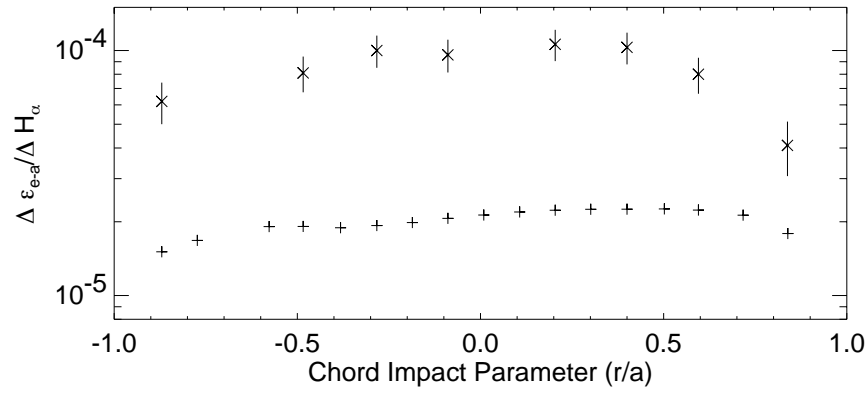


Figure 3.21: Slope versus chord, + are predicted from electron-neutral bremsstrahlung alone, x are the measured values.

### 3.5.7 Continuous Emission from Charge Exchange Recombination

Charge exchange is an important (dominant) process in all MST conditions as evinced by the collision rates in the Lanier thesis[40], reproduced in Figure 3.22. When a neutral atom (or partially

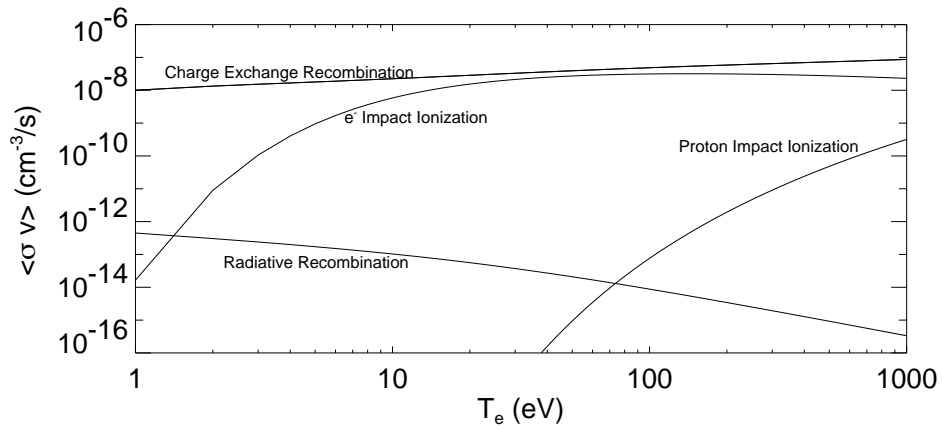


Figure 3.22: Rate coefficients for radiative processes in MST

ionized ion) collides with an ion, there is a finite probability that a charge exchange event will occur. In MST, this is predominantly from a neutral hydrogen (deuterium) atom depositing its

electron in the potential well of a hydrogen ion. This process, depicted in Figure 3.23, predicts discrete line emission as predicted by the Bohr model,  $h\nu = \frac{13.6\text{eV}}{n_i^2 - n_f^2}$ . However, any inelasticity during the interaction leads to a deviation from pure line radiation and includes some continuous

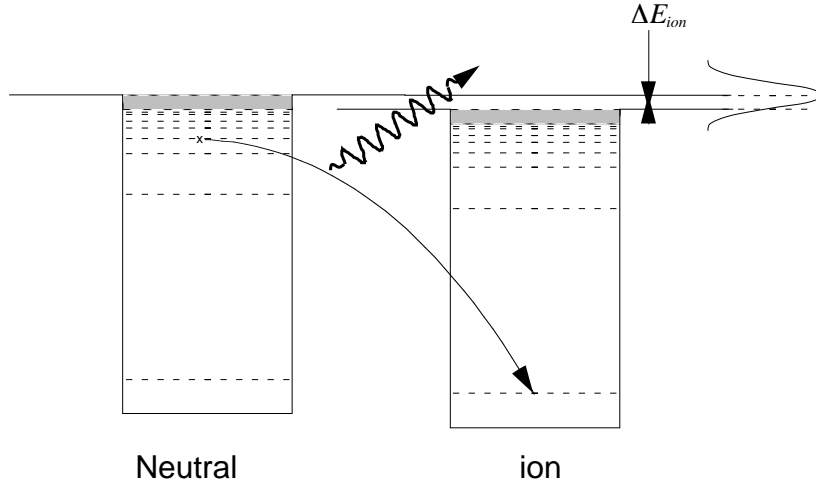


Figure 3.23: Charge exchange cartoon.

emission. As charge exchange is such a probable event in MST, any continuum radiation associated with it may be important. It is found that radiative processes involving ion-atom collisions must be taken into account in the analysis of continuum radiation in the ultraviolet to near-infrared for low-temperature helium plasmas over a wide range of physical conditions[46]. The ion-atom contribution to the continuum is in fact much stronger than the electron-ion and electron-atom (discussed above) parts for very weakly ionized plasmas (with  $T_e \lesssim 3\text{eV}$ ), and the contribution remains non-negligible even as the temperature approaches MST extreme edge values of  $T \sim 10\text{eV}$ . Applying the same considerations to a hydrogen plasma[47] approaching MST-like temperatures yields the discomfoting result that the ion-atom continuum can be considerable, particularly for high neutral density.

In a manner analogous to that described in Section 3.5.6, it can be deduced that the continuous emission from charge exchange can be monitored by  $H_\alpha$  emission. This emission must be propor-

tional to the ion density, neutral density and some function of temperature and density. Invoking local quasineutrality enables this to be cast in terms of the electron density to within a numerical factor. The line integral of this emission is again weighted by the neutral density profile, hence it is primarily weighted to the extreme edge conditions. The ratio between this and the measured  $H_\alpha$  emission is again a constant; therefore the line integrated emission is linear with the measured  $H_\alpha$  signal.

### 3.6 Coping with Pollution

It has been empirically determined that the NIR is polluted by radiation emitted from neutral particles. Two processes described above (electron-neutral bremsstrahlung, 3.5.6, and continuous emission due to charge exchange 3.5.7) predict linear behavior between the emission measured in the NIR and  $H_\alpha$  emission. Thus it is appropriate to describe the continuous emission at 1040nm as the sum of two parts,

$$\epsilon_{1040} = \epsilon_{e-i} + \alpha\gamma_{H\alpha} \quad (3.27)$$

the first is electron-ion emission, and the second is a contribution from neutral particles. Note that the electron-ion term includes all other sources of unchecked pollution in this development. The striking linearity between the NIR and  $H_\alpha$  line integrated signals, (demonstrated in Figures 3.24, 3.28, and 3.29) justifies defining the slope in terms of its line integral

$$M = \int_0^L \epsilon_{1040} dl = \int_0^L \epsilon_{e-i} dl + \bar{\alpha} \int_0^L \gamma_{H\alpha} dl \equiv B + \bar{\alpha}H_\alpha \quad (3.28)$$

where  $B$  is the line integrated electron-ion bremsstrahlung, and  $H_\alpha$  is the measured line integral of the  $H_\alpha$  emissivity. Thus, the linear NIR vs  $H_\alpha$  graph has a y-intercept that represents bremsstrahlung emission. Inspection of the data in Figure 3.24 shows qualitative agreement with

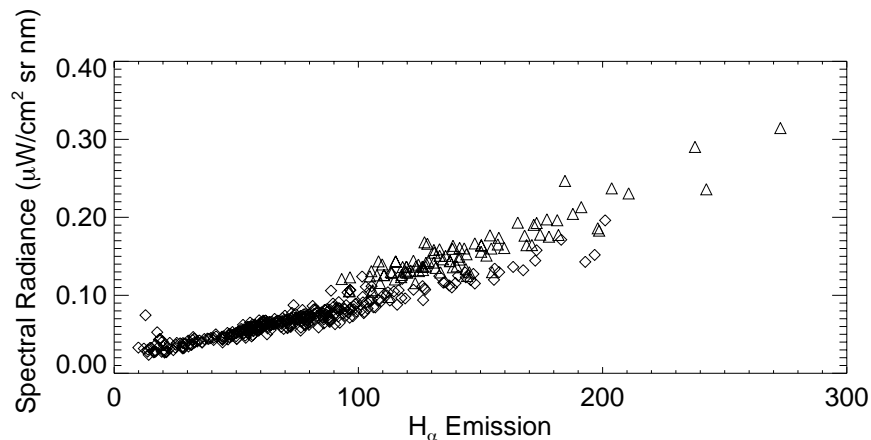


Figure 3.24: Emission at 1040nm vs  $H_{\alpha}$  emission, separated by density. The data represented by diamonds are for low density (average  $\bar{n}_e = 1.1 \times 10^{13} \text{cm}^{-3}$ ) while the triangles represent higher density shots (average  $\bar{n}_e = 2.5 \times 10^{13} \text{cm}^{-3}$ ).

bremsstrahlung emission. Linear fits eye-balled separately for the low and high density data show an increase in the y-intercept value for the higher density, as expected. Although Figure 3.25 shows that  $\bar{\alpha}$  varies weakly with plasma conditions (particularly the electron density), the majority of the light collected for both the NIR and  $H_{\alpha}$  emission emanates from a very narrow radiative shell near the plasma edge. Thus, by taking into account the spatial weighting in the integration in equation 3.28 the slope  $\bar{\alpha} \sim \alpha(\text{edge})$ .

To test the hypothesis that the NIR pollution is proportional to neutral emission, as opposed to a hydrogen line or molecular hydrogen, the experiment was repeated in helium discharges with a He I (587 nm) line used to monitor the neutral density. Figure 3.26 shows that the NIR signal follows the He I in time. Also plotted is the  $H_{\alpha}$  emission, with expected results. The  $H_{\alpha}$  emission is now much, much lower than in hydrogen plasmas (refer to Figure 3.29), so the neutral hydrogen contribution to the NIR emission can be neglected. It is interesting to note that the  $H_{\alpha}$  signal closely follows the He I line in this experiment. One possible explanation is that with the  $H_{\alpha}$  line being so dim, the measurement is significantly affected by the same background that is measured in the NIR. A second possible explanation is emission from the He II line at nearly the same wavelength

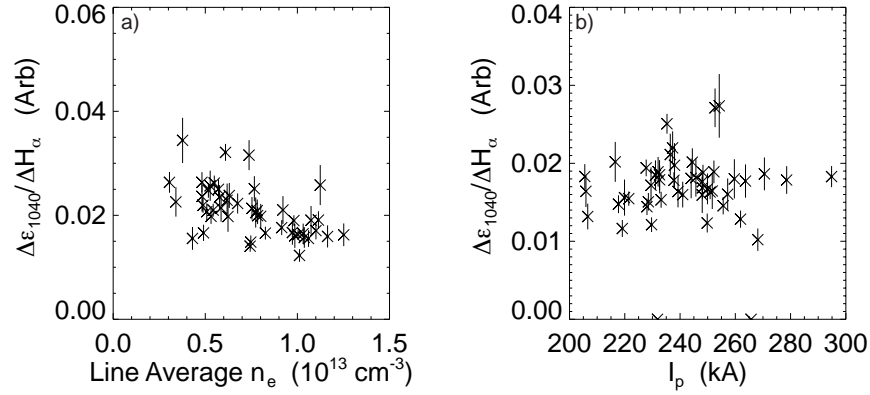


Figure 3.25: NIR -  $H_\alpha$  slope versus  $n_e$  and  $T_e$ . a) is a density scan at constant current (240-250kA); b) is a current scan at constant line-averaged density ( $1.0 - 1.1 \times 10^{13}$ ). There is a slight dependence on average electron density, with no apparent temperature dependence (as  $T_e$  scales with  $I_p$ ).

as the  $H_\alpha$  line ( $h\nu = \frac{Z^2 R_y}{n_i^2 - n_f^2}$  so the 3-2 transition for hydrogen has the same energy as the 6-4 transition for singly-ionized helium). In either case, the light from the  $H_\alpha$  line is unimportant in this experiment. The data in Figure 3.27 show that the NIR emission is again proportional to the neutral emission. These data are collected over a central chord in the NIR array in low current, moderate density discharges ( $n_e \sim 1.0 - 1.2 \times 10^{13} \text{ cm}^{-3}$ ,  $I_p \sim 240 - 260 \text{ kA}$ ). This verifies that the NIR is polluted by light proportional to the neutral particle density. The next step is to remove the pollutant from the signal.

### 3.6.1 Separation of Measured NIR Signal

Equation 3.28 predicts linear behavior between the line integrated emission at 1040nm and the measured  $H_\alpha$  emission, with the y-intercept representing the line integrated bremsstrahlung emission. By simultaneously measuring the NIR and  $H_\alpha$  emission on a given chord, the bremsstrahlung emission is determined by extrapolating the line to zero  $H_\alpha$  emission. The technique is demonstrated in Figure 3.28, where the time traces of the NIR emission and  $H_\alpha$  emission are shown. Every feature in the  $H_\alpha$  signal also appears in the NIR signal, as expected. The dotted lines indi-

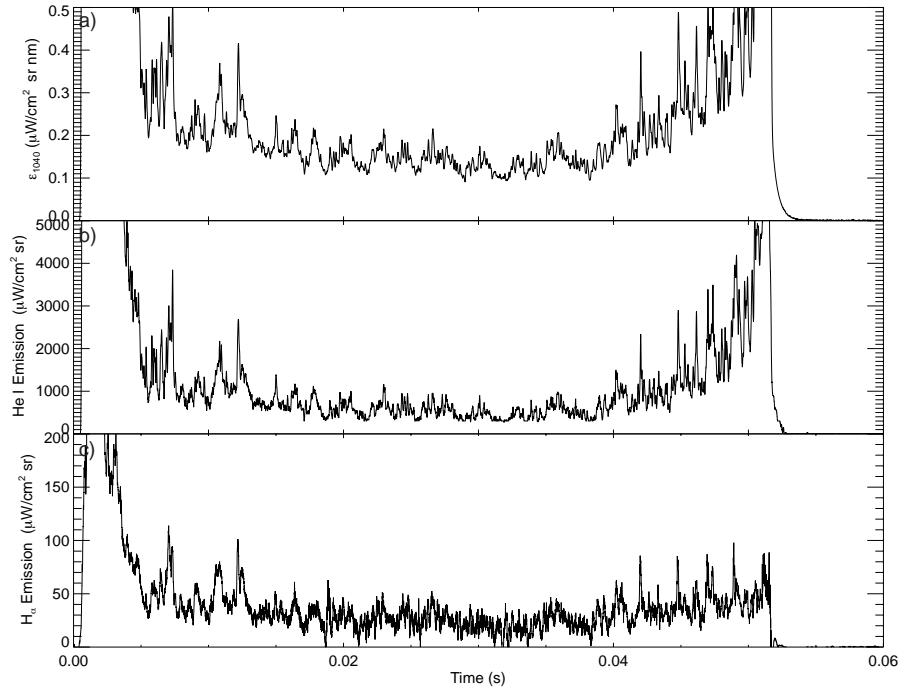


Figure 3.26: The NIR signal closely follows the He I signal with time in He discharges. Also shown is the  $H_{\alpha}$  signal, whose magnitude is down more than an order of magnitude from standard hydrogen discharges.

cate the time range of interest for measuring the bremsstrahlung emission,  $t = 11 - 21$  ms in this case. Rebinning these data to a slower timescale enables a meaningful plot of NIR vs  $H_{\alpha}$  emission. By fitting a line to fifteen data points (the 7 previous and 7 upcoming time points), the slope and intercept are determined as functions of time. The assumption that the slope varies only weakly on plasma conditions is self consistent with averaging over a millisecond in its determination. Finally, the extracted bremsstrahlung signal is plotted versus time. This signal can vary rapidly, and is typically noisy. The uncertainty is due primarily to error in extrapolating to zero on the x axis, while the uncertainty in calibration is effectively negligible in comparison.

The y-intercept 'signal' in this case is only a small fraction of the measured emission; the detector is typically reading between 0.05 and 0.2  $\frac{\mu\text{W}}{\text{cm}^2 \text{sr nm}}$  and the extracted signal is around

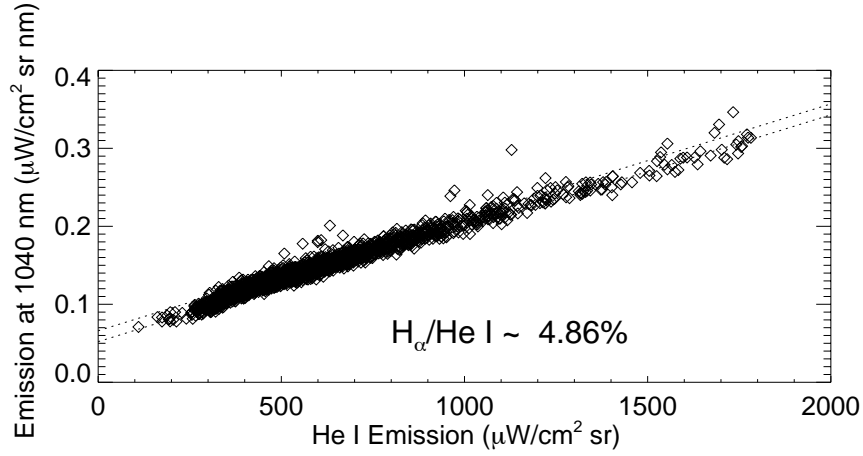


Figure 3.27: Helium plasma corroboration of NIR versus neutral density emission estimate, central chord line average.

$0.02 \frac{\mu\text{W}}{\text{cm}^2 \text{sr nm}}$ . The signal to pollution ratio thus ranges from about 10% to 40%. The situation is improved in PPCD experiments, where the  $H_\alpha$  emission and neutral particle density are greatly reduced. Figure 3.29 shows the similar analysis for a PPCD shot; the y-intercept signal is now over half of the typical NIR signal. This leads to a shorter extrapolation to reach the zero pollution limit and there is a corresponding drop in the uncertainty in the bremsstrahlung level.

It is not of primary concern to quantitatively predict the slope, as the slight sensitivity to edge conditions can make up to a factor of two difference. The two signals should be linearly related; the emission due to electron-neutral bremsstrahlung and charge-exchange recombination are two processes that can account for this experimentally-verified phenomenon. Therefore the slope deduced from the data is justified for extracting the bremsstrahlung signal. Unpolluted bremsstrahlung is not linearly related to  $H_\alpha$ .

### 3.7 Screening Effect of Non-fully Stripped Ions

In Section 1.3, consideration of the interaction between an electron and a point ion and integration over physically reasonable impact parameters led to the collision frequency. Similarly,

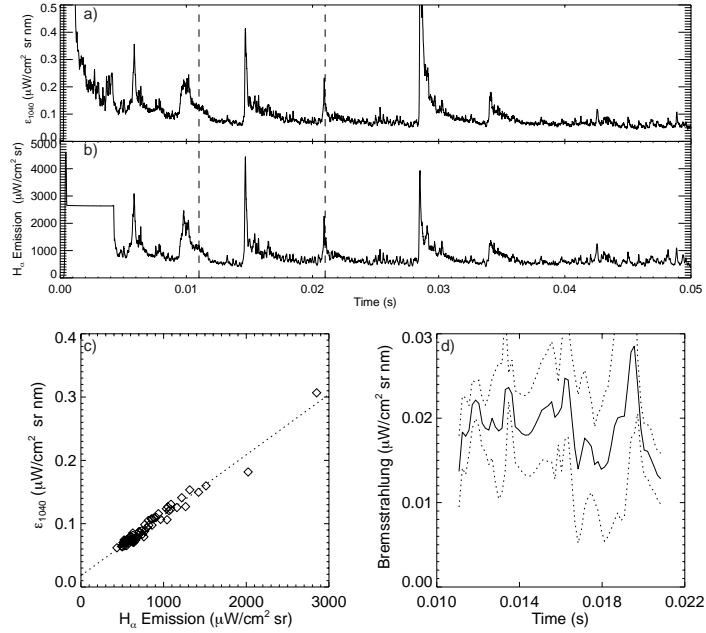


Figure 3.28: NIR, H<sub>α</sub>, and bremsstrahlung. Shot: 1010604057, chord 5. The dotted lines on the bremsstrahlung plot are the upper and lower bounds from uncertainty in determining the y-intercept.

in Section 3.2 the bremsstrahlung emissivity is computed by considering the radiation due to an electron-ion encounter, and again integrating over all incident impact parameters and velocities. In these calculations, the electron and ion are assumed point charges; a good assumption for fully stripped ions. However, in the case of a partially ionized atom, a significant fraction of incident impact parameters and velocities lead to trajectories that penetrate the outer electronic cloud. An illustration of this process is identical to that of Figure 3.18 in the electron-neutral bremsstrahlung discussion. The electrons which penetrate the outermost electrons are influenced by an effective charge which is higher than the atomic charge ( $Z_{nucleus} - N_{bound e^-}$ ), leading to an enhanced collisionality[48]. This results in a real increase in the resistivity and in increase in bremsstrahlung emission. A mathematical development of this effect is presented in the literature[49, 50] and can

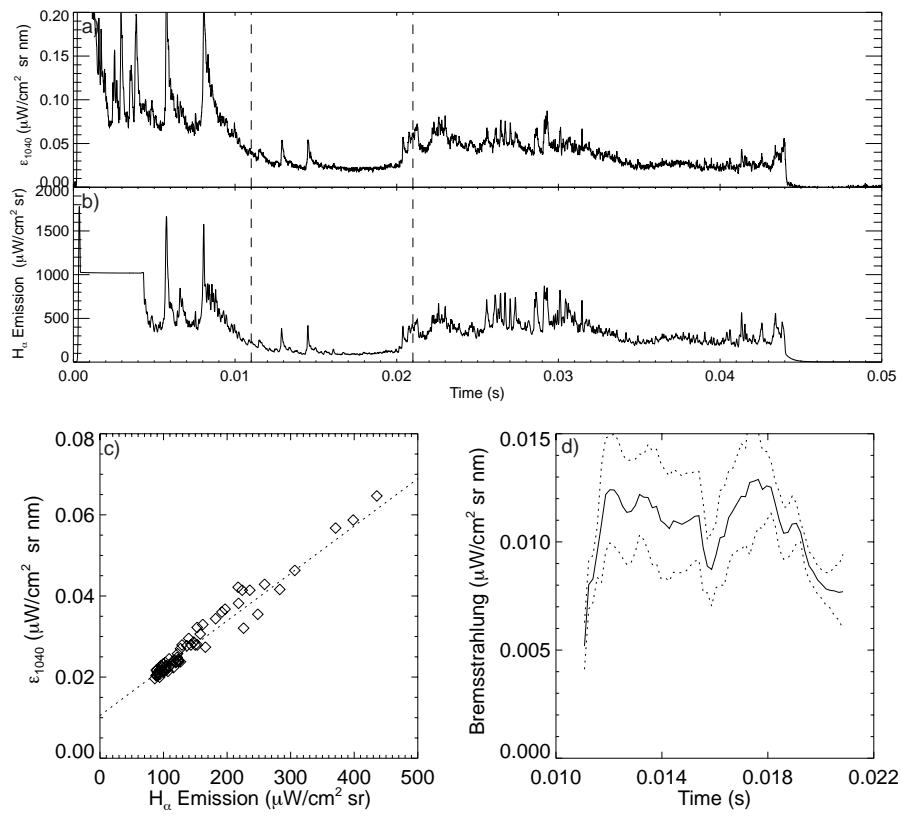


Figure 3.29: NIR,  $H_\alpha$ , and bremsstrahlung. Shot: 1010324086, chord 5.

be summarized for the emission as

$$\epsilon = \epsilon_{ideal} (1 + \lambda_{\omega}^{corr}) \quad (3.29)$$

where

$$\lambda_{\omega}^{corr} = \left[ \left( \frac{Z}{Z_i} \right)^2 - 1 \right] \frac{R_{\alpha}(x)}{K_0(x)} \quad (3.30)$$

and  $Z$  is the nuclear charge,  $Z_i$  is the ionic charge,  $N_e = Z - Z_i$  is the number of bound electrons,  $K_0$  is the Bessel-MacDonald function, and

$$\begin{aligned} x &= \frac{hc/\lambda}{2T_e} \\ R_{\alpha}(x) &= \frac{1}{2} \int_{-\infty}^{\infty} \frac{e^{-x \cosh(\xi)}}{1 + \left( \frac{e^{\xi}}{\alpha} \right)^2} d\xi \\ \alpha &= \gamma^2 \frac{hc/\lambda}{4R_y} \\ \gamma &= \frac{3N_e^{2/3}}{2Z} \end{aligned} \quad (3.31)$$

A calculation following reference [48] is summarized in Figure 3.30, where the correction factor ( $\lambda_{\omega}^{corr}$ , in percent) has been calculated for helium, carbon and oxygen. The lines are cut off where the electron temperature reaches the ionization potential for each charge state. Similar calculations for other MST impurities (boron, nitrogen; not included in the plot for clarity) show similar results: the lower (and particularly the singly ionized) charge states have very large corrections. This effect is particularly pronounced in aluminum; the results are shown in Figure 3.31. Even a small concentration of the low charge states of aluminum will add a significant amount of radiation. As Al II has an ionization potential of less than 20eV, the contamination will be most prevalent at the extreme edge.

There is experimental evidence that this process is significant in MST. Above it was demonstrated that the measured emission in the NIR is polluted by neutral emission, and measures

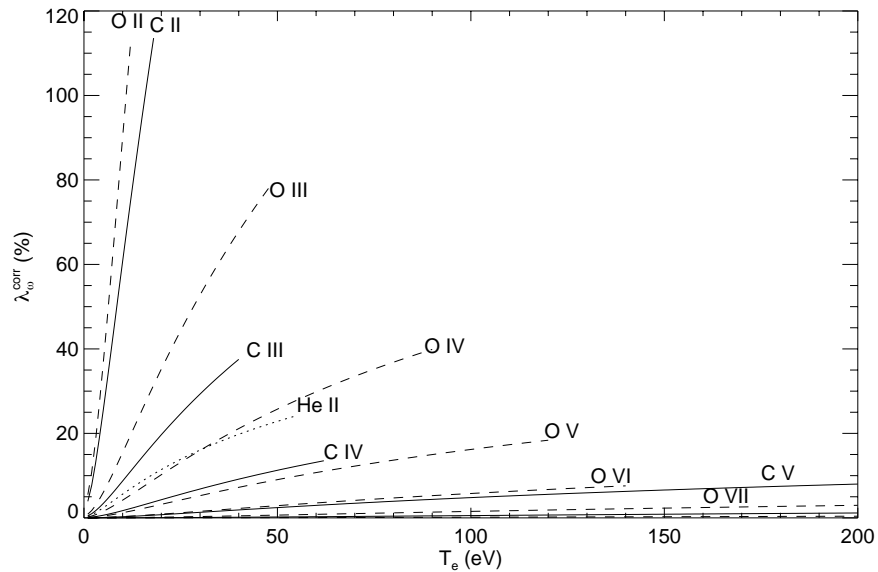


Figure 3.30: Screened potential correction factors for helium (dotted line), carbon (solid line) and oxygen (dashed line). The corrections for C VI, O VII, and O VIII are also plotted, but are very small.

to remove the contamination are moderately successful. However, the excess emission from neutral and partially ionized impurities is not accounted for. Figure 3.32 is a plot of the central chord line integrated NIR and  $H_{\alpha}$  emission in a particularly dirty MST discharge arising from conditioning of a new, deeply inserted edge magnetic probe. In normal (and particularly clean) discharges the  $H_{\alpha}$  and NIR emission mimic each other with time throughout the discharge (see Figures 3.28 and 3.29). In this case, however, a noticeable increase in the NIR signal after about  $t=15$  ms occurs without a corresponding increase in  $H_{\alpha}$  emission. This increase does follow the boron emission, monitored by a B IV line in the impurity monochromator array[13]. Figure 3.33 is a plot of five impurity lines versus time, along with the estimated bremsstrahlung signal found by extrapolation to zero  $H_{\alpha}$  emission. The carbon, aluminum and oxygen signals exhibit normal behavior in time, while the boron signal takes off midway through the discharge. The baseline bremsstrahlung level and the increase with the boron signal are both way too high to be explained

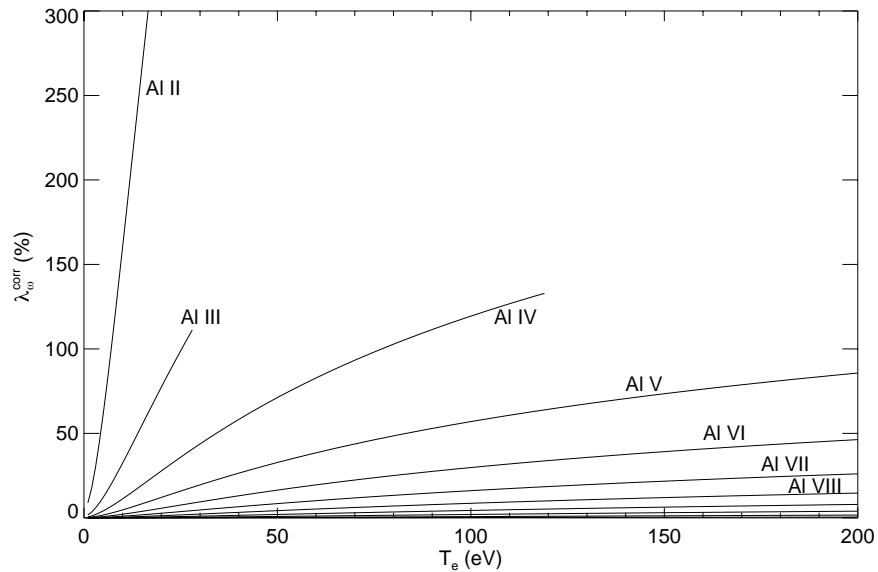


Figure 3.31: Screened potential correction factors for aluminum charge states.

by ordinary electron-ion bremsstrahlung. Making the assertion that lower charge states of boron are present, the increase in emission is more fathomable considering the increased emissivity due to screening. The probe acts as a source of neutral boron well away from the edge of the plasma, at electron temperatures that are approaching 40-50 eV. The screening effect on lower charge states at these temperatures is enormous (referring again to Figure 3.30), and will contribute enough radiation to prevent a meaningful extraction of  $Z_{eff}$  from the emission.

The first alternate explanation must be that a B IV line pollutes the NIR measurement. This is not the case, as there are no boron lines (B IV or lower charge states) anywhere near 1040nm. A second possible explanation that tempts the astute skeptic is that the probe is covered with a boron nitride (BN) shield; thus nitrogen emission may closely follow the boron emission arising from plasma interaction with the probe. Then recalling that a glimmer of line pollution in the NIR is potentially due to a N I line (Section 3.5.1), one could argue that (since it wasn't measured) the N I line could be the primary contributor to the NIR emission in this experiment. While it could be

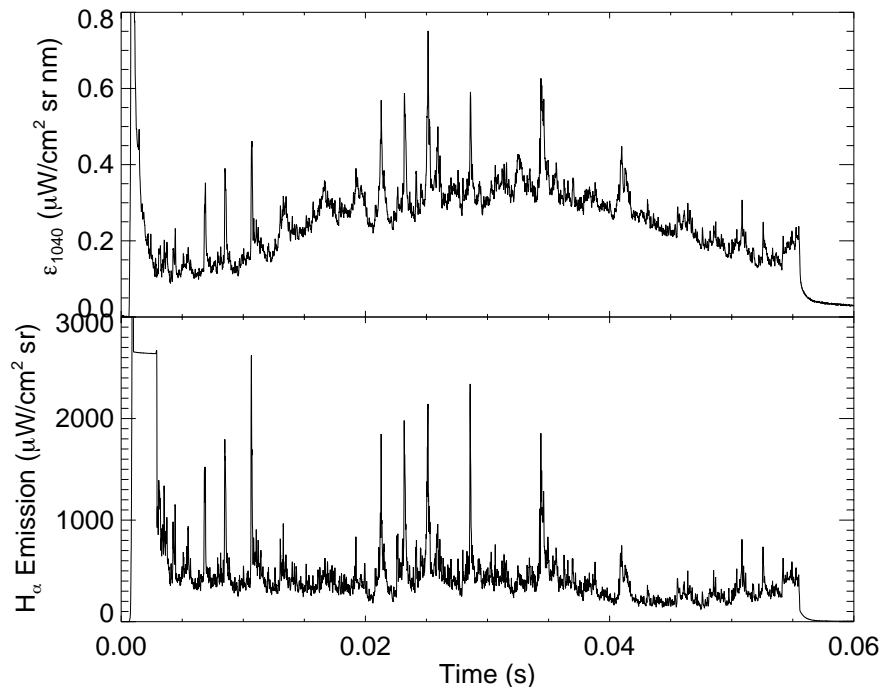


Figure 3.32: NIR and  $H_\alpha$  signals versus time in a dirty plasma. Note the increase in NIR emission without a corresponding rise in  $H_\alpha$  after  $t = 15\text{ms}$ .

an influence in this particular experiment, under normal plasma conditions the nitrogen line is not trouble and the implied  $Z_{eff}$  from the bremsstrahlung signal is still too high; there is a different pollutant.

The effect of screening of non-fully stripped ions is not the only pollutant in MST emission, but this presents real trouble in the deduction of  $Z_{eff}$  from measured emission. The only way to resolve this is with a somewhat complete collisional radiative model of the MST plasma. This is an approachable topic, as it has been successfully implemented on machines with fewer dominant impurities than MST[51], but it is a task that falls well beyond the extent of this dissertation.

Perhaps the most important consequence of the presence of non-fully stripped ions is an actual increase in plasma resistivity. The increase in emissivity for this effect is a direct result of a higher collisionality; this same correction factor  $(1 + \lambda_\omega^{corr})$  must apply to the resistivity contribution

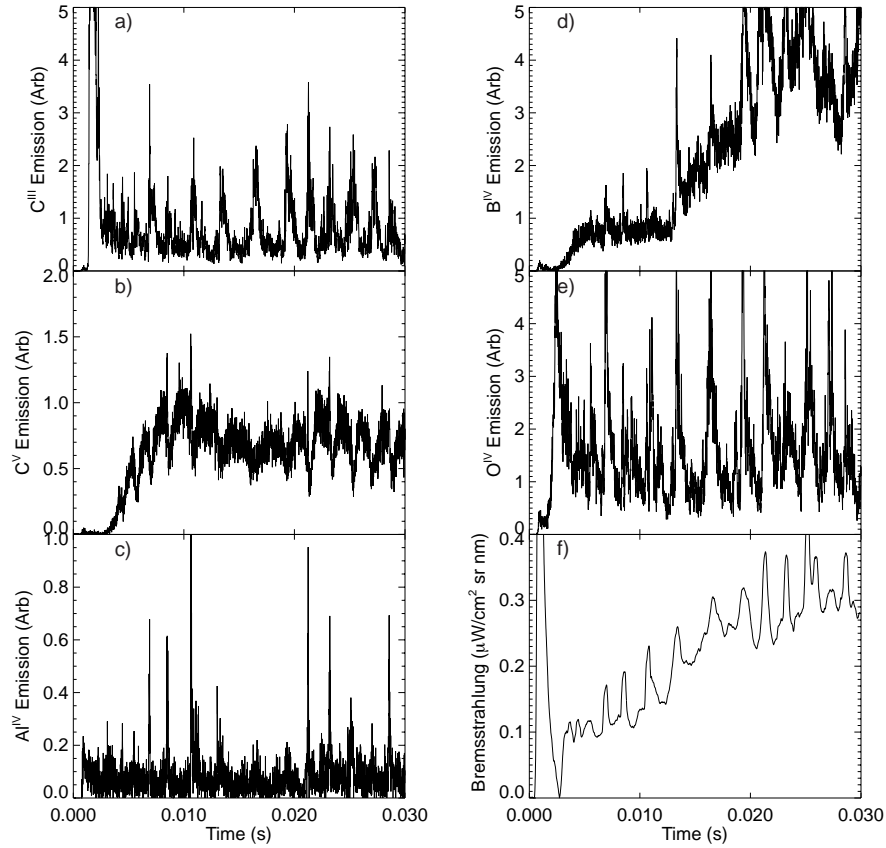


Figure 3.33: Impurity line and bremsstrahlung signals in an impure plasma. The extracted bremsstrahlung signal appears to be polluted by boron as they both increase after  $t = 15$ ms.

of non-fully stripped ions. With an abundance of low charge state impurities (including neutral impurities),  $Z_{eff} \neq \frac{\sum_s n_s Z_s^2}{n_e}$  for the computation of plasma resistivity. Fortunately for the scope of this work, the enhancement to the resistivity is only prevalent in regions where low charge state impurities are prevalent. In the high current, high temperature PPCD experiments studied here, the low charge states are burned through in all but the extreme edge regions (where a comparison between experiment and models is unapproachable for a variety of reasons).

### 3.8 Conclusions

Due to the abundance of potential pollutants and the  $n_e^2$  dependence of bremsstrahlung emission, it is difficult to measure  $Z_{eff}$  in a low density plasma. The case for MST is further weakened, as the cool edge region has several sources of contaminants, particularly neutral hydrogen and low charge state or neutral impurities. Dynamic removal of the neutral hydrogen pollutant through its relationship to  $H_\alpha$  emission under the most favorable conditions (high  $n_e$ ,  $T_e$ ) facilitates a bremsstrahlung attempt in the NIR. This method cannot be extended to low temperature or low density regimes as the primary non-neutral pollutants are the screening effect of non-fully stripped impurities and perhaps low charge state impurity lines (O II, N I, C I). An accurate measurement of  $Z_{eff}$  in these regimes will require collisional radiative modeling of the dominant MST impurities. Finally,  $Z_{eff} \neq \frac{\sum_s n_s Z_s^2}{n_e}$  in calculating the resistivity of the MST edge plasma, as the existence of low charge state impurities leads to an enhanced resistivity.

# Bibliography

- [1] R. J. Goldston and P. H. Rutherford, *Introduction to Plasma Physics*, Institute of Physics Publishing, Philadelphia, PA, 1995.
- [2] J. D. Jackson, *Classical Electrodynamics*, John Wiley and Sons, New York, NY, 1975.
- [3] I. H. Hutchinson, *Principles of Plasma Diagnostics*, Cambridge University Press, New York, NY, 1990.
- [4] T. R. Carson, *Astronomy and Astrophysics* **189**, 319 (1988).
- [5] W. J. Karzas and R. Latter, *The Astrophysical Journal Supplement* **6**, 167 (1961).
- [6] D. G. Hummer, *The Astrophysical Journal* **327**, 477 (1988).
- [7] H. Summers, Private communication.
- [8] A. T. Ramsey, Gaunt factors for visible bremsstrahlung inversions on TFTR, Private communication.
- [9] D. Whyte, Private communication.
- [10] G. Bekefi, *Radiation Processes in Plasmas*, John Wiley and Sons, New York, NY, 1966.
- [11] National Institute of Standards and Technology, Atomic Spectra Database, 2001, <http://physics.nist.gov/PhysRefData/contents.html>.
- [12] H. Abgrall, E. Roueff, X. Liu, and D. E. Shemansky, *The Astrophysical Journal* **481**, 557 (1997).
- [13] J. N. Tabora, D. Craig, and D. J. Den Hartog, Implementation of the impurity monochromator array on MST, PLP Report 1234, University of Wisconsin, Madison, 2000.

- [14] D. G. Whyte, M. R. Wade, D. F. Finkenthal, K. H. Burrell, P. Monier-Garbet, B. W. Rice, D. P. Schissel, W. P. West, and R. D. Wood, *Nuclear Fusion* **38**, 387 (1999).
- [15] E. S. Marmor, R. L. Boivin, R. S. Granetz, J. W. Hughes, and B. Lipschultz, *Review of Scientific Instruments* **72**, 940 (2001).
- [16] S. Castillo, Private communication.
- [17] T. R. Sandin, *Essentials of Modern Physics*, Addison-Wesley, Reading, MA, 1989.
- [18] K. Sawada and T. Fujimoto, *Journal of Applied Physics* **78**, 2913 (1995).
- [19] S. N. Suchard, *Spectroscopic Data: Homonuclear Diatomic Molecules*, Plenum Press, New York, NY, 1976.
- [20] G. H. Dieke, *Journal of Molecular Spectroscopy* **2**, 494 (1958).
- [21] U. Fantz, K. Behringer, J. Gafert, and D. Coster, *Journal of Nuclear Materials* **269**, 490 (1999).
- [22] E. E. Kunhardt and L. H. Luessen, *Electrical Breakdown and Discharges in Gases*, Plenum Press, New York, NY, 1981.
- [23] J. Lawler, Private communication.
- [24] E. F. McCormack, S. T. Pratt, P. M. Dehmer, and J. L. Dehmer, *Journal of Chemical Physics* **98**, 8370 (1993).
- [25] T. E. Sharp, *Atomic Data* **2**, 119 (1971).
- [26] E. F. McCormack and E. E. Eyler, *Physical Review Letters* **66**, 1042 (1991).
- [27] E. Oliva, A. F. M. Moorwood, and I. J. Danziger, *Astronomy and Astrophysics* **240**, 453 (1990).
- [28] T. R. Geballe, *Canadian Journal of Physics* **72**, 782 (1994).
- [29] L. Spitzer Jr. and J. L. Greenstein, *The Astrophysical Journal* **114**, 407 (1951).
- [30] W. B. Latter, P. R. Maloney, D. M. Kelly, J. H. Black, and M. J. Rieke, *The Astrophysical Journal* **389**, 347 (1991).
- [31] R. J. Rudy, P. Erwin, G. S. Rossano, and R. C. Puetter, *The Astrophysical Journal* **384**, 536 (1992).

- [32] J. S. Miller and W. G. Mathews, *The Astrophysical Journal* **172**, 593 (1972).
- [33] D. Pequignot and J. P. Baluteau, *The Astrophysical Journal* **172**, 593 (1972).
- [34] R. J. Rudy, R. D. Cohen, G. S. Rossano, and R. C. Puetter, *The Astrophysical Journal* **362**, 346 (1990).
- [35] R. J. Rudy, R. D. Cohen, G. S. Rossano, P. Erwin, R. C. Puetter, and D. K. Lynch, *The Astrophysical Journal* **380**, 151 (1991).
- [36] R. J. Rudy, G. S. Rossano, P. Erwin, and R. C. Puetter, *The Astrophysical Journal* **368**, 468 (1991).
- [37] C. Armand, J. P. Baluteau, M. Joubert, C. Gry, and P. Cox, *Astronomy and Astrophysics* **306**, 593 (1996).
- [38] R. J. Wilman, A. C. Edge, R. M. Johnstone, C. S. Crawford, and A. C. Fabian, *Monthly Notices of the Royal Astronomical Society* **318**, 1232 (2000).
- [39] M. G. Burton, M. Bulmer, A. Moorhouse, T. R. Geballe, and P. W. J. L. Brand, *Monthly Notices of the Royal Astronomical Society* **257**, P1 (1992).
- [40] N. E. Lanier, *Electron Density Fluctuations and Fluctuation Induced Transport in the Reversed Field Pinch*, PhD thesis, University of Wisconsin-Madison, 1999.
- [41] H. P. Summers, Atomic data and analysis structure, JET Report JET-IR(94)06, Joint European Torus, 1994.
- [42] L. C. Johnson and E. Hinnov, *Journal of Quantitative Spectroscopy and Radiative Transfer* **13**, 333 (1973).
- [43] A. Dalgarno and N. F. Lane, *The Astrophysical Journal* **145**, 623 (1966).
- [44] J. Park, I. Henins, H. W. Herrmann, and G. S. Selwyn, *Physics of Plasmas* **7**, 3141 (2000).
- [45] M. Hayashi, Recommended values of transport cross sections for elastic collision and total collision cross section for electrons in atomic and molecular gases, Internal Report IPPJ-AM-19, Nagoya Institute of Technology, 1981.
- [46] A. A. Mihajlov, A. M. Ermolaev, and M. S. Dimitrijevic, *Journal of Quantitative Spectroscopy and Radiative Transfer* **50**, 227 (1993).

- [47] A. M. Ermolaev, A. A. Mihajlov, L. M. Ignjatovic, and M. S. Dimitrijevic, *Journal of Physics D: Applied Physics* **28**, 1047 (1995).
- [48] M. T. Fall, *Mesure de la Charge Moyenne Ionique, par le Rayonnement Bremsstrahlung dans le Visible, Sur Tore Supra*, PhD thesis, L'Universite Paris xi Orsay, 1991.
- [49] V. D. Kirillov, B. A. Trubnikov, and S. A. Trushin, *Soviet Journal of Plasma Physics* **1**, 117 (1975).
- [50] D. G. Whyte, *Le  $Z_{eff}$  metre du tokamak de vareennes*, Technical Report CCFM RI270f, Centre Canadien de Fusion Magnetique Tokamak de Varennes, 1988.
- [51] L. Carraro, M. Mattioli, F. Sattin, C. Demichelis, J. T. Hogan, W. Mandl, M. E. Puiatti, P. Scarin, and M. Valisa, *Physica Scripta* **55**, 565 (1997).

## Chapter 4

# Resistivity Profile Based on Measured $Z_{eff}$

### Abstract

An upper bound is placed on  $Z_{eff}$  in 400kA PPCD discharges by simultaneously measuring the NIR emission and the primary pollutant on eight poloidal viewing chords. This chapter describes the signal processing and uncertainty analyses utilized. Further removal of pollution is estimated in the edge region, where the implied  $Z_{eff}$  profile becomes unreasonably high. The upper bound  $Z_{eff}$  estimate is higher than the generally accepted  $Z_{eff} = 2$ ; a discussion of the physical reasonability of this follows. A calculation of the resistivity profile based on Spitzer and neoclassical models concludes the chapter.

## 4.1 Bremsstrahlung Measurement of $Z_{eff}$

Owing to the lengthy discussion in Chapter 3, it is possible to remove the bulk of the contaminants from the emission near 1040nm and measure the bremsstrahlung level. The method used to extract bremsstrahlung from the total measured emission described in Section 3.6.1 is re-summarized in Figure 4.1 and leads to a somewhat noisy signal. Reduction of the noise is achieved by ensembling

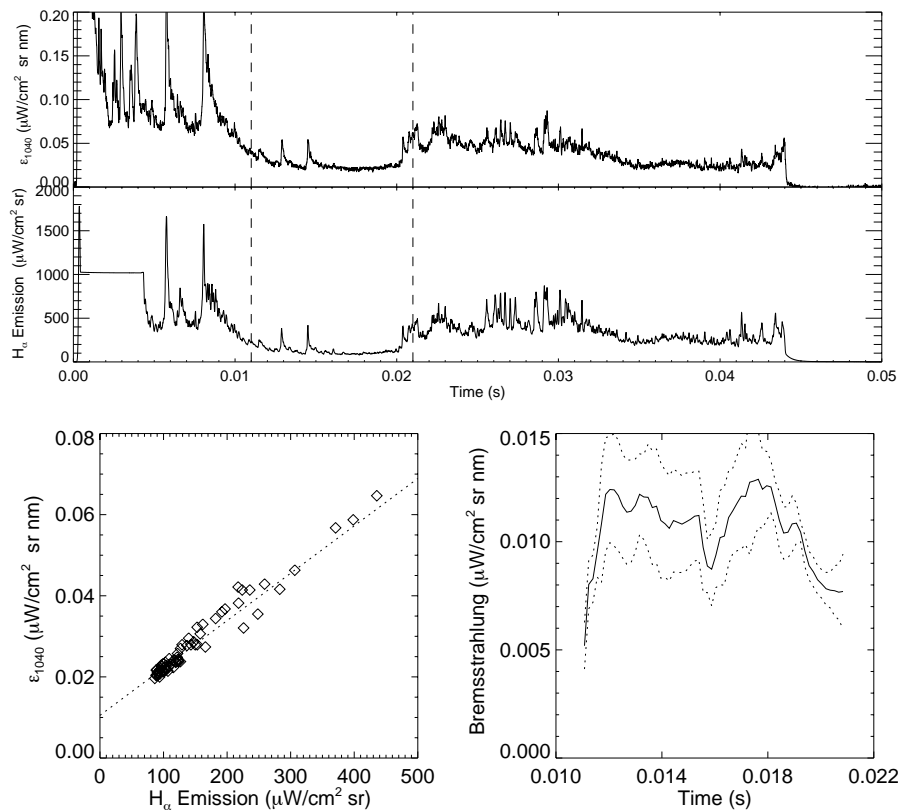


Figure 4.1: NIR,  $H_\alpha$ , and extracted bremsstrahlung. Fitting a line to 15 consecutive time points leads to about 1kHz resolution of the slope and approximately 8kHz resolution of the bremsstrahlung signal.

over many shots. Note that the bremsstrahlung signal is computed prior to ensembling, as opposed to ensembling the NIR and  $H_\alpha$  signals and extracting the bremsstrahlung from them. The reason is that fluctuations actually lead to a better defined slope as the  $H_\alpha$  (and hence NIR) emission jump

considerably, which extends the x-axis over which the line is being fit. Ensembling of the NIR and  $H_\alpha$  signals prior to fitting the line tends to smooth out fluctuations, and hence is not ideal for this analysis. The data presented below are averaged over 423 shots with the errors (not plotted for clarity) computed by taking the standard deviation from the mean; this is valid assuming the error in the bremsstrahlung signal is random. While the first seven and last seven data points in each

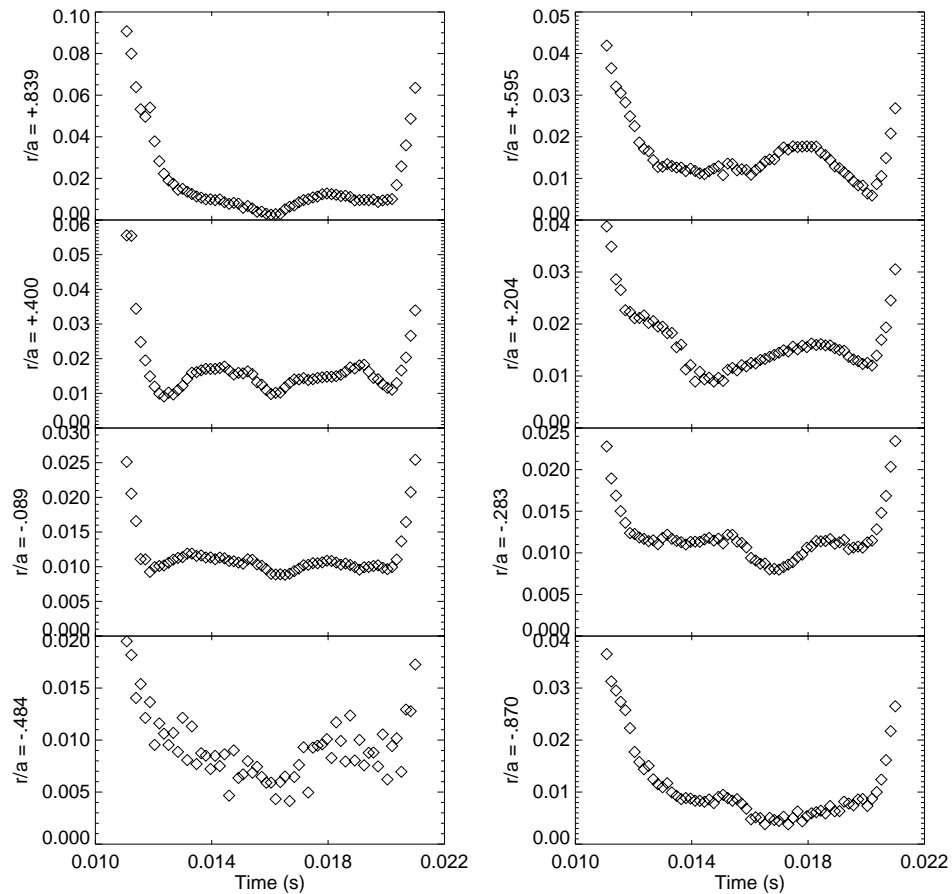


Figure 4.2: Line integrated bremsstrahlung signals (ensbled)

time sequence are not valid due to the analysis technique, the data at  $t < 15$ ms are indicative of a pollutant. Early in the investigated time window, the bremsstrahlung signals are dropping even though the line averaged electron density is steadily ramping upward throughout this time window (see e.g. Figure 1.5). However, after  $t = 16$ ms many of the signals begin to show the expected

increase with electron density. This is consistent with the picture that low charge state impurities are polluting the measurement, and with the increase in electron temperature during PPCD they (mostly) burn through to high charge states making a bremsstrahlung measurement plausible at high temperature and electron density.

MSTFit is used to compute an equilibrium (Chapter 5), and with measured electron density and temperature profiles<sup>1</sup> an attempt to extract  $Z_{eff}$  can proceed. As will be discussed in Chapter 6 it is desired to select a time point when the equilibrium is changing steadily in order to estimate the inductive electric field, and as such  $t = 15.6\text{ms}$  is used as the central value for computing the equilibrium and  $Z_{eff}$  profile. The measured emissivity is inverted under the constraint of zero emissivity at the boundary, with the results shown in Figure 4.3a). The accuracy of the inversion

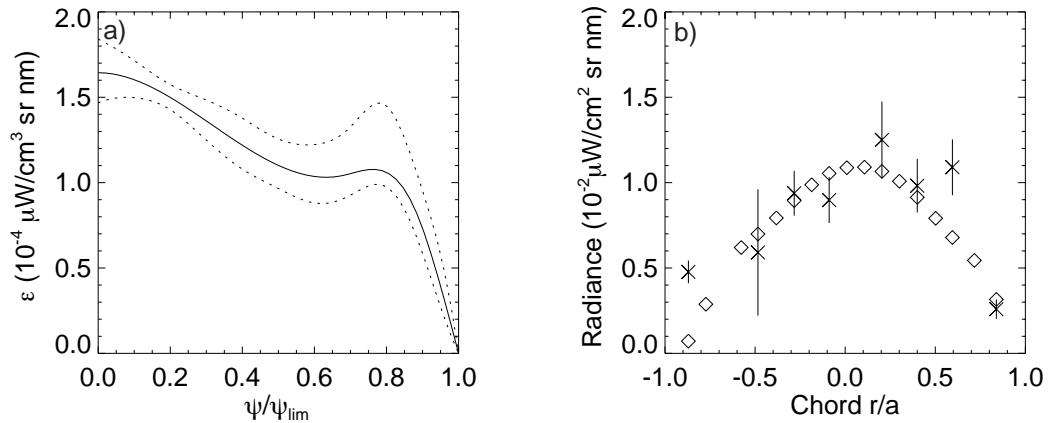


Figure 4.3: a) Inverted bremsstrahlung emissivity. b) data (with error bars) and fit (signals predicted by reconstructed emissivity profile).

is demonstrated in 4.3 b), where the data and uncertainty are shown along with the predicted line integrated emissivity based on the inverted emissivity profile. A Monte Carlo analysis was performed to find the range of inverted profiles that fit the data without an appreciable change in the fit quality. The data are randomly varied within their experimental uncertainty, and several

<sup>1</sup>Many thanks to T.M. Biewer for organizing the large runs to generate this database.

inversions are performed. A standard deviation is determined by enforcing that two thirds of the different inversions fall within  $\pm 1\sigma$  of the best fit. This gives an approximate uncertainty in the inverted emission, sketched by dotted lines in Figure 4.3 a). The uncertainty estimate is potentially low as the model used to invert the emission limits the shape of the possible profiles. Three free parameters are used with boundary conditions of  $\epsilon'(0) = 0$  and  $\epsilon(1) = 0$ . The  $1\sigma$  error shown is used as the estimate in the rest of this work. The  $2\sigma$  envelope (which encompasses 95% of the profiles) shows a considerably larger uncertainty. The number of data to invert ultimately limits the amount of freedom in the model, which limits the uncertainty a Monte Carlo analysis will produce.

With the emissivity determined over the profile,  $Z_{eff}$  can be calculated by solving equation 3.13

$$Z_{eff}(R, Z) = \frac{\epsilon(R, Z)\sqrt{T_e(R, Z)}\lambda^2}{n_e^2(R, Z)\bar{g}_{ff}} \quad (4.1)$$

Using the empirical scaling of the Gaunt factor (equation 3.17),  $Z_{eff}$  is given by

$$Z_{eff}(R, Z) = \left( \frac{\epsilon(R, Z)\sqrt{T_e(R, Z)}\lambda^2}{1.251 (T_e - 8.5)^{0.175} n_e^2(R, Z)} \right)^{1.099}. \quad (4.2)$$

The factor of density squared in the calculation of  $Z_{eff}$  implies that the uncertainty in the inverted density profile weighs heavily in the calculation of the uncertainty in  $Z_{eff}$ . Standard error propagation approximately yields

$$\left( \frac{\delta Z_{eff}}{Z_{eff}} \right)^2 = 1.099 \times \left[ \left( \frac{\delta \epsilon}{\epsilon} \right)^2 + .325 \times \left( \frac{\delta T_e}{T_e} \right)^2 + 2 \times \left( \frac{\delta n_e}{n_e} \right)^2 \right] \quad (4.3)$$

where  $\delta$  denotes the uncertainty in a given quantity. Figure 4.4 shows the density profile along with its uncertainty determined in the same fashion as that described above for the emissivity. The inverted profile matches the data quite well, and the low uncertainty in the line integrated signals

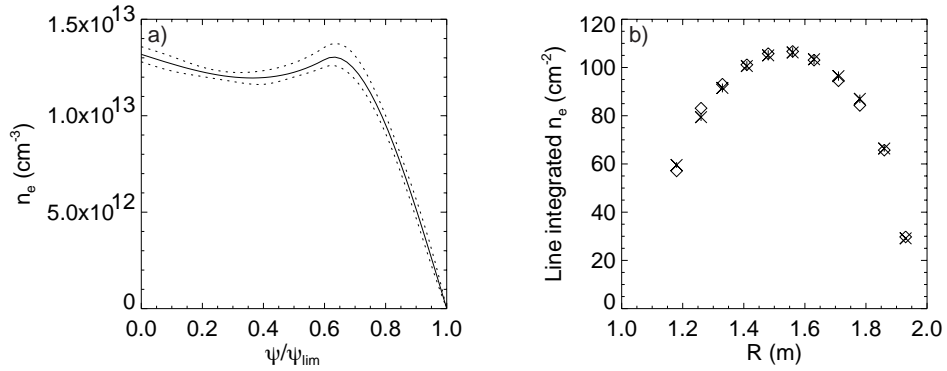


Figure 4.4: Inverted electron density profile, data and fit.

translates to a low uncertainty in the profile, 5% or less over most of the profile. The uncertainty in the temperature profile is found more easily, as the Thomson scattering measurement is localized and no inversion is required. The fit to the temperature data is simply done by minimizing a reduced  $\chi^2$  using a six free parameter fit to the 16 data. Uncertainty is again determined by varying the profile over a range to appreciably change the fit quality. The resulting uncertainty in the temperature profile is shown in Figure 4.5c).

An additional contribution to the uncertainty is required as the empirical scaling of the Gaunt factor differs from the tabulated values by several percent over the range of values for which it is computed. This is accounted for by adding an additional 5% uncertainty in the calculated  $Z_{eff}$  profile. This is in fact quite small in comparison to uncertainties in measured profiles. Figure 4.5 summarizes the calculation of  $Z_{eff}$  and its uncertainty. The emissivity, electron density and temperature profiles are plotted with the uncertainty in their fits, along with the calculated  $Z_{eff}$  profile. The calculated  $Z_{eff}$  profile is on the order of 5 in the core, drops gradually moving toward the mid-radius region, then diverges near the edge. The results are not as discouraging as they appear, as the edge region must be discarded. The presence of pollutant emission is most prevalent at the edge, where low temperatures and the source of neutral impurities are disastrous

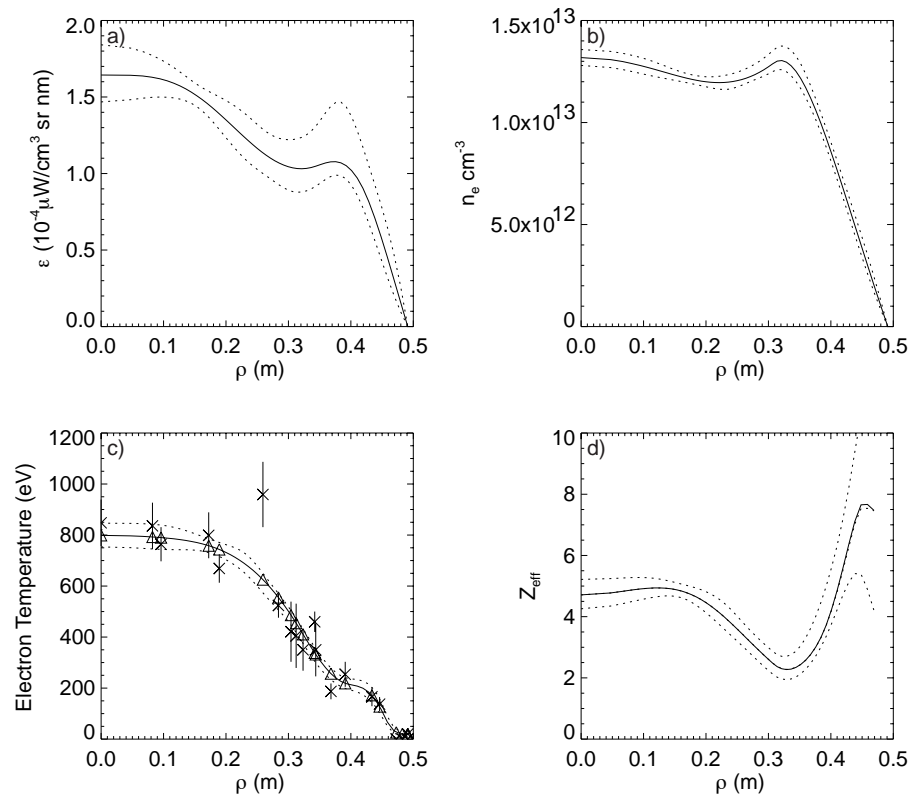


Figure 4.5: Measured emissivity, electron density and electron temperature; computed  $Z_{eff}$ .

to the bremsstrahlung measurement.

The data in Figure 4.3 show more emission on the central viewing chords than on the edge chords. This implies that the inversion of the data gives a reasonable measure of the emission profile (as opposed to inverting extremely edge peaked line integrated signals, where the inversion is extremely uncertain). Assuming a small edge contaminant, physically explicable by either line pollution, screened ion effects or both, the edge  $Z_{eff}$  value can be brought back in line with lower edge values. This is not a new idea;  $Z_{eff}$  measurements in low temperature low density regions are destined to fail and the measurements there are disregarded[1, 2]. In the remainder of this work, quantitative comparisons of the measured  $Z_{eff}$  or resistivity profiles outside  $\rho = .4\text{m}$  will not be

made, and a small edge localized pollutant is assumed. Figure 4.6 is a recalculation of  $Z_{eff}$  with the

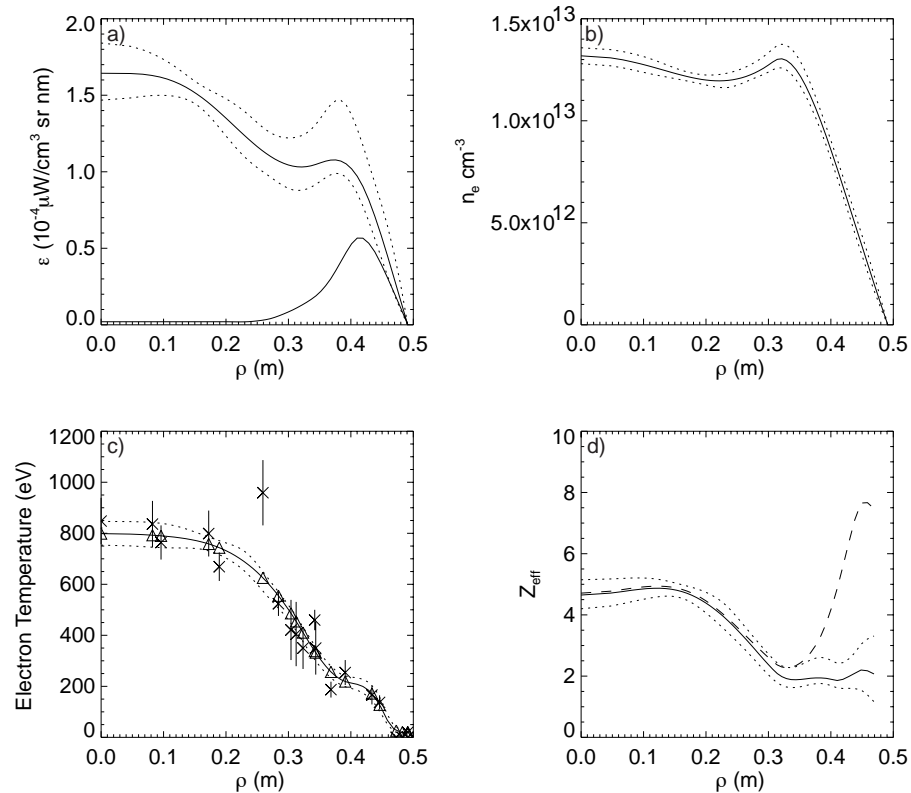


Figure 4.6: Measured emissivity, electron density and electron temperature; computed  $Z_{eff}$ .

modest edge pollutant removed. A consideration of the effect of this ad hoc assumption is worth while. One of the primary outside interests in the  $Z_{eff}$  measurement is an accurate determination of the total Ohmic input power. In the absence of fluctuations, as in PPCD, this is well described by

$$P_{\Omega} = \int \eta J_{\parallel}^2 dV \quad (4.4)$$

and the value for each of the modeled resistivity profiles is tabulated below in Table 4.1.

Profile	$P_{\Omega}$ Neoclassical (MW)	$P_{\Omega}$ Spitzer (MW)
No Correction	3.51	2.47
Edge Light Removed	2.94	1.96
Flat $Z_{eff} = 2$	2.13	1.39

Table 4.1: Total Ohmic input power based on  $Z_{eff}$  assumptions. The difference between the uncorrected and edge-light reduced profiles is a significant change in total power, but the difference between the Spitzer and neoclassical models is larger. A method of estimating  $P_{\Omega}$  independent of  $Z_{eff}$  (see Chapter 6) leads to a value of about 2MW.

There is certainly a change in the power by making this correction, however it is a smaller fractional change than the difference between the Spitzer and neoclassical models for a given  $Z_{eff}$  profile. A different method of computing the total input power that is independent of  $Z_{eff}$  (described in Chapter 6) estimates the input power to be about 2 MW. This adds credibility to the arbitrary amount of light chosen to remove, however quantitative comparisons will not be made in the edge. Later in this work the agreement between the measured resistivity and that based on these models will be investigated. There the focus will be on the central to mid-radius regions, and this correction is not a factor. It should be noted that if the edge pollution is due to the screening effect of non-fully stripped ions, the increased bremsstrahlung emission corresponds to a real increase in resistivity. This is not the case for other types of pollution (e.g. lines) that are perhaps responsible. Without CRM, it is impossible to quantify the screening effect, and as such this very interesting topic is deferred to future work.

## 4.2 Discussion

Is it conceivable that  $Z_{eff}$  is five in the core? There certainly are impurities present in the MST; the plasma is limited one centimeter from an aluminum wall and lines of every shape and color are seen in the spectrum. It would take a fully stripped aluminum concentration of about  $2\frac{1}{2}\%$  (in the absence of other impurities) to explain the locally high  $Z_{eff}$  in the hot core of MST. It is a

well documented result that  $Z_{eff}$  in tokamaks is inversely proportional to average electron density. The standard explanation is that the overall impurity density is relatively constant over plasma conditions, but at high electron density the importance of the impurities decreases. At the extreme low density range of Tore Supra, which incidentally is the same density used in MST for this work, the mean value of  $Z_{eff}$  deduced through bremsstrahlung measurements is above six[3].

One piece of supportive circumstantial evidence (shown in Figure 4.7) is gathered from the measured hard x-ray flux (in the 10-100 keV range) with an array of CdTe detectors.

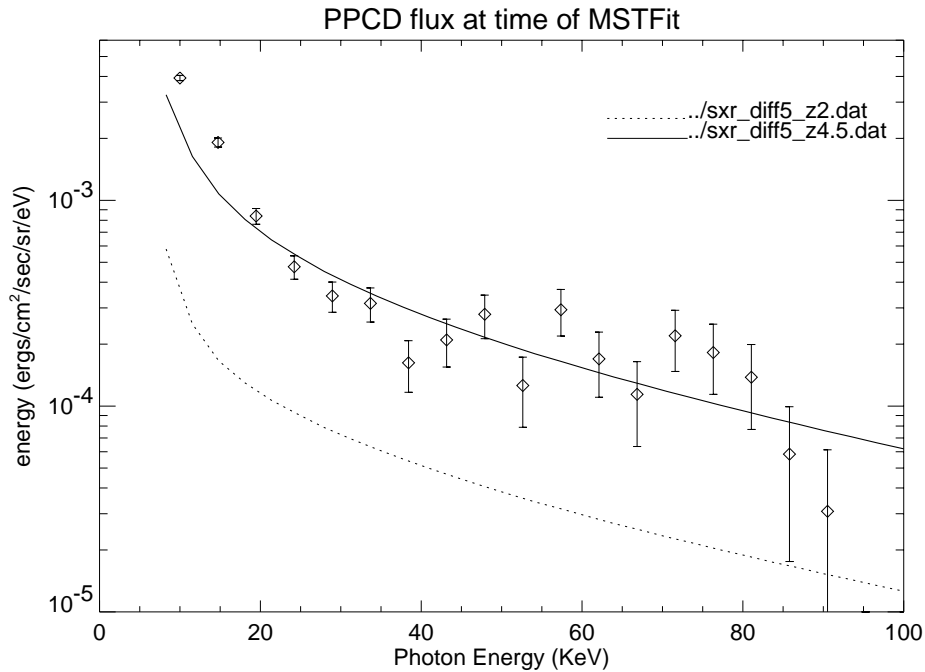


Figure 4.7: Simulations of the hard x-ray flux agree with the data for the measured  $Z_{eff}$  profile. Shown with error bars are the hard x-ray data, the solid line is the simulated flux for the measured  $Z_{eff}$  profile. For comparison's sake, an assumed  $Z_{eff} = 2.0$  (dotted line) profile leads to a much lower predicted flux. Figure courtesy of R. O'Connell, R.W. Harvey, and C.B. Forest

In the discharges studied here (400kA PPCD), there is a significant flux measured due to fast electrons interacting with (predominantly) high  $Z$  impurities. Full modeling of the electron distribution with the CQL3D[4] Fokker Planck calculation grossly (more than an order of magnitude) underestimates the measured flux when assuming a flat  $Z_{eff} = 2.0$  profile. The predicted flux well

matches the data when the measured  $Z_{eff}$  profile is used[5].

These studies are preliminary and are awaiting further spectroscopic data, perhaps in the soft x-ray range, to better constrain the distribution function. However the predicted flux discrepancy is explained by a high core  $Z_{eff}$  value. It is conceivable that  $Z_{eff}$  is five in the core; the evidence against it is quite limited.

#### 4.2.1 Impurity Density Measurements

In low current standard discharges, global power balance indicates that a volume averaged  $Z_{eff}$  is in the ballpark of two[6]. This result is consistent with Lanier's work in estimating impurity charge state densities with the ROSS filtered spectrometer and limited collisional radiative modeling. Unfortunately, a direct comparison with the NIR bremsstrahlung results cannot be made. The bremsstrahlung measurement is unapproachable in those plasma conditions ( $I_p \sim 200\text{kA}$ ,  $n_e \sim 5 \times 10^{12}\text{cm}^{-3}$ ) while the charge state density estimates fail in PPCD discharges, as a steady state assumption cannot be made.

Lanier's results actually indicate a significant  $Z_{eff}$  increase from standard to PPCD plasmas, as emission from high charge state impurities increases dramatically; none more profound than a factor of 30 increase in Al XII emission. Due to changes in neutral density, electron density and electron temperature, the density of  $\text{Al}^{+11}$  does not increase by the same factor, but the increase is certainly substantial.

#### 4.2.2 Rutherford Scattering

An innovative upper bound on  $Z_{eff}$  is being developed by Fiksel and Reardon using the Rutherford scattering diagnostic[7]. Rutherford scattering is used to measure the majority ion temperature in MST by shooting a beam of neutral helium through the plasma. The neutrals undergo an interaction with a background ion, typically the majority ion, and then head down a slightly

different path. A small differential cross section is viewed by a neutral particle analyzer which measures the energy spectrum of the neutrals scattered into the subtended solid angle. The spread in energy contains information about the background ion temperature. If there are a few heavy ions around, there will be a different energy spectrum, as the heavy ions don't recoil and the scattered alphas are nearly at the beam energy. This should be measured as a bump at the beam energy in the neutral particle analyzer, but is not observed. The lack of the measured bump is evidence that the fraction of heavy impurity ions is small. Unfortunately, this argument is currently far from a definitive  $Z_{eff}$  diagnostic. The appropriate cross sections for aluminum have not been calculated, and there are complications with other atomic processes and even some quantum mechanical effects. Even in the limit of no other atomic interactions, to accurately deduce an upper bound on  $Z_{eff}$  requires collisional radiative modeling.

### 4.2.3 Radiated Power

Total radiated power cannot be used to rule out the possibility of a high core  $Z_{eff}$ . A brief summary of the argument is presented here. Consider the total power emitted due to bremsstrahlung, found by integrating equation 3.13 over all wavelength and volume. Although bremsstrahlung emission at a given wavelength is proportional to  $T_e^{-1/2}$ , the integrated power over all wavelengths is proportional to  $T_e^{1/2}$  as

$$P = \int dV \int_0^\infty d\lambda \epsilon(\lambda, r) = \frac{4\pi}{hc} 1.516 \times 10^{-30} \int dV n_e^2 \bar{g}_{ff} Z_{eff} \sqrt{T_e} \quad (4.5)$$

which sums to 1.6kW for a flat  $Z_{eff} = 2.0$  and the measured density and temperature profiles. As the volume element is much smaller near the core, the emission for the  $Z_{eff}$  profile in Figure 4.6 increases only to 2.6kW. This difference is not resolvable within diagnostic limitations. Figure 4.8 shows a typical plot of the radiated power during these PPCD discharges. The power drops during PPCD ( $t = 13-20$ ms), but as these diagnostics typically measure on the order of megawatts,

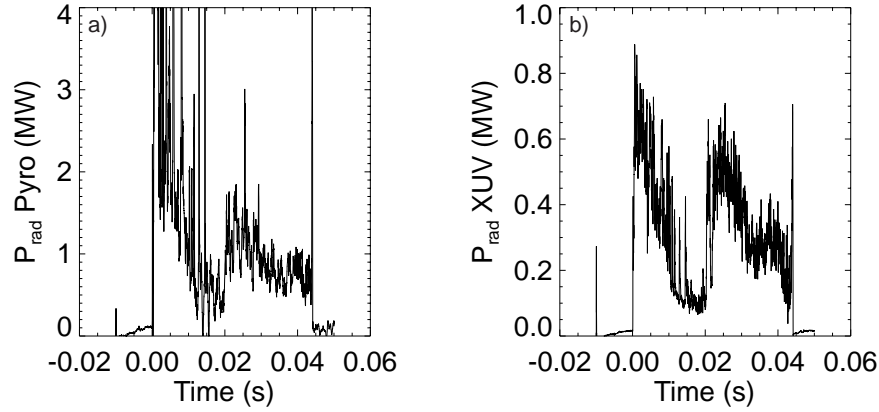


Figure 4.8: The total radiated power drops dramatically with the onset of PPCD (13 - 20ms). This is largely explained by the decrease in neutral hydrogen. Two independent measures of the radiated power (pyrobolometer and XUV diode) show a power during PPCD that cannot be used to rule out the high measured  $Z_{eff}$ .

resolving between 1.6 and 2.6 kW is inconceivable.

In order to explain a  $Z_{eff} = 5$  in the core, there must be a significant density of high-Z impurities. For example, a modest impurity concentration of He, C, O, and N which would lead to a  $Z_{eff} \sim 1.5$  requires a He-like aluminum density of about 3% to account for  $Z_{eff} = 5$ . High Z impurities radiate more than just through bremsstrahlung; line radiation and recombination are two possible alternative mechanisms. A calculation based on the total cooling rate of aluminum[8] shows the total radiation from a 3% Al XII concentration in the MST core is about 6kW[9]. While higher than the pure expected bremsstrahlung emission, this is still much lower than the typical power measured (order MW) with this diagnostic. There is a dramatic shift in the spectrum between standard and PPCD discharges, which brings into question the calibration of the diagnostic. It is impossible to definitively rule out this impurity concentration by the total radiated power.

### 4.3 Resistivity Models

In 1953, Spitzer and Härm[10] made the first correction to the plasma resistivity in equation 1.14 by including the effect of electron-electron collisions. These collisions are not directly responsible for momentum loss, but do change the electron distribution function. The result is a decrease in resistivity

$$\eta_{Sp} = \frac{Z_{eff} e^2 \ln \Lambda}{4\pi \epsilon_0^2 m_e v^3} \times F(Z_{eff}) \quad (4.6)$$

where  $F(Z)$  is well described by

$$F(Z) \simeq \frac{1 + 1.198Z + 0.222Z^2}{1 + 2.966Z + 0.753Z^2} \quad (4.7)$$

and varies between .513 at  $Z = 1$  down to  $\sim .295$  as  $Z \rightarrow \infty$ . The Spitzer resistivity is a very important result, and is predicted for a near-Maxwellian unmagnetized plasma or for a plasma embedded in a uniform magnetic field[11].

Neoclassical corrections[12, 13] take into account the effects of trapped particles arising from poloidally non-uniform field strength in an axisymmetric toroidal geometry. A charged particle moving along a field line is subject to the conservation of kinetic energy and conservation of magnetic moment

$$\begin{aligned} \frac{1}{2} m v_{\parallel}^2 + \frac{1}{2} m v_{\perp}^2 &= W = \text{Constant} \\ \frac{m v_{\perp}^2}{2B} &= \frac{W_{\perp}}{B} = \text{Constant}. \end{aligned} \quad (4.8)$$

This implies that the parallel velocity of the particle will vary as it moves into regions of different field strength. This behavior can be examined mathematically by writing the perpendicular kinetic

energy in terms of the magnetic moment

$$\frac{1}{2}mv_{\parallel}^2 = W - \mu B \quad (4.9)$$

and it is evident that if a particle with sufficiently low kinetic energy moves into a region of stronger field, the parallel velocity becomes zero and it is reflected back to the low field region. A sizable variation of  $|B|$  along a field line can lead to a significant fraction of the particles being trapped. The particle trapping enhances the electrical resistivity as noted by Hirshman and Sigmar[12] in their neoclassical transport review paper. The resulting conductivity (reciprocal of resistivity) reported for all collisionality regimes and values of  $Z_{eff}$  is

$$\sigma = \sigma_{Sp} \times \left[ 1 - \frac{f_t}{1 + \xi(Z_{eff})\nu_{*e}} \right] \times \left[ 1 - \frac{C_R(Z_{eff})f_t}{1 + \xi(Z_{eff})\nu_{*e}} \right] \quad (4.10)$$

where  $f_t$  is the trapped fraction,  $\nu_{*e}$  is the rate of collisional detrapping and  $C_R$  and  $\xi$  are further corrections discussed below.

The calculation of the trapped particle fraction follows the development in Hirshman and Sigmar[12]. The circulating fraction is

$$f_c = \frac{3}{4} \langle B^2 \rangle \int_0^{\lambda_c} \frac{\lambda d\lambda}{\sqrt{1 - \lambda B}} \quad (4.11)$$

where  $\lambda$  is the pitch angle, defined by the ratio of magnetic moment to total kinetic energy  $\lambda = \frac{\mu}{E}$ . The critical value occurs when the pitch angle lies on the boundary of the loss cone,  $\lambda_c = \frac{1}{B_{max}}$  where  $B_{max}$  is the largest field strength along the flux surface. This implies

$$\begin{aligned} \text{circulating: } & 0 \leq \lambda \leq \lambda_c \\ \text{trapped: } & \lambda_c \leq \lambda \leq \frac{1}{B_{min}}. \end{aligned} \quad (4.12)$$

The integration in equation 4.11 is over the pitch angles that lead to circulating particles resulting in the fraction circulating, and the trapped fraction is simply  $f_t = 1 - f_c$ .

In this estimation of the neoclassical effects,  $\nu_{*e}$  is estimated from simple bounce time arguments

$$\nu_{*e} = \frac{2\pi\rho|B|}{\epsilon^{3/2}\lambda_e B_\theta} \quad (4.13)$$

where  $\epsilon = \frac{I_t^2 \pi^2}{8}$  and  $\lambda_e$  is the electron mean free path; the derivation of this outlined in Appendix B.

Collisional detrapping tends to reduce the neoclassical corrections, as a high frequency  $\nu_{*e}$  negates the trapped particle effects in equation 4.10. According to Hirshman and Sigmar, the presence of impurities affects the parallel neoclassical resistivity in two ways, both resulting from enhanced electron collisionality from impurities. This decreases the trapped particle effects both by increasing the effective electron collisionality (the  $\xi$  term in equation 4.10) and by decreasing the friction between the current carrying electrons and trapped electrons with respect to the friction between electrons and ions (the  $C_R$  term in equation 4.10)[12].  $C_R$  and  $\xi$

$$C_R(Z_{eff}) = \frac{0.56(3.0 - Z_{eff})}{Z_{eff}(3.0 + Z_{eff})} \quad (4.14)$$

$$\xi(Z_{eff}) = 0.58 + 0.20Z_{eff} \quad (4.15)$$

are weakly varying functions of  $Z_{eff}$ .

In MST, neoclassical corrections have a significant effect. The trapped particle fraction for the 400kA PPCD discharge considered here is plotted in Figure 4.9 and exceeds 50% in the mid-radius region leading to a significant expected neoclassical effect.

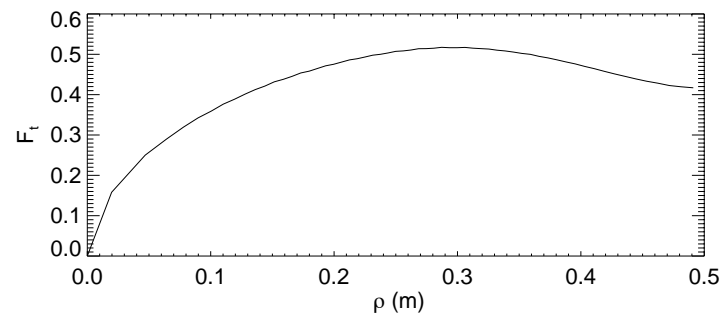


Figure 4.9: Trapped particle fraction in MST, 400kA PPCD discharge.

## 4.4 Modeled Resistivity Profile

The primary result of this labor is shown in Figure 4.10 where resistivity profiles computed from the Spitzer and neoclassical models are shown based on the measured electron temperature and  $Z_{eff}$  profiles. Three sets of lines are plotted based on  $Z_{eff}$  assumptions; in each case the higher line represents the neoclassical model while the lower is the Spitzer model. Upper dotted lines are

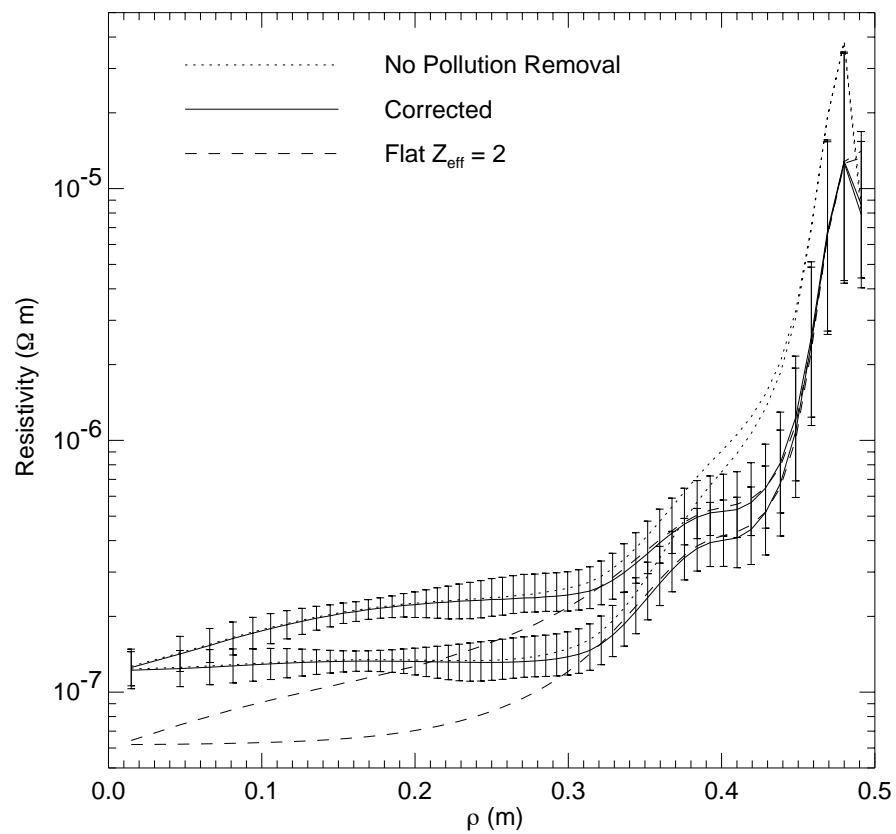


Figure 4.10: Spitzer and neoclassical resistivity profiles based on measured  $T_e$  and measured and hypothesized  $Z_{eff}$  profiles. In each of the three sets of lines, the higher resistivity corresponds to the neoclassical model, while the lower line is the Spitzer model.

non-corrected  $Z_{eff}$  profiles, where the edge values become quite large. Shown with error bars are

the calculated resistivities based on the  $Z_{eff}$  profile with edge pollutant correction. Finally, the lower dashed lines are the calculated resistivity profiles based on the canonical  $Z_{eff} = 2$  profiles. This plot will be seen again in Chapter 7, where a comparison is made between these profiles and a resistivity profile based on a simple Ohm's law and modeled current density and inductive electric field profiles.

## 4.5 Summary

Faint signatures of bremsstrahlung emission have been analyzed to measure  $Z_{eff}$  in an extremely limited region of MST operating parameters. Considerable effort to isolate and account for other radiative processes, which is evidently successful on central viewing chords, is not sufficient on edge viewing chords. A tiny pollutant emission from low charge state lines or continuum prevents a meaningful extraction of  $Z_{eff}$  in the extremely low density region there.

The inverted emissivity profile is well behaved, and with an ad hoc correction for edge pollution an estimate of  $Z_{eff}$  and the plasma resistivity are made. The correction does not affect the results obtained for the plasma core and mid-radius region.

# Bibliography

- [1] M. T. Fall, *Mesure de la Charge Moyenne Ionique, par le Rayonnement Bremsstrahlung dans le Visible, Sur Tore Supra*, PhD thesis, L'Universite Paris xi Orsay, 1991.
- [2] D. Whyte, Private communication.
- [3] S. Boeddeker,  $Z_{eff}$  in Tore Supra, 1998, Private communication.
- [4] O. Sauter, R. W. Harvey, and F. L. Hinton, *Contributions to Plasma Physics* **34**, 169 (1994).
- [5] R. O'Connell, Private communication.
- [6] B. Chapman, Private communication.
- [7] G. Fiksel and Jim Reardon, Private communication.
- [8] D. E. Post and R. V. Jensen, *Atomic Data and Nuclear Tables* **20**, 397 (1977).
- [9] J. Goetz, Private communication.
- [10] L. Spitzer Jr., *Physics of Fully Ionized Gases*, Interscience Publishers, John Wiley and Sons, New York, New York, 1962.
- [11] M. C. Zarnstorff, K. McGuire, M. G. Bell, B. Grek, D. Johnson, D. McCune, H. Park, A. Ramsey, and G. Taylor, *Physics of Fluids B* **2**, 1852 (1990).
- [12] S. P. Hirshman and D. J. Sigmar, *Nuclear Fusion* **21**, 1079 (1981).
- [13] F. L. Hinton and R. D. Hazeltine, *Reviews of Modern Physics* **48**, 239 (1976).

## Chapter 5

# Reconstruction of the RFP Equilibrium: MSTFit

### Abstract

This chapter is a description of the MSTFit equilibrium reconstruction code: a new nonlinear, fixed boundary Grad Shafranov solver for fitting RFP equilibria. Included are discussions of the numerical minimization technique, the fixed boundary Green's table method for computing poloidal flux, and the complete set of diagnostics and the methods used to fit the data from each. Techniques of inverting line integrated signals are described; also included is the method of uncertainty analysis of the fit. Sample fits demonstrate the versatility of the code, and the equilibrium reconstruction with full uncertainty analysis applied to the 400kA PPCD discharge studied in this thesis conclude the chapter.

## 5.1 Introduction

A new toroidally symmetric equilibrium fitting code, MSTFit, has been developed for the Madison Symmetric Torus (MST) reversed-field pinch. MSTFit fits a solution of the Grad Shafranov equation<sup>1</sup>

$$J_\phi = \frac{2\pi FF'}{\mu_0 R} + 2\pi Rp' \quad (5.1)$$

to a set of measurements. Here  $F = RB_\phi = F(\psi)$  and the pressure  $p = p(\psi)$  are functions of poloidal flux only. The solution  $\psi(R, Z)$  is found on a two dimensional grid with a constant flux fixed boundary, provided by the proximity of the conducting shell. A consistent equilibrium is found by specifying the two free functions  $F$  and  $P$ ; the code varies these profiles through a basis function expansion to find the particular solution which best fits the experimental data.

### 5.1.1 Grad Shafranov Equilibrium in an Axisymmetric Torus

The full magnetohydrodynamic equilibrium of a plasma is determined by the integration of Ampere's Law and radial force balance into the Grad-Shafranov equation. MSTFit is a solution to this equation for a circular cross section toroidal device, using the standard cylindrical coordinates shown in Figure 5.1. Axisymmetry implies that  $\frac{\partial}{\partial \phi}$  vanishes, and the absence of divergence of the magnetic field implies

$$\nabla \cdot \mathbf{B} = 0 \implies \frac{1}{R} \frac{\partial}{\partial R} (RB_R) + \frac{\partial}{\partial Z} B_Z = 0. \quad (5.2)$$

---

<sup>1</sup>This form of the equation is equivalent to those in the references and proves demonstrative in description of the code.



The poloidal field (and hence flux,  $\psi$ ) are produced by toroidally flowing currents

$$\mu_0 J_\phi = -\frac{R}{2\pi} \nabla \cdot \left( \frac{\nabla \psi}{R^2} \right) \quad (5.6)$$

by inspection of equation 5.5.

Radial force balance  $\mathbf{J} \times \mathbf{B} = \nabla P$  is used to express the pressure gradient in terms of  $\psi$  and  $\phi$

$$\mathbf{J} \times \mathbf{B} = \left( R J_\phi \nabla \phi + \frac{1}{\mu_0} \nabla F \times \nabla \phi \right) \times \left( F \nabla \phi + \frac{1}{2\pi} \nabla \psi \times \nabla \phi \right) = \nabla P. \quad (5.7)$$

Both  $F$  and  $P$  are assumed functions of poloidal flux only allowing their gradients to be written in terms of  $\psi$  using the chain rule  $\nabla = \nabla \psi \frac{\partial}{\partial \psi}$  in equation 5.7

$$\left( R J_\phi \nabla \phi + \frac{1}{\mu_0} F' \frac{1}{2\pi} \nabla \psi \times \nabla \phi \right) \times (F \nabla \phi + \nabla \psi \times \nabla \phi) = P' \nabla \psi \quad (5.8)$$

where  $'$  denotes  $\frac{\partial}{\partial \psi}$ .

The first term in the expression for  $\mathbf{J}$  and the first term in the expression for  $\mathbf{B}$  are both parallel to  $\hat{\phi}$ , and the second term in each is parallel to  $\nabla \psi \times \nabla \phi$ , so the nonzero terms in the cross product are

$$\begin{aligned} R J_\phi \left( \nabla \phi \times \frac{1}{2\pi} \nabla \psi \times \nabla \phi \right) - \frac{F}{\mu_0} F' (\nabla \phi \times \nabla \psi \times \nabla \phi) &= P' \nabla \psi \\ \left( \frac{R J_\phi}{2\pi} - \frac{F F'}{\mu_0} \right) \frac{\nabla \psi}{R^2} &= P' \nabla \psi \end{aligned} \quad (5.9)$$

This, when simplified, is the Grad-Shafranov equation, written below in the notation employed in MSTFit

$$J_\phi = \frac{2\pi F F'}{\mu_0 R} + 2\pi R P'. \quad (5.10)$$

The two free functions  $F$  and  $P$  specify a consistent equilibrium, fitting the data results in a particular set of  $F$  and  $P$  profiles. Once  $J_\phi$  is specified, a consistent solution to Maxwell's equations is found and all other profiles specific to the equilibrium are determined. The toroidal current density determines the poloidal magnetic field through Ampere's law or by writing the  $\hat{\phi}$  component of the vector potential in terms of  $J_\phi$ . Of particular interest are the parallel current density and  $\lambda$  profiles

$$J_{\parallel} = \frac{\mathbf{J} \cdot \mathbf{B}}{|\mathbf{B}|} \quad (5.11)$$

$$\lambda = \frac{\mu_0 a J_{\parallel}}{|B|} = \mu_0 a \frac{\mathbf{J} \cdot \mathbf{B}}{B^2}. \quad (5.12)$$

Continuing with the development of  $\mathbf{J}$  and  $\mathbf{B}$ , the scalar product can be computed

$$\begin{aligned} \mathbf{J} \cdot \mathbf{B} &= \left( R J_\phi \nabla \phi + \frac{1}{\mu_0} F' \nabla \psi \times \nabla \phi \right) \cdot \left( F \nabla \phi + \frac{1}{2\pi} \nabla \psi \times \nabla \phi \right) \\ &= J_\phi \frac{F}{R} + \frac{1}{2\pi \mu_0 R^2} F' |\nabla \psi|^2 \end{aligned} \quad (5.13)$$

as argued above the first term in the expression for  $\mathbf{J}$  is parallel to the first term in  $\mathbf{B}$ , and the second terms are also parallel. Upon substitution of  $J_\phi$  from equation 5.10

$$\begin{aligned} \mathbf{J} \cdot \mathbf{B} &= \frac{2\pi F^2 F'}{\mu_0 R^2} + 2\pi F P' + \frac{1}{2\pi \mu_0 R^2} F' |\nabla \psi|^2 \\ &= \frac{2\pi F'}{\mu_0} \left[ \left( \frac{F}{R} \right)^2 + \left( \frac{\nabla \psi}{2\pi R} \right)^2 \right] + F P' \\ &= \frac{2\pi F'}{\mu_0} [B_\phi^2 + |\mathbf{B}_p|^2] + 2\pi F P' \\ &= 2\pi \frac{F' B^2}{\mu_0} + 2\pi F P' \end{aligned} \quad (5.14)$$

resulting in

$$J_{\parallel} = 2\pi \frac{F' B^2 + F P'}{\mu_0 |B|} \quad (5.15)$$

$$\lambda = 2\pi a F' + \frac{2\pi \mu_0 a F P'}{B^2}. \quad (5.16)$$

Poloidal current plays a strong role in determining the RFP equilibrium, it is calculated from the difference of parallel and toroidal components

$$\begin{aligned} J_{\theta} &= \frac{\mathbf{J} \cdot \mathbf{B} - J_{\phi} B_{\phi}}{B_{\theta}} \\ &= \frac{\left(2\pi \frac{F' B^2}{\mu_0} + 2\pi F P'\right) - \left(2\pi \frac{F F'}{\mu_0 R} + 2\pi R P'\right) B_{\phi}}{|B_{\theta}|} \\ &= \frac{2\pi}{\mu_0 |B_{\theta}|} (F' B^2 - F' B_{\phi}^2) \\ &= \frac{2\pi}{\mu_0} F' B_{\theta} \end{aligned} \quad (5.17)$$

and is strongly related to the free function  $F'$ . Flux surface averages, defined as

$$\langle A \rangle \equiv \frac{\oint \frac{A dl}{B_{\theta}}}{\oint \frac{dl}{B_{\theta}}} \quad (5.18)$$

for a general quantity,  $A$ , are computed for  $J_{\parallel}$ ,  $\lambda$ , and the safety factor  $q(\psi) = \left\langle \frac{r B_{\phi}}{R B_{\theta}} \right\rangle$  so the equilibrium can be described in a one dimensional sense. The procedure used by the code to compute the averages is described in Section 5.5.1. The effective minor radius used as the 1D ordinate is defined through the volume of a given flux surface as

$$\rho_v = \sqrt{\frac{V_{\psi}}{2\pi^2 R}}. \quad (5.19)$$

### 5.1.2 Reconstructing the RFP Equilibrium

The goal of the equilibrium reconstruction is quite simple. A rather involved calculation determines the axisymmetric solution of Maxwell's equations (applicable in a torus) which satisfies radial force balance  $\mathbf{J} \times \mathbf{B} = \nabla P$  and best fits all the available data.

This general approach is not limited in its ability to accurately predict experimental signals, and is extensible to many free parameters with nearly arbitrary profiles of  $\lambda$  and pressure. The accuracy of the solution is ultimately limited by the data used to constrain the fit.

In the RFP, the pressure gradient contribution to the equilibrium is quite small and thus determination of the  $F'$  profile nearly specifies the equilibrium. The RFP equilibrium is unlike that of the tokamak or stellerator, where equilibrium reconstructions have previously been done. The toroidal field in the central region is largely generated by poloidal current flowing in the plasma edge as opposed to external toroidal field magnets. In MST, the poloidal magnetic field is completely generated by toroidal plasma (and induced vessel) currents. This presents new challenges to the reconstruction process. Furthermore, as the pressure contribution is small, radial force balance implies that the majority of the current in the plasma flows parallel to the magnetic field. This implies that the vast majority of toroidal current flows in the core region of  $r/a < 0.5$ . This has implications on the fitting of edge data, as the poloidal magnetic field behavior is nearly vacuum-like outside of this region.

For the RFP, the majority of the equilibrium information lies in the  $F'$  profile. As  $F = RB_\phi$ , integration of  $F'$  gives the toroidal field strength, and in the limit of zero pressure,  $F F'$  completely specifies the toroidal current density in the plasma. Equation 5.17 shows the poloidal current is also specified by  $F'$ ; the  $\lambda$  profile reduces to  $F'$  in the zero pressure limit. The pressure profile is well constrained by kinetic data, so the burden of equilibrium reconstruction rests on using the magnetic data to constrain  $F'$ .  $F$  itself is directly constrained by measurements of the toroidal flux, the toroidal field at the wall, and the measurement of  $|B|$  on axis. These data set the overall

scale for the gradient of  $F$ , but subtle profile changes are not constrained by these data. Constraint of  $F'(0)$ , along with the overall scale set by measurements of  $F$  nearly constrain the equilibrium.

A combination of the on-axis toroidal current density and toroidal field; or a measurement of the on-axis safety factor helps constrain  $F'(0)$  as these quantities are all related. The on-axis safety factor is

$$q(0) = \frac{2B_\phi(0)}{\mu_0 R J_\phi(0)} = \frac{2a}{R\lambda(0)} = \frac{1}{\pi R F'(0)} \quad (5.20)$$

where it assumed the pressure gradient vanishes at the core in the last step. A constraint on  $J_\phi(0)$  is available through the polarimeter, and an estimate of  $q(0)$  is available through MHD activity. Thus, by adding either the polarimeter or  $q(0)$  information to the MSE and edge data, the the  $F'$  profile is well constrained in the core.

Edge  $F'$  information completes the picture. This is obtained in MSTFit by the HIBP constraint to the equilibrium, which provides information on the line integrated magnetic field through the edge to mid-radius region. Although the  $F'$  information is extremely convoluted, the nonlinear fitting technique of MSTFit is able to utilize the data to help constrain the equilibrium.

The details of MSTFit and the fitting of each diagnostic's data are described in detail below. The code uses a basis function expansion of the  $F'$  profile (Section 5.1.3) in fitting the data to find the best suited equilibrium. The  $F$  and  $FF'$  profiles are found through integration, and the pressure profile is set by kinetic measurements. The close fitting aluminum vessel is treated as a perfect conductor and hence it is a flux surface.

### 5.1.3 Free Parameters

#### $F'$ Free Parameters and Basis Functions

To solve the Grad-Shafranov equation, the toroidal current density contributions from both the  $FF'$  and  $P'$  terms must be computed. MSTFit uses a basis function expansion for  $F'$  (M basis

functions under the constraint of  $F'(1) = 0$ .)

$$F'(\hat{\psi}) = \sum_{i=1}^{M-1} a_i f_i(\hat{\psi}) \quad (5.21)$$

where  $\hat{\psi}$  is the normalized poloidal flux

$$\hat{\psi}(R, Z) = \frac{\psi(R, Z) - \psi_0}{\psi_{lim} - \psi_0} \quad (5.22)$$

$\psi_0$  is the poloidal flux at the magnetic axis (the minimum of the poloidal flux on the grid), and  $\psi_{lim}$  is the value of the poloidal flux on the last closed flux surface, which typically intersects the limiter on the outboard midplane. The normalized flux ranges from zero at the magnetic axis to one at the limiting surface.

The contribution to current,  $FF'$ , is found by integrating  $F'$  from the edge inward. This determines  $F$  to within a constant (the value at the wall), whose value is determined by measurements.

The basis functions used to fit  $F'$  are equivalent to a spline interpolation through  $M$  ordered pairs under the constraint that  $F'$  (and hence toroidal current) goes to zero at the boundary. The number of ordered pairs (hereafter referred to as knots, with 'knot location' corresponding to the ordinate and 'knot value' to the function value of the ordered pair) is determined by user input and is ultimately limited by the amount of data used to constrain the equilibrium.

For a specified set of  $M$  knot locations, there are  $M - 1$  free parameters corresponding to the knot values, with the boundary value of  $F'(1) \rightarrow 0$  removing one free parameter. Figure 5.2 a) illustrates the basis functions for  $M = 4$  knot locations. The actual basis functions are generated through cubic spline interpolation. For the  $j^{th}$  basis function, the  $M$  specified knot locations correspond to the  $x$  values, and  $y$  values are the standard  $j^{th}$  unit vector in  $M$  dimensions. For example, the third basis function in a four knot fit would be the cubic spline interpolation through  $x = [x_1, x_2, x_3, x_4]$  and  $y = [0, 0, 1, 0]$ . Although these basis functions are neither orthogonal

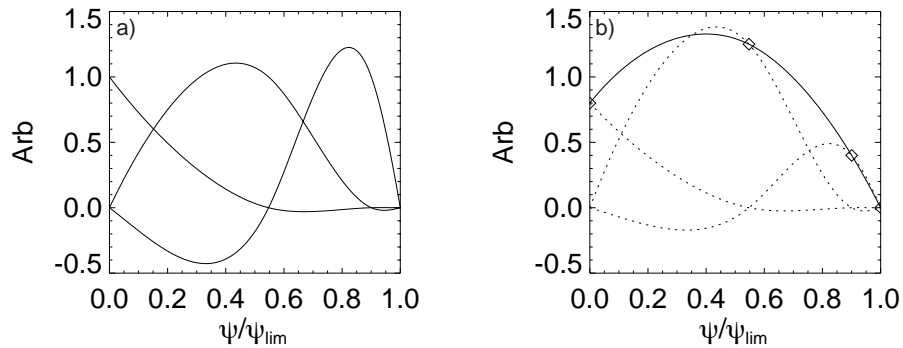


Figure 5.2: a) is a plot of the first, second and third basis function for a 4 knot fit. b) is the reconstruction of a generic profile from these functions. The points indicated as  $\diamond$  on the plot are set as knots. The dotted lines are the contributions from the individual basis functions, and the solid line is the sum of these three. Cubic spline interpolation through the knots reproduces the solid line exactly.

nor normalized, they are linear so that standard basis function expansion is (equation 5.21) used to reproduce a specific profile where the set  $\mathbf{a}$  of free parameters values determines the profile. Figure 5.2 b) demonstrates the equivalence of these basis functions with cubic spline interpolation. The solid line is the cubic spline interpolation drawn through the four example knots (indicated by  $\diamond$  on the plot). The knot values are multiplied by the basis functions, and the scaled basis functions are included as dotted lines. The sum of the three contributions exactly reproduces the solid line.

MSTFit has added more flexibility to this basis function development by allowing the interior knot locations to vary as free parameters in the fit. In this sense, the minimization search actually alters the basis functions used, leading to the designation 'dynamic' basis functions.

In practice, MSTFit does not compute the individual basis functions owing to the nonlinear minimization technique. Each time a call is made to the routine to determine the  $F'$  current density, all the free parameters are specified and the spline interpolation is done directly. This also makes it possible to use tension splines for interpolations; the standard basis function technique cannot allow spline tension as it removes the linearity of the splined basis functions.

### Knot Location Free Parameters

The model specification input file to MSTFit allows the user to select the number of knots for  $F'$  and whether the knot locations are free or fixed. For  $M$  fixed knots, there are  $M - 1$  free parameters in the fit, allowing the knot locations to vary increases the number of free parameters to  $2M - 3$ .

The free parameters here vary over a finite range, particularly true for knot location free parameters which are limited to the open interval  $(0,1)$ . When two or more knot locations are free to vary, they are not allowed to interchange positions, which imposes a further constraint. It is beneficial to allow the minimization routine to search all space, which is realized by mapping the free parameters from the search space of  $(-\infty, \infty)$  to a real space  $(0,1)$ . This mapping procedure is illustrated in Figure 5.3. The knot positions in real space, at  $[0, x_1, x_2, \dots, x_{M-1}, 1]$  are used to

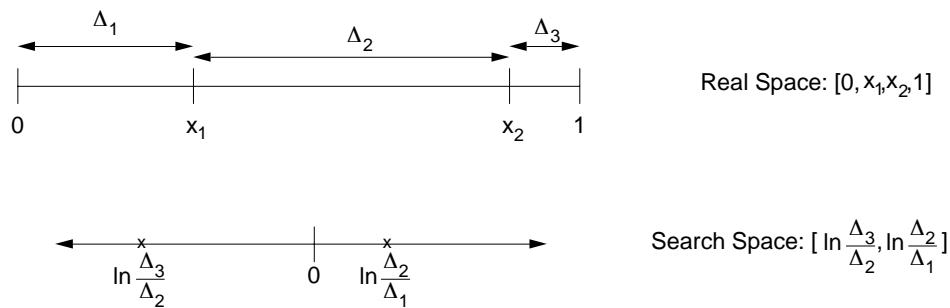


Figure 5.3: Free parameter space transform.

calculate an  $M - 1$  element interval array,  $[\Delta_0, \Delta_1, \dots, \Delta_{M-1}]$  where  $\Delta_i \equiv x_{i+1} - x_i$ . An  $M - 2$  element fractional step array is defined by  $S_f(i) = \frac{\Delta_{i+1}}{\Delta_i}$ . Defining  $\sigma = \ln(S)$  is the final step in converting to search space.

For an evenly spaced set of knot locations, all  $S_i = 1$  and all  $\sigma_i$  are 0. Any other distribution the values will cause  $S$  to deviate from 1. As two knots approach each other, the values for  $\sigma$  can become relatively large; for a set of knots with two successive knots separated by .005 in  $\hat{\psi}$ , values of  $\sigma$  can vary up to  $\sim \pm 5$ . This information is important, as a typical scale length for each free

parameter must be specified for optimized minimization. The inverse map, from search to real space, converts  $\sigma$  back into an  $M$  element knot location array.

In a similar fashion, the free parameters which specify the knot values are allowed to vary on a large interval in search space while corresponding to a physically relevant real space. The  $F'$  profile is constrained to be positive definite (an explicit factor of -1 is included when integrating to obtain  $F$  and  $FF'$ ) by using an exponential mapping,  $r = e^s$ . The search space variable is scaled such that a value of zero leads to a typical value of  $F'(0)$ . The approximate range of extremely peaked to extremely hollow  $F'$  profiles covers a range of which determines the appropriate scale length for this type of free parameter.

### **$P$ Free Parameters and Basis Functions**

MSTFit is capable of fitting the free parameters for the pressure profile in a fashion nearly identical to that described above for  $F'$  by using a similar expansion

$$P(\hat{\psi}) = \sum_{i=1}^{N-1} b_i f_i(\hat{\psi}). \quad (5.23)$$

The boundary condition of zero toroidal current at the edge requires  $P'(1) = 0$ . The difference arises in that  $F'$  is fit and  $F$  is calculated by integration; while for pressure the profile is fit and  $P'$  is computed by differentiation. This method is advantageous due to the nature of the data available for fitting pressure. Measurements of electron and ion densities and temperatures make fitting the pressure profile trivial. It is convenient to fit  $F'$  under a positive definite constraint and calculate  $F$  by integration which restricts the  $FF'$  profile from rapid sign changes and negative central current density (an unphysical condition).

Although MSTFit in general can fit the pressure profile by varying free parameters which determine the profile, this option is typically not exercised. Instead,  $P'$  is determined by profile fits to kinetic data rather than by fitting magnetic signals; mapping to the new flux geometry is

performed on each iteration. The computational benefit of reducing the number of free parameters is very significant.

## 5.2 Solution Method

MSTFit uses an up-down symmetric unstructured triangular mesh grid as shown in Figure 5.4. Each point on the grid ( $R_i, Z_i$ ) is associated with a toroidal current filament, a poloidal flux, and an area element at that location. The two dimensional plasma is represented by 1D arrays denoted  $\mathbf{I}_\phi$ ,  $\psi_p$ , etc. which is beneficial for bookkeeping within the code and allows many calculations to be represented by simple matrix multiplication. The MST plasma is surrounded by a close fitting aluminum shell which is assumed to be a surface of constant flux.

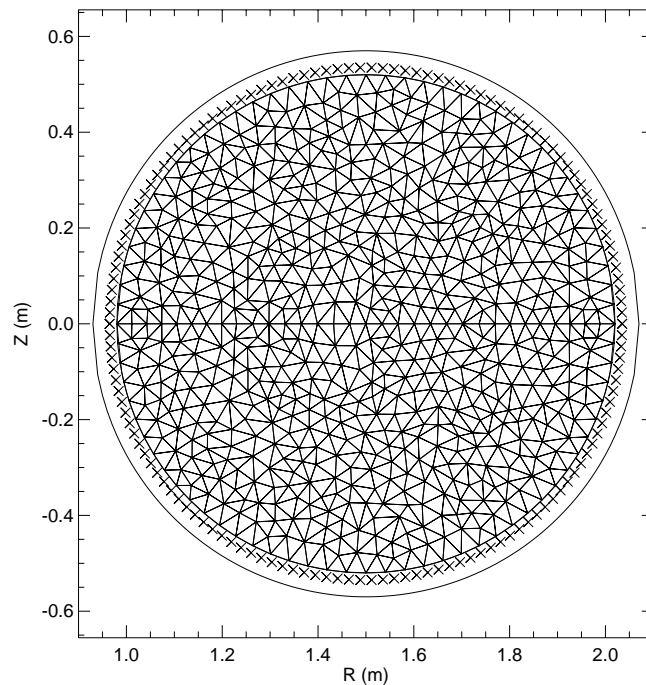


Figure 5.4: Triangular mesh grid used, plasma and vessel.

An equilibrium is determined by finding a consistent set of currents  $\mathbf{I}_\phi$  and fluxes  $\psi_p$  related by

equations 5.5 and 5.10 given profiles of  $P'$  and  $FF'$ . A nonlinear iterative routine then adjusts the profiles of  $FF'$  and  $P'$ , searching through a large number of equilibria to find the one which best matches measurements. The code follows the flow chart shown in Figure 5.5. The main points are highlighted here, each step is described in detail in the subsequent sections. First, an initial guess to the equilibrium is made using the MPFM (described above in Section 1.2.3). After initialization

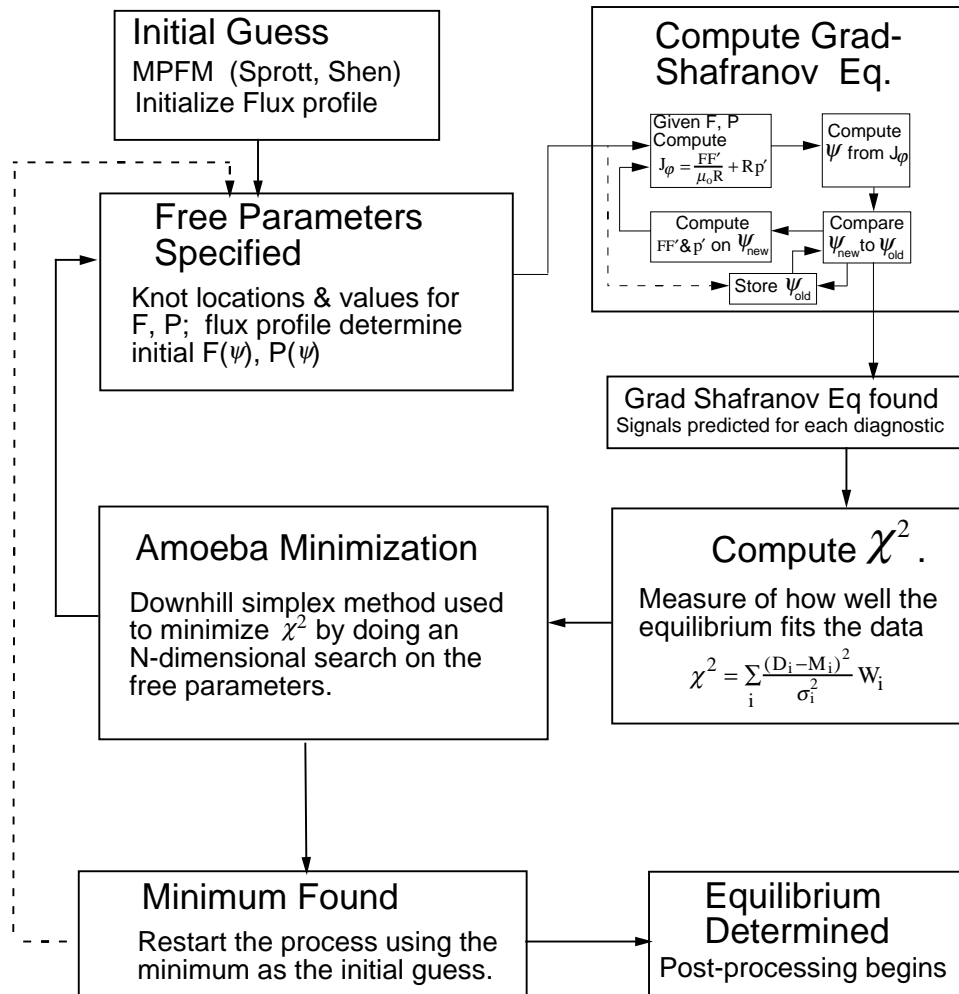


Figure 5.5: MSTFit flow chart.

of the current and magnetic field profiles, the initial values of the free parameters are determined which match the MPFM magnetic field profiles. The code then iteratively computes a consistent

Grad-Shafranov equilibrium, and evaluates it based on the agreement between the measurements and the signals predicted from the computed equilibrium. The agreement is quantified by a reduced  $\chi^2$  cost function. A multidimensional minimization (Amoeba) is then performed on  $\chi^2$  by varying all of the free parameters. Once an optimal equilibrium is found several post processing routines are performed.

### 5.2.1 Initialization

The starting point for MSTFit, like any non-linear minimization, is a guess. The current density and magnetic field profiles are initialized according to the MPFM (see Section 1.2.3). The number and type, initial values, and scale lengths of the free parameters of the fit are also determined during the initialization phase.

Shifted circular flux surfaces are mapped onto the plasma mesh (shown in Figure 5.4) to extend the cylindrical MPFM to the initial guess in the toroidal development. The poloidal flux is then normalized according to equation 5.22 and the algebraically specified MPFM profiles are mapped from their cylindrical  $r/a$  axis onto the normalized flux axis. The result is not a consistent solution to the Grad-Shafranov equation, but is sufficient to estimate a set of free parameters which describe the initial magnetic field profiles. The code typically takes a set of free parameters and converts them to specific  $F'$  and  $P$  profiles; an inverse process is used during initialization. The specified profile (for either  $F'$  or  $P$ ) determines the values of free parameters which reproduce these profiles to a suitable accuracy. With the free parameters specified, the code is initialized and the minimization process commences.

### 5.2.2 Computation of Grad Shafranov Equilibrium

Once an initial guess for the solution  $\psi(R, Z)$  has been specified and the profiles of  $F$ ,  $F'$ , and  $P$  are specified as a function of  $\hat{\psi}$ , it is a simple iterative process to arrive at a consistent Grad-

Shafranov equilibrium. A trivial application of the Grad-Shafranov equation gives  $J_\phi$  on the grid. The iterative process begins as the toroidal current on the grid is used to recalculate the poloidal flux on the grid. This process is carried out using the Green's table method described below. The result of the computation (in general) is a different poloidal flux distribution;  $F'$  and  $P$  must then be mapped onto the new spatial profiles of flux coordinate. The code continues to recompute  $J_\phi$  and  $\psi$  until the change in flux between successive steps becomes satisfactorily small, at which point a consistent combination of toroidal current and poloidal flux are found; a Grad-Shafranov equilibrium is obtained.

### Green's Table Method

Computing the poloidal flux on the grid can be a computationally burdensome process, as the poloidal flux at any given grid point depends on the toroidal current at all other points (including toroidal currents flowing in the shell) leading to more than  $N^2$  computations to determine the flux on the  $N$  point grid. The Green's table method reduces this problem to matrix multiplication, greatly reducing the computational burden. An additional benefit of this method is the elegance in which the flux-conserving aluminum shell is treated.

Equation 5.6 can be solved to find  $\psi$  from  $J_\phi$  and boundary condition using a Green's function solution. The general toroidal Green's function computes the poloidal flux at the point  $(R, Z)$  due to a unit toroidal current at  $(R', Z')$ , i.e.

$$\psi_{pol}(R, Z) = \iint_{A'} G(R', Z'; R, Z) J_\phi(R', Z') dA' \quad (5.24)$$

where

$$\frac{-R}{2\pi\mu_0} \nabla \cdot \left( \frac{\nabla G}{R^2} \right) = \delta(R - R') \delta(Z - Z'). \quad (5.25)$$

In a vacuum (no conducting shell), this is[1]

$$G(R', Z'; R, Z) = \frac{\mu_0}{\pi k} \left( \frac{R'}{R} \right)^{1/2} \left( \left( 1 - \frac{1}{2} k^2 \right) K(k) - E(k) \right) \quad (5.26)$$

with  $E(k)$  and  $K(k)$  elliptic integrals of the first kind and  $k^2 = \frac{4RR'}{(R+R')^2 + Z^2}$ . Physically, the Green's function is the amount of flux at point  $(R', Z')$  due to a unit current at  $(R, Z)$ ; this is equivalent to the mutual inductance between two toroidal coils at  $(R, Z)$  and  $(R', Z')$ .

For the one dimensional grid of  $N$  points, the source integration over  $dA'$  is replaced by a summation over the set of grid points

$$\psi_{pol}(R, Z) = \sum_j G(R'_j, Z'_j; R, Z) I_\phi(R'_j, Z'_j) \quad (5.27)$$

By defining  $\psi_{pol\ i}$  as the poloidal flux at the  $i^{th}$  grid point  $(R_i, Z_i)$ , equation 5.27 implies

$$\begin{aligned} \psi_{pol\ i} &= \sum_j G(\mathbf{R}_i, \mathbf{R}_j) \cdot I_{\phi\ j} \\ \boldsymbol{\psi}_{pol} &= \mathbf{G} \cdot \mathbf{I}_\phi \end{aligned} \quad (5.28)$$

where the  $N \times N$  matrix  $\mathbf{G}$  computes the flux at any point on the grid due to currents on the the grid. In a similar fashion, the spatial derivatives of  $G(R', Z'; R, Z)$  are tabulated which construct the components of the poloidal magnetic field,  $B_R$  and  $B_Z$ .

### Modeling of Flux Conserving Shell

The result in equation 5.28 is indeed the flux at the  $i^{th}$  grid point due to all the current filaments in the plasma grid. However, the toroidal current flowing in the close fitting conducting shell also contributes to the flux. Two options exist: one could use the free space Green's function and explicitly determine the toroidal currents in the shell, or find a Green's function which satisfies the boundary condition of constant flux on the shell, which in effect implicitly finds the necessary

shell currents. The second option is exercised here. The upper half of the shell is modeled as  $M = 72$  toroidal current filaments, and the lower half is determined by forcing up-down symmetry. Extending equation 5.28 to include the vessel contributions mandates a second term

$$\psi_{pol} = \mathbf{G}_p \cdot \mathbf{I}_\phi + \mathbf{G}_v \cdot \mathbf{I}_{ves} \quad (5.29)$$

where the subscript  $\mathbf{G}_p$  has been added to denote the plasma table. In the second term,  $\mathbf{G}_v$  is an  $N \times M$  matrix where  $G_{v\ ij}$  is the flux at the  $i^{th}$  point on the plasma grid due to the  $j^{th}$  vessel current filament. Determining the total flux then requires the values of the distributed toroidal vessel currents.

Previous work has incorporated extra free parameters for modeling vessel currents. A set of virtual fluxloop diagnostics at the conducting boundary were used to constrain the vessel currents to meet the flux conserving assumption. That work was done in a free boundary framework and used several unnecessary free parameters to describe the vessel currents. Here the fixed boundary Green's function is determined by finding the image currents in the shell that give constant flux on the vessel for each toroidal current filament

$$\mathbf{I}_{ves} = \mathbf{M} \cdot \mathbf{I}_\phi \quad (5.30)$$

via the matrix  $\mathbf{M}$ .

To compute the proper tables, and in essence convert the free boundary code to a fixed boundary code, a new Green's table  $\mathbf{G}_a$  is created with  $M_2 = 145$  field points distributed poloidally around the upper half of the conducting shell. The choice of 145 elements is somewhat arbitrary; it is necessary to use more flux points than there are current filaments in the shell to ensure a smooth

behavior between the individual filaments. The poloidal flux at the boundary is then

$$\begin{aligned}\psi_{pol}(a) &= \mathbf{G}_{ap} \cdot \mathbf{I}_\phi + \mathbf{G}_{av} \cdot \mathbf{I}_{ves} \\ &= (\mathbf{G}_{ap} + \mathbf{G}_{av} \cdot \mathbf{M}) \cdot \mathbf{I}_\phi\end{aligned}\tag{5.31}$$

where  $\mathbf{G}_{ap}$  and  $\mathbf{G}_{av}$  are the matrices that compute boundary flux due to currents in the plasma and vessel, respectively. Applying the flux conservation constraint implies that the vessel will respond in a way as to produce zero net flux due to a given current in the plasma. The specific set of vessel currents that result in zero net flux can be calculated for a unit current anywhere on the plasma grid. As the set of appropriate vessel currents is different for each current filament in the plasma grid, an  $M_2 \times N$  matrix ( $\mathbf{I}_{ves0}$ ) is defined such that the  $j^{th}$  column of the matrix is the set of vessel currents that cancel the boundary flux due to a unit current at the  $j^{th}$  plasma grid position. To determine the vessel currents that cancel the boundary flux due to the  $j^{th}$  unit current, a vector of zeroes is designated as the result of the  $j^{th}$  row in equation 5.31

$$\vec{\mathbf{0}} = (\mathbf{G}_{ap})_j + \mathbf{G}_{av} \cdot (\mathbf{I}_{ves0})_j\tag{5.32}$$

The column vector  $(\mathbf{I}_{ves0})_j$  is then determined by solving the matrix equation (or set of over-specified linear equations) 5.32, by singular value decomposition of  $\mathbf{G}_{av}$ . This procedure is repeated for all elements in the plasma grid, and a complete matrix  $\mathbf{I}_{ves0}$  is constructed. The set of flux conserving vessel currents are used to convert a Green's table from the free boundary to the fixed boundary solution as

$$\mathbf{G}_{fixed} = \mathbf{G}_p + \mathbf{G}_v \cdot \mathbf{I}_{ves0}.\tag{5.33}$$

This procedure modifies all tables that have been computed for the same plasma and vessel grids. Figure 5.6 demonstrates the high numerical accuracy to which this procedure holds. The boundary

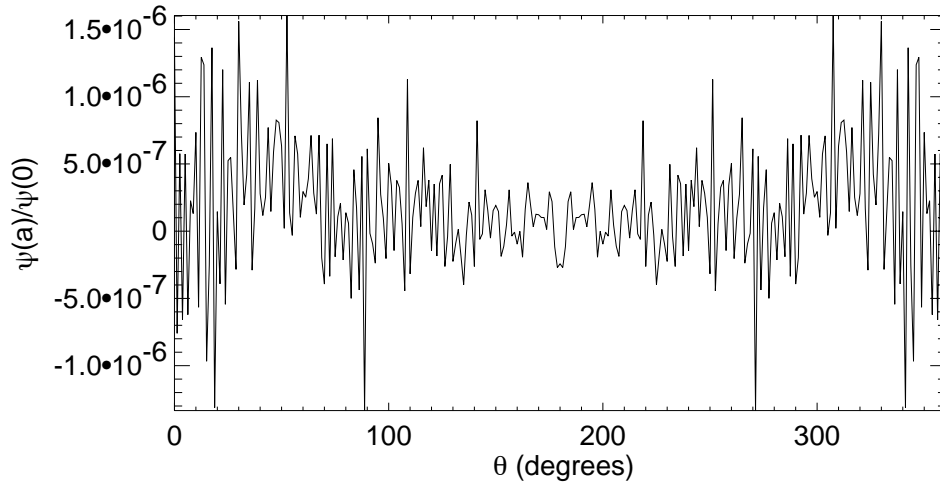


Figure 5.6: Flux on boundary (normalized to central flux) considering ideal shell. This is zero to within floating point accuracy.

flux (normalized to the central value) shows no more than a  $10^{-4}\%$  error on the grid, probably due to floating point accuracy during the matrix inversion. The corrections to the Green's functions due to the vessel current is demonstrated in Figure 5.7. Plots a) and b) use the free boundary tables for computing the flux due to unit currents. Panel a) represents a current placed outboard from the center, slightly above the midplane. Panel b) is a current placed near the inboard midplane. Clearly the flux surfaces do not match the vessel. The lower plots c), d) are the flux computed for the same two current filaments using the fixed boundary table, and the outer flux surfaces conform to the shell.

Computation of the Green's tables is computationally burdensome, often taking over an hour of CPU time on a 500MHz machine. However, these computations are computed prior to running the code, and need only be loaded into memory to run MSTFit. Thereafter, the computation of flux is a very fast matrix multiplication.

The usefulness of this method goes beyond the computation of flux on the plasma grid, as any repeated calculation of poloidal flux or magnetic field on a given set of points in space can be

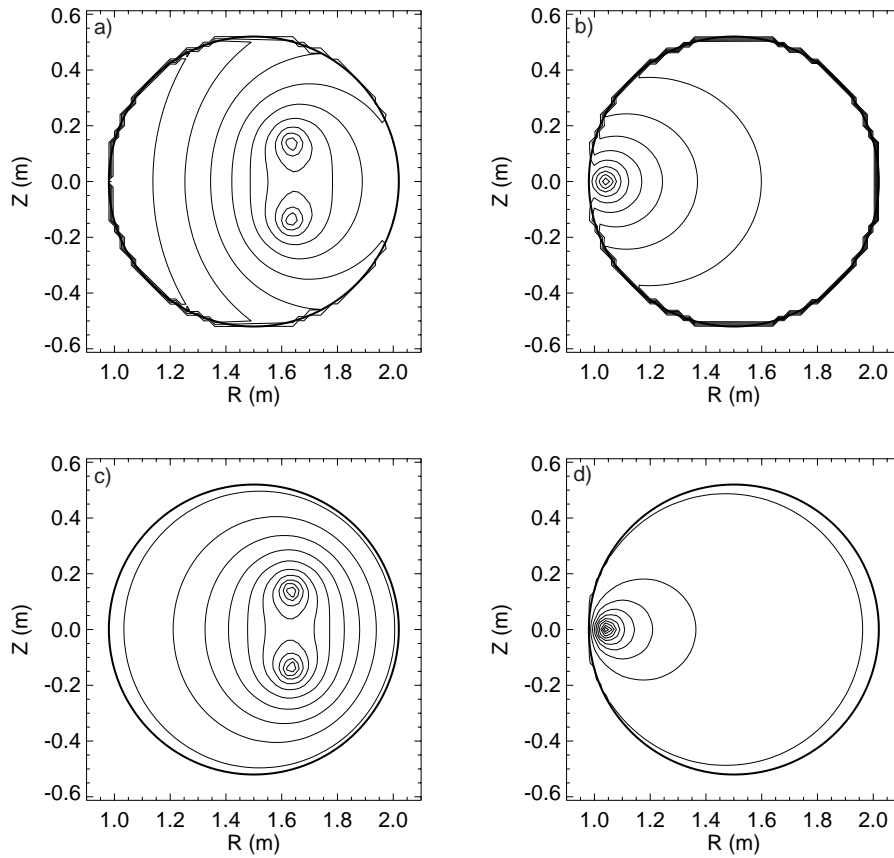


Figure 5.7: Flux due to a unit current calculated using free and fixed boundary Green's tables. a) and b) use the free boundary tables for computing the flux due to unit currents. c) and d) are the flux computed for the same two current filaments using the fixed boundary tables.

approached with a Green's table. Examples include inversions of line integrated signals and fitting magnetic data at fixed locations.

### 5.2.3 Comparison to Data

Once the Grad-Shafranov equilibrium is known, the magnetic field and all other equilibrium profiles are fully determined inside the shell. The next step in determining the fit is comparing the measured data to the signals predicted from the current iteration of the equilibrium. The method of evaluation

is computing a weighted reduced  $\chi^2$

$$\chi_\nu^2 \equiv \frac{1}{\nu} \sum_i \frac{(D_i - M_i)^2}{\sigma_i^2} W_i \quad (5.34)$$

where each datum  $D_i$  is specified with an experimental uncertainty  $\sigma_i$  and a user-supplied weighting factor  $W_i$ . Here  $\nu$  is the number of degrees of freedom, equal to the number of independent data being fit minus the number of free parameters in the model. From the equilibrium profiles, a predicted signal  $M_i$  is made for each measurement. The exact method for computing the predicted signal is different for each diagnostic and varies considerably in complexity. The diagnostics currently in use will be considered individually in detail in Section 5.4; here it suffices to assert that from a specified equilibrium, signals can be predicted for all diagnostics and a cost function is evaluated. Minimization of the cost function is done with the downhill simplex method described below.

### 5.2.4 Minimization

The problem has been reduced to finding the equilibrium which minimizes  $\chi^2$ . MSTFit employs the services of Amoeba[2] to perform the nonlinear multidimensional minimization using the downhill simplex method[3].

The downhill simplex method is typically less efficient than some methods<sup>2</sup> but was selected for this application based on its merits. A brief description of the simplex helps validate this choice. A simplex in  $N$  dimensions is a set of  $N+1$  points and the lines intersecting them, for example a two dimensional simplex is a triangle. The cost function (to be minimized) is evaluated at all  $N+1$  points of the simplex, and the minimum is found by systematically modifying the simplex by moving the highest point to a better region in free parameter space. The moves are specified via

---

<sup>2</sup>The Powell method, e.g, is typically more efficient, but hard to implement for the complicated MSTFit free parameters.

an algorithm consisting of four steps.

Figure 5.8 illustrates these in three dimensions, where the initial simplex (a tetrahedron) consists of 4 points shown as circles and the solid lines connecting them. The modified simplex is shown by dashed lines connecting the stationary initial points with the modified point (shown as a box). The first attempted step is called a reflection, Figure 5.8 a), where the point on the simplex with the highest value is identified, and that point is reflected through the  $(N - 1)^{th}$  dimensional structure defined by the remaining  $N$  points of the simplex. In three dimensions and a four point simplex, a reflection of the high point is through the plane defined by three lower points. The subsequent moves are all contingent upon the functional value at the new point on the simplex. If reflecting the high point leads to a function value that turns out to be the minimum on the simplex, the step length is doubled and the reflected point is moved out twice as far. This is called an expansion, Figure 5.8 (b).

If reflection of the high point leads to a functional value that is the highest on the simplex, then the reflection is ignored. The new point on the simplex is then set at half the distance from the original point to the  $(N - 1)^{th}$  dimensional structure. This step is contraction along one dimension, Figure 5.8 c), from the high point of the simplex.

In other cases, the value on the new point of the simplex will be somewhere between the highest and lowest points on the rest of the simplex. In this case, the new highest point is singled and it is moved in the same fashion as above.

The fourth possible move is a  $N$  dimensional contraction, Figure 5.8 d), toward the low point. The  $N$  high points on the simplex move half the distance directly toward the lowest point. This step will be tried if none of the three steps described above can make the highest point on the simplex find a value lower than at least one other point. The process continues until the maximum deviation across the simplex is smaller than a specified tolerance.

The minimization algorithm shows that the step size changes logarithmically as it can either

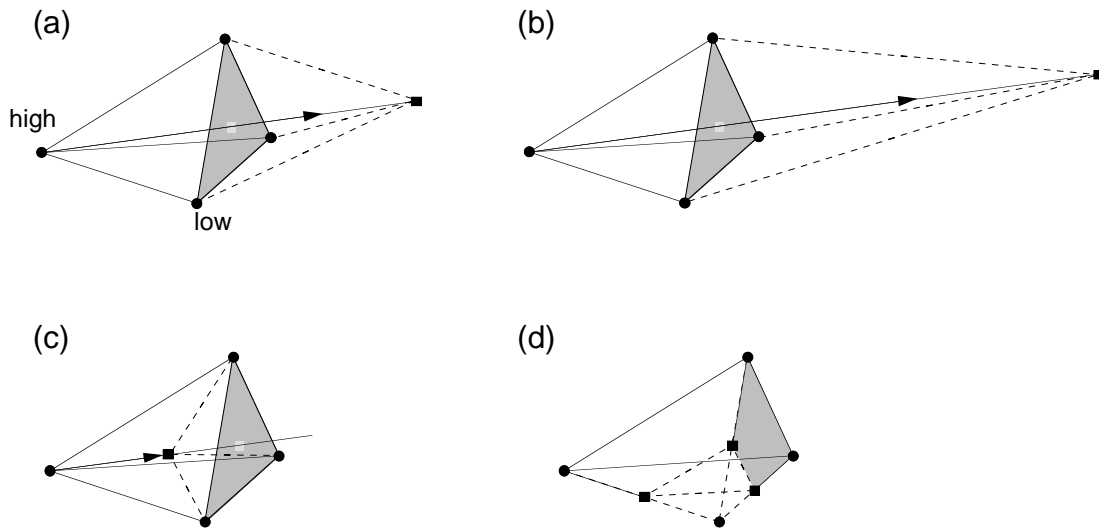


Figure 5.8: An illustration of a three dimensional simplex and the four possible steps Amoeba will use to find the minimum. a) shows the initial simplex, with high and low points identified, and reflection of the simplex. b) is expansion of the simplex, c) is contraction of the simplex away from the high point, and d) is an N-dimensional contraction toward the lowest point.

double or halve according to what directs it toward the minimum. This is advantageous in the MSTFit application, as some of the free parameters are varied over an infinite interval while corresponding to finite values, as described above in Section 5.1.3.

### 5.2.5 Code Termination

The result of the minimization routine is the set of free parameters which uniquely specify the  $FF'$  and  $P'$  profiles, and therefore the equilibrium, which best fits the data. When the code initially produces a solution, the entire process is started over using the solution as the initial guess. This technique helps ensure that the minimum found is an absolute as opposed to local extremum. The second solution produced is then accepted as the best equilibrium for the data presented. The user of the code should be wary if a significant change in  $\chi^2$  arises between the first and second minimizations; a third iteration may be necessary. The free parameters are mapped to profiles for  $F'$  and  $p$ , and the equilibrium magnetic field and current density profiles are computed. The code

then starts a series of post processing routines that will be discussed in Section 5.5.

### 5.3 Linear versus Nonlinear Fitting

MSTFit differs from other equilibrium reconstructions (e.g. EFIT) as it employs a fully nonlinear fitting routine. A linear equilibrium reconstruction writes the free functions  $F$  and  $P$  in terms of a basis function expansion, just as MSTFit. For each type of fitting, the equilibrium is specified by the vectors  $\mathbf{a}$  and  $\mathbf{b}$ . The computational difference is quite simple. MSTFit employs a nested, doubly-iterative technique to find the best equilibrium. It computes many consistent Grad-Shafranov equilibria (iteratively) and compares the predicted signals of each to the data. A linear code simultaneously fits the data while converging on a consistent Grad-Shafranov equilibrium. Thus, the linear code must only find one consistent equilibrium. The iterative process is somewhat more involved than the MSTFit counterpart, but the linear code is still much faster. It is restricted to fitting data that can be linearly related to the free parameters.

The advantage of the non-linear fitting is the ability to incorporate more complicated data. One important example of this is the HIBP constraint to MSTFit, which supplies a strong constraint to the magnetic field profiles. In the limit of infinite computational resources, the nonlinear fitting is clearly superior due to its greater flexibility.

### 5.4 Data Fitting

MSTFit is set up to accept data from almost any existing MST diagnostic and use it to constrain the equilibrium. Anything that can measure or be related to the magnetic field, temperature, density, current, or moments of these quantities can be used. On each iteration of the code, a consistent Grad-Shafranov equilibrium is presented to the  $\chi^2$  function for evaluation, where expected signals are predicted and compared to the data. The quantity computed for a each equilibrium is given

Diagnostic	Constraints
$F, \Theta, I_p$	$B_\phi(a); \Phi$
Poloidal Array	$\beta_p, l_i$ (Global pressure; internal inductance)
Insertable Rogowskii	Edge $J_{  }$ ( $r/a > .8$ )
Insertable $\dot{B}$ Probe	Edge $B_\phi, B_\theta$ ( $r/a > .8$ )
Polarimeter	$\int n_e B_z dl$
$q(0)$	$F'(0)$ (ratio of $B_\phi(0)/J_\phi(0)$ )
MSE	$B_\phi(0)$
HIBP	$\int \mathbf{v} \times \mathbf{B} dl$ through mid-radius region

Table 5.1: Collection of diagnostics MSTFit has incorporated into fitting. The set of internal magnetic constraints provide information on the core and mid-radius  $B_\phi, J_\phi$  and  $B_\theta$ .

by equation 5.34

$$\chi^2 = \sum_i \frac{(D_i - M_i)^2}{\sigma_i^2} W_i \quad (5.35)$$

and described in Section 5.2.3. The remainder of this section describes the specific steps MSTFit goes through to compute the predicted signals, and what modifications (if any) are made to the raw data before fitting.

### 5.4.1 External Diagnostics

Several diagnostics that give a global description of the plasma are made with diagnostics external to the plasma. Various moments of  $F$  and  $F'$  can be determined by external magnetics.

#### Plasma Current, Field Reversal and Pinch Parameters

The plasma current, total toroidal flux, and toroidal magnetic field at the wall are all required to reconstruct the equilibrium. The measurements of these quantities are made outside the plasma boundary. The total current is measured by a Rogowskii loop that fits snug against the inside of the vacuum vessel, encircling the total toroidal plasma current. The toroidal flux is similarly measured

by a loop around the inside of the vacuum vessel. The toroidal field at the wall is determined as a function of  $R$  by Ampere's law and a measurement of the toroidal field current flowing in the shell. The value at the wall varies according to the  $1/R$  dependence, and by convention described below the toroidal field at the wall is measured at  $R = .97 R_0$ .

The most common signals used to categorize MST discharges<sup>3</sup>,  $F$ ,  $\Theta$  and  $I_p$ , are related to the boundary field and toroidal flux.  $F$  and  $\Theta$  relate the edge toroidal and poloidal magnetic field values to the total toroidal flux,

$$F = \frac{B_\phi(a)}{\langle B_\phi \rangle} \quad (5.36)$$

$$\Theta = \frac{B_\theta(a)}{\langle B_\phi \rangle} \quad (5.37)$$

where  $\langle B_\phi \rangle$  is the average toroidal field over a cross section. However, both  $B_\phi$  and  $B_\theta$  vary poloidally on the boundary; as seen for  $B_\phi$  in the Grad-Shafranov development above and in the poloidal field asymmetry measurement of  $B_\theta$ . The specific location where edge field measurements are made is determined by using the definition of  $F \equiv 1$  for a vacuum toroidal field

$$B_\phi(R) = \frac{R_0 B_{\phi 0}}{R}. \quad (5.38)$$

The flux for a vacuum field is computed using MST's dimensions (1.5m major radius, .52m minor radius) by direct integration

$$\Phi_V = \langle B_\phi \rangle \pi a^2 = \int B_\phi \cdot dA = \int_{R-a}^{R+a} \frac{R_0 B_{\phi 0}}{R'} 2\sqrt{a^2 - (R' - R)^2} dR' = R_0 B_{\phi 0} \times 0.584446. \quad (5.39)$$

Substituting the vacuum field specified in equation 5.38 and the corresponding toroidal flux (equa-

---

<sup>3</sup>Note that this  $F$  is different than  $F = RB_\phi$  in the Grad-Shafranov development.

tion 5.39) into equation 5.36 gives

$$1 = \frac{R_0 B_{\phi 0} / R}{\langle B_{\phi} \rangle / \pi a^2} = \frac{R_0 B_{\phi 0} \pi a^2}{0.584446 \times R \times R_0 B_{\phi 0}} \quad (5.40)$$

which leads to the result  $R = 1.4535\text{m}$ .

The predicted signals for the plasma current, toroidal flux and edge toroidal field are very simple. The plasma current is the total of the toroidal filament current values on the plasma grid. The toroidal flux is found easily as  $F$  is determined on  $\psi$  for the specified equilibrium;  $\Phi = \sum F/R dA$  over the plasma grid. The edge toroidal field is predicted by taking the quotient of  $F(\hat{\psi} = 1, R = 1.4535\text{m})/1.4535\text{m}$  as outlined above.

### Poloidal Asymmetry Factor

An array of sixteen Mirnov probes sketched in Figure 5.9, poloidally distributed at one toroidal location, are used to measure the poloidal magnetic field at the wall. The  $m=0$  and  $m=1$  components

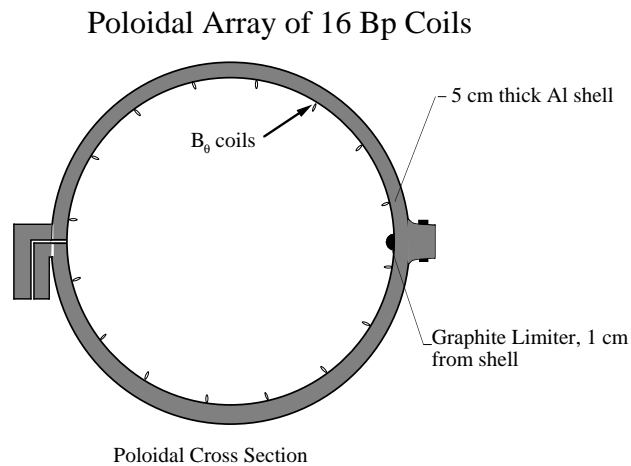


Figure 5.9: The poloidal array of Mirnov Coils.

subject to up-down symmetry are given by[4]

$$B_{\theta}(a, \theta) \simeq \frac{\mu_0 I_p}{2\pi a} \left[ 1 + \frac{a}{R_0} \left( \beta_p + \frac{l_i}{2} - 1 \right) \cos\theta \right] \quad (5.41)$$

where

$$l_i = \frac{2 \int_0^a B_{\theta}^2 r dr}{a^2 B_{\theta}^2(a)} \quad (5.42)$$

is the normalized internal inductance, which carries information about the toroidal current density profile. This shows that the amplitude of the  $m=1$  component gives information about the plasma pressure (through  $\beta_p$ ) and the current profile.

The poloidal array data are an important constraint to the equilibrium although experimental limitations apply. Each coil produces a signal proportional to the rate of changing magnetic flux through its effective area ( $N A \simeq 3\text{cm}^2$ ). The signal is integrated to give the magnetic field as a function of time at the position of the coil. This diagnostic is most susceptible to errors due to misalignment and miscalibration. The alignment of the coil is checked and if necessary corrected for on each shot. Prior to the plasma current at  $t = 0$ , there is a strictly toroidal field. Monitoring the poloidal array signals at  $t < 0$  and relying on the  $1/R$  dependence of the vacuum toroidal field leads to a quantitative measure of  $B_{\phi}$  pickup in the  $B_{\theta}$  coils. The magnetic field of the RFP is predominantly poloidal at the wall, making this correction and errors associated with it quite small. The situation is different when measuring  $B_{\phi}$  near the wall, where misalignment detects a fraction of the poloidal field which can lead to significant error.

To lessen the effect of high uncertainty in the coil calibrations, a spatial filter is applied to the data prior to fitting. The signals are Fourier decomposed, and the  $m=0, 1$  and  $2$  cosine terms are kept, and the  $m=0$  component is normalized to total plasma current. Figure 5.10 shows the results of this processing. Specific coils show a large deviation from the filtered data, but observation of

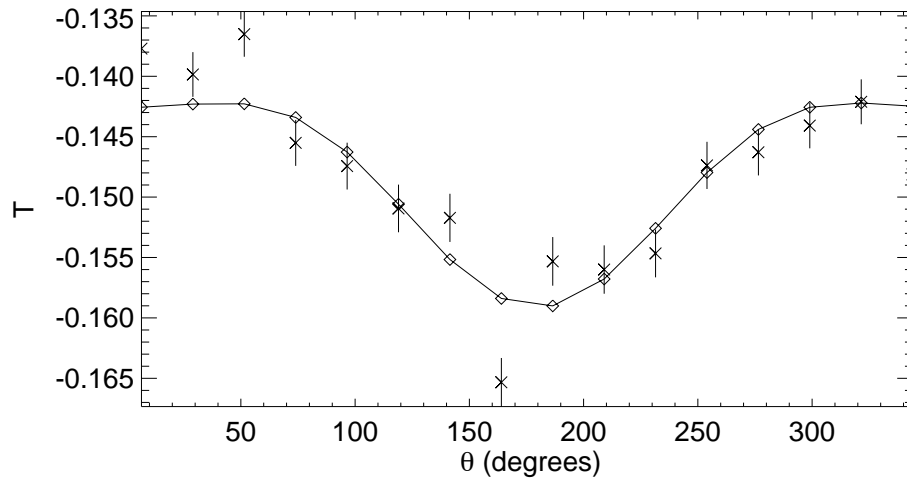


Figure 5.10: Poloidal array data correction.

these data over a large set of plasma parameters has shown this error to be systematic, almost certainly due to calibration error.

Fitting these data is done quite easily in the minimization process using the Green's table technique outlined in Section 5.2.2. The poloidal magnetic field at the location of each coil is predicted through a simple matrix multiplication of the Green's table and the plasma current array.

### 5.4.2 Edge Diagnostics

The edge of MST is cool compared to other fusion research devices, allowing insertable probes to diagnose the outer regions ( $r/a > 0.8$ ) of the plasma. These probes can measure current density, magnetic field, electron temperature and density. An accurate measurement of the edge values and gradients of these quantities has a significant impact on the reconstructed equilibrium.

### Edge Current Measurement

In lower current MST discharges, insertable probes can be inserted to measure edge properties directly. An insertable Rogowskii probe has been used to measure the edge current profile for different types of MST discharges using ensembling techniques over many shots. Data are input as current measurements at specific probe insertion depths; the predicted signal from an equilibrium is a very simple interpolation of the current profile onto a specified set of (R,Z) coordinates corresponding to the locations of the measurements. A particularly interesting example of these data, which MSTFit has used to constrain the equilibrium, is edge profile measurements in 200kA standard versus PPCD discharges. Figure 5.11 shows the change in parallel current density. The

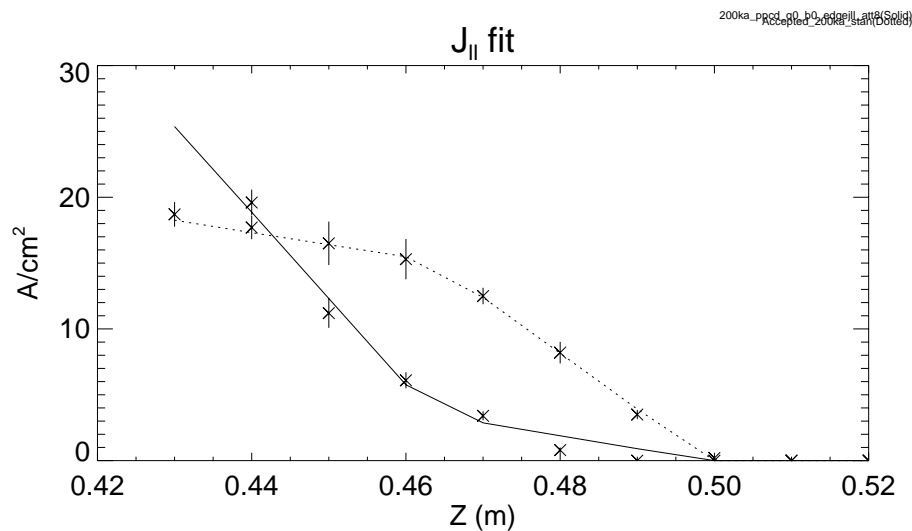


Figure 5.11: Rogowskii data (shown as points with error bars, and the MSTFit reconstructed edge profile. Two cases are shown: standard discharge (dotted line) and PPCD (solid line).

reconstructed equilibrium well fits the data by addition of an extra free parameter in the extreme edge. Unfortunately, these data do little to constrain the central profile, which can only be accomplished through internal diagnostics. As these data are acquired by an insertable probe, this is limited to low current discharges and is not considered further in this dissertation.

### Edge Magnetic Field

A second type of edge probe utilized by MSTFit is an edge magnetic field sensing probe. The particular probe of interest has a stack of 12 sensing coils which alternate between  $B_\phi$  and  $B_\theta$  at 0.5cm spacing. The advantage of this probe over others available is the ability to measure time resolved edge profiles on a single shot basis. Similar to the edge current measurement, the predicted signals are computed by interpolating the profiles of  $B_\phi$  and  $B_\theta$  onto the specified (R,Z) values of each measurement. As with the edge current measurement, details of the edge magnetic profile can be reproduced with the addition of free parameters, but the field values in the core are not further constrained.

### Edge Density and Temperature

Edge values of the electron density and temperature prove to be a valuable constraint to the pressure profile. These are measured in the extreme edge with an insertable three-tipped Langmuir probe, described in detail in reference[5]. These data, like the data from other pressure diagnostics discussed in Section 5.4.4, are not fit in the equilibrium reconstruction; thus it is not necessary to predict an expected Langmuir probe signal from the Grad-Shafranov equilibrium. The temperature data are used in conjunction with the Thomson scattering system to determine the best fit of the electron temperature. Likewise, the density data are used to help constrain the electron density in the extreme edge, where the interferometers provide little information.

### 5.4.3 Internal Magnetics

Accurate reconstruction of the equilibrium cannot be accomplished from edge measurements alone. MST has collected a set of passive internal diagnostics which together constrain the central current density, magnetic field, and field line pitch angle.

## Polarimetry Measurement

In 1845, Michael Faraday discovered that the polarization of a light source will be altered as it travels through a magnetic field in the direction of propagation. Only 155 years later, an eleven channel polarimeter colinear with the FIR interferometer is operational on MST[6]. A sketch of the diagnostic<sup>4</sup> is shown in Figure 5.12.

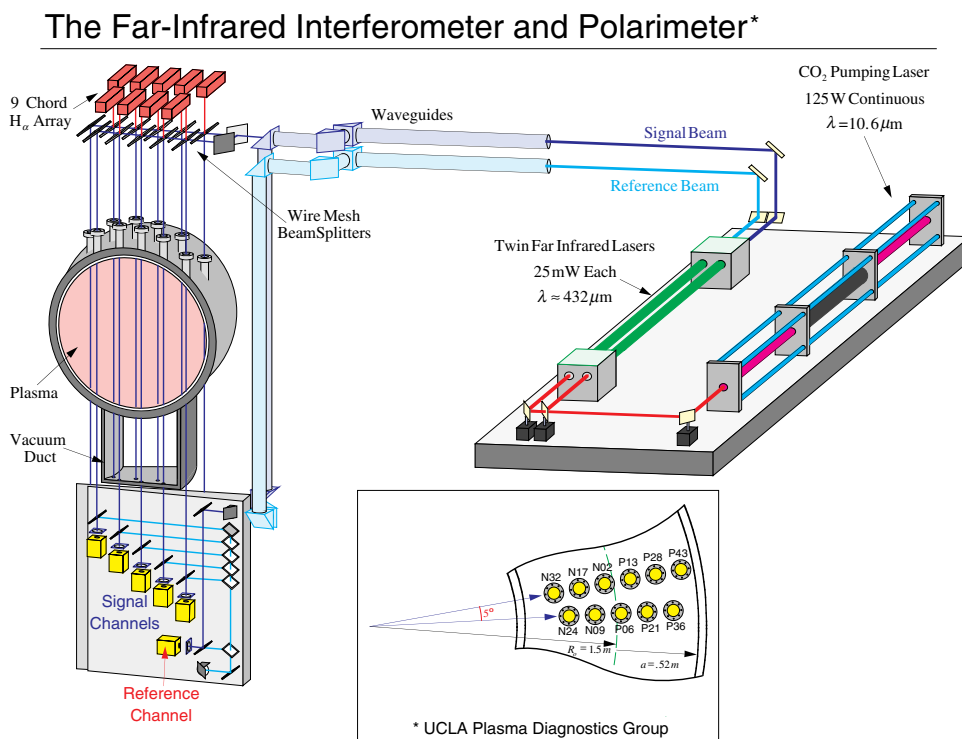


Figure 5.12: The FIR/polarimeter diagnostic

These data constrain the toroidal current density near the axis of the machine, which is crucial to accurate reconstructions of the parallel current density and magnetic field profiles. The data

<sup>4</sup>Figure courtesy of the FIR folks, Terry, Lanier, et. al.

are fully processed before being imported to MSTFit, appearing as a rotation angle (in degrees) for each chord.

A set of predicted Faraday rotation signals is made during each iteration of MSTFit. Density profile information from the FIR is required to fit the polarimetry signals. A Green's table technique is employed to compute the flux and vertical magnetic field on the FIR grid (53 vertical points along each FIR chord, resulting in a spatial resolution ranging from 2cm on the central chord to about 1cm on edge chords). First, an inversion of the FIR signals is performed which results in a density profile as a function of flux,  $n_e(\psi)$ . Utilizing the Green's function to compute the flux on the FIR grid, the local density is computed at each point on the grid. A similar Green's table is used to directly compute  $B_Z$  at each point on the grid as well. The predicted signals are then computed in degrees by

$$\phi \text{ [degrees]} = 1.5 \times 10^{-20} \lambda^2 \times 10^{-3} \int_0^L n_e B_Z dl \quad (5.43)$$

where the wavelength of the FIR laser is 433 microns. The equilibrium is then constrained by comparing the predicted signals to the measured signals following equation 5.35 on each of the eleven chords.

### Safety Factor

Although there is no diagnostic on MST which directly measures the axis value of the safety factor, there is a way to deduce some information about its value. A toroidally distributed array of coils along the inner surface of the vacuum vessel monitors the magnetic fluctuation activity in MST. Fourier analysis reveals amplitudes of suspected core modes. The vulnerable assumption in fitting  $q(0)$  in this manner is that in order for a core mode ( $m = 1, n = 5, 6, 7, 8, \dots$ ) to have a large amplitude, its rational surface must be present in the plasma.

The amplitudes calculated for a given  $n$  is the sum over all poloidal mode numbers,  $m$ . To utilize

the  $q(0)$  fitting, one must resolve between  $m=0$ ,  $m=1$  and  $m>1$  modes, as only the  $m=1$  component can be used to make claims about the core MHD activity. Assuming there is no fluctuating radial current at the conducting shell  $\tilde{J}_r(a) = 0$  the fluctuating field must obey

$$\left(\nabla \times \tilde{B}\right)_r \Big|_a = i \left(k \times \tilde{B}\right)_r = 0 \quad (5.44)$$

Writing  $k = \frac{m}{a}\hat{\theta} + \frac{n}{R}\hat{\phi}$  and  $\tilde{B}$  in terms of toroidal and poloidal components leads directly to

$$m = \frac{a}{R} \frac{\left|\tilde{B}_\theta\right|}{\left|\tilde{B}_\phi\right|} n. \quad (5.45)$$

Thus, with both the poloidal and toroidal fluctuating field amplitudes, the poloidal mode number can be resolved. In the MST, the innermost core mode with an appreciable  $m=1$  amplitude is typically  $n=6$  or  $n=5$ . Figure 5.13 shows the mode amplitude and average  $m$  for the  $n = 5, 6$ , and  $7$ . The implications on constraining  $q(0)$  vary with time in these signals. Prior to  $t = 10$ ms, the average  $m$  calculation does not yield a good  $m=1$  for any of the core modes, so no information is available. From  $t = 10$  to  $t = 15$ ms, the amplitude of the  $n=6$  mode is significantly higher than that of the  $n=5$  with the exception of a burst corresponding to a sawtooth crash at 14ms. These data indicate that away from the crash, the axis value of  $q$  lies between  $1/6$  and  $1/5$ . After  $t = 15$ ms, the total fluctuation amplitude is dramatically decreased with the onset of PPCD. After  $t = 19$ ms, there is a sharp increase in the  $n=6$  amplitude, which can be construed as evidence that  $q(0) > \frac{1}{6}$  there. There are conditions in MST (not shown here), where this type of analysis gives strong evidence that  $q(0) > \frac{1}{5}$  and this proves a valuable constraint in the equilibrium reconstruction.

The fitting of the data by the code is slightly different than a standard diagnostic, but quite straightforward. The on axis limit of  $q$  is given by

$$q(0) = \frac{2B_\phi(0)}{\mu_0 R J_\phi(0)}. \quad (5.46)$$

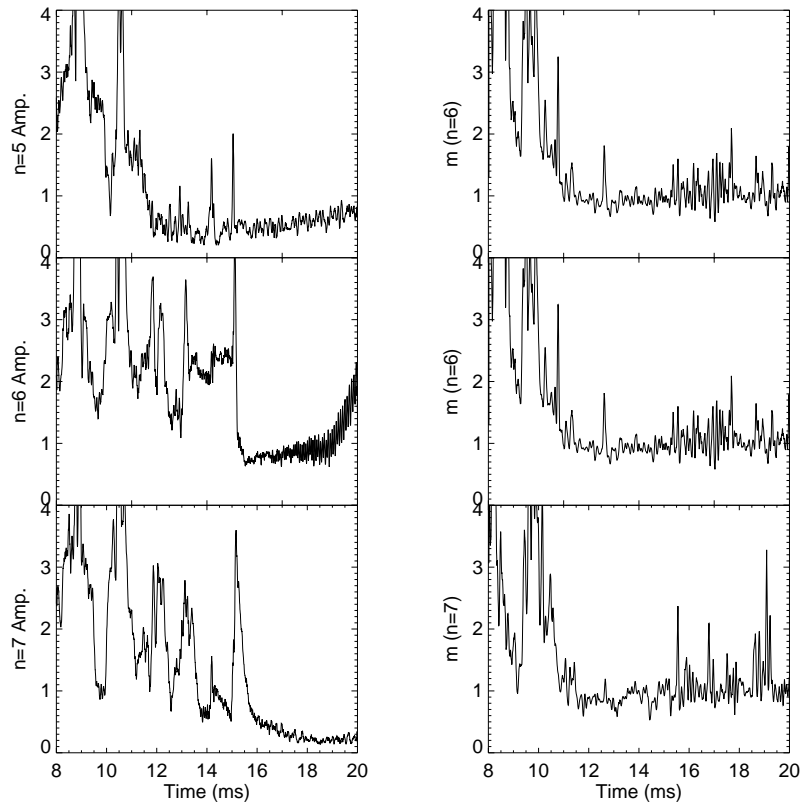


Figure 5.13: Analysis of data leading to an estimated  $q(0)$  input to MSTFit. This example shot is 3-May-1999, shot 87.

The values of  $B_\phi$ ,  $J_\phi$ , and  $R$  at the magnetic axis are readily accessed from the specified equilibrium, and a comparison to the input quantity is made. However, as  $q(0)$  is not a specific measurement but rather a range of values with a lower bound, the contribution to  $\chi^2$  is not as described in equation 5.35 and is illustrated in Figure 5.14. Typically, the contribution to  $\chi^2$  is parabolic with an apex where the predicted equals the measured value; the width is determined by the experimental uncertainty and weight. As always, a contribution to the cost function must be added when the predicted fit disagrees with the data. Here,  $\chi^2$  is enhanced when the predicted fit is less than the specified  $q(0)$ , but no contribution is added for higher predicted  $q(0)$ .

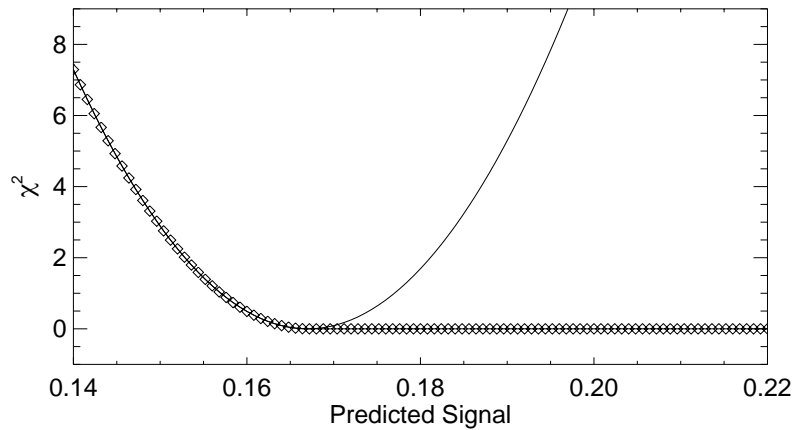


Figure 5.14: Contribution to  $\chi^2$  for normal data fitting (solid) and for  $q(0)$  fitting ( $\diamond$ ). Here the measurement is set at 0.167

### Motional Stark Effect Measurement of B

The recent addition of a diagnostic neutral beam on MST has provided a measurement of the magnitude of the B field near the axis through the motional Stark effect[7]. A sketch<sup>5</sup> of the diagnostic is shown in Figure 5.15. The optics used to collect light from the Stark manifold of the  $H_\alpha$  line intersect the neutral beam near the core of MST over a sample volume centered at ( $R = 1.56, Z = 0$ ). The neutral beam is directed along a line such that the endpoints of the sample volume are at (1.541, .046) and (1.579, -.046). Processing of data is done independently;  $|B(0)|$  is reported in tesla. Fitting is quite easy, as the  $F$  profile is specified by the equilibrium guess;  $B_\phi$  is simply calculated by averaging  $\frac{F}{R}$  over the fixed volume.

### Heavy Ion Beam Trajectory

MSTFit is different from most other equilibrium reconstruction codes as it utilizes a fully nonlinear algorithm in fitting the data. This enables a novel constraint to the equilibrium provided by the

---

<sup>5</sup>Courtesy of G. Fiksel, D. Craig et al.

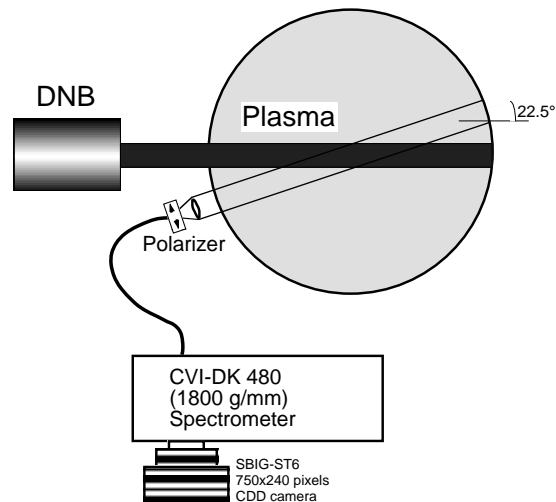


Figure 5.15: The MSE diagnostic

Heavy Ion Beam Probe (HIBP), sketched<sup>6</sup> in Figure 5.16. The probe directs a stream of singly ionized sodium ions into the plasma at a specified velocity (speed and direction) set by a series of focusing plates and the beam energy[8]. The ions travel across the plasma according to the Lorentz force which is dominated by the  $v \times B$  term for the high energy ( $\sim 40 - 80\text{keV}$ ) ions. During the transit across the plasma, many of the ions undergo a second ionization and their trajectory changes. A second port, separated from the injection port in  $R$ ,  $Z$ , and  $\phi$ , collects some of the secondary ions and directs them onto a set of detectors, again utilizing steering and focusing plates. It was determined experimentally that secondary ions were not detected except under a very specific set of plate voltages, which vary with plasma parameters. The lack of secondaries

<sup>6</sup>Figure courtesy of Demers, et. al.

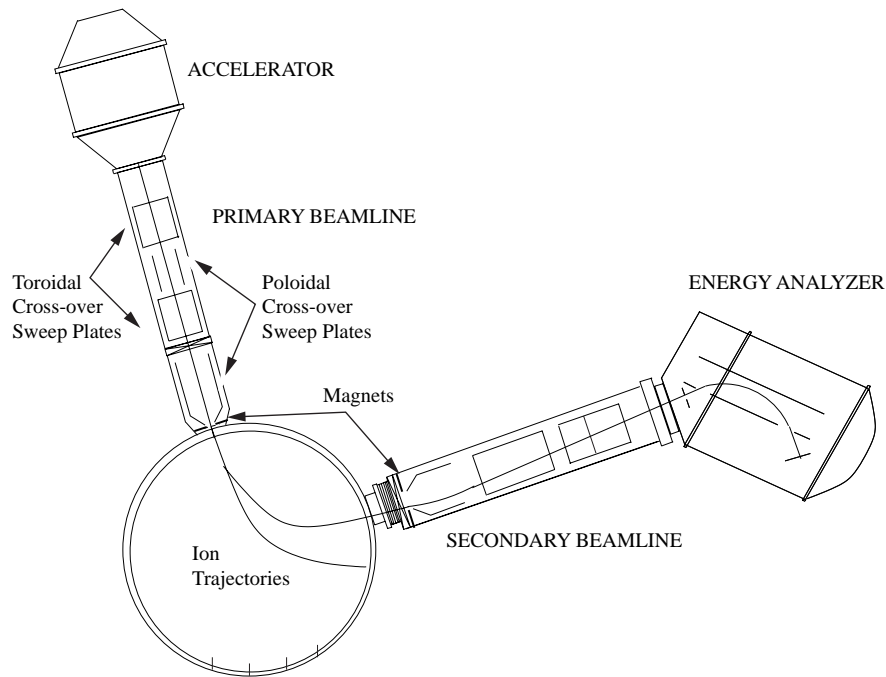


Figure 5.16: The HIBP diagnostic

results from the ion trajectories missing the exit port altogether. This is summarized in Figure 5.17, where ionizations along the primary beam lead to a stream of secondary beams (illustrated in a) as an  $R,Z$  projection, and in b) as a top view of the torus) which are incident on the vacuum vessel at different locations. Figure 5.17 c) is a view of the exit port, with projections of secondary beams originating from different ionization points along the primary beam. Only a select few of the trajectories intersect the exit port and fewer still are directed by the secondary sweep plates to the detectors.

Utilizing the nonlinear algorithm in MSTFit, this information is used to constrain the magnetic field profiles. The HIBP accelerator energy and plate voltages specify the velocity and position of both the particles injected into the machine and the secondaries incident upon the exit port which

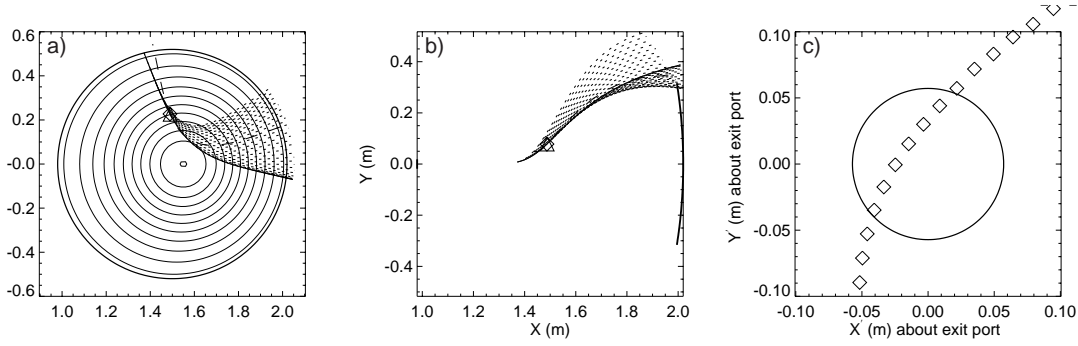


Figure 5.17: The HIBP ion trajectories are used to constrain the equilibrium. Ionizations along the primary beam lead to a stream of secondary beams: a) is an R,Z projection, b) is top view of the torus; x,y. c) is a view of the exit port, with projections of secondary beams incident on the shell.

are steered to the detectors. MSTFit then uses this information to trace the orbit of the primary ions and the reverse of the secondary orbit into the machine. In an experiment where signal is observed, the two trajectories must intersect at some point in the plasma and the two trajectories must be tangent to each other at this point.

An HIBP term is added to the  $\chi^2$  given by

$$\chi_{HIBP}^2 = \sum_{i=1}^{N_{orbit}} W_i \left[ x \left( \frac{\Delta D_i}{.005} \right)^2 + (1-x) \left( \frac{\Delta v_i}{.05} \right)^2 \right] \quad (5.47)$$

where  $N_{orbit}$  is the number of pairs of trajectories to fit,  $W_i$  is the weight assigned to the  $i^{th}$  trajectory pair,  $x$  is a user-controlled parameter used to shift the fitting emphasis from closest approach (high  $x$ ) to tangency of the orbits at their minimum separation (low  $x$ );  $\Delta D_i$  is the closest approach between the primary and secondary orbits, and  $\Delta v_i$  is the difference in velocity vector (direction only) at the point of intersection. This contribution to the cost function mimics equation 5.35.

The datum for both the intersection and tangency conditions is zero; the fact that secondary ions appear on the detector are a measurement that the primary and secondary orbits intersect

at some point in the plasma, and the velocities of the primary and secondary are tangent at that point. The predicted signal for each, ( $\Delta D_i$  and  $\Delta v_i$  described in detail below) is found by tracing the primary beam and the reverse of the secondary beam into the plasma column. The closest approach distance is found simply by looking at the deviation between each pair of points from the two trajectories. After determining  $\Delta D_i$  in this fashion, the velocity unit vector is calculated at the points on the primary and secondary orbits at the point of closest approach. The difference in these vectors is computed as  $\Delta v_i$ , or the deviation from perfectly tangent beams. By considering only the direction, different speeds (energies) between the primary and secondary beams are not confused with non-tangent orbits. The values of .005m and .05 (dimensionless) which appear in the denominators of equation 5.47 are nominal uncertainties, corresponding to the typically estimated beam width at the points of interest in the plasma; and the somewhat arbitrary value of 0.05 for uncertainty in tangency is chosen due to empirically determined code stability and results.

#### 5.4.4 Pressure Diagnostics

Reconstruction of the equilibrium requires a pressure profile, but the pressure measurement diagnostics in MST do not produce profiles in a single shot, and are often not used in a given experiment. An estimate is made using the central line averaged electron density (measured by the CO<sub>2</sub> interferometer) and plasma current, which are available for all shots and times during normal MST operations. The central electron temperature in MST has been measured[9] over the full range of plasma current and electron density, and an empirical power law fit shows that  $T_e(0)$  varies roughly as  $I_p^{1.09}$  and  $\bar{n}_e^{-.34}$ . A standard temperature profile is then scaled to match the projected central temperature for a given current and density. Similarly, a standard measured density profile is scaled to match the line integrated value. The pressure profile for the equilibrium reconstruction is the product of these two profiles with a modest 25% ion contribution added. For data sets that have full pressure profile information, this step is unnecessary and is overlooked in

favor of the measurements.

## Electron Temperature

The Thomson scattering diagnostic on MST (illustrated<sup>7</sup> in Figure 5.18) provides an instantaneous measurement of electron temperature on one of 16 view points. The very reproducible nature of

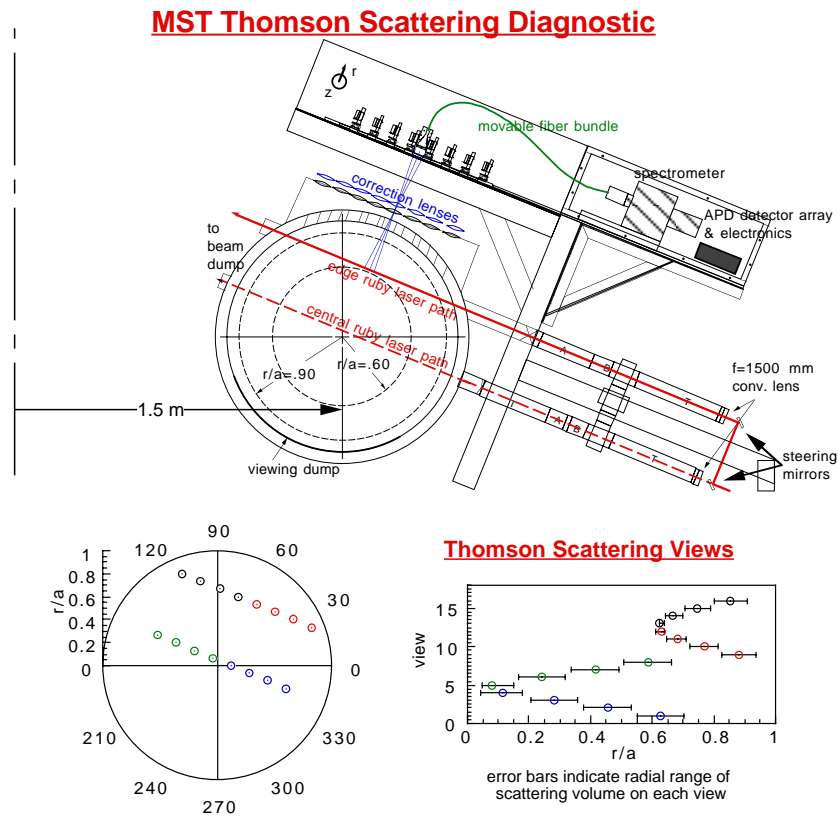


Figure 5.18: Ruby laser Thomson scattering diagnostic on MST.

MST discharges enables a compilation of a temperature profile, which is representative of all the shots in the group, by taking several measurements at several views over the course of an experimental campaign. The localized measurements in  $(R,Z)$  are mapped onto a normalized flux axis using a Green's table to compute the flux at each viewpoint. A smooth curve is drawn

<sup>7</sup> Figure courtesy of T.M. Biewer.

through the data using a spline interpolation, resulting in a temperature profile  $T_e(\psi)$ . This is used to constrain the pressure profile, and it is fundamental to the energy transport analysis routine. These data are received in MSTFit as a temperature and an uncertainty given in eV. Processing of the raw signals to obtain the temperature is done completely external to the code.

### **Electron Density Profile**

The electron density profile also plays a key role in the pressure constraint and energy transport analysis, as well as being an integral part of the particle transport analysis routine. The electron density information is submitted to MSTFit as the line integrated signal along eleven vertical chords of the FIR interferometer shown above in Figure 5.12. The signals are inverted on the proper flux geometry, assuming  $n_e = n_e(\psi)$ . A detailed description of the inversion process employed by MSTFit is found in Section 5.5.2. The full inversion of the density profile is necessary to interpret other measurements, including polarimetry and  $Z_{eff}$  measurements.

## **5.5 Output**

After finding the best solution to the Grad Shafranov equation, MSTFit runs a variety of post processing routines. As they are key to the work in this dissertation, a full description of a computation of the equilibrium quantities in a one-dimensional flux surface volume-based coordinate and inversions of line integrated signals is included. Further post processing routines, including energy and particle transport analyses, and a one dimensional cylindrical stability analysis are described in Appendix B.

### **5.5.1 Equilibrium Quantities**

The Grad-Shafranov equilibrium found specifies the magnetic field and current density profiles on the two dimensional grid. It is useful to limit the post processing routines to one dimension when

possible, so the flux surface average of many important profiles is taken. The flux surface average of a general quantity  $A$  is defined in equation 5.18

$$\langle A \rangle \equiv \frac{\oint \frac{A dl}{B_\theta}}{\oint \frac{dl}{B_\theta}}. \quad (5.48)$$

The computation of the average is performed by defining a local Jacobian,  $J = r/B_\theta$  where  $r$  is the set of minor radius values along a given flux surface.  $J$  is a two dimensional array where the columns are  $r/B_\theta$  along a given surface, and a column exists for each flux surface. The computation proceeds by computing the flux surface average of  $A$  on the  $i^{\text{th}}$  flux surface by replacing the integration in equation 5.48 by a discrete summation

$$\langle A \rangle_i = \frac{\sum_j A_j J_{ij}}{\sum_j 1 \times J_{ij}}. \quad (5.49)$$

MSTFit computes flux surface averages of several equilibrium profiles. A summary of the outputs is presented in Appendix B with detailed descriptions where necessary.

## 5.5.2 Inversions

### One Dimensional Inversion

Inversion of a general quantity,  $S$ , begins by assuming  $S$  is a function of poloidal flux only and expanding it in terms of  $N$  basis functions

$$S = S(\psi) = \sum_{i=1}^N a_i f_i(\psi) \quad (5.50)$$

where the set of coefficients  $\mathbf{a}$  uniquely determine the profile. The basis functions used in the inversion routines are the same as dynamic spline interpolation functions described above in Section 5.1.3. A minimization routine is used to vary the locations of the non-endpoint knots to find

the set of basis functions which best fit the data. The predicted signal  $M$  is the line integral over the specified profile, so for the  $j^{\text{th}}$  chord in an array

$$M_j = \int_j dl_j S(\psi_j) = \int_j dl_j \sum_{i=1}^N a_i f_i(\psi_j). \quad (5.51)$$

The summation over the index of the basis function  $i$  is independent of the integration over the flux encountered along the  $j^{\text{th}}$  chord, so

$$M_j = \sum_{i=1}^N a_i \int_j dl_j f_i(\psi_j). \quad (5.52)$$

For a given flux geometry and set of basis functions, the matrix  $\mathbf{G}$  is defined as

$$G_{ij} = \int_j dl_j f_i(\psi_j) \quad (5.53)$$

giving

$$M_j = \sum_{i=1}^N a_i G_{ij} \quad \text{or} \quad \mathbf{M} = \mathbf{G} \cdot \mathbf{a} \quad (5.54)$$

where the set of predicted measurements on all chords,  $\mathbf{M}$ , is written in terms of matrix multiplication. The set of coefficients which best fits the data is then found by inverting  $\mathbf{G}$  and minimizing the difference between the predicted signals and the data,

$$\chi^2 = \sum_j \frac{(M_j - D_j)^2}{\sigma_j^2} W_j^2 \quad (5.55)$$

where  $\sigma_j$  is the experimental uncertainty and  $W_j$  is a weighting factor assigned to the  $j^{th}$  chord.

Proceeding with the solution, a scaled design matrix,  $\mathbf{H}$ , is defined as

$$H_{ij} = \frac{G_{ij} W_j}{\sigma_j} \quad (5.56)$$

and an accompanying scaled measurement,  $\mathbf{b}$ , is

$$b_j = \frac{D_j W_j}{\sigma_j}. \quad (5.57)$$

The minimization problem in equation 5.55 is now equivalent to

$$\mathbf{H} \cdot \mathbf{a} - \mathbf{b} = 0 \quad (5.58)$$

or simple matrix inversion to find  $\mathbf{a}$ . In practice, the matrix is not square as the number of free parameters in the fit is smaller than the number of measurements. Matrix inversion must therefore be replaced by solving an over-specified set of linear equations, for which singular value decomposition is used. The inversion process (from equation 5.53 on) is repeated many times, as the basis functions are varied in an overall minimization of  $\chi^2$ .

This inversion technique is quite successful at fitting the line integrated density data, but it fails miserably for both the  $H_\alpha$  and uncorrected NIR emission. This is a result of the invalid assumption that the quantity to be inverted is a function of flux only, made in equation 5.50.

### **Two Dimensional Inversion**

A two dimensional inversion has been developed for fitting the extremely asymmetric  $H_\alpha$  and NIR emission data, by assuming that the quantity to be inverted can be described as a function of flux

plus an asymmetric term

$$S = S_1(\psi) + S_2(R, Z) = \sum_{i=1}^N a_i f_i(\psi) + a_{N+1} f_{N+1}(R, Z). \quad (5.59)$$

The empirically developed asymmetric contribution is a unit Gaussian centered near the limiter at the outboard midplane, with the width and precise location left as fitting parameters. The position and width of the asymmetric term are specified prior to inversion, and the R and Z values along each chord are known. This allows the computation of the same matrix  $\mathbf{G}$  from equation 5.53, but the final row of the matrix is now

$$G_{N+1,j} = \int_j dl_j f_{N+1}(R_j, Z_j). \quad (5.60)$$

The solution is then exactly the same as in the one dimensional case above, again employing singular value decomposition. This method successfully fits the line integrated emission signals, as shown in Figure 5.19. In a), the inverted one dimensional component is plotted along with the flux surface average (dotted line) of the emission. Figure 5.19 b) is a contour plot of the asymmetric contribution, c) is the total two-dimensional emission, and d) shows the line integrated data and the fit predicted by this emissivity profile. The line integrated data show a distinct asymmetry between the inboard and outboard chords which is evidently well described by this model.

## 5.6 Uncertainty Analysis of Equilibrium

### 5.6.1 Error in Equilibrium Quantities

A complete uncertainty analysis must be performed in order to determine confidence levels in the equilibrium quantities. In principle, a Monte Carlo analysis can be performed on the equilibrium calculation. Data such as the plasma current, edge magnetic field measurements, polarimetry sig-

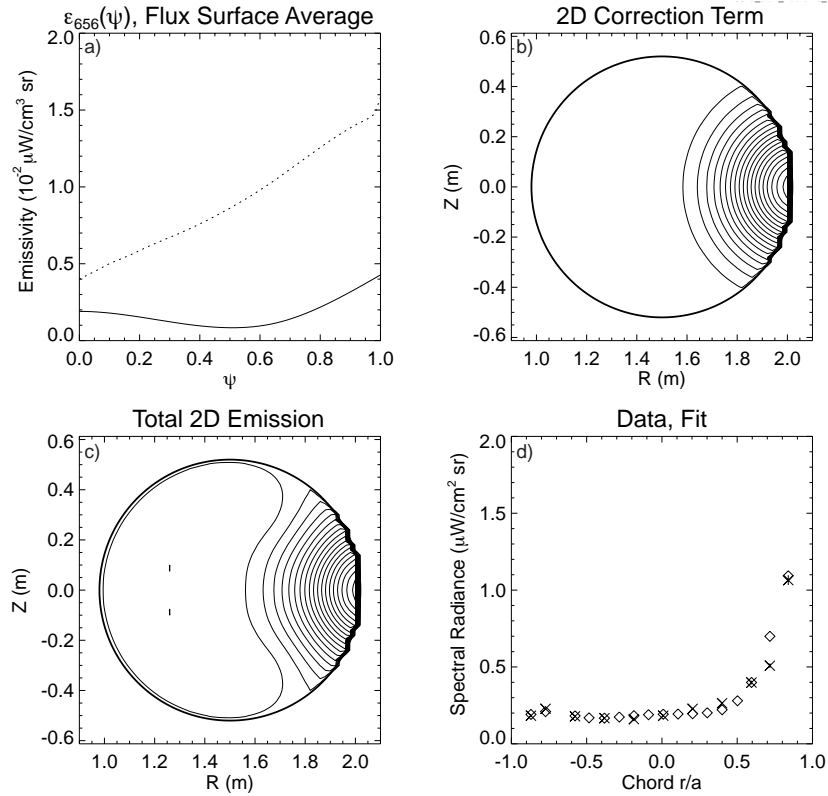


Figure 5.19: Two dimensional inversion of  $H_\alpha$  emission. Clearly the in-out asymmetry cannot be reproduced with a one dimensional inversion

nals, etc. can be varied within their uncertainty, and the equilibrium fitting can be computed for many sets of the varied data. This is computationally burdensome, as a single equilibrium reconstruction can take twenty minutes or more. Some relief may be provided by using the unperturbed equilibrium as the initial guess to successive equilibria computations, but the process is still prohibitively slow.

MSTFit instead uses a semi-analytic approach to estimating the uncertainty in the equilibrium free parameters. The minimized quantity,  $\chi^2$  is a function of  $N$  variables (the free parameters of

the fit denoted by  $\mathbf{a}$ ), and can be Taylor expanded about the minimum

$$\chi^2 = \chi_0^2 + \sum_{i=1}^N \frac{\partial \chi_0^2}{\partial a_i} \delta a_i + \frac{1}{2} \sum_{i=1}^N \sum_{j=1}^N \frac{\partial^2 \chi_0^2}{\partial a_i \partial a_j} \delta a_i \delta a_j + O(\delta a^3) \quad (5.61)$$

where  $\chi_0^2$  is the function minimum and  $\delta a_i$  is the deviation of the  $i^{\text{th}}$  free parameter from its value at the minimum. The first derivative of  $\chi_0^2$  at the minimum must be zero, implying that near a local minimum, the value of  $\chi^2$  can be approximated as a quadratic in each free parameter. Figure 5.20 is a plot of the  $\chi^2$  space for a typical equilibrium. The distance a given free parameter must vary

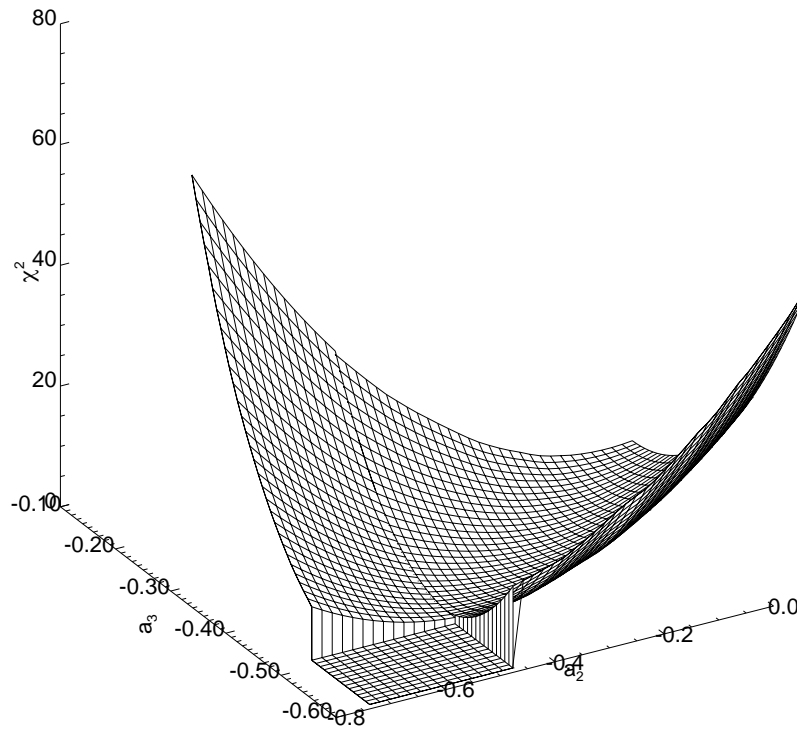


Figure 5.20: Surface plot of  $\chi^2$ , typical equilibrium. The x and y axes are two free parameters varied about their minimum. The quadratic nature of the surface near the minimum is illustrated by excluding the front left quadrant from the plot.

from the minimum to increase the  $\chi^2$  a specified amount is proportional to the standard deviation

in that parameter's value. It is shown in the literature[10, 11] that varying a parameter  $a_i$  by one standard deviation leads to a reduced  $\chi^2$  increase of one. Thus, in the vicinity of the minimum the assertion

$$\chi^2 = \frac{\delta a_i^2}{\sigma_i^2} + C \quad (5.62)$$

holds where  $C$  is a function of all other  $a_j$ .

Each free parameter is varied independently to compute the second derivative in the vicinity ( $\chi^2 \leq \chi_0^2 + 1$ ) of the minimum, and the uncertainty in a given free parameter is

$$\sigma_j^2 = 2 \left( \frac{\partial^2 \chi^2}{\partial a_j^2} \right)^{-1} \quad (5.63)$$

In practice, the code tabulates  $\chi^2$  values versus each free parameter near the minimum. These are fit to the quadratic equation described in equation 5.62 to determine the standard deviation in the free parameter.

The final step is to use the Monte Carlo approach to vary the set of free parameters within their calculated uncertainties and compute the equilibrium quantities for each set. This is much faster than the full Monte Carlo approach, where the bulk of the computation time is spent determining the free parameters. The resulting envelope on output profiles (such as  $q$ ,  $B$ , or  $J$ ) is the experimental uncertainty in that quantity. Results of this analysis are shown in Figure 5.21 for a standard discharge.

### 5.6.2 Sensitivity Study to Internal Diagnostics

It is of considerable interest to determine how well each diagnostic constrains the equilibrium. Varying the experimental uncertainty in a given diagnostic and computing the change in the quadratic fit to the  $\chi^2$  surface determines the sensitivity of each diagnostic to a given free parameter.

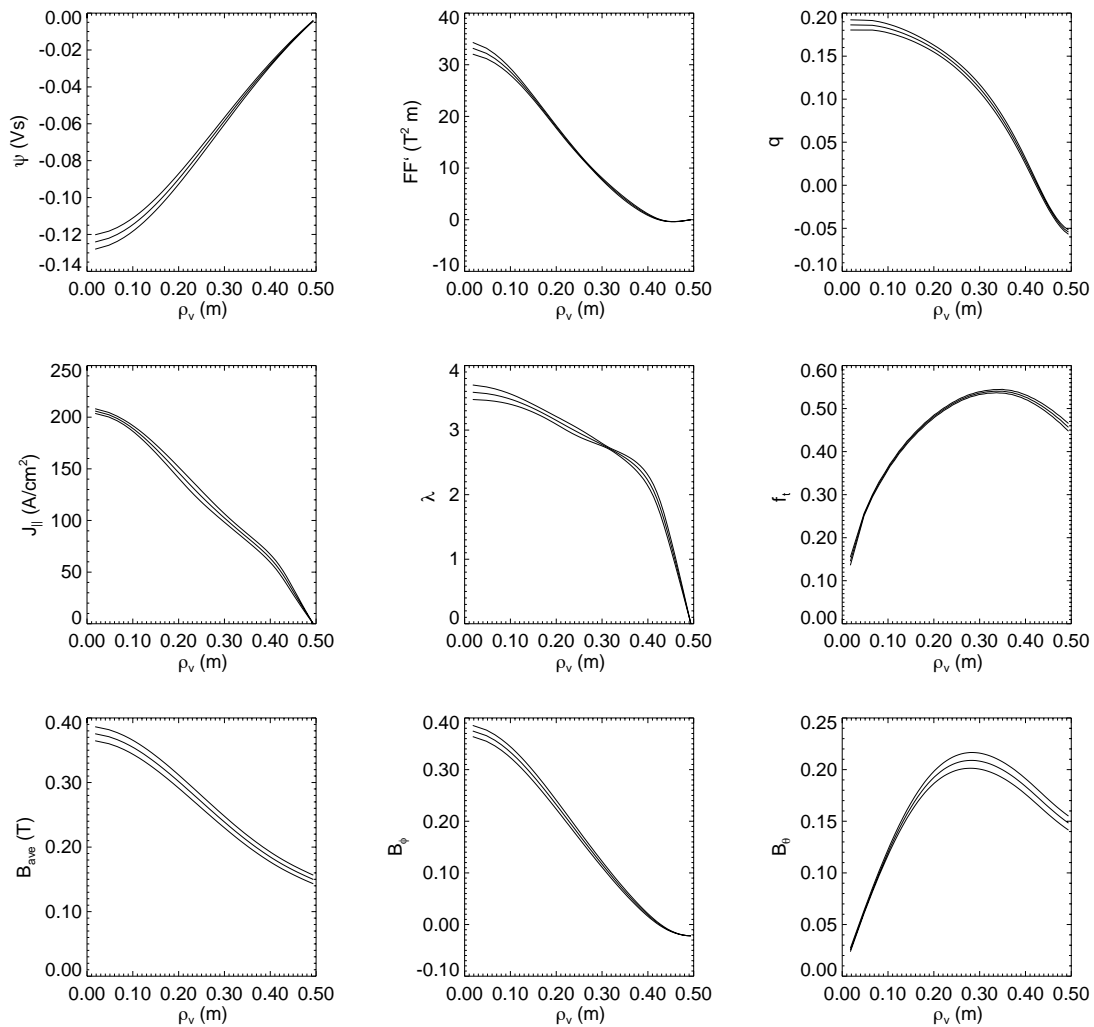


Figure 5.21: Uncertainty in computed equilibrium quantities. The envelope is computed by varying the free parameters within their experimental uncertainty determined by the quadratic fit to the  $\chi^2$  surface near the minimum.

For example, it is intuitive that the MSE measurement of  $B_\phi(0)$  will constrain the central magnetic field strongly. This is verified in Figure 5.22, where the  $\chi^2$  parabolas are plotted versus the free parameter corresponding to  $F'$  on axis for varying uncertainties in the measurement. The central (steepest) parabola is for a 1% experimental uncertainty, followed by 5, 10 and 25% uncertainties. As the lines for the 10 and 25% uncertainties nearly overlay, it is inferred that an experimental uncertainty of that level would not strongly constrain the equilibrium.

The same analysis is applied to the other internal diagnostics and the results are included in Table 5.1. The results are not as easy to interpret, as the the  $q(0)$  fitting does not have a well defined parabolic  $\chi^2$  contribution, and the HIBP and polarimeter are line integrated measurements which further convolutes these studies. However, the results obtained are qualitatively valid and

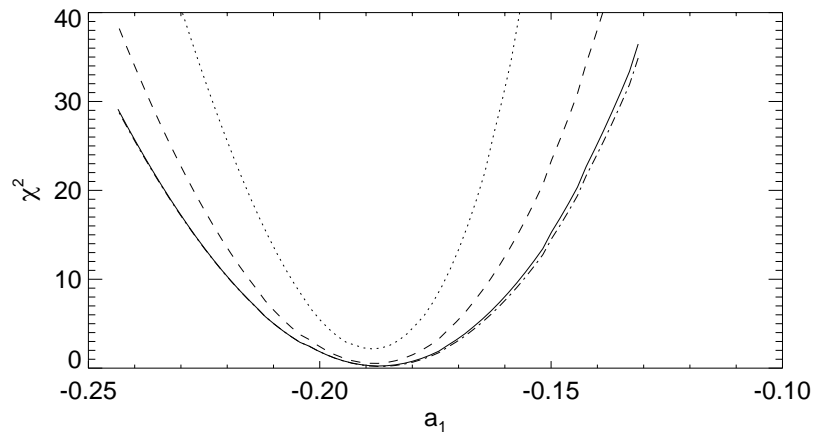


Figure 5.22: Sensitivity of  $F'(0)$  free parameter to the MSE diagnostic. The central steep parabola (dotted line) is the  $\chi^2$  contribution for a 1% uncertainty. Below are the lines for 5, 10 and 25% uncertainty.

are again in agreement with intuition. The best constrained fit, of course, is the one with the most diagnostics.

### 5.6.3 Error Introduced by Modeling

The procedures described above address the effects of experimental uncertainty on the computed quantities, but ignore any error introduced by modeling. The initial setup of the model, specifically the number of free parameters and the initial locations of the knots, can in theory lead to variations in the computed quantities. This effect has been studied in detail. The number of free parameters used obviously has an effect on the calculated equilibrium. Adding free parameters leads to a decrease in the overall  $\chi^2$ , but cannot be extended to an indefinite number. The first limit is from statistical considerations; adding a new free parameter must lead to an improvement in the reduced  $\chi^2_\nu = \chi^2/\nu$  where  $\nu$  is number of degrees of freedom (number of data points minus number of parameters to be determined from them). The default setup for MSTFit is five free parameters; which typically leads to four degrees of freedom. Adding another free parameter is not justified unless it leads to a overall  $\chi^2$  reduction of 25%. Violation of this limit is not easily detected, as one has to rerun certain datasets with different models. A hard limit occurs if the above condition is seriously violated and the number of free parameters approaches the number of data, which usually ends in a crashing of the code.

The initial locations of the knots can influence the calculated equilibrium in the fixed knot case. The effect of knot positioning has been studied and it is a noticeable effect which varies strongly on the particular dataset. It is recommended that several initial positions be tried to measure the effect on a particular dataset, or preferably use the free knot option. There is no noticeable effect of initial positions in the free knot location development, as the minimization samples points that span the entire range of possible knot locations during minimization.

## 5.7 Reconstructed MHD Equilibrium

Presented here is the culmination of several years of code and diagnostic development, relying heavily on the experimental work of the entire MST group and collaborators. Equilibria have been

computed for a variety of plasma conditions, extending over the entire operating range of some MST parameters; the plasma current ranges from 150kA to 500kA, reversal parameter  $F$  from -2.0 to + 0.05, and line averaged electron density from 0.4 to  $3.0 \times 10^{13} \text{cm}^{-3}$ .

As it is not pertinent to the present work to catalog the entire range of MST parameters, three cases have been selected which illustrate the versatility of the code. The base case is a well-diagnosed<sup>8</sup> 400kA standard shot, prior to a sawtooth crash. The second fit is a 400kA standard shot immediately following the sawtooth crash, (presumably in a relaxed state), and the third is a 400kA PPCD shot.

Figures 5.23 - 5.25 are summaries of the equilibrium fitting for these three cases. Each shows the reconstructed surfaces of poloidal flux, which very closely resemble circles with a magnetic axis shifted approximately 6cm from the geometric ( $R = 1.50\text{m}$ ) axis. The global quantities used to constrain the fit are tabulated and in cases away from the sawtooth crash, the input quantities and fit values match. In the fit near the crash, competing data from the internal constraints leads to a small error in the reconstructed plasma current and hence  $\Theta$ . With improvements to both the MSE and polarimeter slated for the near future<sup>9</sup>, the accuracy of the reconstruction near the crash will improve. The Faraday rotation data (shown with error bars) and fit predicted from the equilibrium (solid line) help demonstrate the accuracy of the fit. The magnetic field profiles (total: dashed line, toroidal: solid line, poloidal: dotted line) are shown versus radius, along with the MSE datum and fit. The Thomson scattering measured electron temperature profile and estimated ion temperature<sup>10</sup> profile are used with the electron density to constrain the pressure profile.

---

<sup>8</sup>Biewer spearheaded the experimental campaign.

<sup>9</sup>Time resolution of the MSE system will be improved, and a third laser will allow simultaneous density and polarimetry measurements in the FIR system.

<sup>10</sup>Estimates are based on limited impurity (CHERS, IDS) and majority (Rutherford scattering)  $T_i$  measurements.

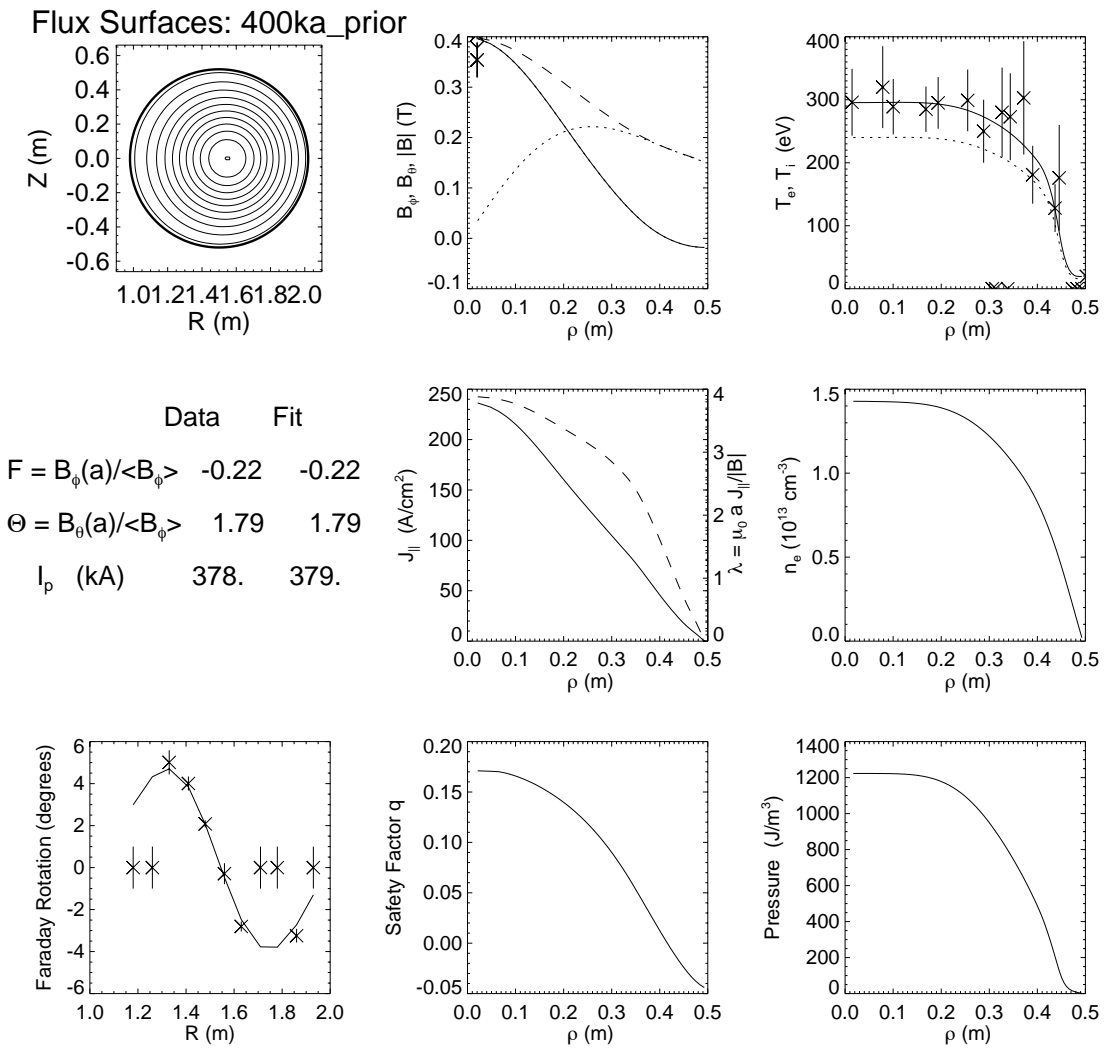


Figure 5.23: Summary of equilibrium reconstruction: 400kA standard shot  $\sim$  1ms prior to a sawtooth crash.

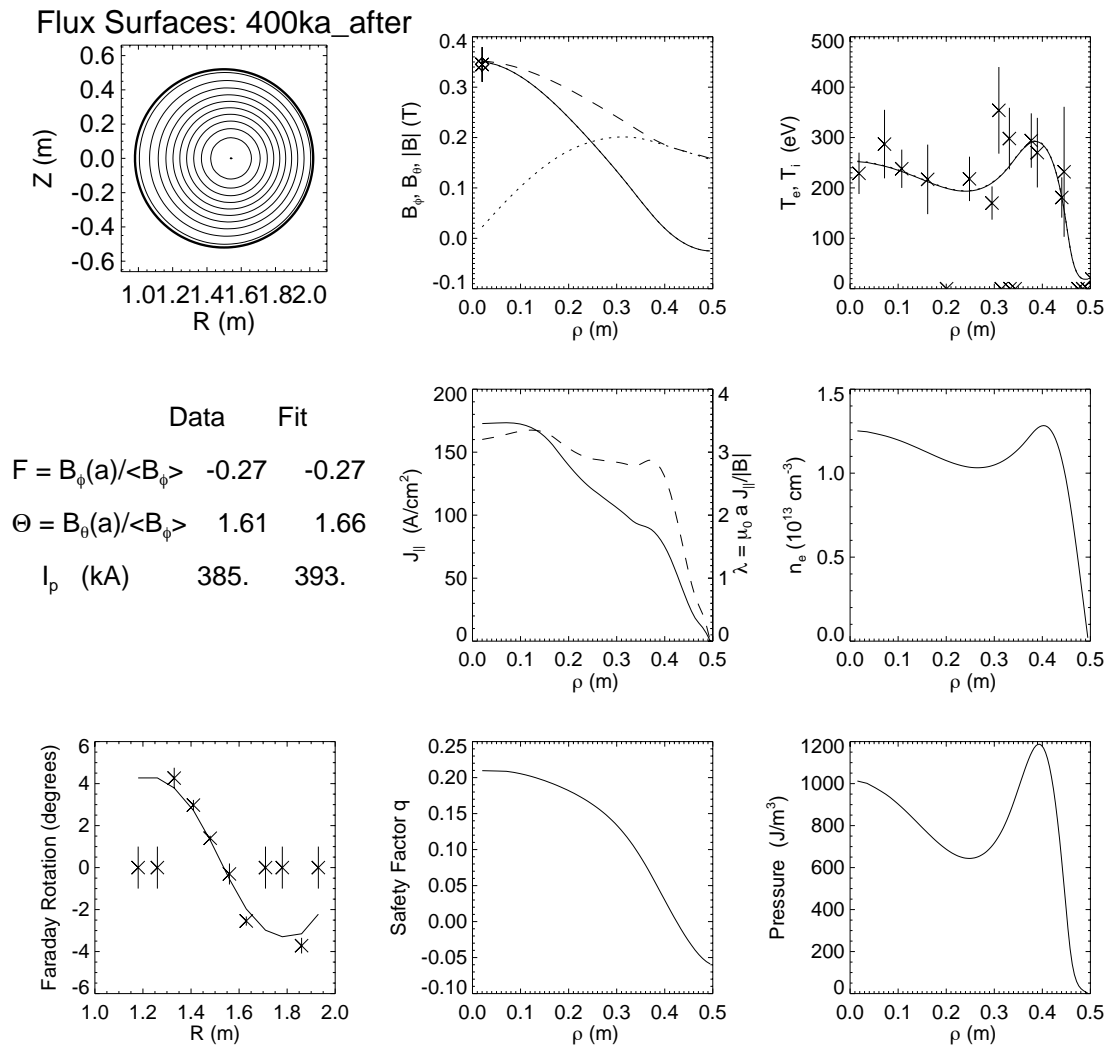


Figure 5.24: Summary of equilibrium reconstruction: 400kA standard shot immediately following a sawtooth crash.

## Flux Surfaces: ppcd\_2001\_15p6

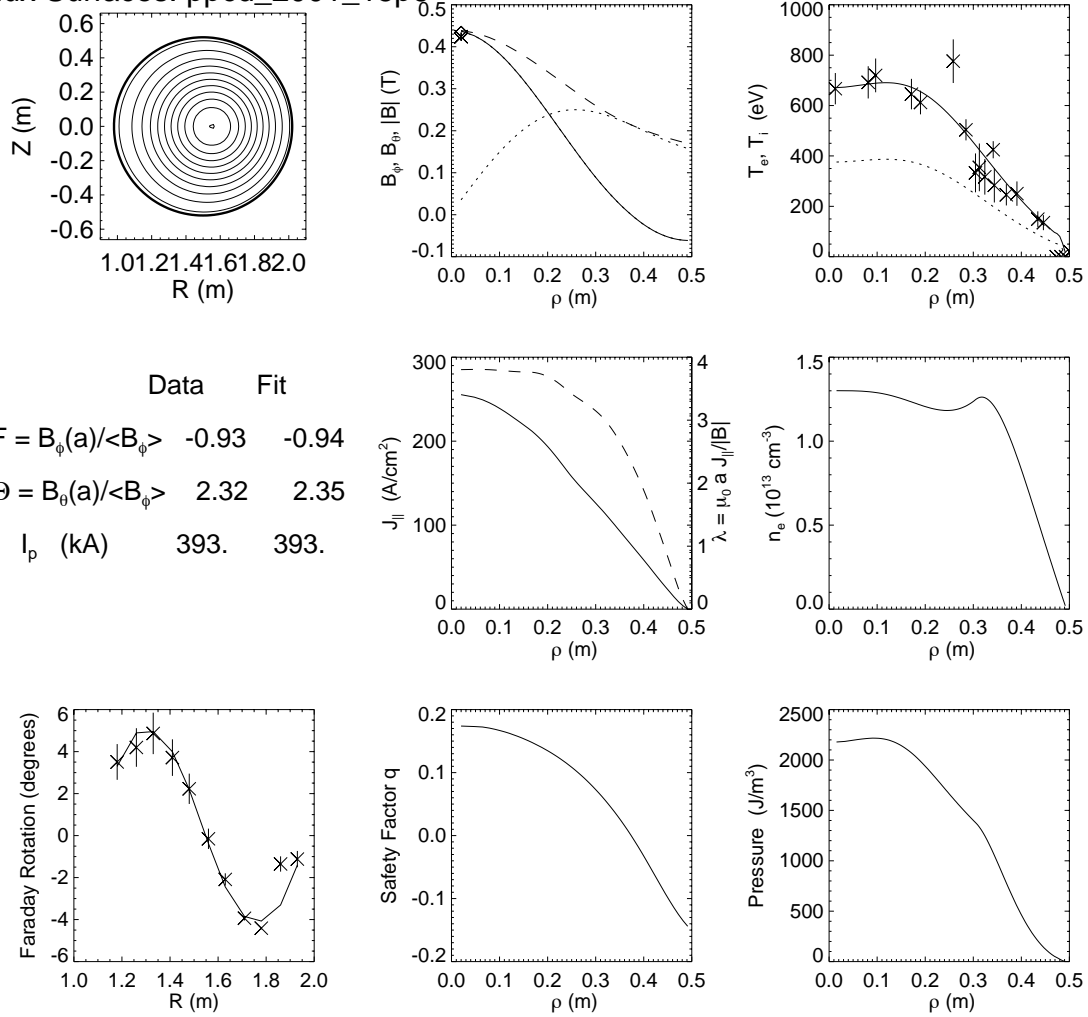


Figure 5.25: Summary of equilibrium reconstruction: 400kA PPCD shot at 15.6ms. This equilibrium is the focus of the work in this dissertation.

The current density, safety factor, magnetic field and  $\lambda$  profiles are compared prior to and following the sawtooth crash in Figure 5.26. Here, the solid line represents the equilibrium prior to the crash. The axis value of  $q$  is low (approaching the cut off of the  $m=1, n=6$  mode), while the parallel current density and  $\lambda$  profiles are peaked, indicative of an unrelaxed state. After the sawtooth crash, the expected profile flattening of both the parallel current density and  $\lambda$  due to relaxation has occurred. The axis value of  $q(0)$  has increased to above 0.20, predicting a measurable  $m=1, n=5$  mode amplitude following the sawtooth crash.

In the second comparison, shown in Figure 5.27, the same profiles are plotted for the base case (unrelaxed standard plasma) and a PPCD plasma. The results are interesting. While the parallel current density on axis peaks, the accompanying rise in toroidal field measured by MSE indicates that  $q$  and  $\lambda$  on axis are relatively constant. Furthermore, as the gradient in the parallel current density increases, the change in magnetic field actually leads to a flattening of the  $\lambda$  profile. This is consistent with the heuristic picture that tearing modes are stabilized, as gradients in  $\lambda$  (the source of free energy) decreases and magnetic shear increases (noted by the substantial change in slope of  $q$ ).

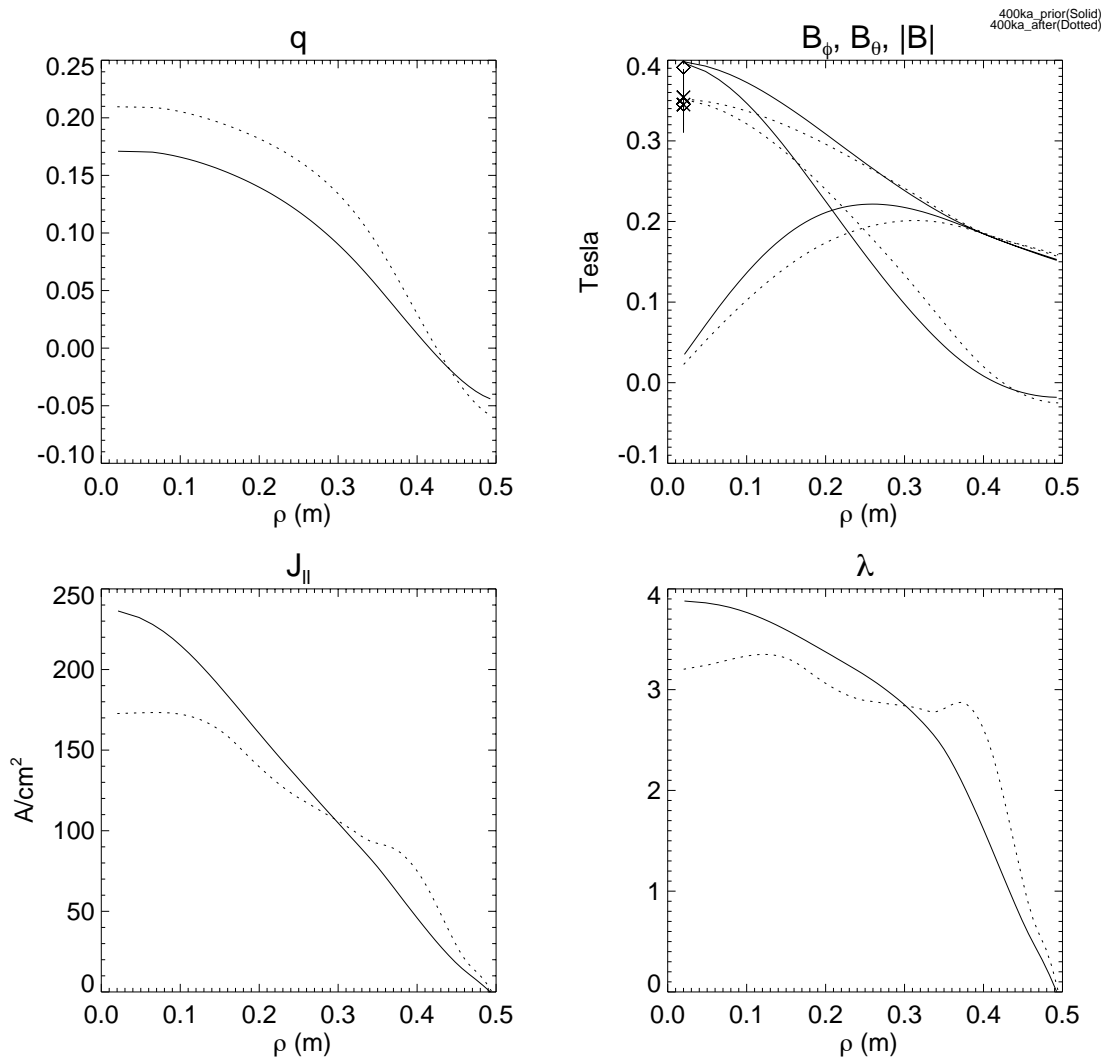


Figure 5.26: Comparison of equilibria: pre and post sawtooth crash, 400kA discharge.

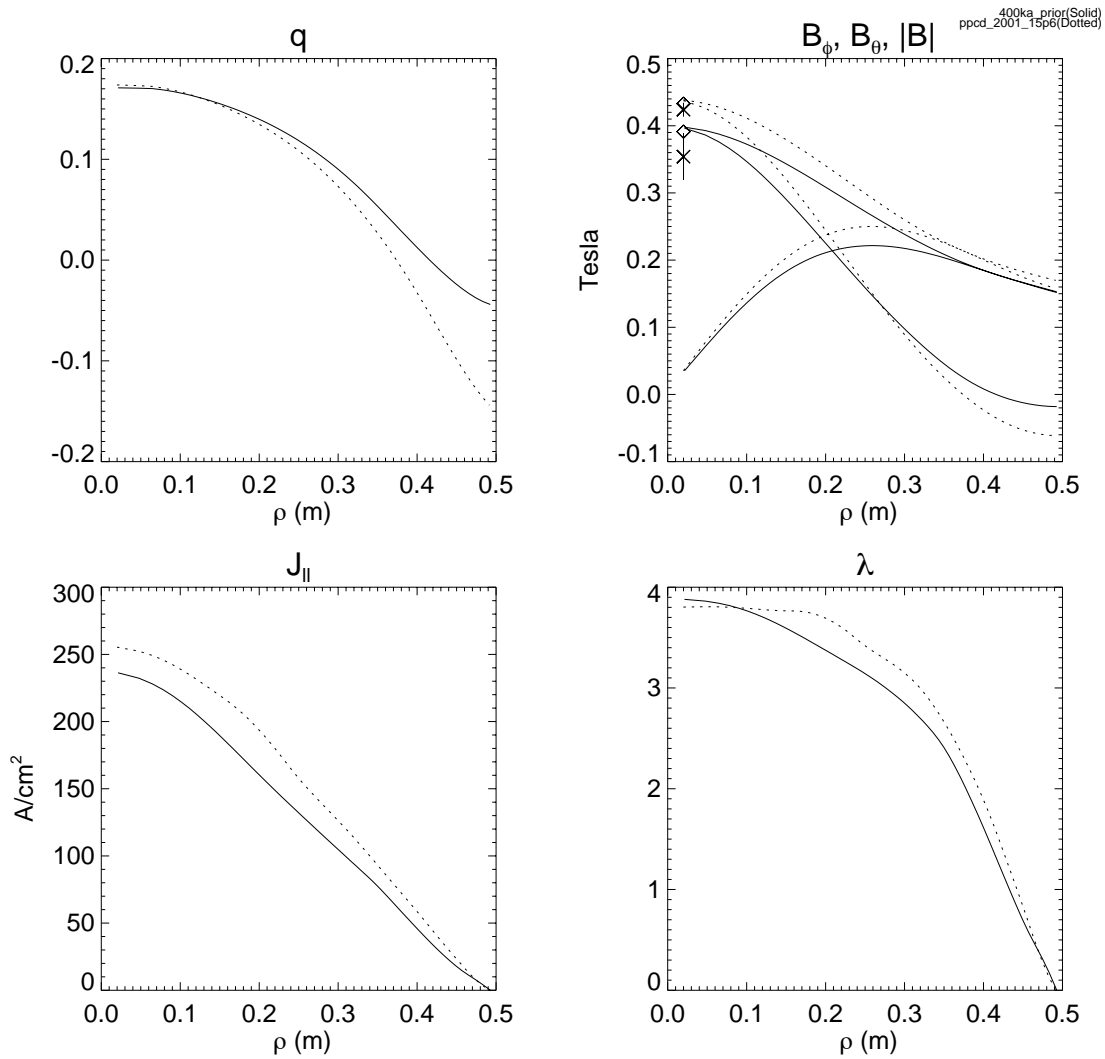


Figure 5.27: Comparison of equilibria: pre-sawtooth standard versus a PPCD discharge, 400kA discharge.

## 5.8 Analysis of 400kA PPCD Discharge

The computation of the electric field and effective resistivity profiles in the following chapters require equilibrium current density and magnetic field profiles. In order to make a comparison to the modeled resistivity profiles, an uncertainty estimate is also needed. The equilibrium, constrained by the external magnetics, polarimeter, MSE and  $q(0)$  constraint has computed, and is shown above in Figure 5.25. The uncertainty analysis method outlined in Section 5.6.1 is applied to this equilibrium, and the results are shown in Figure 5.28. With the internal diagnostics in place, the uncertainty in many of the equilibrium quantities is quite small. However, as will be elucidated in Chapter 6, the large uncertainty in the poloidal magnetic flux near the core has extreme implications on the electric field and hence power deposition profiles.

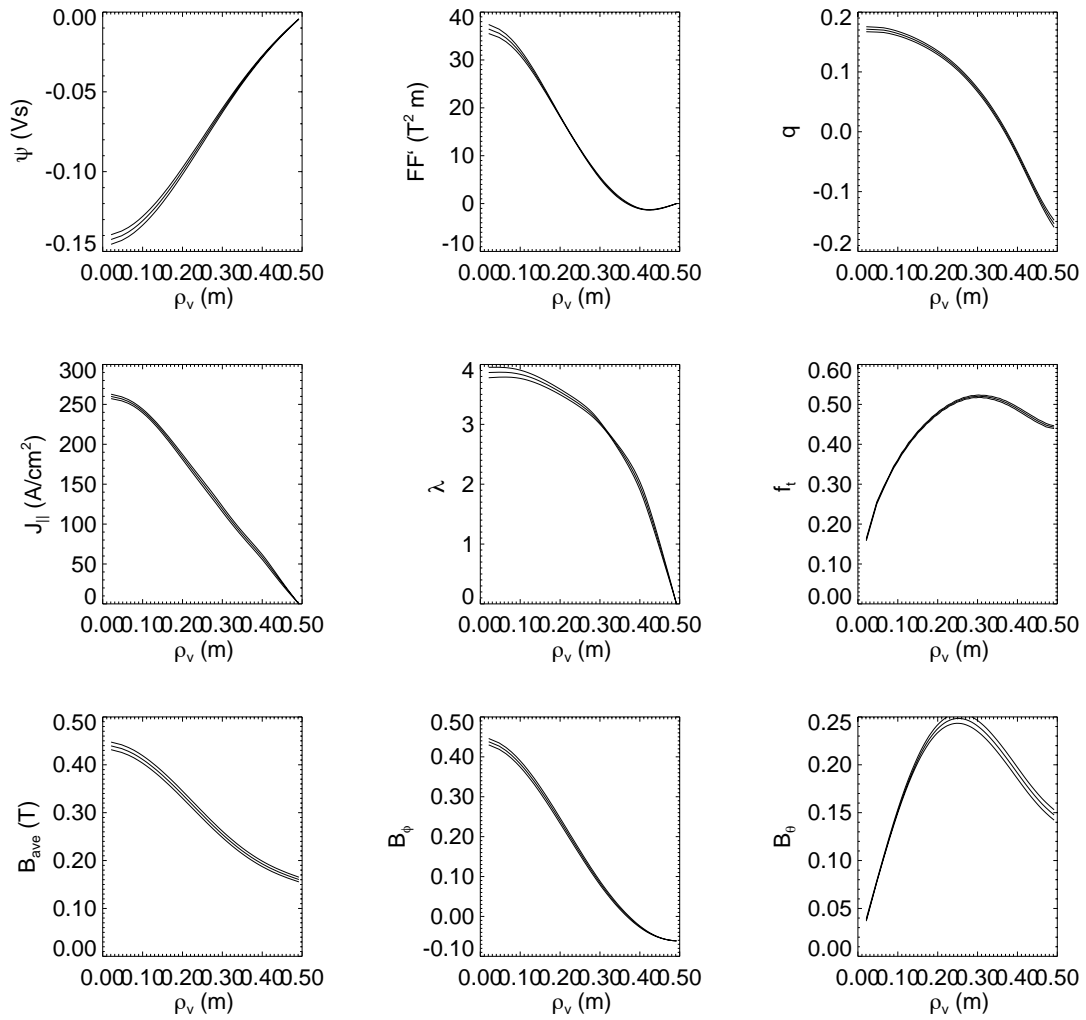


Figure 5.28: Uncertainty in computed equilibrium quantities for the 400kA PPCD discharge.

## 5.9 Summary

MSTFit is a new toroidal equilibrium reconstruction code developed for the RFP with the ability to fit data from all diagnostics. The numerical technique is a conglomeration of well developed techniques with modifications which are well suited for the Madison Symmetric Torus RFP. The free boundary toroidal current loop Green's tables have been modified to impose the boundary constraint of a close fitting conducting shell, and a full nonlinear search of parameter space is employed to find the equilibrium which best fits the data. The set of post processing routines are useful for inversion of line integrated data and facilitate particle and energy transport and MHD stability analyses. The code has been applied in this work to measure the parallel current density profile using edge magnetics, the MSE diagnostic, the FIR polarimeter and a well measured pressure profile. This result is necessary in a study of plasma resistivity through Ohm's law, performed in the remainder of this dissertation for the equilibrium reconstructed in Figure 5.25, with the uncertainty in the equilibrium quantities plotted in Figure 5.28. This information is crucial in the comparison with the modeled resistivity profiles and its experimental uncertainty.

# Bibliography

- [1] J. D. Jackson, *Classical Electrodynamics*, John Wiley and Sons, New York, NY, 1975.
- [2] W. H. Press, B. P. Flannery, S. A. Teukolsky, and W. T. Vetterling, *Numerical Recipes in C: The Art of Scientific Computing*, Cambridge University Press, New York, NY, 1988.
- [3] Nelder and Mead, *Computer Journal* **7**, 308 (1965).
- [4] J. P. Freidberg, *Ideal Magnetohydrodynamics*, Plenum Press, New York, NY, 1987.
- [5] C.-S. Chiang, *Measurement of Electrostatic Fluctuations and Particle Transport in an Improved-Confinement RFP*, PhD thesis, University of Wisconsin-Madison, 2000.
- [6] D. L. Brower, Y. Jiang, W. X. Ding, S. D. Terry, N. E. Lanier, J. K. Anderson, C. B. Forest, and D. H. Holly, *Review of Scientific Instruments* **72**, 1077 (2001).
- [7] D. Craig, D. J. Den Hartog, G. Fiksel, V. I. Davydenko, and A. A. Ivanov, *Review of Scientific Instruments* **72**, 1008 (2001).
- [8] J. Lei, U. Shah, D. R. Demers, K. A. Connor, and P. M. Schoch, *Review of Scientific Instruments* **72**, 564 (2001).
- [9] S. Hokin, A. Almagri, M. Cekic, B. Chapman, N. Crocker, D. Den Hartog, G. Fiksel, J. Henry, D. Holly, H. Ji, S. Prager, J. Sarff, W. Shen, M. Stoneking, and C. Watts, Global confinement and edge transport measurements in the MST reversed field pinch, PLP Report 1123, University of Wisconsin, Madison, 1993, Poster Presented at 20th EPS Conference on Controlled Fusion and Plasma Physics.
- [10] P. R. Bevington and D. K. Robinson, *Data Reduction and Error Analysis for the Physical Sciences*, McGraw-Hill, New York, NY, 1992.
- [11] R. A. Arndt and M. H. MacGregor, *Methods in Computational Physics* **6**, 253 (1966).

## Chapter 6

# Determination of the Inductive Electric Field Profile

### Abstract

Determination of the parallel inductive electric field profile is fundamental to understanding the electrical resistivity. Under some conditions  $E_{\parallel}(\rho)$  can be determined from the evolution of flux determined from a time sequence of equilibria. This method has been successful in finding  $E_{\parallel}$  in standard MST discharges, where the electric fields are mainly governed by the resistive decay of magnetic flux. This technique, however, is inadequate when the equilibrium is rapidly changed by an applied electric field at the onset of PPCD. A new technique solves the time derivative of the Grad-Shafranov equation and finds the profile of  $\frac{\partial J_{\phi}}{\partial t}$  which best fits the experimental data. In this development, measured edge loop voltages and time derivatives of the signals used in equilibrium reconstruction are fit to determine the spatial profiles of the time derivatives of magnetic flux.

## 6.1 Introduction

The study of current diffusion in the RFP is not approachable without a measure of the inductive electric field profile. Under the assumptions of axisymmetry and a simple Ohm's law,  $E_{||} = \eta J_{||}$ , the only sources for electric fields are the applied voltages at the toroidal and poloidal gaps and inductive electric fields arising from the resistive consumption of magnetic flux. Thus, accurate modeling of the time rate of change of magnetic flux yields the loop voltage (and electric field) profiles and it is clear that the time derivative of the magnetic equilibrium must be determined.

Two independent techniques have been employed to find electric field. First, a time series of reconstructed equilibria has been constructed and a finite differencing technique approximates the time derivative. The second is a new technique, which solves the time derivative of the Grad-Shafranov equation constrained by time derivatives of magnetic signals. Both methods have a limited range of applicability. The finite differencing is well suited to slowly varying discharges in which magnetic flux is evolving linearly in time (approximately constant voltage).

Together with the current profile determined from MSTFit, the electric field profiles specify the necessary information to investigate Ohm's law, the deposition of power into the plasma, and plasma electrical resistivity. Although not fundamental to this thesis, the total dissipated power calculation serves as an evaluation of the results. In order to extract the resistivity profile in the absence of MHD fluctuations, it is necessary to have both the  $J_{||}$  and  $E_{||}$  profiles. The current density is a standard output of the equilibrium reconstruction; the electric field can be calculated from the derivative of the equilibrium through Faraday's law. Namely, the toroidal loop voltage and hence electric field are calculated from the time rate of change of poloidal flux. Similarly, the poloidal loop voltage and electric field are found from the time derivative of toroidal flux. Both loop voltage profiles are determined to within a constant boundary term, set by the voltage measured at their respective gaps.

### 6.1.1 Calculation of Parallel Electric Field

Both the poloidal and toroidal inductive electric fields can be found from Faraday's Law and the modeled time rate of change of magnetic flux. By the definition of poloidal flux

$$\psi_{pol} = \int_{R_b}^R \mathbf{B}_\theta \cdot d\mathbf{A} = \psi_b + \psi \quad (6.1)$$

the value is determined to within a boundary value corresponding to the flux in the core. Faraday's law states that the time rate of change of magnetic flux leads to an electric field developing in a sense to oppose the change, by definition

$$\begin{aligned} \oint E_\phi \cdot dl &\equiv -\frac{d\psi}{dt} \\ &= -\frac{\partial\psi_b}{\partial t} - \frac{\partial\psi(R, Z)}{\partial t} \end{aligned} \quad (6.2)$$

where  $\frac{\partial\psi_b}{\partial t}$  is the opposite of the voltage at the poloidal gap. The toroidal loop voltage profile is then

$$V_\phi(R, Z) = \left( V_{pg} - \frac{\partial\psi(R, Z)}{\partial t} \right) \quad (6.3)$$

$$E_\phi(R, Z) = \frac{1}{2\pi R} \left( V_{pg} - \frac{\partial\psi(R, Z)}{\partial t} \right). \quad (6.4)$$

Similarly, the toroidal flux (and its time derivative) can be computed, allowing the poloidal loop voltage and electric field to be calculated. The toroidal flux is defined by

$$\Phi = \int B_\phi dA = \iint \frac{F(\psi(R, Z))}{R} dA \quad (6.5)$$

where the integration is over a subsection of the poloidal area. The poloidal loop voltage is then

$$\begin{aligned}
 V_\theta &\equiv \oint_l E_\theta \cdot dl \\
 &= -\frac{d\Phi}{dt} \\
 &= -\frac{d}{dt} \int_{A,l} \frac{F}{R} dA
 \end{aligned} \tag{6.6}$$

where  $l$  is a closed path defining the area  $A$ ; or

$$V_\theta(\psi) = -\frac{d}{dt} \int_{\psi_0}^{\psi} \left\langle \frac{F(\psi)}{R} \right\rangle \frac{\partial A}{\partial \psi} d\psi \tag{6.7}$$

in terms of flux coordinates.

For studies of resistivity, the parallel component of the electric field is required

$$E_{||} = \frac{\langle \mathbf{E} \cdot \mathbf{B} \rangle}{B} = \frac{1}{B} (\langle E_\theta B_\theta \rangle + \langle E_\phi B_\phi \rangle) \tag{6.8}$$

where  $\langle \rangle$  denotes flux surface average. The two terms to calculate are found in terms of the results for loop voltages above. The toroidal term is just a simple execution of the flux surface average

$$\langle E_\phi B_\phi \rangle = \left\langle \frac{V_\phi}{2\pi R} B_\phi \right\rangle = \frac{F}{2\pi} \left\langle \frac{\partial \psi}{\partial t} \Big|_{R,z} \right\rangle \tag{6.9}$$

where the toroidal voltage is determined in equation 6.4 from the rate of change of poloidal flux.

The poloidal term is determined by considering the definition of the flux surface average

$$\begin{aligned}
 \langle E_\theta B_\theta \rangle &= \frac{\oint \frac{E_\theta B_\theta dl}{B_\theta}}{\oint \frac{dl}{B_\theta}} \\
 &= \frac{\oint E_\theta dl}{\oint \frac{dl}{B_\theta}} \\
 &\equiv \frac{\frac{d}{dt} \Phi}{\oint \frac{dl}{B_\theta}}
 \end{aligned} \tag{6.10}$$

where the last step has utilized Faraday's law and  $\Phi$  is the toroidal flux. There are two components which contribute to  $\frac{d}{dt}\Phi$ : the change of toroidal magnetic field and movement of the flux surface.

The time rate of change of toroidal flux must be determined by

$$\begin{aligned}\frac{d}{dt}\Phi &= \frac{d}{dt} \int_0^a B_\phi dA = \int_0^a \frac{\partial B_\phi}{\partial t} 2\pi\rho d\rho + \int B_\phi \frac{d}{dt} dA \\ &= \int_0^a \frac{\partial B_\phi}{\partial t} 2\pi\rho d\rho + \oint B_\phi \hat{\phi} \cdot (d\mathbf{l} \times v_\rho)\end{aligned}\quad (6.11)$$

where the change in area is written in terms of the velocity of a constant  $\rho$  surface. This velocity is found by considering the total time derivative of the constant  $\rho$  surface

$$\frac{d}{dt}\rho = 0 = \left. \frac{\partial \rho}{\partial t} \right|_{R,Z} + \mathbf{v} \cdot \nabla \rho \quad (6.12)$$

and since  $\nabla \rho \equiv 1$ ,

$$v_\rho = - \frac{1}{|\nabla \rho|} \left. \frac{\partial \rho}{\partial t} \right|_{R,Z} = - \left. \frac{\partial \rho}{\partial t} \right|_{R,Z} \quad (6.13)$$

where  $v_\rho$  is the component of the velocity normal to the surface. The second term on the right hand side of equation 6.11 is

$$\oint B_\phi v_\rho dl = \left\langle B_\phi B_\theta \frac{\partial \rho}{\partial t} \right\rangle \oint \frac{dl}{B_\theta} \quad (6.14)$$

which is a computable term from the equilibrium and derivative quantities. Collecting terms from equations 6.9 through 6.14 gives a parallel electric field

$$E_{||} = \frac{1}{B} \left\langle \frac{V_\phi}{2\pi R} B_\phi \right\rangle + \int_0^a \frac{\partial B_\phi}{\partial t} 2\pi\rho d\rho + \left\langle B_\phi B_\theta \frac{\partial \rho}{\partial t} \right|_{R,Z} \right\rangle \oint \frac{dl}{B_\theta}. \quad (6.15)$$

This calculation requires the equilibrium magnetic fields, the internal toroidal loop voltage profile,

the time derivative of the toroidal flux, and the time derivative of the flux surface coordinate  $\rho$ . These are calculated in one of two ways, through the finite difference technique (Section 6.2.1) or through the time derivative fitting technique (Section 6.3.5).

Figure 6.1 shows the results of these calculations using the finite difference technique on standard MST plasmas where  $\langle \mathbf{E} \cdot \mathbf{B} \rangle$  is plotted, along with the toroidal (dotted) and poloidal (dashed) contributions. Plot a) contains the toroidal and poloidal loop voltage profiles, b) is the equilibrium magnetic field profiles, c) is the equilibrium current density profile, d) is the  $\langle \mathbf{E} \cdot \mathbf{J} \rangle$  power deposition profile, e) is the parallel, poloidal and toroidal electric field profiles, f) is the  $\langle \mathbf{E} \cdot \mathbf{B} \rangle$  profile, g) is the  $\langle \mathbf{J} \cdot \mathbf{B} \rangle$  profile, and h) is the effective resistivity profile.

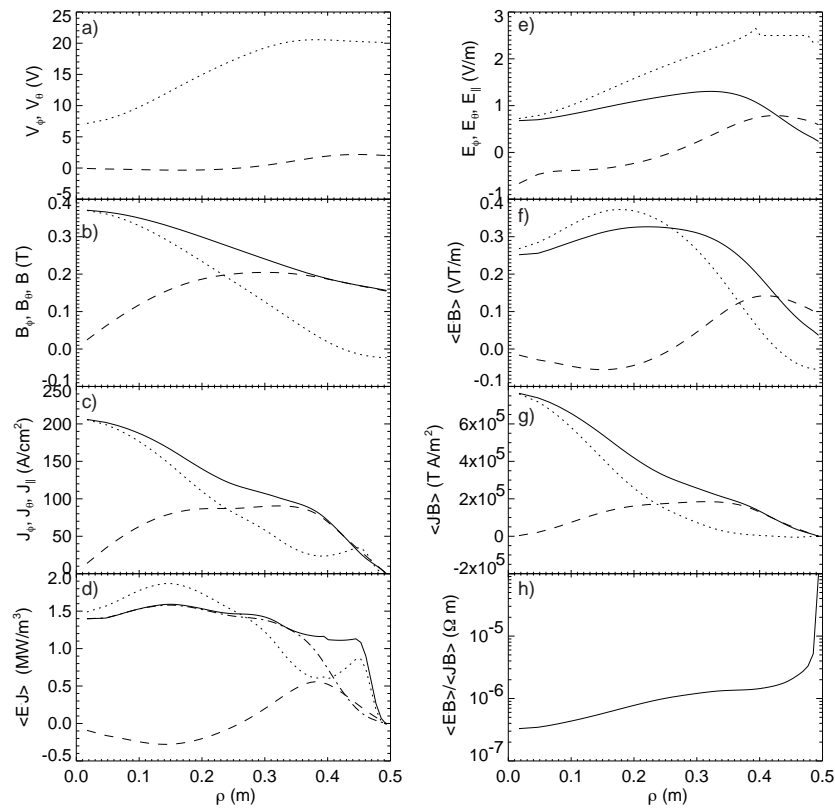


Figure 6.1: Plotted here are the results of the finite difference technique applied to the standard plasma. Total fields are drawn in solid lines, while dotted lines indicate toroidal and dashed poloidal contributions.

### 6.1.2 Power Deposition Profile

One of the primary results of the above development is the ability to calculate the power deposition profile, useful in heat transport and other studies. For a single charge  $q$ , the rate of work done by external electromagnetic fields  $\mathbf{E}$  and  $\mathbf{B}$  is given by the scalar product of the Lorentz force and velocity, or  $P = q\mathbf{v} \cdot \mathbf{E}$ . The magnetic force is perpendicular to the velocity and does not contribute to dissipation. For a continuous distribution of charge

$$P = \int \mathbf{E} \cdot \mathbf{J} dV \quad (6.16)$$

is the power deposited inside some volume. Without a modeled electric field profile, the total Ohmic input power can be estimated in the nearly MHD-free PPCD plasmas by asserting that  $E_{||} = \eta J_{||}$ .

An alternative approach that makes no assumptions about Ohm's law is generally better suited to the problem. Using Maxwell's equations to eliminate current density, one obtains[1]

$$\mathbf{E} \cdot \mathbf{J} = -\frac{d}{dt} W_{mag} - \nabla \cdot \mathbf{S} \quad (6.17)$$

where  $W_{mag} = \frac{B^2}{2\mu_0}$  is the magnetic energy density and  $\mathbf{S}$  is the Poynting vector given by

$$\mathbf{S} = \frac{1}{\mu_0} \mathbf{E} \times \mathbf{B} \quad (6.18)$$

which is the electromagnetic energy flow through a surface (units of energy per unit area per unit time). In order to compute the flux surface average of the Poynting flux and its divergence, it is useful to work with the total power through the surface

$$P = S_r A = \frac{1}{\mu_0} (2\pi R 2\pi \rho E_\theta B_\phi - 2\pi R 2\pi \rho E_\phi B_\theta) \quad (6.19)$$

where the area of a surface is  $2\pi R 2\pi\rho$ . The first term on the right hand side of equation 6.19 is found directly from the equilibrium and derivative quantities

$$2\pi R 2\pi\rho E_\theta B_\phi = 2\pi\langle RB_\phi\rangle\langle V_\theta\rangle \quad (6.20)$$

where  $\langle V_\theta\rangle$  is the product of the poloidal electric field and length. The second term in the right hand side is easily computed by integrating around the poloidal path to complete the area

$$2\pi R 2\pi\rho E_\phi B_\theta = \oint V_\phi B_\theta dl = \langle V_\phi B_\theta^2\rangle \oint \frac{dl}{B_\theta} \quad (6.21)$$

and writing the product of the toroidal electric field and distance as  $V_\phi$ . In the final step above, the definition of the flux surface average has been utilized to obtain a form easily computed from the equilibrium and derivative quantities.

Recalling equation 6.17, the radial component of  $\nabla \cdot \mathbf{S}$  and derivative of stored magnetic energy are required to compute the power deposition. The divergence is calculated as

$$\nabla \cdot \mathbf{S}_r = \frac{1}{\rho} \frac{\partial}{\partial \rho} (\rho S_r) = \frac{1}{A} \frac{\partial}{\partial \rho} (A S_r) \quad (6.22)$$

where the fact that the area is linear in  $\rho$  is used to incorporate the total power through a surface (equation 6.19). The remaining term to calculate is the time rate of change of magnetic energy density which is determined on the R,Z grid in the finite difference development; a simple flux surface average is computed. The results are shown in Figure 6.2, where the total power deposition is plotted along with the individual components of  $\nabla \cdot \mathbf{S}$  (dotted line) and the  $\frac{d}{dt} W_{mag}$  (dashed line).

The beauty of this result is simple: the power deposition profile is determined without a measurement of  $Z_{eff}$ . It offers no insight whatsoever as to the nature of Ohm's law or resistivity in

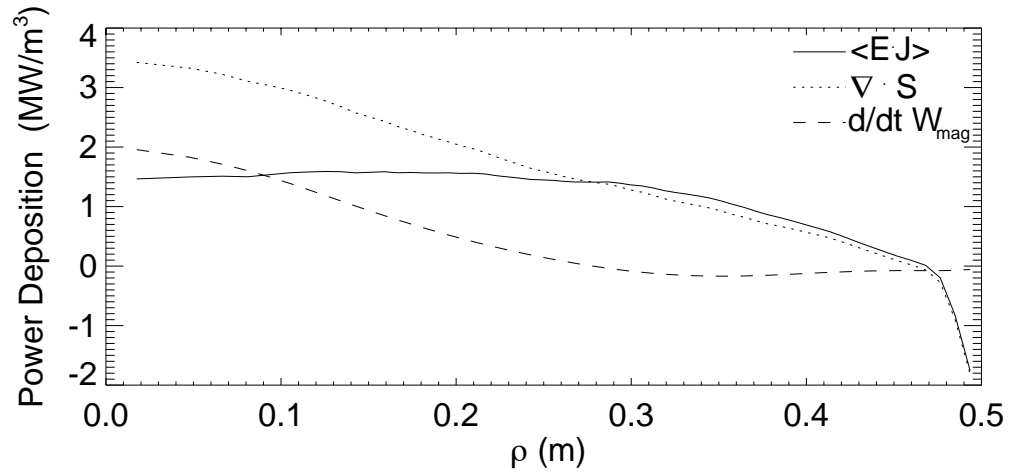


Figure 6.2: The computed power deposition profile through Poynting flux methods applied to the 400kA standard discharge. The dotted line is the divergence of  $S$ , dashed line is rate of change of stored magnetic energy.

the reversed field pinch, so it is not of primary interest in this work. However, heat transport and energy confinement calculations can proceed without a measurement of  $Z_{eff}$ . For the case shown here, the total electromagnetic power incident on the plasma boundary (Poynting flux through the shell) is 7.6MW, with 1.0MW going into a volume integrated net increase of magnetic energy. The net Ohmic input power is then 6.6MW which corresponds to an energy confinement time[2] of roughly 1.2ms which is consistent with previous estimates.

## 6.2 Finite Difference of Equilibria

The inductive electric field profiles in a plasma can be found by taking finite differences of a time series of the magnetic equilibria[3]. This method is quite straightforward in its application to MSTFit results. The output of the code specifies the flux functions  $F$  and  $P$ , as well as the

toroidal current density and poloidal flux on the two dimensional grid.

After fitting several equilibria in time, (in this development, 4 fits spaced evenly at half-millisecond intervals are investigated), the values of  $F$ ,  $P$ ,  $\psi$  and all the derived quantities are fit to a line versus time at each point in space. Computations of electric fields and voltages are closely related to the equilibrium output, e.g. the toroidal loop voltage at any point in the plasma is the sum of contributions due to internal changes in poloidal flux and the applied boundary value

$$V_\phi(R, Z) = -\frac{\partial\psi(R, Z)}{\partial t} + V_{pg} = -\frac{\psi(R, Z)|_{t+\Delta t} - \psi(R, Z)|_t}{\Delta t} + V_{pg} \quad (6.23)$$

where the two point derivative can be replaced by a slope determined from linear regression from more equilibria.

This method inherently assumes that the equilibrium is evolving linearly in time, an assumption that must hold at some time scale according to Taylor expansion arguments. However, in the limit of small time steps the uncertainties in successive equilibria propagate to intolerably high uncertainties in the derivative as

$$\sigma_{V_\phi} = \frac{\sqrt{2}\sigma_\psi}{\Delta t}. \quad (6.24)$$

This assumption also clearly rules out this method for a series that contains a sawtooth crash, when non-inductive electric fields overwhelm the inductive contribution on a much faster time scale.

It has been empirically determined that the finite difference approach is well suited to high current standard discharges, where the sawtooth cycle approaches 6 milliseconds. In Figure 6.3, ensemble averages of the operational signals are shown along with an indication of when the equilibria in the series are computed.

There is a long period of linear evolution where magnetic flux consumption induces the parallel electric field. The linear evolution assumption holds over a two millisecond window after the

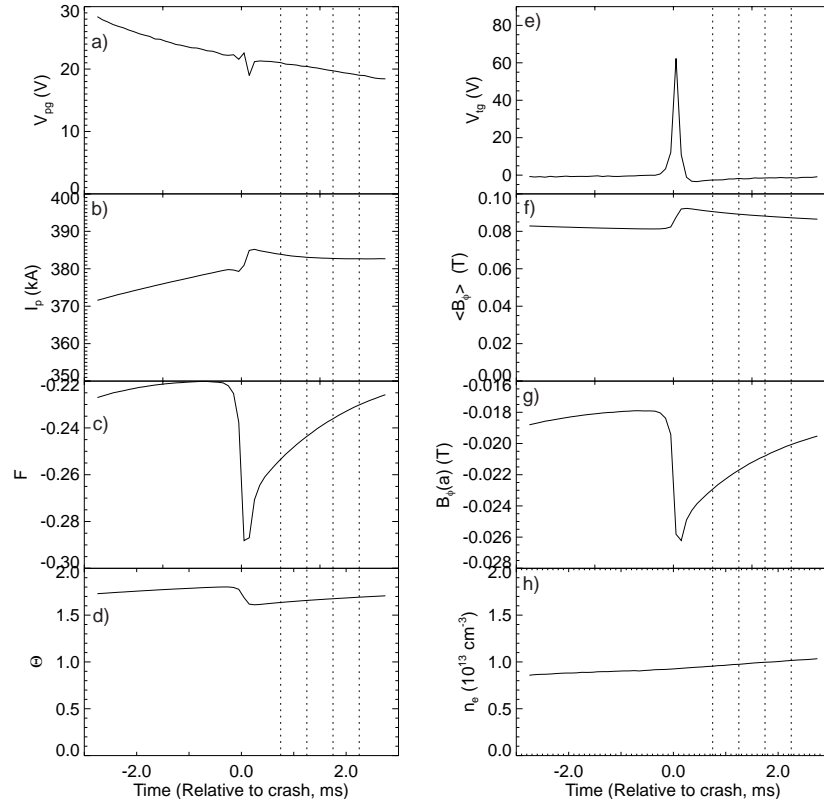


Figure 6.3: Operational signals through a sawtooth cycle. The vertical dotted lines indicate the times at which the equilibria are fit to calculate the electric field profile.

sawtooth crash, enabling a sequence of equilibria at half millisecond intervals to determine the time derivative of the magnetic equilibrium. During this interval, the applied poloidal gap voltage drops by about 2V, while the toroidal gap voltage varies even less. The small change in voltage is a prerequisite to the linear evolution assumption. As the loop voltage in the plasma is the derivative of the magnetic flux, a constant voltage is the result of a linearly changing flux. If there is a large time rate of change of voltage in the plasma, then there is a second time derivative of the magnetic flux and the linear assumption is invalid.

### 6.2.1 Application of Finite Difference Technique to Standard Plasma

The reconstructed equilibria have a finite uncertainty, and as all the available data are fit during the solution it is common to see small deviations between the data and the best fit for a given diagnostic. Two pieces of evidence here provide a promising outlook for the time slices indicated above. Figure 6.4 indicates the MSTFit reconstructed data for the four equilibria used. Although perfect

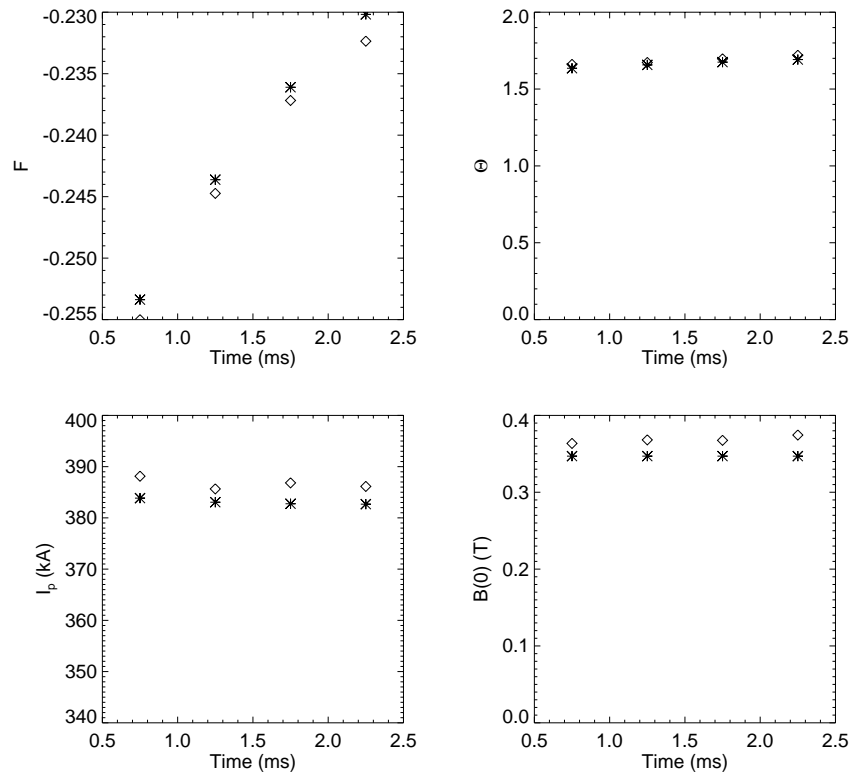


Figure 6.4: MSTFit agreement with data for four time steps after the sawtooth crash. Although the reconstructed equilibria (shown as  $\diamond$ ) systematically miss the data (shown as  $*$ ) for some diagnostics, the time derivatives seem to be well matched.

agreement between the data (shown as  $*$ ) and fit (shown as  $\diamond$ ) is not achieved, the derivatives seem to match fairly well. It is necessary to establish the linearity of the evolution on the reconstructed equilibrium on the (R,Z) grid; Figure 6.5 shows this at four sample locations which span a large range of minor radius ( $\rho = .01\text{m}$  to  $.48\text{m}$ ). Shown are the evolution of poloidal flux, toroidal

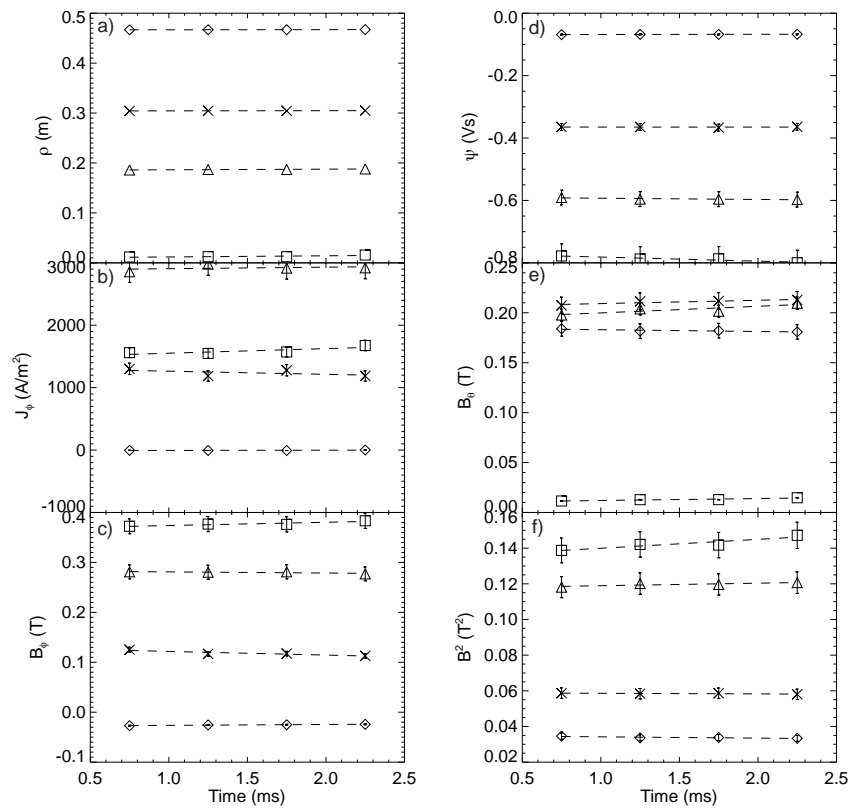


Figure 6.5: MSTFit results versus time for four sample spatial points.

current, and magnetic fields (poloidal, toroidal, total<sup>2</sup>). Although high uncertainty (particularly in the core, discussed below) is a byproduct of taking these derivatives, the standard signals are well enough behaved that this analysis gives meaningful results, presented in Figures 6.1 and 6.2.

### 6.2.2 Finite Difference Calculation in PPCD Plasma

Recalling Figure 6.3, there was a very small change ( $\lesssim 1\text{V/ms}$ ) change in the applied voltages during the linear evolution of the equilibrium in the standard discharge. Analysis following the steps above fails in PPCD discharges. Figure 6.6 is a plot of the operational signals during the

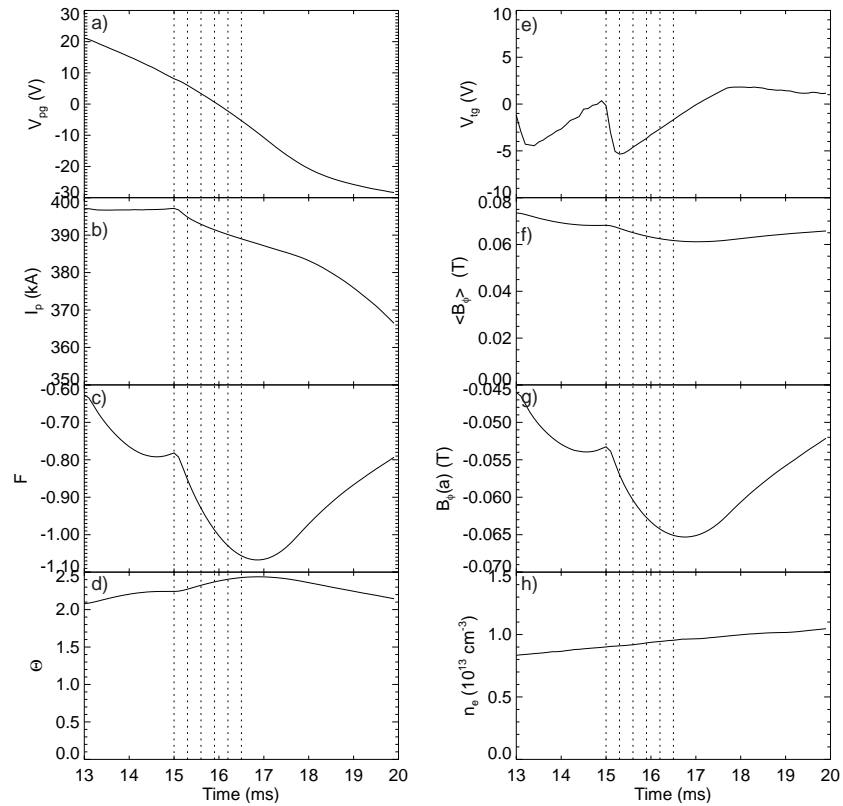


Figure 6.6: Operational signals through PPCD. The vertical dotted lines indicate the times at which the equilibria are fit to calculate the electric field profile.

evolution of PPCD and the times at which equilibria are computed for the finite difference methods.

The reconstructed equilibria (shown as  $\diamond$ ) very well match the input data (shown as  $*$ ) in Figure 6.7.

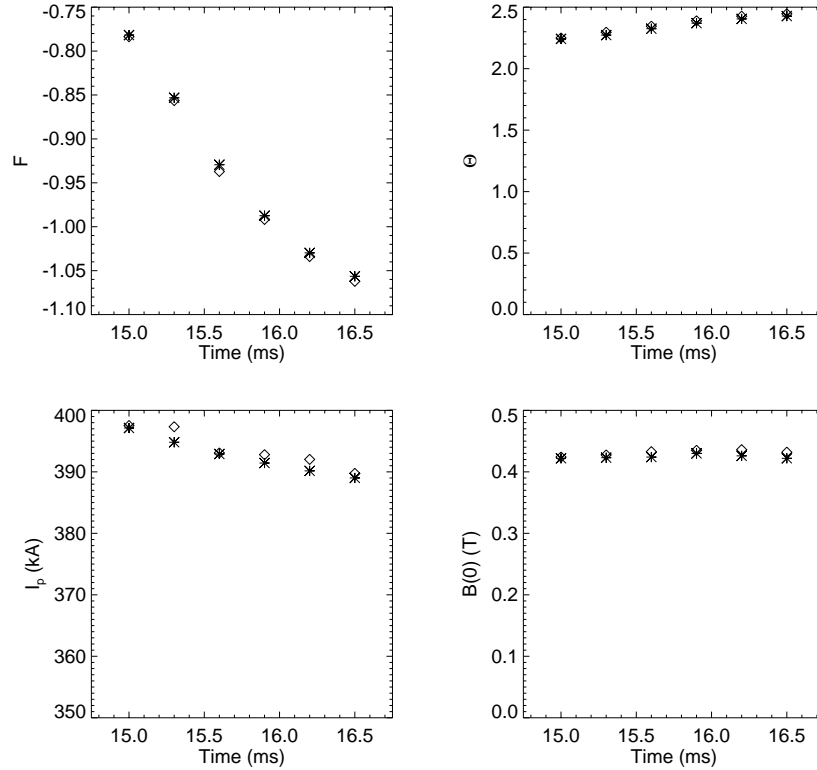


Figure 6.7: MSTFit results for six time steps during PPCD. Reconstructed equilibria are plotted as  $\diamond$ , while the data are plotted as \*. Good agreement is achieved in these fits.

The evolution of the reconstructed equilibria with time is shown in Figure 6.8. Although the change in flux appears to be well behaved, the actual voltage in the plasma is the sum of the boundary value and the  $\frac{\partial\psi}{\partial t}$  components; in the PPCD discharge the boundary value (gap voltage) is changing rapidly. The case is further weakened by considering the uncertainty in the measured slope. Figure 6.9 demonstrates that in the central region, the uncertainty in the slope is quite large. The allowed range of slopes that fit these data varies between  $\pm 50$  Volts. Although this high core uncertainty affects the standard results to some degree, it is much better than the PPCD case as the time steps can be taken significantly farther apart without violating the linear evolution assumption. Blindly proceeding with this analysis in PPCD discharges often leads to unphysical

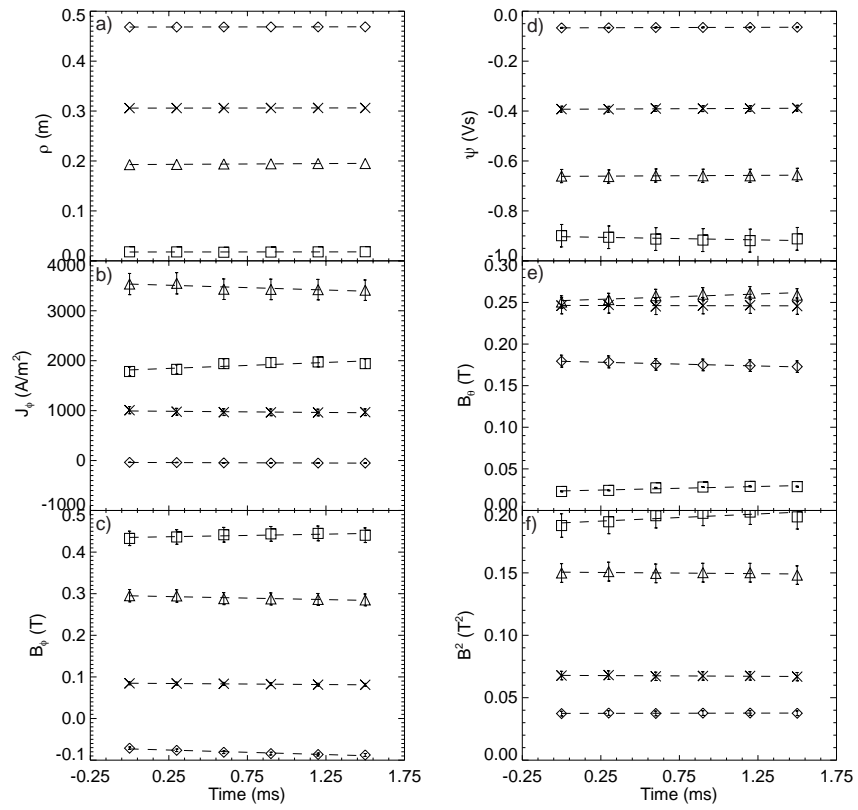


Figure 6.8: MSTFit results versus time for four sample spatial points, PPCD plasma.

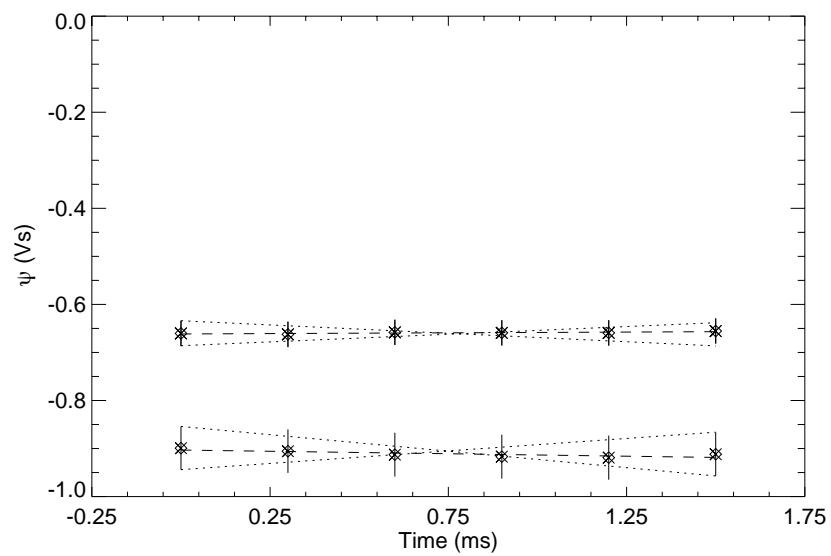


Figure 6.9: The upper line is at  $\rho = .14m$ , the lower is at  $.03m$ . Uncertainties in flux are computed as described in Section 5.6. The allowed slope ranges from significant and positive to significant and negative.

results of negative current in the core and a negative total input power.

### 6.3 Time Derivative Fitting

The failure of the finite time step method of finding the electric field for PPCD plasmas, due to the rapidly changing applied gap voltages, has motivated a new technique. The nonlinear minimization technique used by MSTFit can be applied to the similar problem of determining the time derivative of the MHD equilibrium and hence the inductive electric field. This facilitates studies of the non-inductively (dynamo) driven current, dissipation of Poynting flux and Ohmic input power in PPCD discharges. The Grad-Shafranov equation in this development is written as

$$J_\phi = \frac{2\pi F F'}{\mu_0 R} + 2\pi R P' \quad (6.25)$$

or the toroidal current is described by two profiles. By assumption, changes in toroidal current must be related to changes in  $F$  and  $P$ , or

$$\left. \frac{\partial J_\phi}{\partial t} \right|_{R,Z} = \left. \frac{\partial}{\partial t} \right|_{R,Z} \left( \frac{2\pi F F'}{\mu_0 R} + 2\pi R P' \right) \quad (6.26)$$

where the partial time derivative must be taken to obtain the working form of this equation. As MSTFit solves the Grad-Shafranov equation on a fixed grid in real cylindrical coordinates  $(R, Z)$ , the full time derivative of the toroidal current density is

$$\left. \frac{\partial J_\phi}{\partial t} \right|_{R,Z} = \frac{2\pi}{\mu_0 R} \left[ \left. \frac{\partial F}{\partial t} \right|_\psi F' + F \left. \frac{\partial F'}{\partial t} \right|_\psi + (F'^2 + F F'') \left. \frac{\partial \psi}{\partial t} \right|_{R,Z} \right] + 2\pi R \left( \left. \frac{\partial P'}{\partial t} \right|_\psi + P'' \left. \frac{\partial \psi}{\partial t} \right|_{R,Z} \right). \quad (6.27)$$

Extending the chain rule to include derivatives of  $R$  and  $Z$  is unnecessary for the fixed grid.

This equation is then iteratively solved in a fashion similar to the equilibrium solution. The

profiles of  $F$ ,  $p'$  and  $\psi$  (and thus  $F'$ ,  $F''$  and  $p''$ ) are supplied by the equilibrium solution, requiring two free functions  $\frac{\partial F}{\partial t}$  and  $\frac{\partial p}{\partial t}$  to be specified. In practice, these functions of poloidal flux are mapped onto a normalized flux grid as in MSTFit.

Due to the geometrical nature of the Green's function relating toroidal current density to poloidal flux (recall Section 5.2.2), this inversion is identical to the equilibrium modeling

$$\psi = \mathbf{G} \cdot \mathbf{J}_\phi \Rightarrow \frac{\partial \psi}{\partial t} = \mathbf{G} \cdot \frac{\partial \mathbf{J}_\phi}{\partial t}. \quad (6.28)$$

An iterative solution to the Grad-Shafranov equation is necessary for the equilibrium reconstruction as it is inherently cast in a transcendental form due to the relationship of current, flux and the free functions  $F(\psi)$  and  $p(\psi)$ . This is not the case for the time derivative fitting, as the free functions are functions of the determined poloidal flux, not its time derivative. A non-iterative solution technique is discussed as future work (Section 7.3.2), however instead of inverting the somewhat involved matrix equation, the technique employed here is a reliable iterative method paralleling the MSTFit algorithm.

### 6.3.1 Evaluation of Solution

After determining  $\frac{\partial \psi}{\partial t}$ , the time derivative of the equilibrium is specified for a given iteration of the free parameters. As in the equilibrium calculation, a set of predicted signals must be compared with the measurements. Instead of fitting equilibrium data such as magnetic field, plasma current, safety factor or polarimetry signals, the focus is now on the time derivatives of these types of signals. There are several diagnostics that give useful time derivative information of both edge and internal magnetics, summarized in Table 6.1.

Diagnostic	Constraints
$\frac{d}{dt} I_p$	$\frac{d}{dt}$ Total poloidal flux
$\frac{d}{dt} F$ and $\frac{d}{dt} \Theta$	Boundary value of $\frac{d}{dt} B_\phi$
$V_{tg}$	Derivative of total toroidal flux
$V_{pg}$	Boundary value of $V_\phi$
Poloidal Array	$\frac{d}{dt} \beta_p$ and $\frac{d}{dt} l_i$
MSE	$\frac{d}{dt} B_\phi(0)$

Table 6.1: Current set of diagnostics fit in solution to the time derivative of the Grad-Shafranov equation.

### 6.3.2 Edge Magnetics

The edge magnetic diagnostics fundamental to the equilibrium calculation are also utilized in the derivative fitting. The time derivative of the total plasma current is easily fit on each iteration by totaling the rate of change of toroidal current density on the 2D grid over area. The time rate of change of toroidal flux (as measured by the toroidal gap voltage) is similarly fit by totaling the time rate of change of toroidal magnetic field over area on the entire grid. The time rate of change of toroidal field at the wall is exactly reproduced, as the computation of  $\frac{\partial F}{\partial t}$  is computed by integration of its gradient, and the additive constant is set by the edge data. The poloidal array of  $B_\theta$  coils provides useful information as well. The derivative of each signal  $\frac{\partial B_\theta(a, \theta)}{\partial t}$  as a function of angle shows a definite spatial structure, approximated by m=0 and m=1 nearly up-down symmetric behavior. These data are very easy to fit with the same Green's table used to predict the field in the MSTFit equilibrium reconstruction.

### 6.3.3 Internal Magnetics

#### Motional Stark Effect

The MSE measurement of on axis B field is a very strong constraint on the equilibrium reconstruction; likewise, the rate of change of B(0) is a very strong constraint on the time derivative fitting. The fitting of the data is quite easy compared to the acquisition of the data. Until very recent upgrades<sup>1</sup> the time resolution of the MSE diagnostic was poor. Nonetheless, through ensembling techniques and variation of neutral beam injection time, the evolution of the central field can be measured. Measurements at several time slices throughout PPCD on a 1.5ms time base are linearly interpolated to the time slice of interest.

Fitting is trivial as

$$\frac{d}{dt}B_\phi = \frac{\frac{d}{dt}F}{R} = \frac{\frac{\partial F}{\partial t} + F' \frac{\partial \psi}{\partial t}}{R} \quad (6.29)$$

where  $F$  and  $F'$  are specified by the equilibrium, and  $\frac{\partial F}{\partial t}$  and  $\frac{\partial \psi}{\partial t}$  are provided by the current iteration of the derivative of the equilibrium.

This proves to be a very powerful constraint, as most of the unphysical results obtained in the finite difference technique of PPCD discharges lead to predicted signals that are in disagreement with the limited B(0) evolution data.

#### Polarimeter

An enigmatic internal diagnostic in the time derivative fitting is the polarimeter. The fitting is somewhat involved and uncertain due to the number of inversions required, however the potential elegance of this constraint makes it hard to ignore. An inversion of the time derivative of the

---

<sup>1</sup>To be implemented, July 2001.

electron density brings about a fair amount of error. Recall equation 5.43

$$\phi \text{ [degrees]} = 1.5 \times 10^{-20} \lambda^2 \times 10^{-3} \int_0^L n_e B_Z dl. \quad (6.30)$$

Utilization of the time derivative of the polarimetry signals requires a measurement of the density and the derivative of the density. The time derivative of the density on a given FIR chord is

$$N = \int_0^L n_e dl \rightarrow \frac{dN}{dt} = \int_0^L \frac{dn_e}{dt} dl = \int_0^L \left( \frac{\partial n}{\partial t} + \frac{\partial n(\psi)}{\partial \psi} \frac{\partial \psi}{\partial t} \right) dl \quad (6.31)$$

where both contributions are measured. Similarly the derivative of the Faraday rotation signal is

$$\frac{d\phi}{dt} = \alpha \frac{d}{dt} \int_0^L n_e B_Z dl = \alpha \int_0^L \frac{dn_e}{dt} B_Z dl + \alpha \int_0^L n_e \frac{dB_Z}{dt} dl. \quad (6.32)$$

The total time derivative for the density consists of two terms, the sum of which is measured by the interferometer. Inversion of the signals yields a total  $\frac{dn_e}{dt}$  as a function of flux and can be mapped onto the (R,Z) values of the chords for integration. The derivative of the vertical magnetic field is quite easy to find, as the Green's table used for computing the flux along the (R,Z) values of the FIR chords is also used to compute the magnetic field there,

$$\begin{aligned} \psi_{\text{FIR}} &= G_{\text{FIR}} \cdot J_\phi \quad \text{and} \quad \frac{\partial \psi_{\text{FIR}}}{\partial t} = G_{\text{FIR}} \cdot \frac{\partial J_\phi}{\partial t} \\ B_{Z \text{ FIR}} &= G_{Z \text{ FIR}} \cdot J_\phi \quad \text{and} \quad \frac{\partial B_{Z \text{ FIR}}}{\partial t} = G_{Z \text{ FIR}} \cdot \frac{\partial J_\phi}{\partial t}. \end{aligned} \quad (6.33)$$

Fitting the time derivatives of the polarimetry signals is computationally cheap, (compared to fitting the signals themselves in the equilibrium calculation), as the density profile, time derivative of density profile, and equilibrium magnetic field profile need be computed only once, as opposed to once per iteration. The only computation made on every iteration is the time rate of change of vertical field, which is simple matrix multiplication with the appropriate Green's table.

Time derivative of polarimetry data has not yet been incorporated into the fitting of the electric field. The measured change in signal is made of two parts, one related to a change in magnetic field and the other related to a change in electron density. In fitting the electric field the contribution due to the change in magnetic field is utilized, however the portion of the signal due to the electron density change is much larger. This leads to taking the difference of two similar-sized numbers to obtain data. Attempts to fit these data will wait until diagnostic upgrades allow simultaneous measurement of the polarization change and electron density, as lower uncertainties are expected.

### 6.3.4 Pressure Diagnostics

The pressure profile evolution is determined from electron density profile measurements with the FIR interferometer and time resolved electron temperature measurements with Thomson scattering[2]. The database generated contains full pressure profiles at several time slices throughout the PPCD experiment. A simple linear evolution is assumed between the measurements at  $t = 15.0\text{ms}$  and  $t = 16.5\text{ms}$ , and thus the rate of change of the pressure profile is determined. Neglecting the  $\frac{\partial P}{\partial t}$  terms introduces a noticeable error and inhibits accurate reconstruction of the other measurements.

### 6.3.5 Results of Time Derivative Fitting, PPCD Plasma

Presented here is the best fit to the time derivative data for the 400kA PPCD discharge. The data include the time derivatives of the total plasma current, and  $F$  and  $\Theta$  through the total toroidal flux and toroidal field at the wall. A substantial constraint is made with limited data from the MSE measurement of the on-axis magnetic field strength. A measurement at  $t = 15\text{ms}$  and a second measurement at  $t = 16.5\text{ms}$  give identical values for  $B(0)$  in this ensemble. It is reasoned that the derivative of this signal must be small at  $t = 15.6\text{ms}$ , incorporated into the fitting by using a data value of zero with a modest uncertainty of  $0.5\text{T/s}$ . Figure 6.10 shows the agreement between

the reconstruction and fit. Figure 6.11 shows the results of the electric field and equilibrium

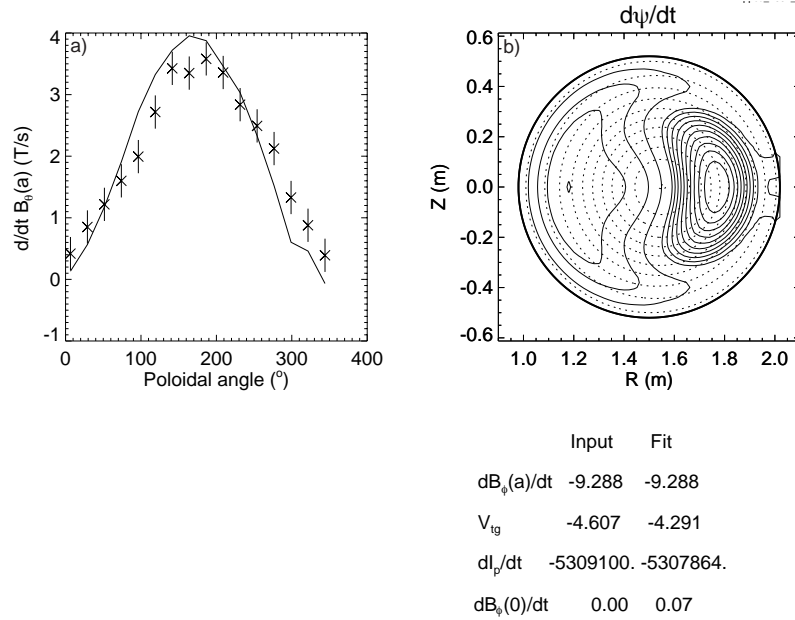


Figure 6.10: Data, reconstructed fit for time derivative reconstruction of the time derivative of the Grad-Shafranov equation. Good agreement is noted between the 0-D parameters, as well as quantitative agreement with the poloidal array signal derivatives.

calculations, total parallel fields are shown with solid lines along with the toroidal (dotted) and poloidal (dashed) contributions. Plot a) contains the toroidal and poloidal loop voltage profiles, b) is the equilibrium magnetic field profiles, c) is the equilibrium current density profile, d) is the  $\langle \mathbf{E} \cdot \mathbf{J} \rangle$  power deposition profile, e) is the parallel, poloidal and toroidal electric field profiles, f) is the  $\langle \mathbf{E} \cdot \mathbf{B} \rangle$  profile, g) is the  $\langle \mathbf{J} \cdot \mathbf{B} \rangle$  profile, and h) is the effective resistivity profile.

The electric field profiles are checked for accuracy by computing the Ohmic input power through the Poynting method, summarized in Figure 6.12. This method predicts an Ohmic input power of 1.9 MW (the difference of the volume integrated divergence of Poynting flux: 2.7MW, and the volume integrated rate of change of magnetic energy: 0.8MW). This implies roughly a fivefold

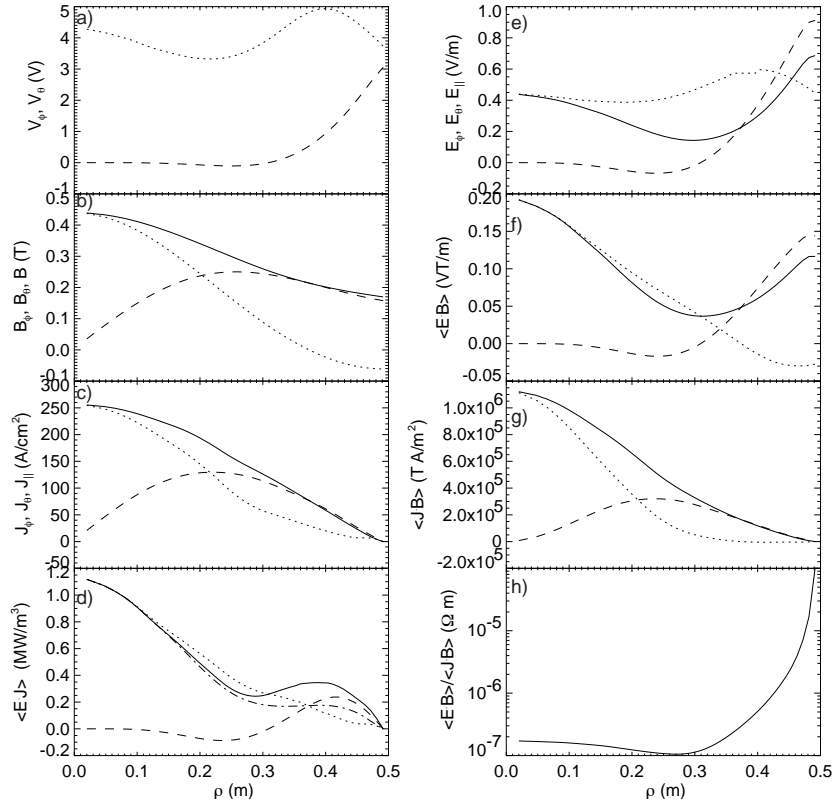


Figure 6.11: E field and equilibrium profiles calculated via fitting the time derivatives of measurements.

increase in energy confinement over the standard 400kA discharge<sup>2</sup>. The total Ohmic input power also roughly agrees (recall Table 4.1) with the volume integrated Ohmic input power using the Spitzer model with the edge-light corrected  $Z_{eff}$  profile (2.1 MW).

## 6.4 Ohm's Law and Resistivity

While these global numbers add veracity to the derivative and electric field calculations, the focus of this work is on resistivity. It is asserted that in the nearly MHD free PPCD plasmas, a simple Ohm's law is applicable  $\eta = E_{||}/J_{||}$  and the resistivity profile is measured by parallel electric field

<sup>2</sup>Consult with Biewer for all quoted confinement results and refined values.

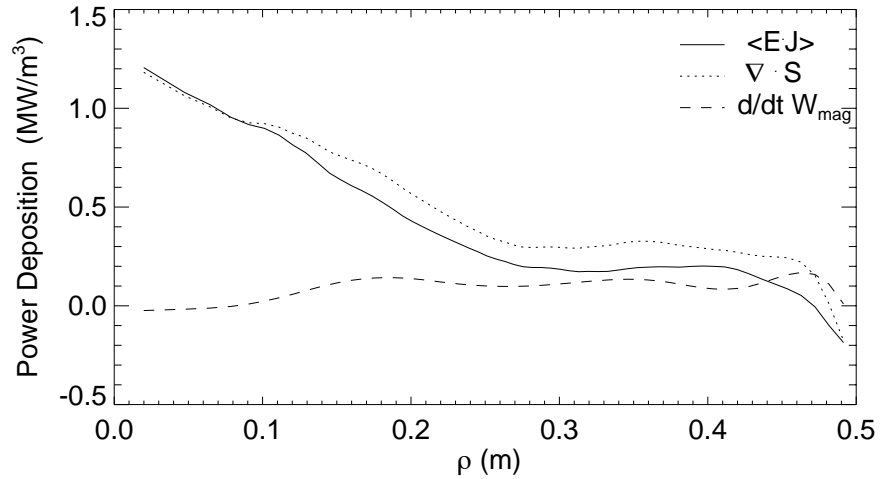


Figure 6.12: Power deposition profile calculated for PPCD discharge. Results are completely independent of any  $Z_{eff}$  information.

and current density profiles. Results in Figure 6.11 are applied to compute the resistivity and predict the  $Z_{eff}$  profile necessary to explain it in Figure 6.13.

## 6.5 Uncertainty in Electric Field

The uncertainty in the electric field is a fairly difficult topic to approach. The finite time difference results are well suited for an uncertainty estimate based on error propagation from the equilibrium quantities and simple difference techniques. However, just as the uncertainty in the MSTFit reconstructions was significantly affected by the model, the results for the electric field are very sensitive to the model set up. As an analytic method to find the uncertainty in this modeling does not yet exist, the time-tested method of Monte Carlo was implemented. Error analysis shows that the high ( $\sim 2 \times 10^{-7} \Omega\text{m}$ ) core resistivity is robust. The model parameters were varied over a significant range in 50 trials. The resulting electric field, resistivity, and implied  $Z_{eff}$  profiles varied in response. An envelope encompassing 2/3 of the resulting profiles was computed, and this

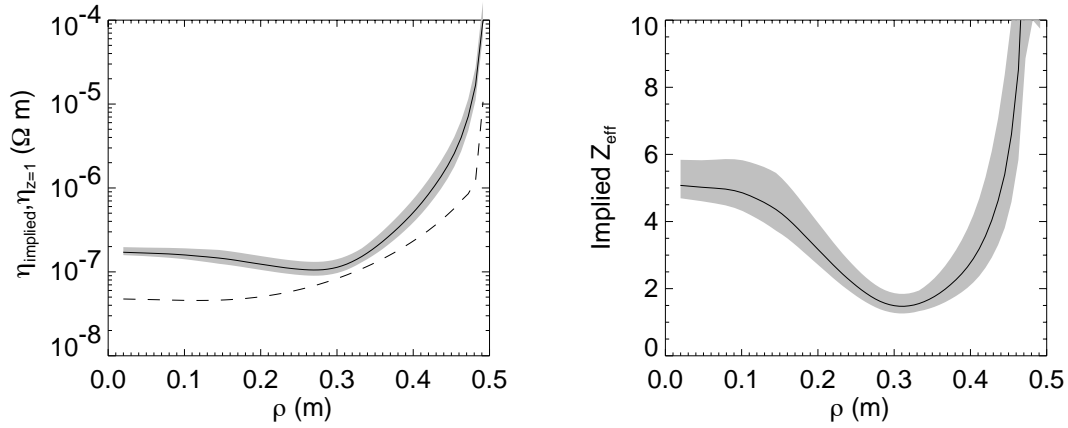


Figure 6.13: Ratio of parallel electric field to parallel current density; the resistivity profile given a simple Ohm’s law. For comparison, the Spitzer model for  $Z_{eff} = 1$  is plotted with a dashed line. On the right is the necessary  $Z_{eff}$  profile to match the effective resistivity with the Spitzer model.

was defined as  $\pm$  one standard deviation, shown as the shaded region in Figure 6.13.

## 6.6 Conclusions

The inductive electric field profile is determined, to within modest (better than a factor of two) uncertainty, for the 400kA PPCD discharge studied in this thesis. The total input power, as calculated by the Poynting flux, is in rough agreement with expectations from energy confinement time and  $Z_{eff}$  estimates. The electric field and parallel current density profiles are used to predict a resistivity profile under the assertion of a simple Ohm’s law, enabling a comparison with the Spitzer and neoclassical models.

# Bibliography

- [1] J. D. Jackson, *Classical Electrodynamics*, John Wiley and Sons, New York, NY, 1975.
- [2] T. M. Biewer, To be Published in Dissertation, Energy Confinement Measurements and Calculations.
- [3] C. B. Forest, K. Kupfer, T. C. Luce, P. A. Politzer, L. L. Lao, M. R. Wade, D. G. Whyte, and D. Wroblewski, *Physical Review Letters* **73**, 2444 (1994).

## Chapter 7

# Conclusions: Agreement of Measured and Modeled Resistivity Profiles

### Abstract

In this chapter, the results of the previous chapters are highlighted, and the results for the 400kA PPCD plasma are brought together. The modeled (Spitzer and neoclassical) resistivity profiles from Chapter 4, the parallel current density profile from Chapter 5, and the parallel electric field profile from Chapter 6 are used to compare a simple Ohm's law with experiment; rough agreement with the Spitzer model is observed. Neoclassical theory is not challenged, as the conductivity enhancing effect of fast electrons is not quantitatively addressed. Concluding this chapter is a discussion of future work this dissertation has motivated.

## 7.1 Summary

This dissertation began with an introduction to the RFP equilibrium and measurements of current density and electric field profiles. A review of electrical resistivity in a plasma naturally brought up a definition of  $Z_{eff}$ , and techniques to measure it were discussed. It was argued that a simple Ohm's law  $\langle E_{\parallel} \rangle = \eta \langle J_{\parallel} \rangle$  is valid during PPCD plasmas, where the magnetic fluctuation amplitude is very low. Chapter 2 laid the groundwork for quantitative spectroscopic measurements presented in this dissertation by a thorough description of the wavelength and intensity calibration of the necessary equipment. Chapter 3 reviewed the emission in the visible and NIR in MST, focusing on finding a region to measure bremsstrahlung. Several pollutants were identified in different wavelength regions. It was concluded that the simultaneous measurement of  $H_{\alpha}$  (to monitor neutral hydrogen density) and NIR emission in a hot, high density plasma enables extraction of the bremsstrahlung level. This method of active mantle radiation removal may prove useful elsewhere in the fusion community, as all bremsstrahlung measurements are plagued with edge-localized pollution. Also concluded was that the standard definition of  $Z_{eff} \equiv \frac{\sum_s n_s Z_s^2}{n_e}$  is inadequate in the presence of non-fully stripped ions. Collisional radiative modeling is necessary to quantitatively treat the problem; further discussion of this point is in the future work section.

The result of Chapter 4 is the Spitzer and neoclassical model resistivity profiles based on electron temperature and  $Z_{eff}$  measurements in 400kA PPCD plasmas. The parallel current density for this plasma is determined with MSTFit and several diagnostics; treated in detail in Chapter 5. This is the first internally constrained measurement of the current profile in a hot reversed field pinch. Chapter 6 presents two techniques to calculate the parallel electric field profile. A finite difference technique, which has been used successfully in the past, is applicable to standard discharges but fails in PPCD due to the externally imposed rapid change of equilibrium. A new technique, which solves the time derivative of the Grad-Shafranov equation while fitting the time derivatives of magnetic signals, is used to find the parallel electric field in 400kA PPCD discharges.

## 7.2 Results

Integration of the results of the previous three chapters enables a comparison of the effective resistivity  $\eta = \frac{\langle E_{\parallel} \rangle}{\langle J_{\parallel} \rangle}$  with the Spitzer and neoclassical models. Figure 7.1 is this comparison. The

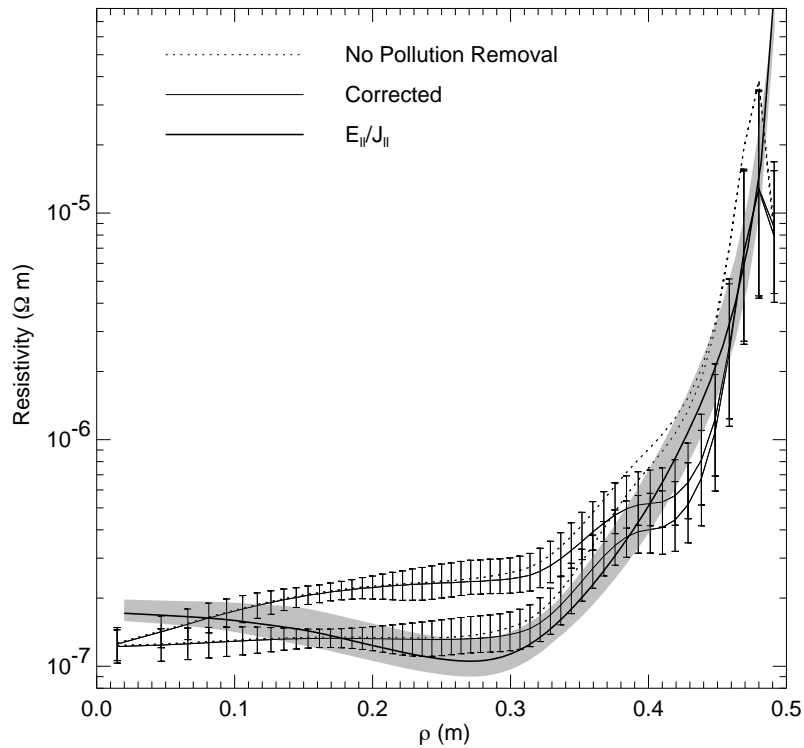


Figure 7.1: Best modeling leads to the resistivity profile described by the thick line.

two lines shown with error bars are the Spitzer (lower) and neoclassical (upper) models; the solid line with a shaded uncertainty band is the effective resistance,  $\eta = \frac{E_{\parallel}}{J_{\parallel}}$ . Also shown with dashed lines are the Spitzer and neoclassical resistivity models without removal of the edge pollution. The effective resistivity profile is in rough agreement with the Spitzer model from just outside the core through the mid-radius region. Neoclassical theory is not challenged, as conductivity enhancing effects of fast electrons have not yet been determined. A quantitative comparison is not justified in

the extreme edge, however the effective resistivity line falls between the 'corrected' and uncorrected lines for both the Spitzer and neoclassical models. With improvements to the  $Z_{eff}$  measurement through CRM, this edge uncertainty may be better resolved.

The primary result of this dissertation is that in nearly MHD free plasmas, the effective resistivity from an assumed simple Ohm's law ( $\eta = \frac{E_{\parallel}}{J_{\parallel}}$ ) is consistent with the Spitzer model. This is somewhat different than expectations, as calculations show a significant neoclassical effect due to particle trapping. This may be resolved with an explanation as simple as fast electrons. The measured hard x-ray flux (Section 4.2) is indicative of a significant fast electron population which reduces the resistivity. It is conceivable that fast electron effects nearly counteract the neoclassical resistivity enhancement. This is perhaps the most pressing issue raised in the future work section below.

## 7.3 Future Work

There are a number of open issues this thesis has addressed. Future work can be pursued on many fronts, here they are organized under three headings.

### 7.3.1 Resistivity, $Z_{eff}$ Measurements

In order to better specify the resistivity, there are a few avenues to pursue. In this dissertation, an experimentally sound solution is proposed for the widespread problem of excess (non-bremsstrahlung) light in attempted bremsstrahlung measurements. The method used to circumvent the excess light is to measure the pollution directly and use it to extract the bremsstrahlung component. Better understanding of the radiative processes at work may further improve this measurement, and perhaps allow a  $Z_{eff}$  measurement in standard MST plasmas.

### Collisional Radiative Modeling

A robust measurement of  $Z_{eff}$  awaits a complete collisional radiative model of the MST plasma. This would entail quantitative spectroscopic monitoring of several charge states of each of the dominant impurities through line radiation. Combined with electron density and temperature, neutral density, and radial transport profiles, the density profile of each charge state is determined. Calculation of the effective ionic charge by  $Z_{eff} = \frac{\sum_s n_s Z_s^2}{n_e}$  is then trivial. Recalling, however, the discussion in Section 3.7, this definition of  $Z_{eff}$  is not adequate to describe the collisionality (and thus resistivity) of the MST edge plasma. Sorting out non-fully stripped ion effects in bremsstrahlung measurements is conceivable with accurate profiles of each impurity state.

### Fast Electron Conductivity Enhancement

An obvious extension to this work is the inclusion of non-maxwellian (fast) electron effects on the conductivity, and this work is already in progress. As there is a known fast electron population due to the measured flux of hard x-rays, the effective resistivity must include a conductivity enhancement. This effect will bring the results in this work closer to the expected neoclassical prediction.

Quantitative incorporation of fast particle effects on the resistivity profile is already beginning with CQL3D simulations. In order to improve the modeling, measurements in the soft x-ray range will be needed. Currently the input to the code is a thermalized distribution below 1 keV and a fast population at 10-100keV. Data in the intermediate range will greatly improve the certainty in the modeled distribution function and hence the computed resistivity.

### Direct Measurement of Edge Resistivity

It is nearly impossible to discern the resistivity in the edge from spectroscopic measurements, as there is an abundance of pollutant emission from a variety of possible sources. A direct measurement of the edge resistivity is plausible with an oscillating edge field and a  $\dot{B}$  probe capable of

measuring the temporal and spatial behavior near the edge. The oscillating poloidal current drive (OPCD) team is leading an effort to perform these experiments in the near future. The OPCD experiment drives a large oscillatory current in the vacuum vessel, leading to a sinusoidal variation in  $B_\phi$  at the wall. In low MHD periods, this field diffuses classically and presents an opportunity to directly measure the resistivity through the attenuation and phase change of the penetrating field. An insertable probe originally designed and constructed to constrain edge  $B_\theta$  and  $B_\phi$  profiles for MSTFit equilibrium reconstructions is ideally suited to directly measure edge resistivity. Very limited data (shown in Figure 7.2 is an average over 9 shots) show the expected behavior. The

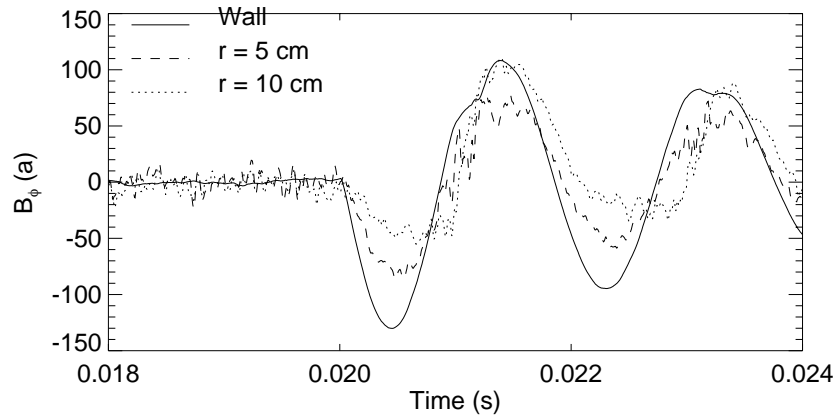


Figure 7.2: An oscillating toroidal field is applied at the wall, an insertable edge probe tracks the penetration of the field to  $r = 5\text{cm}$  and  $r = 10\text{cm}$  from the wall.

data is most reliable on the first falling edge at  $t = 20\text{ms}$ ; after this sawtooth activity complicates the interpretation. The first half cycle shows a definite attenuation of the field with radius and a slight phase lag with radius. Modeling of the problem[1] gives a reasonable resistivity value. It is not to be compared with the resistivities quoted in this work, as the edge conditions (electron temperature and density) are much different for these plasmas.

### 7.3.2 Equilibrium and Electric Field Modeling

It is a certainty that MSTFit modeling will continue. The latest version of MSTFit and the library associated with it have now topped 122,000 lines of code. Code maintenance and improvement are unending tasks as there are always numerous upgrades in the works. The time derivative fitting of the the Grad-Shafranov equation presents an exciting new method for determining the electric field profile. Accuracy of the fits will greatly improve with diagnostic upgrades, particularly time resolution of the MSE measurement.

#### Non-Iterative Solution to Time Derivative Fitting

A second possible improvement to the time derivative fitting is the implementation of a more direct solution to the problem. An iterative solution to the Grad-Shafranov equation is necessary for the equilibrium reconstruction, as  $F$  and  $p$  are functions of poloidal flux as determined by the toroidal current density; thereby putting the Grad-Shafranov equation in a transcendental form

$$J_\phi = \frac{2\pi F(g(J_\phi))F'(g(J_\phi))}{\mu_0 R} + 2\pi R P'(g(J_\phi)). \quad (7.1)$$

This is not the case for the time derivative fitting, as the free profiles are functions of the (specified) flux profile; in this problem  $\frac{\partial J_\phi}{\partial t}$  is well determined for a given set of free parameters describing the free functions. The direct solution is found by algebraic manipulation of equation 6.27 and substitution of equation 6.28 resulting in

$$\frac{\partial J_\phi}{\partial t} = \mathbf{H}^{-1} \cdot \left[ \frac{2\pi}{\mu_0 R} \left( F'(\psi) \frac{\partial F(\psi)}{\partial t} + F(\psi) \frac{\partial F'(\psi)}{\partial t} \right) + 2\pi R \frac{\partial p'(\psi)}{\partial t} \right] \quad (7.2)$$

where all quantities written as functions of flux are two dimensional matrices, as the flux is specified on the (R,Z) grid.  $\mathbf{H}$  is a matrix related to the Green's table ( $\mathbf{G}$ ) and the equilibrium quantities

by

$$\mathbf{H} = \mathbf{I} - \left[ \frac{2\pi}{\mu_0 R} (F'^2(\psi) + F(\psi)F''(\psi)) + 2\pi R p''(\psi) \right] \cdot \mathbf{G} \quad (7.3)$$

with  $\mathbf{I}$  denoting the diagonal identity matrix. While this development shows it is not necessary, in this work we have continued (for reliability) to use the iterative method developed for solving the Grad-Shafranov equation rather than attempting to invert the somewhat involved matrix equation 7.2.

### 7.3.3 General

The work presented in Section 3.5.4 (the identification of the structured molecular dissociation continuum in the visible range, measured at 350, 420, 500, and 520nm) opens the door for a new molecular hydrogen density diagnostic. An absolute measurement of the emissivity at these wavelengths along with further atomic (molecular) physics calculations can determine the density of molecular hydrogen. This would be useful in refined measurements of particle confinement time, as the electron sourcing due to molecular ionization can be important[2] and its contribution is ignored in current calculations.

# Bibliography

[1] J. Sarff, Private communication.

[2] K. Sawada and T. Fujimoto, *Journal of Applied Physics* **78**, 2913 (1995).

## Appendix A: Multicolor Background Survey

This appendix has three sections. The first plots the wavelength response of the individual bandpass filters, which are important to the measurements presented, but too burdensome to include in the text of this dissertation. The second section shows the line integrated profile measurements of the various colors (inversions not included, but are easily recomputed with MSTFit routines). These data are necessary for constructing Table 2.1 and, as they will certainly remain unpublished elsewhere, are included as they may prove helpful if the proposed molecular hydrogen diagnostic (Section 7.3.3) is pursued. This motivation carries into the third section, where the background emission measured along a central chord is plotted versus  $H_\alpha$  emission on an adjacent chord. This helps elucidate the difference in the background emission between the visible and in the near infrared on MST.

### A.1 Visible and NIR Continuum Wavelength Response

Absolute measurements of the continuum emission require an accurately determined wavelength response function. Shown in Figures A.1 - A.7 are the wavelength response functions at the target wavelength of each along with the response at the 656.3nm ( $H_\alpha$ ). The second plot is required to quantify the contamination of  $H_\alpha$  emission in the visible bremsstrahlung measurements. In each plot, the upper line is the lamp emission with no filters in place, the lower plot is the measured emission with the filter(s) in place, and the transfer function is the ratio of the two traces. The measurement at 1040nm is limited by the CVI spectrometer.

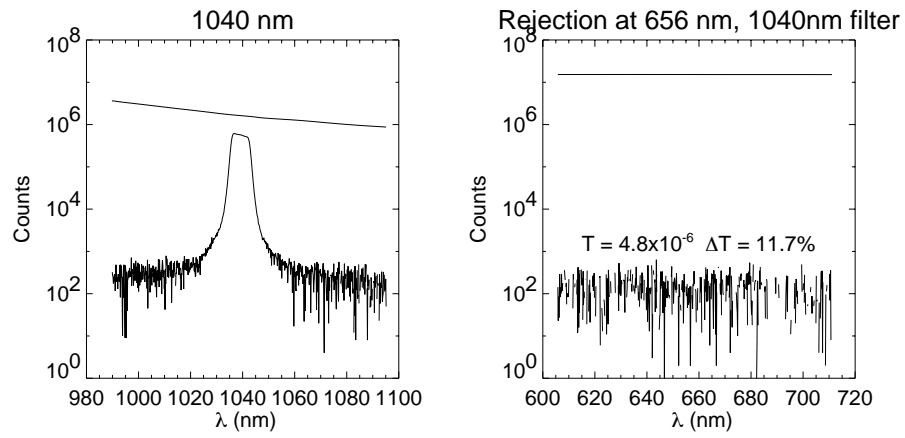


Figure A.1: Filter rejection measurement: 1040nm pass band filter

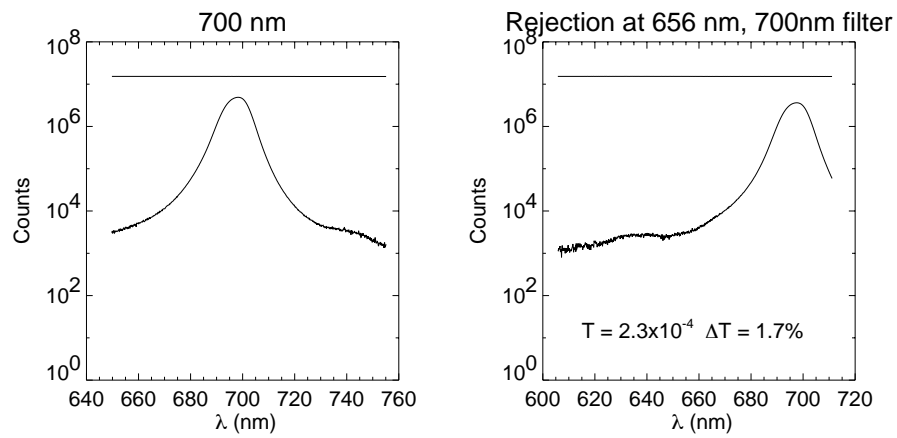


Figure A.2: Filter rejection measurement: 700nm pass band filter

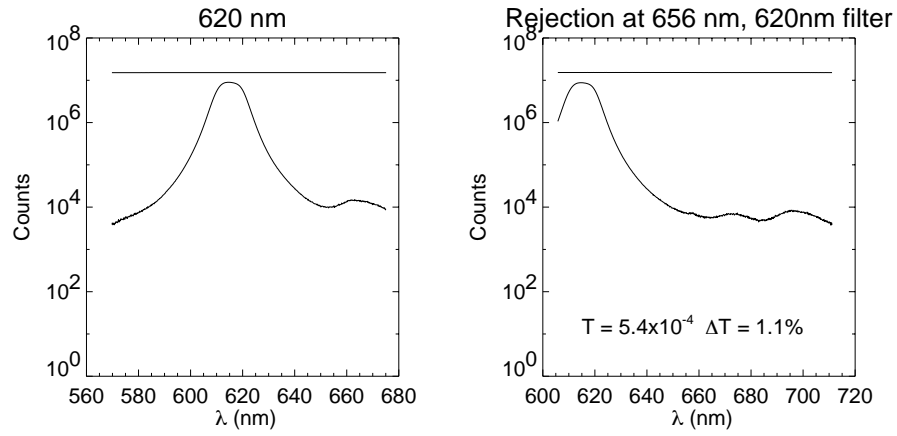


Figure A.3: Filter rejection measurement: 620nm pass band filter

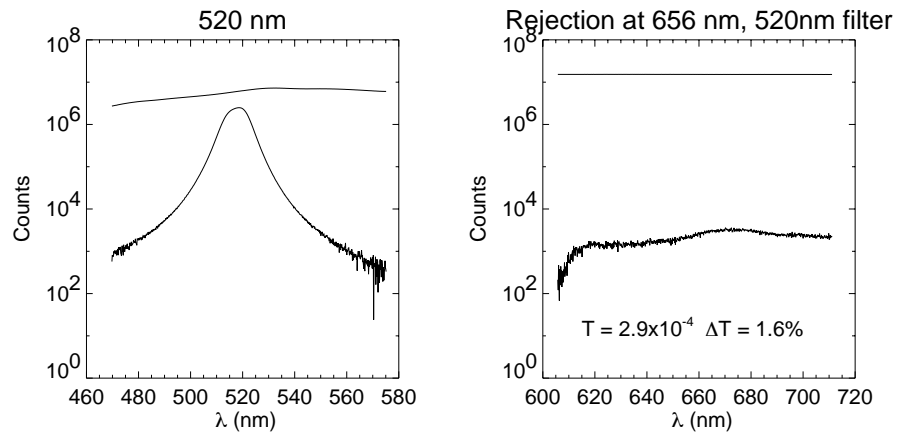


Figure A.4: Filter rejection measurement: 520nm pass band filter

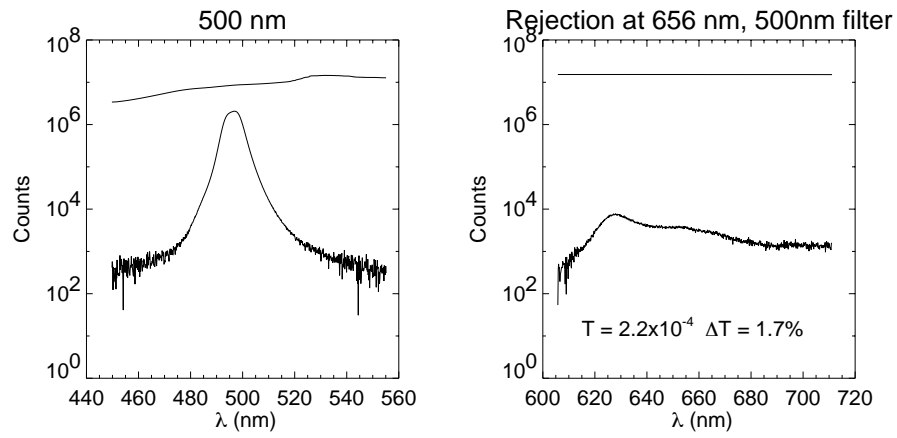


Figure A.5: Filter rejection measurement: 500nm pass band filter

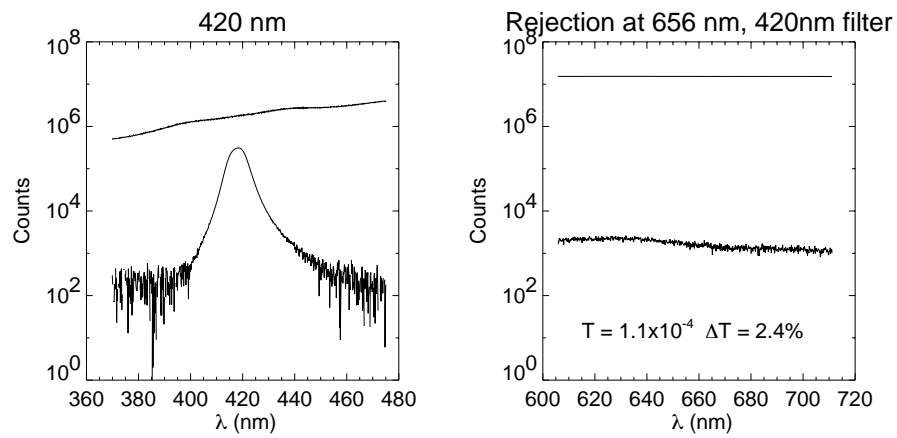


Figure A.6: Filter rejection measurement: 420nm pass band filter

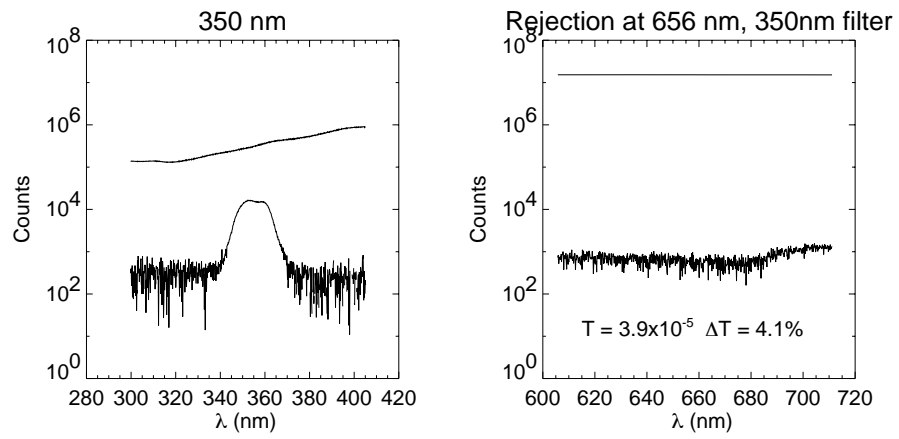


Figure A.7: Filter rejection measurement: 350nm pass band filter

## A.2 Line Integrated Signals

Presented here is a line integrated profile for each color, obtained by averaging the emission on a given viewing chord over 10 shots, then repeating the procedure on a different chord. An 11 point profile is obtained in 110 good shots in this manner. These data are taken from quiet periods between sawtooth crashes in 200kA standard ( $C_1$ ,  $C_2$  only) discharges. It should again be noted that the continuum behavior in the 700nm measurement is not well measured due to pollution from a He I line at 707nm.

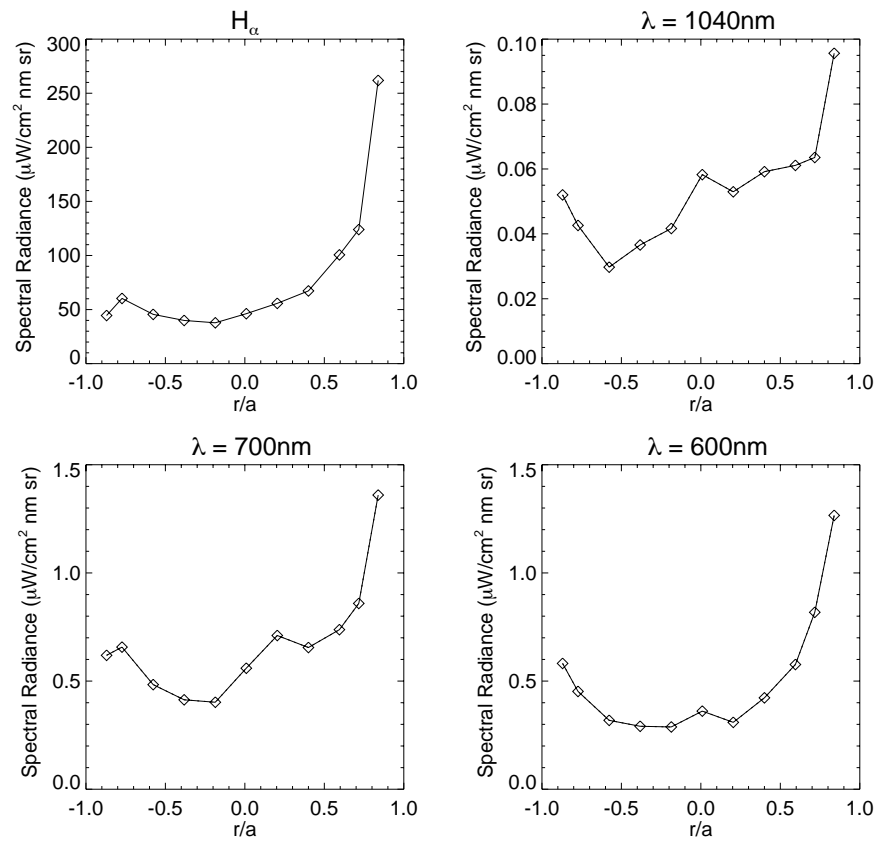


Figure A.8: Line integrated profiles for  $H_\alpha$  and three bremsstrahlung attempts

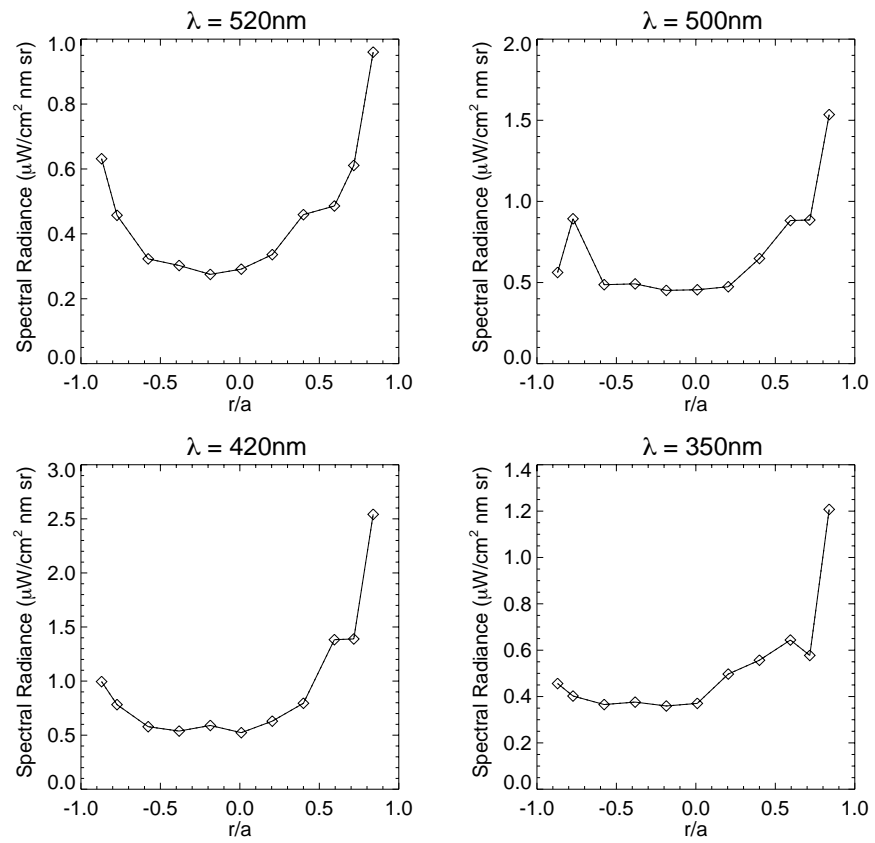


Figure A.9: Line integrated profiles for four visible bremsstrahlung attempts

### A.3 Behavior of Continuum Measurements Versus $H_\alpha$ Emission

Scatter plots of continuum emission versus  $H_\alpha$  emission at each wavelength are presented here. If the continuum were (mostly) bremsstrahlung, there should be no apparent trend between these signals. However, the continuum in MST is dominated by molecular and atomic hydrogen emission. These data, again taken from quiet periods between sawtooth crashes in 200kA standard ( $C_1$ ,  $C_2$  only) discharges, were key in determining which wavelength to choose for the bremsstrahlung attempt. The measurement at 1040nm shows good linearity in  $H_\alpha$ , enabling a linear extrapolation technique to remove the neutral pollutant contribution. As the short visible wavelengths are dominated by emission from dissociation of  $H_2$  molecules, they behave differently. These data are perhaps a key to measuring the density of molecular hydrogen in MST, as well as determining its effect on the electron source rate.

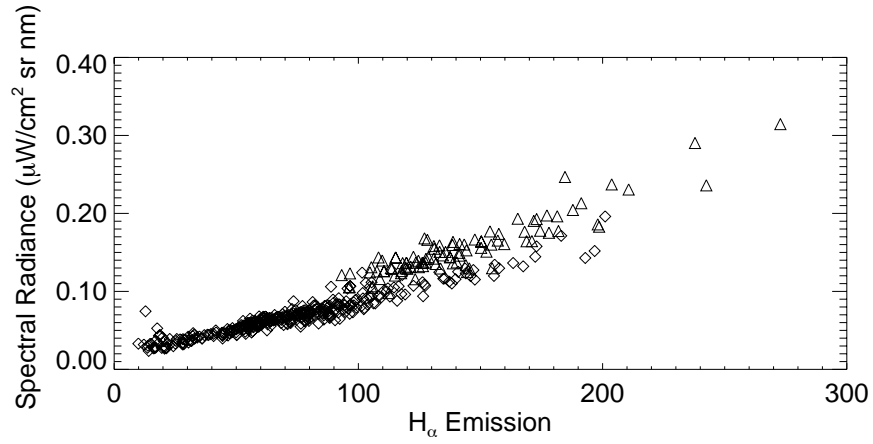


Figure A.10: Emission at 1040nm vs H<sub>α</sub> emission, separated by electron density. the data represented by diamonds are for low density (average  $\bar{n}_e = 1.1 \times 10^{13} \text{cm}^{-3}$ ), while the triangles represent high electron density (average  $\bar{n}_e = 2.5 \times 10^{13} \text{cm}^{-3}$ ).

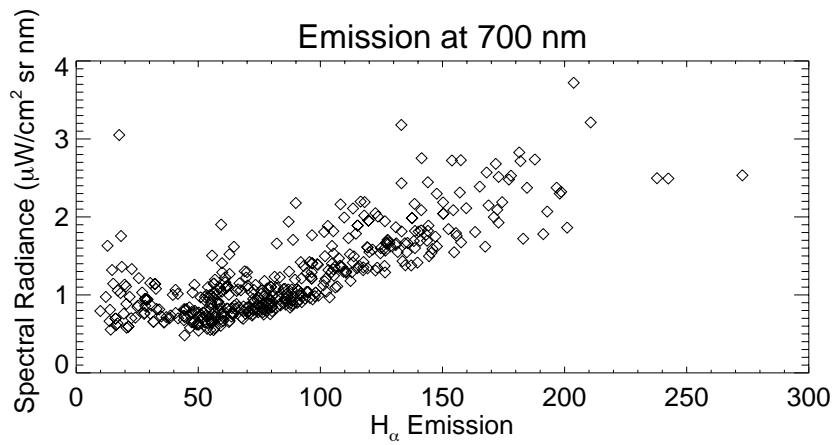
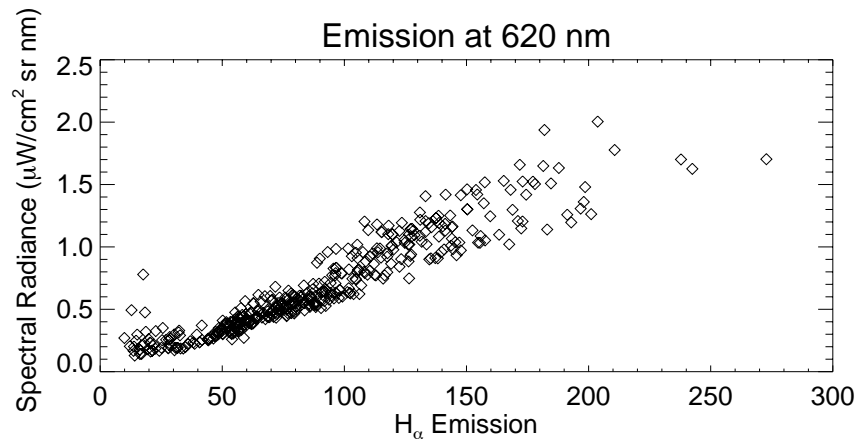
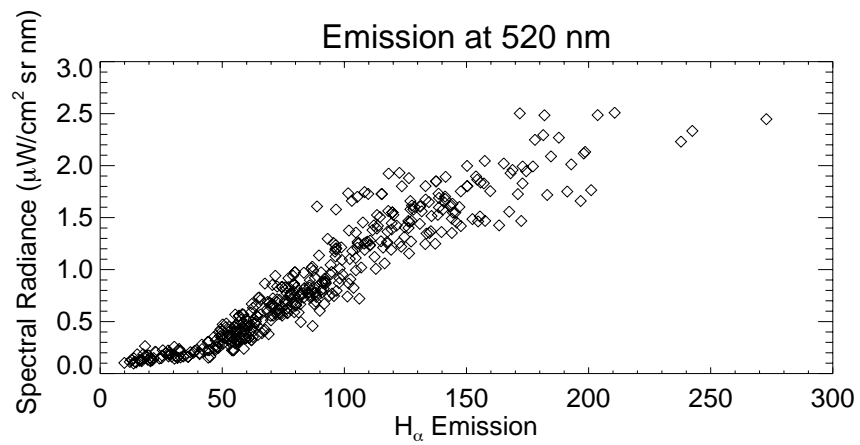
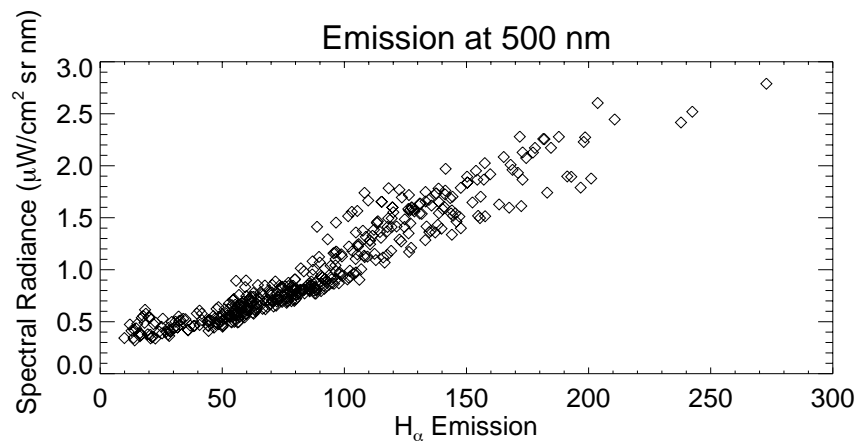
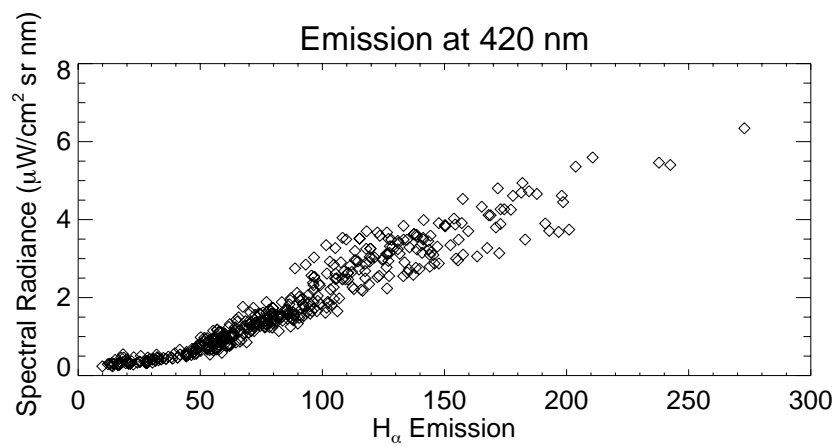


Figure A.11: Emission at 700nm vs H<sub>α</sub> emission

Figure A.12: Emission at 620nm vs  $H_\alpha$  emissionFigure A.13: Emission at 520nm vs  $H_\alpha$  emission

Figure A.14: Emission at 500nm vs  $H_\alpha$  emissionFigure A.15: Emission at 420nm vs  $H_\alpha$  emission

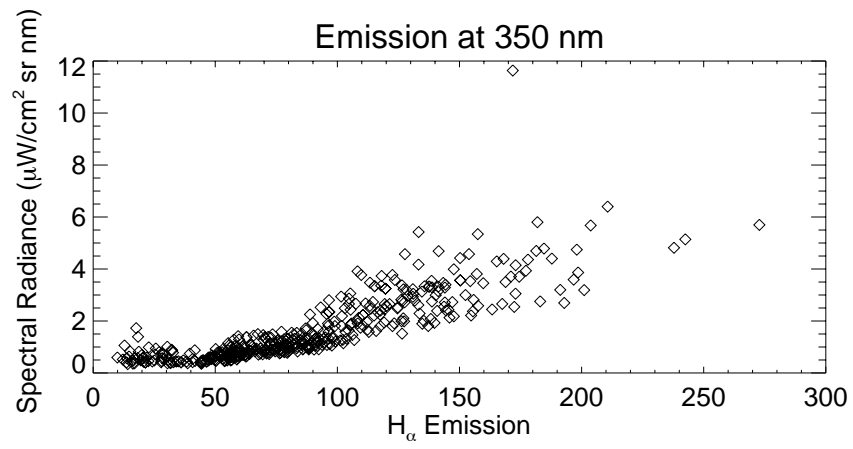


Figure A.16: Emission at 350nm vs  $H_\alpha$  emission

## Appendix B: MSTFit Outputs

### B.1 Equilibrium Quantities

After determining the consistent Grad-Shafranov equilibrium which best matches all the experimental data, a variety of post processing routines are run. Listed in Table B.1 are the current list of flux-surfaced averaged profiles and 0D quantities calculated by the standard MSTFit output. A more thorough treatment now follows for the Suydam critical pressure limit, internal inductance and trapped fraction. The interested reader can refer to Freidberg[1], Chen[2], or Goldston and Rutherford[3] for more details on the other quantities. The Suydam criterion for marginal stability to interchange modes is[1]

$$\frac{rB_\phi^2}{\mu_0} \left( \frac{q'}{q} \right) + 8p' > 0 \quad (\text{B.1})$$

from which a critical pressure gradient can be determined. A pressure gradient exceeding the value specified in equation B.1 is unstable to interchange modes, thereby predicting an upper bound on the RFP pressure profile. The calculation of the trapped particle fraction follows the development in Hirshman and Sigmar[4]. The circulating fraction is

$$f_c = \frac{3}{4} \langle B^2 \rangle \int_0^{\lambda_c} \frac{\lambda d\lambda}{\sqrt{1 - \lambda B}} \quad (\text{B.2})$$

where  $\lambda$  is the pitch angle, defined by the ratio of magnetic moment to total kinetic energy  $\lambda = \frac{\mu}{E}$ . The critical value occurs when the pitch angle lies on the boundary of the loss cone,  $\lambda_c = \frac{1}{B_{max}}$

where  $B_{max}$  is the largest field strength along the field line. This implies

$$\begin{aligned} \text{circulating: } & 0 \leq \lambda \leq \lambda_c \\ \text{trapped: } & \lambda_c \leq \lambda \leq \frac{1}{B_{min}}. \end{aligned} \tag{B.3}$$

The integration in equation B.2 is over the pitch angles that lead to circulating particles resulting in the fraction circulating, and the trapped fraction is simply  $f_t = 1 - f_c$ . This calculation, along with accurate equilibrium reconstruction, facilitates a quantified study of the neoclassical effect on the resistivity in MST.

Profile	Description
$\psi$	poloidal flux coordinate
$\rho_v$	length coordinate defined by plasma volume
$F$	$RB_\phi$
$F'$	$\frac{\partial F}{\partial \psi}$
$P$	Pressure
$P'$	Pressure gradient
$J_\phi$	Toroidal current density
$ B $	Magnetic field strength
$B_\theta$	Poloidal magnetic field
$B_\phi$	Toroidal magnetic field
$B_{min}$	Minimum $ B $ on a surface
$B_{max}$	Maximum $ B $ on a surface
$f_t$	Trapped particle fraction*
$J_{  }$	$\frac{\mathbf{J} \cdot \mathbf{B}}{ \mathbf{B} }$
$\lambda$	$\frac{\mathbf{J} \cdot \mathbf{B}}{ \mathbf{B} ^2}$
$\Phi$	Toroidal flux enclosed from 0 to $\psi$
$q$	safety factor, $\langle \frac{rB_\phi}{RB_\theta} \rangle$
$dqdr$	$\frac{\partial q}{\partial \psi}$
$s$	Magnetic shear, $\frac{\rho_v}{q} \frac{\partial q}{\partial \psi}$
$w$	Magnetic well, $2 \frac{V}{\langle B^2 \rangle} \frac{d}{dV} \langle \mu_0 p + B^2/2 \rangle$
$R_{surf}$	Center of flux surface
$C_{surf}$	Circumference of flux surface
$P'_{crit}$	Suydam pressure gradient limit*
$W_{mag}$	Total magnetic energy enclosed from 0 to $\psi$
$W_{kin}$	Total kinetic energy enclosed from 0 to $\psi$
$K$	Magnetic helicity $\int \phi d\psi - \phi(a)\psi(a)$
$\beta$	Ratio of pressure to magnetic pressure, $\frac{2\mu_0 P}{ \mathbf{B} ^2}$
$P_{ave}$	0D: Volume average pressure, $\frac{\int p dV}{V}$
$\beta_p$	0D: Poloidal $\beta$ , $\frac{2\mu_0 P_{ave}}{B_\theta^2(a)}$
$\beta_t$	0D: Toroidal $\beta$ , $\frac{2\mu_0 P_{ave}}{B_\phi^2(a)}$
$l_i$	0D: Normalized internal inductance, $\frac{2}{a^2 B_\theta^2(a)} \int_0^a B_\theta^2 r dr$

Table B.1: Standard MSTFit flux-surface averaged and 0D quantities.

## B.2 Particle Transport Analysis

A set of subroutines has been developed to compute the particle flux, source rate and confinement time from measurements of  $H_\alpha$  emission and electron density. This analysis was motivated by and conducted in collaboration with Lanier[5]. The profiles computed are listed in the Table B.2 and a summary of the calculations is included.

Defining  $S$  as the rate of particles entering and  $R_L$  as the rate of particles leaving the volume bounded by some surface  $\psi$ , it is clear that

$$S - R_L = \frac{\partial n}{\partial t} \quad (\text{B.4})$$

where  $n$  is the average particle density in the sample region. In MST, the electron source rate  $S$  is dominated by ionization of atomic hydrogen and the electron loss rate is dominated by diffusive transport (as opposed to atomic recombination) processes. The flux of particles leaving the surface  $\Gamma_r = nv_r$  is related to the  $R_L$  by

$$\int dA \Gamma_r = \int dV R_L = \int dV \left( S - \frac{\partial n}{\partial t} \right) \quad (\text{B.5})$$

by particle conservation. Considering a toroidal (flux) surface defined by a minor radius  $\rho$  and assuming the particle diffusion is constant on the flux surface implies

$$2\pi\rho 2\pi R \Gamma_r = \int_0^\rho \left( S - \frac{\partial n}{\partial t} \right) \frac{\partial V}{\partial \rho} d\rho \quad (\text{B.6})$$

upon integration of the left hand side of equation B.5. The electron source  $S$  is obtained through a measurement of  $H_\alpha$  emission as the number of  $H_\alpha$  photons is directly proportional to the number of hydrogen ionizations[5] over the electron temperature range of MST. Inversion of the  $H_\alpha$  signals gives a source profile, and inversion of the time derivatives of the FIR interferometer signals leads

directly to the  $\frac{\partial n}{\partial t}$  profile.

The particle diffusion rate of electrons is defined by the measured flux,  $\Gamma_r = D\nabla n_e$ , or

$$D = \frac{\Gamma_r}{\nabla n_e} \quad (\text{B.7})$$

where the derivative of the density profile (a function of flux) is easily computed.

A particle confinement time is defined as the number of particles in a volume divided by the particle source rate into that volume. This is calculated on each of the toroidal flux surfaces used in this analysis by

$$\tau_p^*(\rho) = \frac{\int_0^\rho n \frac{\partial V}{\partial \rho} d\rho}{\int_0^\rho (S - \frac{\partial n}{\partial t}) \frac{\partial V}{\partial \rho} d\rho} \quad (\text{B.8})$$

where the global particle confinement time is the value at the plasma boundary  $\tau_p = \tau_p^*(\rho = a)$ .

Finally, the measurement of the  $H_\alpha$  and  $n_e$  profiles allows a calculation of the neutral particle density in MST[5] by

$$n_H = \frac{H_\alpha}{A n_e \langle \sigma v \rangle} \quad (\text{B.9})$$

where the constant A is the ratio of  $H_\alpha$  photons to ionizations, quoted as 0.08-0.09 for MST parameters, and  $\langle \sigma v \rangle$  is the ionization rate which is weakly dependent on temperature but is on the order of  $2 \times 10^{-8} \text{ cm}^{-3} \text{ s}^{-1}$  in MST.

Profile	Description
$n_e$	electron density
$\nabla n_e$	electron density gradient
$\frac{\partial n_e}{\partial t}$	time derivative of electron density
$S$	electron source rate
$\Gamma_r$	Radial particle flux
$D$	Particle diffusion rate, $\frac{\Gamma_r}{\nabla n_e}$
$n_H$	Neutral hydrogen density
$\tau_p^*$	effective flux surface particle confinement time
$\tau_p$	Particle confinement time

Table B.2: Standard Outputs of Particle Transport Analysis

In MST, the  $H_\alpha$  emission (and hence source profile) is not a good function of flux, so the two dimensional inversion described above is used to find  $S(R,Z)$ . The flux surface average  $\langle S \rangle$  is computed and used in the transport analysis here, making these results representative of the one dimensional behavior. In reality, the  $H_\alpha$  emission and hence calculated quantities of particle flux, diffusion and neutral density are much higher on the outboard edge of MST.

The results here go beyond the scope of a particle transport analysis. For a complete energy transport analysis, the heat loss contribution due to particle loss and convection must be computed.

### B.3 Energy Transport Analysis

The energy transport analysis package in MSTFit is centered around a calculation of the electron thermal heat conduction  $\chi_e$  and energy confinement time developed by Biewer[6]. This utilizes the equilibrium reconstruction for geometry and all available data (and estimates where data aren't available) for electron and ion density, temperature and their respective gradients. Table B.3 is a list of the quantities returned by the energy transport analysis code. Many of them are passed in as data or input from other processing routines. A brief description of the computed quantities follows for electrons; results for ions are made by replacing electron by ion in all subscripts except where noted. The interested reader is referred to the Biewer thesis for a detailed description of this analysis.

#### Resistivity Calculation

Collisions between particles in the plasma are the fundamental cause of electrical resistivity. The temperature and density profiles are used to calculate thermal velocities ( $v_{th,e} = \sqrt{T_e/m_e}$ ) collision

frequencies and collision lengths. The following results are taken from Goldston and Rutherford[3]

$$\begin{aligned}
\nu_{ei} &= \sqrt{\frac{2e_e}{\pi^3 m_e T_e^3} \frac{Z_{eff} n_e e_e^2 \ln \Lambda}{12 \epsilon_0^2}} \\
\nu_{ee} &= \sqrt{\frac{2e_e}{\pi^3 m_e T_e^3} \frac{n_e e_e^2 \ln \Lambda}{12 \epsilon_0^2}} \\
\nu_{ii} &= \sqrt{\frac{e_e}{\pi^3 m_i T_i^3} \frac{Z_{eff}^3 n_e e_e^2 \ln \Lambda}{12 \epsilon_0^2}} \\
\nu_{en} &= n_H \sigma_{en} \sqrt{\frac{T_e}{m_e}} \\
\lambda_e &= \frac{v_{th,e}}{\nu_{ei} + \nu_{ee} + \nu_{en}} \\
\lambda_i &= \frac{v_{th,i}}{\nu_{ei} + \nu_{ii}}
\end{aligned} \tag{B.10}$$

with  $\sigma_{en} \sim 5 \times 10^{-19} m^2$  obtained from the NRL formulary[7]. The quantity  $\nu^*$  turns up in the calculation of the neoclassical resistivity as a factor which determines collisional detrapping[4]. This term tends to reduce the trapped particle effects, as collisions remove the particle from its trapped orbit. The value is the ratio of an effective collision frequency to the bounce frequency  $\nu^* = \frac{\nu_{eff}}{\omega_{bounce}}$  where  $\nu_{eff} = \nu_{ei}/\epsilon$  and  $\omega_{bounce} = \frac{\sqrt{\epsilon} L}{v_{th,e}}$ . The term  $L$  corresponds to the distance traveled in traversing a trapped orbit  $L = 2\pi\rho\frac{B}{B_0}$ , and  $\epsilon = \frac{f_i^2 \pi^2}{8}$ .

With  $\nu^*$ , all the quantities necessary to compute the resistivity[8] are available, and

$$\eta_{Sp} = 1.04 \times 10^{-4} \frac{Z_{eff} \ln \Lambda}{T_e^3 / 2f(Z_{eff})} \tag{B.11}$$

where the Coulomb logarithm[2] is

$$\ln \Lambda = \ln \left( 1.547 \times 10^{10} \sqrt{\frac{T_e^3}{n_e}} \right) \tag{B.12}$$

and the electron-electron collision correction[8] to the resistivity is given by

$$f(Z) = \frac{1. + 2.96Z + 0.753Z^2}{1. + 1.198Z + 0.222Z^2}. \quad (\text{B.13})$$

The neoclassical correction is two additional multiplicative factors to the Spitzer result. The importance of each term is more apparent in the expressions for conductivity,  $\sigma = \eta^{-1}$ ,

$$\sigma_{neo} = \sigma_{Sp} \times \left[ 1 - \frac{f_t}{1 + \xi(Z_{eff})\nu_{*e}} \right] \times \left[ 1 - \frac{C_R(Z_{eff})f_t}{1 + \xi(Z_{eff})\nu_{*e}} \right]. \quad (\text{B.14})$$

In this equation,  $f_t$  is the trapped fraction,  $\xi(Z_{eff})$  is the effective electron collisionality, and  $C_R(Z_{eff})$  is the conductivity reduction due to electron-electron collisions[4]. The two collisionality terms vary with  $Z_{eff}$  as

$$\xi(Z) = 0.58 + 0.20Z \text{ and } C_R = \frac{0.56 \times (3.0 - Z)}{Z(3.0 + Z)}. \quad (\text{B.15})$$

These calculations show that with a measured temperature, density and  $Z_{eff}$  profile, two dimensional equilibrium modeling of the magnetic field supplies all the information needed to calculate the neoclassical resistivity profile.

### Heat Flux Balance

A full treatment of energy flux in the plasma is necessary to compute the electron thermal conductivity profile. The sum total of the heat flux

$$\sum \text{All Heat Flux} = \frac{\dot{W}_e}{A} = \frac{1}{A} \frac{\partial}{\partial t} \int_V n_e T_e dV \quad (\text{B.16})$$

where  $\dot{W}_e$  is the time rate of change of stored thermal energy, which is positive for a net increase in time of the volume integrated product of electron density and temperature. Identification of the

primary contributors to heat flux for the electrons leads to

$$\frac{\dot{W}_e}{A} = \frac{P_\Omega}{A} - \frac{P_{rad}}{A} - \frac{P_{ei}}{A} - \dots + \chi_e n_e \nabla T_e + \frac{5}{2} D T_e \nabla n_e \quad (\text{B.17})$$

where A is the area of a toroidal flux surface and the sign convention employed assigns a negative value to flux moving outward through the surface and a positive value for flux moving in. It should be noted that the only term supplying energy to the electrons is through  $P_\Omega = \int \eta J_\parallel^2 dV$ ;  $P_{rad}$  is the magnitude of the radiated power lost,  $P_{ei} = 3 \frac{m_e}{m_i} (T_e - T_i) \nu_{ei}$  is positive for power delivered from the electrons to the ions (and carries an explicit minus sign in the equation above); a positive D and  $\chi_e$  are both indicative of energy flux moving out, as the gradients of the electron density and temperature are both negative. Equation B.17 is rewritten in terms of a net heat flux,  $Q_e$  as

$$\chi_e n_e \nabla T_e + \frac{5}{2} D T_e \nabla n_e = - \frac{P_\Omega - \dot{W}_e - P_{rad} - P_{ei} - \dots}{4\pi^2 R \rho} \equiv -Q_e \quad (\text{B.18})$$

The result for ions is somewhat similar, but there is no  $P_\Omega$  or  $P_{rad}$  as these are assumed to affect the electron energy only; the sign on the  $P_{ei}$  term must be reversed as it now represents the source

$$\chi_i n_i \nabla T_i + \frac{5}{2} D T_i \nabla n_i = - \frac{P_{ei} - \dot{W}_i - P_{rad} - P_{ei} - \dots}{A} \equiv -Q_i \quad (\text{B.19})$$

Solving for the thermal conductivities gives

$$\begin{aligned} \chi_e &= \frac{-Q_e - \frac{5}{2} D T_e \nabla n_e}{n_e \nabla T_e} \\ \chi_i &= \frac{-Q_i - \frac{5}{2} D T_i \nabla n_i}{n_i \nabla T_i} \end{aligned} \quad (\text{B.20})$$

where the sign of  $\chi_e$  will be positive for an outward flow of energy, as  $Q_e$  is positive and larger than the convected portion ( $DT\nabla n$ ) and the temperature gradient in the denominator is negative. It is also apparent that a value for D is necessary to determine a numerical value for  $\chi$ . Ideally,

the data to measure  $D$  are collected and the result is computed as described in Section B.2. If this is not available,  $\chi$  is computed for several modeled values of  $D$ ,

$$\begin{aligned}
 \text{Classical: } D_{cl} &= \frac{\eta P}{B^2} \\
 \text{Bohm: } D_{Bohm} &= \frac{T_e}{16eB} \\
 \text{Stochastic: } D_{st} &= \sqrt{\frac{\pi}{8}} \frac{Q_e}{n_e T_e \left( \frac{-\nabla n_e}{n_e} - \frac{3}{2} \frac{\nabla T_e}{T_e} - \frac{eE_A}{T_e} \right)}.
 \end{aligned} \tag{B.21}$$

$D_{cl}$  is estimated[2] from a radial velocity found by taking the perpendicular component of Ohm's law and is orders of magnitude lower than the measured diffusion. The Bohm diffusion coefficient is a semi-empirical formula which has modest agreement with experiment[2]. The calculation of  $D_{st}$  is based on the free streaming of particles through regions of radial magnetic fluctuations. A positive radial electric field

$$E_A = -\frac{T_e}{en_e} \nabla n_e - \frac{\nabla T_e}{2e} \frac{6\Gamma T_e - Q_e}{2\Gamma T_e - Q_e} \tag{B.22}$$

develops to impede the electron diffusion and enforce ambipolar transport.

### Energy Confinement Calculation

The energy confinement time is defined as the total energy stored in the plasma divided by the rate at which power is lost. This requires a measurement of the Ohmic input power and the rate at which energy is stored (the time rate of change of stored energy), as

$$\tau_{Ee} = \frac{W_e}{P_\Omega - \dot{W}_e}. \tag{B.23}$$

A second global parameter of interest is the poloidal  $\beta$  defined as

$$\beta_p = \frac{\frac{1}{V} \int P dV}{\frac{B_\theta^2(a)}{2\mu_0}}. \quad (\text{B.24})$$

These quantities are useful in evaluation of the RFP plasma.

Profile	Description
$T_e, T_i$	electron, ion temperature
$\nabla T_e, \nabla T_i$	electron, ion temperature gradient
$n_e, n_i$	electron, ion density
$\nabla n_e, \nabla n_i$	electron, ion density gradient
$P, \nabla P$	Pressure, Pressure gradient
$\frac{\partial}{\partial t} T_e, n_e$	Time derivatives $T_e, n_e$ (and $T_i, n_i$ )
$W_e, W_i$	Stored electron, ion energy
$\frac{\partial}{\partial t} W_e, W_i$	Time derivative of stored energy
$Z_{eff}$	Effective ion charge
$\nu_{ei}, \nu_{en}$	Collision frequencies: electron-ion, electron-neutral
$\nu_{ee}, \nu_{ii}$	Collision frequencies: electron-electron, ion-ion
$\nu^*$	Bounce frequency
$\eta_{Spitzer}, \eta$	Spitzer, neoclassical resistivity
$n_H$	Neutral hydrogen density
$S$	electron source rate
$\Gamma_r$	Radial particle flux
$D_{meas}$	Measured particle diffusion rate
$D_{cl}$	Classical particle diffusion rate
$D_{Bohm}$	Particle diffusion rate, Bohm calculation
$D_{st}$	Stochastic field diffusion rate
$E_a$	Ambipolar radial electric field
$P_{ei}$	Electron to ion heating rate
$P_{rad}$	Radiated Power
$Q_e, Q_i$	Electron, ion heat flux
$\chi_e, \chi_i$	Electron, ion thermal conductivity
$\beta_p$	Poloidal $\beta$
$\tau_p$	Particle confinement time
$\tau_e$	Energy confinement time

Table B.3: Standard outputs of energy transport analysis.

## B.4 MHD Stability Analysis

A result of MSTFit is an accurate reconstruction of the parallel current profile, which has implications on the MHD stability. MSTFit does not have its own stability analysis package, however the code is capable of calling other IDL or Fortran routines. Currently, MSTFit is set up to call RESTER[9] with the equilibrium information. RESTER is a one dimensional pressureless  $\Delta'$  calculation which gives insight to ideal and resistive MHD stability of the dominant modes in MST.

## B.5 EQDSK Files

To maximize the utility of the reconstructed equilibrium, MSTFit has been programmed to write an output file of the EQDSK type. These files contain the equilibrium information in a format used by several important codes including the CQL3D Fokker-Planck code and GENRAY radio frequency ray tracing code. This has proved beneficial to the overall research effort on MST.

# Bibliography

- [1] J. P. Freidberg, *Ideal Magnetohydrodynamics*, Plenum Press, New York, NY, 1987.
- [2] F. F. Chen, *Introduction to Plasma Physics and Controlled Fusion*, Plenum Press, New York, NY, 1984.
- [3] R. J. Goldston and P. H. Rutherford, *Introduction to Plasma Physics*, Institute of Physics Publishing, Philadelphia, PA, 1995.
- [4] S. P. Hirshman and D. J. Sigmar, *Nuclear Fusion* **21**, 1079 (1981).
- [5] N. E. Lanier, *Electron Density Fluctuations and Fluctuation Induced Transport in the Reversed Field Pinch*, PhD thesis, University of Wisconsin-Madison, 1999.
- [6] T. M. Biewer, To be Published in Dissertation, Energy Confinement Measurements and Calculations.
- [7] J. D. Huba, NRL plasma formulary, 1998, NRL/PU/6790-98-358.
- [8] L. Spitzer Jr., *Physics of Fully Ionized Gases*, Interscience Publishers, John Wiley and Sons, New York, New York, 1962.
- [9] C. R. Sovinec, *Magnetohydrodynamic Simulations of Noninductive Helicity Injection in the Reversed Field Pinch and Tokamak*, PhD thesis, University of Wisconsin-Madison, 1995.